Morphogenesis and Cell Wall Mechanics of *Saccharomyces cerevisiae*

DISSERTATION

zur Erlangung des akademischen Grades
Doctor rerum naturalium
(Dr. rer. nat.)

im Fach
Biophysik

eingereicht an der
Lebenswissenschaftlichen Fakultät
der Humboldt-Universität zu Berlin

von
Dipl.-Biophys. Björn Goldenbogen

Präsidentin der Humboldt-Universität zu Berlin:
Prof. Dr.-Ing. Dr. Sabine Kunst

Dekan der Lebenswissenschaftlichen Fakultät:
Prof. Dr. Bernhard Grimm

Gutachter/innen:

1. Prof. Dr. Dr. hc. Edda Klipp
2. Prof. Dr. Andreas Herrmann
3. Prof. Dr. Thomas Günther-Pomorski

Tag der mündlichen Prüfung: 14. Juni 2019

Björn Goldenbogen
Morphogenesis and Cell Wall Mechanics of Saccharomyces cerevisiae
September 16, 2019
Humboldt-Universität zu Berlin
Theoretical Biophysics
Department of Biology
Faculty of Life Sciences
Invalidenstr. 42
10115 Berlin

Abstract

The generation of different cell shapes, or morphogenesis, is a central question in biology and is of particular importance for a comprehensive understanding of model organisms, such as baker's yeast *Saccharomyces cerevisiae*. Cell shape and integrity of *S. cerevisiae* are determined by its cell wall, a mainly elastic composite structure, providing a counter force against the osmotic pressure gradient between interior and exterior of the cell. This pressure gradient also serves as driving force for the plastic deformation of the cell wall required for cellular growth. However, the mechanical processes underlying the generation of the various shapes yeast can adopt are poorly understood, so far. Particularly interesting are the requirements for local cell wall properties and their impact on growth dynamics. Using a combined theoretical and experimental approach, I study two prominent modes of yeast morphogenesis in my thesis, budding and mating, to find common principles and differences regarding the mechanics of the cell wall. In the first part, I present a biophysical model for the coupled isotropic expansion of mother and bud during vegetative growth that accurately describe the measured volume dynamic of single yeast cells. The highly interlinked model predicts a distinction between the mechanical cell wall properties of mother and bud. Utilizing AFM-based multi-parametric imaging, I show that the cell wall elasticity does not differ between those two cell compartments and propose that the visco-plastic properties are the distinguishing features instead. Constraining the model with two completely independent data sets of single-cell volume trajectories, obtained from light microscopic images, provided further estimations on the visco-plastic cell wall properties and other key growth parameters, such as the total osmolyte uptake rate. The second part of my thesis focuses on the visco-elastic properties of the yeast cell wall. Using AFM-based nano-rheology on the cell wall *in vivo* I confirm that the cell wall responses mainly elastically to an applied force and further demonstrate that the cell wall shows structural damping behavior. Based on the latter observation, I discuss the possibility to describe the cell wall analogous to a soft glassy material. In the last part, I address the influence of a spatially and temporally varying cell wall elasticity on directed growth during yeast mating morphogenesis. On the basis of time resolved high resolution maps of topography and cell wall elasticity obtained with AFM *in vivo*, I show that generation of the characteristic shmoo shape requires a distinct pattern of cell wall elasticity, including substantially softer material at the shaft and stiffer material at the tip, the site of active growth. My work shows that local viscoelastic-plastic properties of the cell wall govern the morphogenesis of *S. cerevisiae*. The

acquired knowledge will help to decipher molecular mechanisms underlying not only yeast growth, but also that of other walled cells.

Zusammenfassung

Die Entstehung der unterschiedlichen Zellformen, auch Morphogenese genannt, ist eine zentrale Frage der Biologie und hat besondere Bedeutung für Modellorganismen, ist das Wissen darum doch notwendig diese in Gänze zu verstehen. Ein solcher Modellorganismus ist die Bäckerhefe *Saccharomyces cerevisiae*, deren Zellform und -integrität von ihrer Zellwand bestimmt wird. Die Zellwand ist eine hauptsächlich elastische Verbundstruktur, die eine Gegenkraft zum osmotischen Druckgradienten erzeugt, der zwischen Zellinnerem und -äußerem herrscht. Dieser Druckgradient dient dabei auch als treibende Kraft der plastischen Verformung der Zellwand, die für das Zellwachstum erforderlich ist. Bisher sind jedoch die mechanischen Prozesse, die der Erzeugung der verschiedenen Formen zugrunde liegen, welche Hefen annehmen können, nur unzureichend verstanden. Dabei sind die Anforderungen an die lokalen Zellwandeigenschaften und deren Einfluss auf die Wachstumsdynamik von besonderem Interesse.

Mithilfe eines kombinierten theoretischen und experimentellen Ansatzes untersuche ich in meiner Dissertation zwei markante Varianten der Hefemorphogenese, Knospung und Paarung, um gemeinsame Prinzipien und Unterschiede bezüglich ihrer Zellwandmechanik zu finden. Im ersten Teil stelle ich ein biophysikalisches Modell für die gekoppelte isotrope Ausdehnung von Mutter und Knospe während des vegetativen Wachstums vor, das die gemessene Volumendynamik einzelner Hefezellen genau beschreiben kann. Das hochgradig vernetzte Modell sagt einen Unterschied der mechanischen Zellwandeigenschaften von Mutter und Knospe voraus. Mit Hilfe AFM-basierter multiparametrischer Bildgebung zeige ich, dass sich die Zellwandelastizität zwischen diesen beiden Zellkammern nicht unterscheidet und schlage vor, dass sich diese in ihren visko-plastischen Eigenschaften unterscheiden müssen. Die Beschränkung des Modells mittels zweier unabhängiger lichtmikroskopischer Datensätze von Volumentrajektorien von Einzelzellen lieferte zusätzliche Erkenntnisse über die visko-plastischen Zellwandeigenschaften sowie andere wichtige Wachstumsparameter, z.B der Gesamtaufnahmerate von Osmolyten. Der zweite Teil meiner Arbeit beschäftigt sich mit den viskoelastischen Eigenschaften der Hefezellwand. Mit Hilfe von AFM-basierter Nanorheologie der Zellwand *in vivo* kann ich einerseits bestätigen, dass die Zellwand hauptsächlich elastisch auf eine aufgebrachte Kraft reagiert, und andererseits zeigen, dass diese strukturdämpfendes Verhalten aufweist. Gestützt auf die letztgenannte Beobachtung diskutiere ich die Möglichkeit, die Zellwand analog zu einem “soft glassy” Material zu beschreiben. Im letzten Teil befasse ich mich mit dem Einfluss einer räumlich und zeitlich variierenden Zellwandelastizität auf das gerichtete Wachstum während der Paarungsmorphogenese.

Anhand von mit AFM *in vivo* gewonnenen zeitlich und räumlich aufgelösten Karten der Zelltopographie und der Zellwandelastizität kann ich zeigen, dass die Erzeugung der charakteristischen Shmoo-Form ein bestimmtes Elastizitätsmuster der Zellwand erfordert, welches ein deutlich weicheres Material am Schaft sowie ein steiferes Material an der Spitze des Paarungsauswölbung beinhaltet. Meine Arbeit zeigt, dass die lokalen viskoelastisch-plastischen Eigenschaften der Zellwand die Morphogenese von *S. cerevisiae* bestimmen. Die gewonnenen Erkenntnisse werden dazu beitragen, die molekulare Mechanismen zu entschlüsseln, welche nicht nur dem Hefewachstum, sondern auch dem anderer bewandeter Zellen zugrunde liegen.

Contents

1 Introduction **1**

1.1 Such a small Organsim! 1
1.2 Life Cycle and Growth Modes 3
1.3 The Cell Wall of *S. cerevisiae* 6
1.3.1 Cell Wall Structure of *S. cerevisiae* 7
1.3.2 Cell Wall Mechanics of Yeast 9
1.4 Outline of the Thesis 11

2 Methods **13**

2.1 Mathematical Volume and Shape Models 13
2.1.1 Mechanics of Thin Pressurized Shells 13
2.1.2 Derivation of the SCGM 17
2.2 Experimental Methods 21
2.2.1 Yeast Strains Culture Conditions 21
2.2.2 Microfluidic Experiments 22
2.2.3 Atomic Force Microscopy 24
2.2.4 Nano-Rheology 30
2.2.5 Scanning Electron Microscopy 43

3 Cell Expansion during Vegetative Growth **45**

3.1 The Single-Compartment Growth Model 47
3.1.1 Characteristics of the SCGM 50
3.2 The Coupled SCGM - a Combined Model for Mother and Bud Expansion 53
3.2.1 Coupling of the Compartments 53
3.2.2 Distinguishing Property between Mother and Bud Cell Wall . 54
3.2.3 Cell Volume at Birth and at Cell Division 55
3.3 Local Cell Wall Elasticity of Mother and Bud 57
3.4 Estimation of Key Parameters of the cSCGM from Temporal Volume Data of Mother and Bud 60
3.4.1 Analysis of *data set 1* (Inhouse) 60
3.4.2 Analysis of *data set 2* (provided by Gilles Charvin) 62

3.5 Discussion on Vegetative Single Cell Growth 68

4 Visco-Elasticity of the Yeast Cell Wall 75
4.1 Nano Rheology of the Cell Wall 75
4.2 Complex Shear Modulus 79
4.3 Structural Damping Model 82
4.4 Discussion and Remarks on Soft Glassy Rheology 84

5 Cell Wall Elasticity Pattern Shapes Yeast during Early Mating Morphogenesis 89
5.1 Yeast Mating Morphogenesis 89
5.2 The Shmoo as Mechanical Steady State Model 93
5.3 Turgor Pressure Estimation 96
5.4 Cell Wall Elasticity Pattern Obtained with AFM 97
5.4.1 Temporal Elasticity Pattern 103
5.5 Dynamic cell wall model for shmoo formation 106
5.6 Assessment of Local Cell Wall Strain Profiles for Shmooing Cells . . . 113
5.7 Discussion on Mating Morphogenesis 116

6 Conclusion & Outlook 125
6.1 Cell Wall Elasticity & Cell Shape 125
6.2 Plastic Cell Wall Expansion & Cellular Growth 127
6.3 Yielding & Yield Criteria 129

Bibliography 131

A Appendix 147
A.1 Code 147
A.1.1 The SCGM in Antimony 147
A.1.2 The cSCGM in Antimony 151
A.2 Tables 153
A.3 Figures 154

Nomenclature 169

Abbreviations 173

Declaration 179

1 Introduction

> *Each time I have identified an intriguing aspect of the cancer problem, I have found that it could be approached more effectively in the simpler eukaryotic cell, Saccharomyces cerevisiae, than the human cell.*
>
> **— Leland H. Hartwell**
> *Nobel Lecture, 2001*

> *All the small things.*
>
> **— Blink-182**
> *Enema of the State, 1999*

Each chapter will be preceded by a statement, like this, clarifying the contributions of others to the work presented in the chapter and, where appropriate, a citation of the publication the chapter is based on.

1.1 Such a small Organsim!

Although utilized by mankind for thousands of years, it remained invisible until 1680, when Anton van Leeuwenhoek observed small globules and related them to the fermentation of beer. It attracted bakers as well as Nobel price laureates. It has been intensively studied for more than 100 years by generations of scientists, yet we can still learn from and about it.

This organism is *Saccharomyces cerevisiae*, also known as baker's, brewer's or budding yeast (hereinafter also referred to as yeast). It is a unicellular fungus, which belongs to the phylum of ascomycota. Despite its intensive cultivation, still little is known about the natural environment of *S. cerevisiae*. Based on its usage in wine production for several thousand years, the mayor habitat of *S. cerevisiae* is commonly thought to be the surface of fruits. However, it has also been isolated from bark

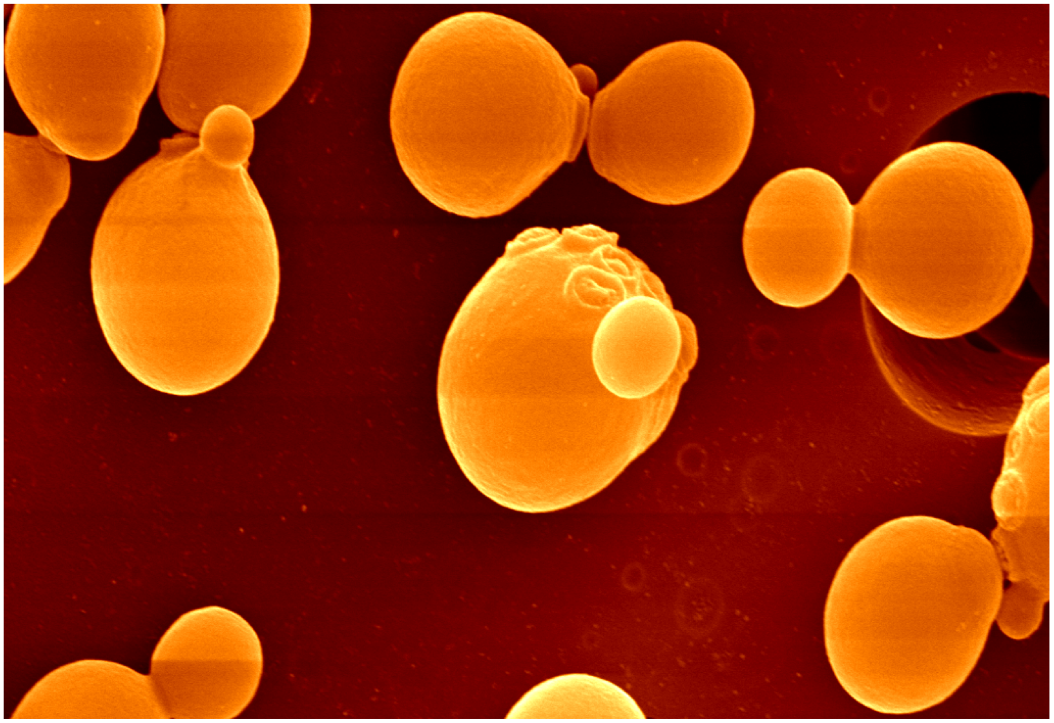

Fig. 1.1.: Different stages of budding. Colorized electron micrograph of vegetatively growing mating type a (MATa) cells. Bud and birth scars as well as different sized buds are clearly identifiable.

(Sniegowski *et al.*, 2002), soil (Goddard & Greig, 2015), and intestines of insects such as fruit-flies (Shehata *et al.*, 1955) and wasps (Stefanini *et al.*, 2016). Adapted to periods of drought and rain, *S. cerevisiae* proliferates under a variety of osmotic conditions (Knight & Goddard, 2015). As a fungus, yeast is an eukaryote, which has become one of the most important model organisms for genetic research, not least due to its simple cultivation conditions and manipulation possibilities. The comprehensive information gathered on the genome, metabolome and signaling pathways further allows a systemic examination of the whole organism to gain a deeper understanding of the choreography of cellular processes. Such systemic analyses demand not only information on the cell morphology and its dynamics, but also on the processes, which define them. Of the various cell shapes that yeast can adopt, I focus particularly on two distinct shapes and their morphogenesis (Fig. 1.2) to find common principles and distinguishing features. Morphogenesis of *S. cerevisiae* is inextricably linked with the cell wall, as the main structural element of the cell. An understanding of yeast morphogenesis is therefore not possible without a deeper knowledge of the cell wall, its structure and its mechanics.

1.2 Life Cycle and Growth Modes

Morphogenesis of *S. cerevisiae* is complex as it comprises different growth modes as well as different shapes (Kron & Gow, 1995; Wedlich-Soldner & Li, 2008). Depending on the external conditions *S. cerevisiae* growth either in its yeast-form, as pseudohyphae or forms spores or mating projections. Yeast lacks, however, one typical growth mode of fungi: hyphal growth. Hyphae are characterized by long and branched chains of single nucleated cells that are separated by septa and exhibit continuous apical growth. Furthermore, yeast can also initiate biofilm formation (Reynolds & Fink, 2001). In its predominant form which was also named after it, yeast proliferates as small spherical or ellipsoidal cell, which depending on the budding pattern form extended or smaller cell aggregates. Judging by his drawings, such a small cell cluster was exactly was L. van Leeuvenhook observed in his microscope, when yeast was visible for the human eye for the first time. In this thesis I examine the coupled isotropic growth during budding and the directed growth during the mating morphogenesis. Both growth modes as well as the connection between them will be explained in more detail in the following.

Yeast's main vegetative growth is budding, a form of asymmetric cell division where a smaller daughter cell is developing from a larger mother cell Fig. 1.2. The new born daughter cell, i.e. freshly separated from its mother, then passes through a defined set of events and checkpoints the so called cell cycle. During first phase of the cell cycle, G1 phase, the cell has to increase its size by isotropic growth until it has reached the minimum cell size required to continue the cell cycle. This checkpoint is called start and marks the transition from G1 to S phase. During S phase the DNA is replicated and the formation of the bud begins then , which continues to grow through the subsequent cell cycle phases, whereby, the bud expanses faster than the mother cell (Hartwell & Unger, 1977; Ferrezuelo *et al.*, 2012). For bud initiation, the cell surface is protruded at a predetermined position. The underlying polarization process, which determines the position of the bud at the surface, is a complex and highly regulated process and is described elsewhere (Slaughter *et al.*, 2009; Chiou *et al.*, 2017). The growing bud remains stable during bud expansion (Cabib & Arroyo, 2013) and is only connected to the mother via a small yet stable opening in their cell surfaces. This connection, known as bud neck is stabilized on both sides of the plasma membrane. At the outside, neck stabilization is realized by stiffening of cell wall, while at the inside it is achieved by formation of septin ring, a cytoskeletal structure first discovered in yeast (Mostowy & Cossart, 2012). In the subsequent G2 phase, the nucleus is transported via microtubules to the bud neck, which is a prerequisite for chromosome separation and mitosis in M phase.

The cell division cycle is finished with cytokinesis and separation of the cell walls of mother and daughter cell. Traces of this budding event remain visible at the surfaces of both cells, as can be seen in Fig. 1.1. Both mother and daughter can enter a next cell division cycle, although the daughter has to spend more time in G1 phase, due to its smaller size (Di Talia *et al.*, 2007). The regulation cell cycle is highly choreographed by a network of cyclins and cyclin dependent kinases (Hayles & Nurse, 1986; Forsburg & Nurse, 1991).

When nutrients become limiting yeast has different response strategies (Neiman, 2011). Cells can either enter a stationary phase and thereby reduce their demand on nutrients or proliferate as chains of elongated cells to search the environment for a new nutrient source. The latter is referred to as filamentous or invasive growth and occurs upon nitrogen depletion. Invasive growth is a from of pseudohyphal growth, as the cytoplasms remain separated and the cells are only connected by their cell walls in contrast to true hyphae. If nitrogen starvation is accompanied by limitation to a poor carbon source, *S. cerevisiae* can undergo sporulation and thereby enter a phase of persistence and enhanced resistance. The different responses to nutrient limitation, however, do not necessarily have to be mutually exclusive. For example, Piccirillo & Honigberg (2010) showed that invasive growth can be coordinated with sporulation.

In the initial step of sporulation (Neiman, 2011), four haploid nuclei are formed by meiosis in the cytoplasm of the cell, two of each mating type, MATa and mating type α (MATα). A *de novo*-formed plasma surrounds the nuclei and separates the prospores from the cytoplasm of the mother cell, which eventually becomes the ascus. In the second step, starting after closure of the prospore membrane, the spore wall is assembled. Like the prospore membrane, the spore wall is assembled *de novo*, containing additional components compared to the vegetative cell wall, such as chitosan and dityrosine (F. M. Klis, Boorsma, *et al.*, 2006). In parallel to the cell wall assembly, the chromatin is compacted in the spore nucleus. Upon spore wall completion, the original mother cell collapses around the spores and forms the tetrahedral mature ascus. The formed spores are more resistant to environmental stresses and, thus, enable yeast to survive in harsh conditions in this dormant state. When nutrient sources are available again, germination is initiated and the meiotic spores re-enter the mitotic cell cycle. To enable volume expansion and budding, the germination process entails partial loosening of the cell wall, increasing the susceptibility of the cell to external stresses (Joseph-Strauss *et al.*, 2007). Revived spores either proliferate as haploids by entering the cell division cycle or mate with a cell of opposite mating type.

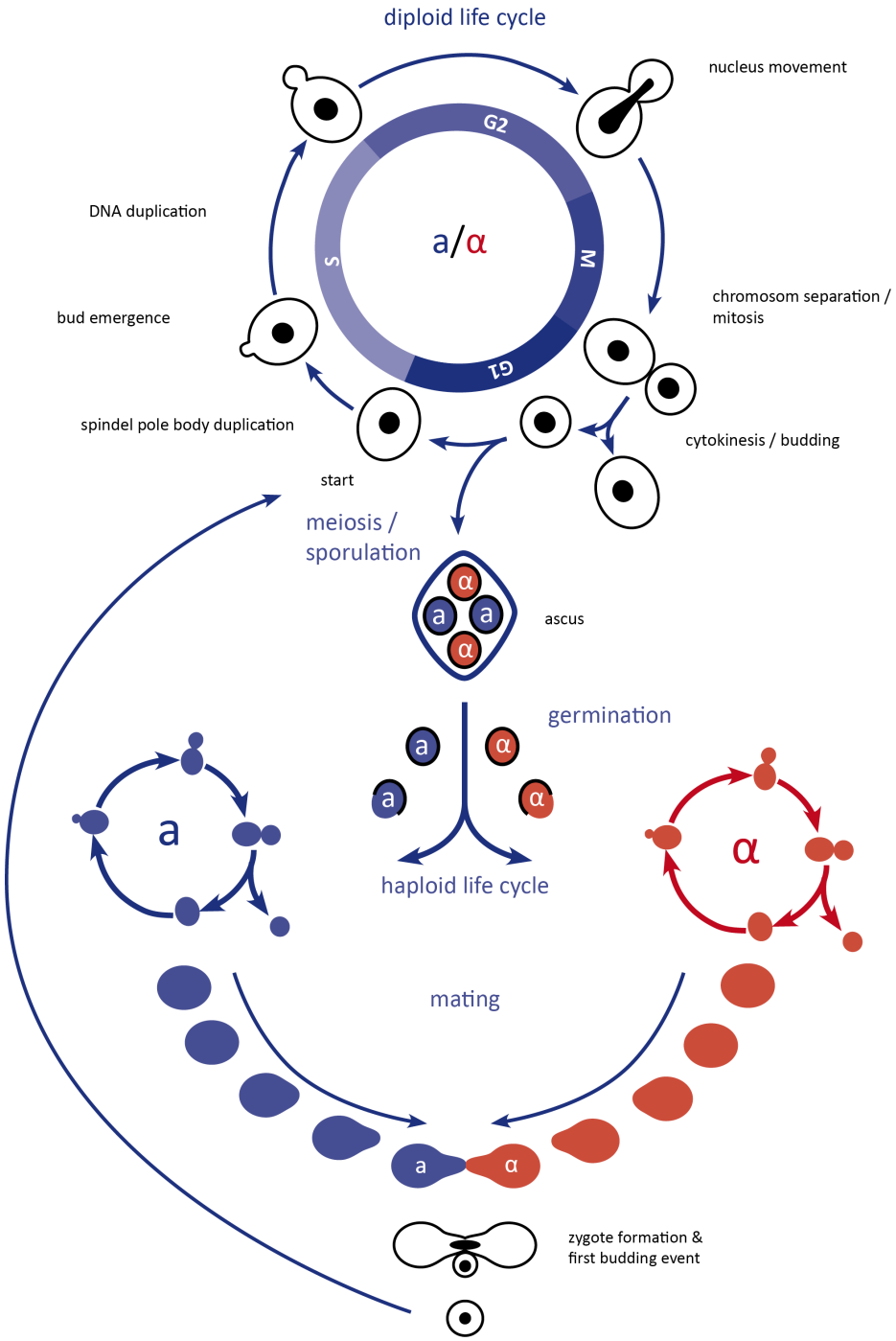

Fig. 1.2.: Yeast life cycle. Stages of the yeast morphogenesis, relevant to this thesis, and its connections are shown. The vegetative cell cycle of diploid cell (white) with nucleus (black) is shown in the top while the sexual cycle is illustrated in the bottom. Sexual cycle comprises meiosis, sporulation, germination and mating morphogenesis. Without mating partner present, haploid cells of both mating types, MATα (blue) and MATa (red), can pause the sexual cycle by entering a vegetative cell cycle.

To sense nearby mating partners, haploid cells communicate via mating type specific pheromones, which they release into their surroundings. When the external pheromone concentration reaches a certain threshold, cells arrest their cell cycle in G1 phase and start to grow towards their mating partners (Fig. 1.2 bottom). Interestingly, although low pheromone dosages do not trigger cell cycle arrest, they switch the growth pattern of yeast to filamentous growth. Filamentous growth presumably serves as non-directional search algorithm, as it allows the cells to spread farther and, thus, reduce the distance to potential mating partners (Erdman & Snyder, 2001; Frýdlová *et al.*, 2007). Mating cells meet with the tip of their mating projections and undergo cell fusion by controlled dissolution of the cell wall at the contact zone and subsequent membrane fusion. Eventually, karyogamy completes zygote formation. A more detailed description of the Mating morphogenesis is provided in Sec. 5.1. Although yeast cells are able to proliferate as haploids, mating provides obvious advantages, such as the increased tolerance to mutations in diploids, and therefore native yeasts possess the ability to switch their mating type. Most laboratory yeast strains, however, were intentionally deprived of this ability.

All aforementioned modes of morphogenesis lead to distinct cell shapes that have to be generated and maintained by the cell wall. Its structure and biochemical composition will be explained in the following.

1.3 The Cell Wall of *S. cerevisiae*

As fungus, *S. cerevisiae* is enveloped by a cell wall that is composed of a strong but elastic composite material. The cell wall is the outermost boundary of the cell and as such has to fulfill a variety of tasks. In his book *Fungal cell wall: structure, synthesis, and assembly.* Ruiz-Herrera (2012) assigned seven main functions to the cell wall:

1. resistance to pressure gradient
2. resistance to harmful physical, chemical, and biological aggression
3. provision for cell shape
4. recognition of external surfaces, inert or biological
5. reception of external stimuli
6. selective permeability for molecules (size exclusion)

7. accumulation of molecules important to the physiology of the cell, including nutrition

In context of morphogenesis, generation and maintenance of the cell shape and the provision of a counterforce against the necessary pressure gradient is of particular importance. The cell wall is central to the survival and the evolutionary success of yeast: It constitutes $\sim 20\,\%$ of the cell dry weight (Valentín *et al.*, 1987; Fleet, 1991; Aguilar-Uscanga & François, 2003; Yin *et al.*, 2007), up to $\approx 17\,\%$ of the cell volume (Yamaguchi *et al.*, 2011) and $\sim 20\,\%$ of all non-essential genes show a cell wall related phenotype, when knocked out (Groot *et al.*, 2001). The thickness of the cell wall averages between $115\,\mathrm{nm}$ to $120\,\mathrm{nm}$ (Dupres, Y. Dufrêne, *et al.*, 2010; Yamaguchi *et al.*, 2011) and can be subdivided by transmission electron micrography into two layers: an electron-transparent inner layer and an electron-dense outer layer, which account for $\sim 86\,\mathrm{nm}$ and $\sim 34\,\mathrm{nm}$ of the cell wall thickness (Baba *et al.*, 1989; Osumi, 1998). Although coupled to the plasma membrane, the cell wall is separated from it by the periplasmic space. The cell wall properties are tightly coupled to its function and result from the underlying structure and composition of the cell wall, which I will describe in the following sections.

1.3.1 Cell Wall Structure of *S. cerevisiae*

The cell wall is made up largely by polysaccharides ($\sim 85\,\%$) and proteins ($\sim 15\,\%$) which can be assigned to three different components: β-glucan, mannan and chitin. All cell wall components can be covalently linked to form complexes of higher order (Orlean, 2012). The relative amount of these components is not fixed but can vary depending on the growth phase, nutrition source or external cues and stresses (Orlean, 2012).

Glucan

The β-glucan accounts for $30\,\%$ to $50\,\%$ of the cell wall dry weight and can be distinguished into β-1,3-glucan and β-1,6-glucan according to the type of the glycosidic bond. The predominant β-glucan structures, with an polymerization degree of ~ 1400, are β-1,3-glucan chains with β-1,3-glucan side branches linked by β-1,6-glucan. These β-1,3-glucan chains exhibit a coiled spring like-structure and are held responsible for the elasticity and tensile strength of the cell wall (F. Klis & Mol, 2002). $10\,\%$ of the glucan represent the less polymerized (~ 140 glucose units) β-1,6-glucan chains, with occasional side branching β-1,3-glucan. Compared to the

microfibrillar structure of β-1,3-glucan, the structure of β-1,6-glucan is more flexible and amorphous. β-1,3-glucan is synthesized *de novo* from uridine diphosphate glucose (UDP-Glc) at the plasma membrane and elongated as well as branched inside the cell wall. The synthesis is regulated by the yeast cell wall integrity signaling pathway (CWI) via Rho1, which is the regulatory subunit of the β-1,3-glucan synthase. In contrast, the biosynthesis of β-1,6-glucan remains a mystery to a large extend (Aimanianda *et al.*, 2009).

Chitin

Chitin is a minor component of the lateral cell wall, constituting only $1\,\%$ to $2\,\%$ of the cell wall dry weight. Furthermore, its deposition in the lateral cell wall of a daughter cell occurs not until after cytokinesis (Shaw *et al.*, 1991). Nevertheless, chitin is enriched at the bud neck and in the septum between mother and bud before cell separation. The chitin ring at the bud neck is retained by the mother as bud scar after septation. Several old and fresh bud scars can be seen in Fig. 1.1. Furthermore, chitin deposition can be increased as response to an external stimulus. The chitin content, is for example, three- to four-fold increased after exposure to mating pheromone.

Chitin consists of linear chains of β-1,4-linked GlcNAc, synthesized from uridine diphosphate glucose N-acetylglucosamine (UDP-GlcNac) by three different synthases (CS I, CS II, CS III). About $40\,\%$ to $50\,\%$ of the chitin chains are covalently attached to β-1,3-glucan. Furthermore, the chitin chains can form microfibrillar structures, which, when stabilized by hydrogen bonds, can adopt a crystalline form. By conferring a stretching resistance to the cell wall, this crystalline form helps to stabilizes crucial surface areas as the bud neck or the septum.

Mannan

Mannan refers to the variety of highly mannosylated cell wall proteins (CWPs) which predominantly constitute the electro dense outer layer of the cell wall and thereby shield the inner glucan layer from external glycosylhydrolases. Two classes of CWPs can be distinguished that are covalently attached to β-glucan, protein with internal repeatss (PIRs)-CWPs and glycosylphosphatidylinositol (GPI)-CWPs. While PIR-CWP is presumably coupled to β-1,3-glucan, GPI-CWP is predominately linked to β-1,6-glucan via remnants of its GPI-anchor. On the one hand, these mannoproteins improve the stability of the cell wall by shielding and cross-linking the glucan

network. On the other hand, they provide the possibility for specific adhesion, e.g. by a-agglutinins, which link both mating partners during zygote formation. The expression of those non-enzymatic CWPs varies between different cell cycle phases, during sporulation or mating and in response to cell wall stresses or shifts in aerobic conditions (Orlean, 2012).

Cell Wall Modification

Only part of the glucan network is synthesized *de novo* at the plasma membrane, elongation, branching and cross-linking of the polysaccharide chains takes place inside the cell wall. Furthermore, the cell wall composition and structure is altered subsequently during the morphological changes described above. All this processes require enzymatic active proteins inside the cell wall.

A variety of proteins, which can either be cell wall bound or unbound, have already been identified with putative or confirmed cell wall related enzyme activity, such as the endoglucanase/glucanosyltransferase Bgl2 or the exo-β-1,3-glucanase Exg1. However, there are still proteins whose roles remained unclear, e.g. Ccw12 which except for the localization to the sites of active growth, such as budding site, septum, lateral wall of the daughter cell or tip of the mating projection, could not be assigned to a specific task yet (Ragni *et al.*, 2011).

The mechanical properties and processes that I will present in this thesis are foundations for the assignment of molecular structure and modifying enzymes to their function for the modification of the cell wall and thereby the morphogenesis of yeast. The example of Ccw12 shows, however, that this assignment should not only include proteins with known or putative enzymatic activity, but also proteins whose function is still unknown. For further information on cell wall structure and composition please refer to reviews by F. Klis & Mol (2002), Lesage & Bussey (2006), and Orlean (2012).

1.3.2 Cell Wall Mechanics of Yeast

Although required, the knowledge on biochemical processes and components which constitute the cell wall is not sufficient to explain the morphogenesis of *S. cerevisiae*. Additionally, an understanding of the physical mechanisms and properties of the cell and its cell wall is necessary. Green (1969) wrote concerning morphogenesis:

> "The information relating metabolic and genetic alterations to form can take on causal meaning only when the alterations can be specifically connected to components of the physical mechanisms of growth."

The cell wall mechanics comprise the physical state, i.e. the stresses and strains inside the wall, as well as the physical properties, which include spatial dimension and response characteristics to an applied force. This response can be elastic, viscous, plastic or a combination thereof. As aforementioned, the cell wall of yeast is thought to be mainly elastic. During morphogenesis, however, the cell wall has to deform irreversibly, i.e. plastically, in addition.

Among the variety of approaches to measure the mechanics of morphogenesis (Routier-Kierzkowska & R. S. Smith, 2013), three have been repeatedly used to determine the elastic properties of the yeast cell: whole-cell compression, cell wall nano-indentation and osmo-shock experiments. While in the first two approaches the cells are directly exposed to a defined loading force, the force onto the cell wall is controlled indirectly by varying the external osmolyte concentration in the latter (Martinez de Marañon *et al.*, 1996; Schaber *et al.*, 2010). Although increasing or decreasing the osmotic pressure gradient results in increased or decreased stresses in the cell wall, the precise determination of the applied force is more difficult. Both direct approaches, whole-cell compression and cell wall nano-indentation, provided estimates on the cell wall elasticity, which differ, however, by two orders of magnitude. Estimation of Young's modulus (YM), which is a measure for the elasticity of the material, from cell compression experiments by micro-manipulation ranged from $100\,\mathrm{MPa}$ to $300\,\mathrm{MPa}$ (A. E. Smith, Zhang, Thomas, *et al.*, 2000; A. E. Smith, Moxham, *et al.*, 2000; Chaudhari *et al.*, 2012), while YM values from nano-indentation experiments with atomic force microscopy (AFM) ranged from $0.5\,\mathrm{MPa}$ to $2.5\,\mathrm{MPa}$ (Touhami *et al.*, 2003; Svaldo Lanero *et al.*, 2006; Alsteens, Dupres, *et al.*, 2008; Dague *et al.*, 2010; Suchodolskis *et al.*, 2011). This inconsistency has not been resolved yet, though it has been shown that for strong indentation of pressurized shells the force response is governed by the pressure and not by the material property of the shell (Vella *et al.*, 2012). Therefore, the measurement of the whole cell compression experiments can be biased by the turgor pressure.

One advantage of the nano-indentation method is, that it allows *in situ* measurements of the cell wall and has, therefore, the potential to resolve the local cell wall elasticity. This was exploited in the studies of Touhami *et al.* (2003) and Pillet *et al.* (2014), in which they reported regions of stiffer cell wall material, e.g. in regions of previous budding events, so called bud scars. Such local variations in the mechanical properties of the cell wall are a central aspect of the morphogenesis of walled cells.

In particular, the nascent cell wall of fungi is thought to posses different mechanical properties (Ruiz-Herrera, 2012). For yeast, however, time resolved information on the mechanical properties of cell wall during morphogenesis were still missing.

So far, I only addressed the elastic response of the cell wall, yet cell walls of fungi and plants can also show plastic or viscoelastic-plastic behavior (Taiz, 1984; J. K. Ortega, Gamow, *et al.*, 1975; Ruiz-Herrera, 2012; J. K. E. Ortega, 2017), particularly in regions of active growth. While several studies on the viscoelastic-plastic response of plant cell walls have already been reported (D. J. Cosgrove, 1985; D. J. Cosgrove, 2016), information for the yeast cell wall is still lacking. Further concepts and details regarding the cell wall mechanic will be explained and discussed in the corresponding chapters.

1.4 Outline of the Thesis

In this study, I focus on two prominent modes of growth in yeast, budding and mating, to identify common principles and differences in the morphogenesis by using a combined theoretical and experimental approach. From an *a priori* mathematical model for the coupled expansion of mother and bud during the vegetative growth, I generate the hypothesis that the cell wall must differ between the mother and bud compartment, either in its elasticity or in its extensibility. Subsequently, I test the hypothesis regarding the compartment dependent elasticity of the cell wall on *in vivo* data acquired with state of the art AFM. Estimations on crucial growth parameters of this model based on large scale single cell size measurements will complete the first subproject of my thesis (Sec. 3.1). In Sec. 4 of my study, I apply a nano-rheological approach to determine the viscoelastic properties of the cell wall and compare the results to the estimations on the cell wall extensibility. Based on these measurements, I show that the cell wall exhibits structural damping behavior and discuss the applicability of a soft glassy rheology model to the cell wall.

In the last part (Sec. 5), I focus on the mating morphogenesis. In this context, I investigate directed growth and the impact of an inhomogeneous elasticity pattern of the cell wall on cell shape and growth dynamics by applying finite-element modeling and AFM. The obtained time-resolved elasticity maps reveal the dynamics of a characteristic pattern during the formation of a mating projection, including substantial softening of the protrusion shaft and maintenance of the initial elasticity at the tip. Accounting for the observed elasticity pattern, dynamic cell wall models provide estimations on the strain inside the cell wall during tip growth and raise

questions about its regulation. In addition, complementary osmo-shock experiments confirm the predictions on cell wall strain from these models.

The observations and implications I present, underline how much we can still learn from this small organism, *S. cerevisiae*.

2 Methods

2.1 Mathematical Volume and Shape Models

In the following section I will focus on the theoretical background of the presented models, its derivations and assumptions. Further some important basic concepts will be explained.

2.1.1 Mechanics of Thin Pressurized Shells

From a mechanical point of view walled cells, as plant or fungal cells, can be seen as pressurized shells, whose shape often follows a rotational symmetry. Under this assumption, simple relationships can be formulated, connecting the local curvature of the cell surface, the cell wall thickness d or the lateral stresses σ and strains ε in cell wall with cellular properties, such as the turgor pressure P. If the cell shape follows rotational symmetry the local geometry of the surface can be characterized by the principle curvatures, namely the circumferential curvature κ_θ and the meridional curvature κ_s. From these geometrical considerations the principle stresses and strains can be deduced, as depicted in Fig. 2.1.

Stress

Mechanical stress describes the forces inside a material, exerted from neighboring elements onto each other. According to Flügge (1973) the corresponding in-plane stresses with respect to curvature for a rotationally symmetric shell is given by:

$$\sigma_\theta = \frac{P}{2d\kappa_\theta(s)}, \quad \sigma_s = \frac{P}{2d\kappa_\theta(s)}(2 - \frac{\kappa_s(s)}{\kappa_\theta(s)}). \tag{2.1}$$

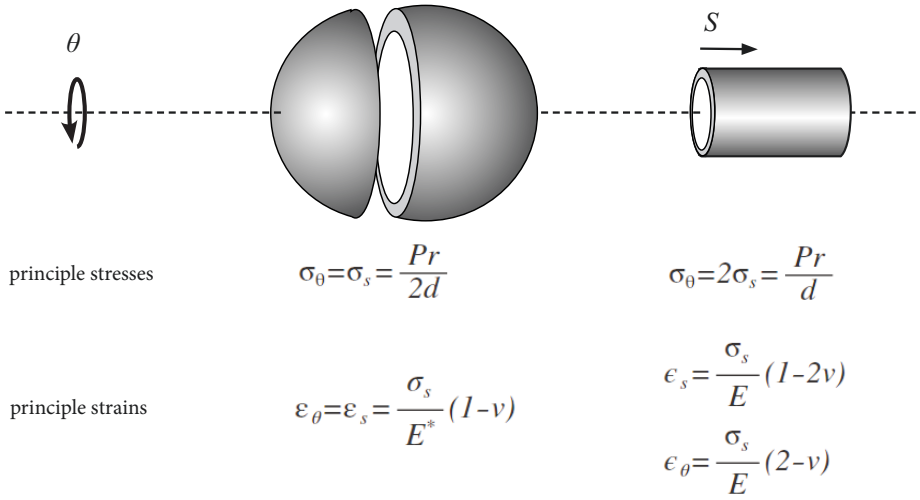

Fig. 2.1.: Principle stresses and strains for rotational symmetric shells, assuming linear elasiticity

When calculating the in-plane stresses of a spherical shell it is helpful to consider the forces acting on the cross section of sphere as depicted in Fig. 2.2. The force F_p arising from the internal pressure P acting on the cross section area is given by

$$F_p = P\pi r^2, \tag{2.2}$$

and the force F_w arising from the stress σ_θ inside wall acting on the surrounding ring can be written as

$$\begin{aligned} F_w &= \sigma_\theta \pi((r+d)^2 - r^2), \\ &\cong 2\sigma_\theta \pi r d, \quad (d \ll r). \end{aligned} \tag{2.3}$$

Considering that in steady state the sum of the forces acting on the cross section of a half sphere need to be zero, $F_p + F_w = 0$, the in-plane stress can be calculated by

$$\sigma_\theta = \frac{Pr}{2d}. \tag{2.4}$$

We can also obtain this relation if we consider Eq. 2.1 and the fact that the symmetry of a sphere demands that both mutually perpendicular in-plane stresses are equal $\sigma_\theta = \sigma_s$, as well as the principle curvatures $\kappa_\theta = \kappa_s = 1/r$. To compare different stress states using a single distinct value, e.g. if yielding needs to be considered, the

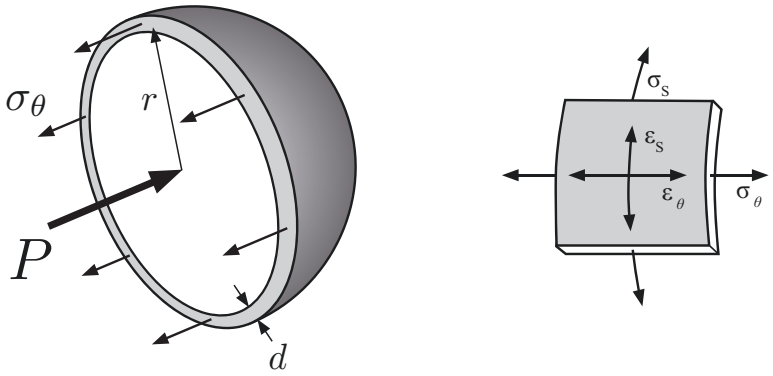

Fig. 2.2.: Principle stresses in a spherical shell

von Mises stress is a widely used measure (Yu *et al.*, 2006). Thereby the von Mises stress σ_{VM} for a given rotationally symmetrical thin shell is given by :

$$\sigma_{\text{VM}} = \sqrt{\sigma_\theta^2(s) + \sigma_s^2(s) - \sigma_s(s)\sigma_\theta(s)}. \tag{2.5}$$

Strain

Mechanical strain describes the relative material deformation. Whereby the engineering strain ε^e is the approximation of the true strain ε_t for small displacements

$$\varepsilon^e = \frac{x - x_0}{x_0}, \quad \mathrm{d}\varepsilon^t = \frac{\mathrm{d}x}{x}. \tag{2.6}$$

From the contour lengths s and S and the radii r and R_{ref} of the expanded and relaxed shell, both principle in-plane strains, the meridional strain $\varepsilon_s(s)$ and the circumferential strain $\varepsilon_\theta(s)$ can be calculated by

$$\varepsilon_\theta(s) = \frac{r(s) - R_{\text{ref}}(s)}{R_{\text{ref}}(s)}, \quad \varepsilon_s(s) = \frac{ds - dS}{dS}. \tag{2.7}$$

The volumetric strain ε_V, an approximation for the change in volume of a shell element, is given by

$$\varepsilon_V = \varepsilon_\theta(s) + \varepsilon_s(s). \tag{2.8}$$

Linear Elasticity

The constitutive relationship between the in-plane strain and stress $\vec{\varepsilon}$ assuming linear elasticity and isotropic material properties is given by (Flügge, 1973)

$$\begin{bmatrix} \varepsilon_\theta(s) \\ \varepsilon_s(s) \end{bmatrix} = \frac{1}{E^*(s)} \begin{bmatrix} 1 & -\nu \\ -\nu & 1 \end{bmatrix} \cdot \begin{bmatrix} \sigma_\theta(s) \\ \sigma_s(s) \end{bmatrix}. \tag{2.9}$$

Where E^* is the elastic modulus or YM of the cell wall material for plane elasticity and relates to the elastic modulus in 3D by:

$$E^* = \frac{E}{(1-\nu^2)}. \tag{2.10}$$

Combining Eq. 2.9 and Eq. 2.1, the relationship between the meridional and circumferential strain, which solely depends on the geometry and the Poisson's ratio, can now be formulated as

$$\varepsilon_s(s) = \varepsilon_\theta(s) \frac{(1-2\nu)\kappa_\theta(s) + \nu\kappa_s(s)}{(2-\nu)\kappa_\theta(s) - \kappa_s(s)}. \tag{2.11}$$

With the definition of the strains in Eq. 2.7 this can be rearranged to

$$ds = \left(\left(\frac{r(s)}{R_{\text{ref}}(S)} - 1 \right) \frac{(1-2\nu)\kappa_\theta(s) + \nu\kappa_s(s)}{(2-\nu)\kappa_\theta(s) - \kappa_s(s)} - 1 \right) dS. \tag{2.12}$$

Eq. 2.12 was used to calculate the meridional strains in mechanical steady-state cell wall model (SM) from a given axis-symmetrical geometry and a given relaxed state (Bernal *et al.*, 2007). Combining Eq. 2.9 with estimations on meridional and circumferential strains the positional elastic modulus $E^*(s)$ can be calculated from (Bernal *et al.*, 2007)

$$E^*(s) = \frac{R_{\text{ref}}}{r(s) - R_{\text{ref}}} \left(\frac{P}{2d\kappa_\theta(s)} \left(2 - \frac{\kappa_s(s)}{\kappa_\theta(s))} \right) - \nu \frac{P}{2d\kappa_\theta(s)} \right). \tag{2.13}$$

In the special case when the shell is spherical, the equation for E^* can be simplified, using the definition of the strains together with Eq. 2.4 and Eq. 2.9,

$$E^*(r) = (1-\nu) \frac{PrR_{\text{ref}}}{2d(r - R_{\text{ref}})}. \tag{2.14}$$

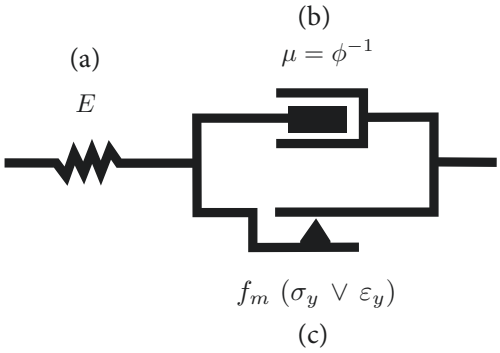

Fig. 2.3.: The Bingham-Norton element reflect the elastic perfectly viscoelastic-plastic response. As mechanical circuit the element couples a Hookean element or spring (a) in series with a viscoelastic-plastic Bingham element (b,c). The Bingham element in turn couples a dashpot (b) with viscosity μ and a and Saint-Venant element (c) in parallel. Where both stress σ_y and strain ε_y can serve as yield criterion.

This formula was used to compare the E-values at tip and base of shmooing cells obtained in nano-indentation experiments with E-values at the same positions obtained from osmotic shock experiments.

For better comparison to the dynamic model, the arc length s is plotted from the tip instead of the base in all figures (see Fig. 5.3).

2.1.2 Derivation of the SCGM

Turgor Pressure

In this subsection the ordinary differential equation (ODE) for the turgor pressure will be deduced as one of the three governing ODEs of the single-compartment growth model (SCGM), basing on the mechanics of thin shells and a spherical geometry.

As derived in Sec. 2.1.1, the thin shell relation provides both, a description of the in-plane circumferential strain $\varepsilon = \varepsilon_\theta = \varepsilon_s$ and a relation between the pressure on the shell, the turgor pressure Π_t, and the cell wall in-plane stress σ. The true strain is given by:

$$\mathrm{d}\varepsilon = \frac{\mathrm{d}r}{r}. \tag{2.15}$$

To reflect both the elastic and the plastic deformation of the cell wall in response to an effective internal pressure a mechanical circuit was used. In this circuit two principle mechanical elements are coupled in series, a Hookean element and a Bingham-Norton element as depicted in Fig. 2.3. In such a circuit the stress acting on each element equals the total stress acting on that circuit $\sigma = \sigma_{\text{Hook}} = \sigma_{\text{Bingham}}$, while the total strain is the sum of the individual strains of each element

$$\mathrm{d}\varepsilon = \frac{\mathrm{d}r}{r} = \frac{\mathrm{d}r_{\text{Hook}}}{r} + \frac{\mathrm{d}r_{\text{Bingham}}}{r}. \tag{2.16}$$

This holds true for the time derivative as well:

$$\dot{\varepsilon} = \frac{\mathrm{d}\varepsilon}{\mathrm{d}t} = \frac{\mathrm{d}}{\mathrm{d}t}\left(\frac{\mathrm{d}r_{\text{Hook}}}{r}\right) + \frac{\mathrm{d}}{\mathrm{d}t}\left(\frac{\mathrm{d}r_{\text{Bingham}}}{r}\right). \tag{2.17}$$

Note, that a dot above a variable represents the time derivative of that variable $\dot{x} = \frac{\mathrm{d}x}{\mathrm{d}t}$. For each element a constitutive relationship can be formulated. Assuming linear elasticity as in Eq. 2.9, the constitutive relationship between strain and stress for the Hookean element reads

$$\varepsilon_{\text{Hook}} = \frac{1-\nu}{E}\,\sigma_{\text{Hook}}. \tag{2.18}$$

While the constitutive relationship of the visco-plastic Bingham element relates stress with strain rate instead of strain,

$$\dot{\varepsilon}_{\text{Bingham}} = \phi\, f_m(\sigma, \sigma_{\text{y}}) \quad \text{where } f_m = \begin{cases} \sigma, & \text{if} \quad \sigma > \sigma_{\text{y}} \\ 0, & \text{else} \end{cases}. \tag{2.19}$$

Here, the plastic deformation of the cell wall is modeled, according to Lockhart (1965), as an irreversible viscous expansion, which starts when the stress σ rises above a yield stress σ_{y}. The irreversibility of the plastic deformation is reflected in f_m, which allows only for expansion but prevents compression. Since the wall stress scales linearly with the inner pressure Π (Eq. 2.4) we introduced a critical turgor pressure Π_c as yield criterion. Here the coefficient ϕ represents the plastic extensibility which is the inverse of the viscosity μ .

Utilizing the pressure stress relation from Eq. 2.4 and rearranging Eq. 2.18 and Eq. 2.19 provides descriptions for the strain and strain rate,

$$\varepsilon_{\text{Hook}} = \frac{1-\nu}{E}\,\frac{\Pi_t\, r}{2\, d}, \tag{2.20}$$

$$\dot{\varepsilon}_{\text{Bingham}} = \frac{\phi\, r}{2\, d}\, f_m(\Pi_t, \Pi_c). \tag{2.21}$$

To formulate the total strain rate of the serial arranged mechanical elements of Eq. 2.17 we need to consider the time derivative of Eq. 2.20,

$$\dot{\varepsilon}_{\text{Hook}} = \frac{1-\nu}{E\, 2\, d}\,(\dot{\Pi}_t r + \Pi_t \dot{r}). \tag{2.22}$$

Combining this equation with with Eq. 2.21 we obtain the description of the total circumferential strain rate with respect to the cell radius r,

$$\frac{\dot{r}}{r} = \frac{1-\nu}{2Ed}(\dot{\Pi}_t r + \Pi_t \dot{r}) + \frac{\phi r}{2d} f_m(\Pi_t, \Pi_c). \tag{2.23}$$

Rearranging Eq. 2.23 provides us with an ODE for the turgor pressure of a spherical walled cell,

$$\dot{\Pi}_t = \frac{2Ed}{1-\nu}\frac{\dot{r}}{r^2} - \Pi_t \frac{\dot{r}}{r} - \frac{E\phi}{(1-\nu)} f_m(\Pi_t, \Pi_c). \tag{2.24}$$

To distinguish between elastic and plastic deformation Eq. 2.24 was split into two coupled ODEs, by defining a reference radius R_{ref}. Where R_{ref} is equal to the relaxed radius of the elastic expansion, i.e. $\Pi_t < \Pi_{crit}$. Considering Eq. 2.21 the first ODE describes the strain rate of R_{ref} with

$$\frac{\dot{R}_{\text{ref}}}{R_{\text{ref}}} = \frac{\phi r}{2d} f_m(\Pi_t, \Pi_c). \tag{2.25}$$

The second ODE results form the corresponding adaptation of Eq. 2.24 and is the ODE for Π_t, which was implemented in the SCGM. It reads

$$\dot{\Pi}_t = \frac{2Ed}{r^2 R_{\text{ref}}}\left(\dot{r} R_{\text{ref}} - r\dot{R}_{\text{ref}}\right) - \Pi_t \frac{\dot{r}}{r}. \tag{2.26}$$

Water Flux over a Membrane

Volumetric change of cells is generally accompanied by water fluxes. In this subsection the equation for water flux across the cytoplasmic membrane of a walled cell, as it was used in the SCGM, will be deduced. Driven by the acting hydrostatic and osmotic pressure differences, Δp and $\Delta\Pi$, respectively, the outward facing volume flow of water J_w over a membrane is according to Kedem & Katchalsky (1958):

$$J_w = L_p \, A(r) \, (\Delta p + \sigma_r \Delta\Pi). \tag{2.27}$$

The hydraulic conductivity per unit area L_p represents the inverse of the flow resistance to the acting pressure and the reflection coefficient σ_r describes the permeability of the membrane to solutes. Note that σ_r is not to be mistaken for the mechanical stress σ in a continuous material. Given the incompressibility of water and that the considered membrane encloses a volume, e.g. the cytoplasmic membrane, the water influx over the membrane must equal the change in volume,

$$\dot{V} = J_w^{in} = -J_w. \tag{2.28}$$

For the SCGM we specified Eq. 2.28 further. Since water influx is restricted to the surface of a spherical cell, the problem can be reduced to one dimension,

$$\begin{aligned} \dot{V} &= \frac{\mathrm{d}V(r)}{\mathrm{d}r} \, \dot{r}, \quad \text{with} \quad V(r) = \frac{4}{3} \, \pi \, r^3 \\ &= 4 \, \pi \, r^2 \, \dot{r}, \\ &= A(r) \, \dot{r}, \end{aligned} \tag{2.29}$$

where $A(r)$ is the surface area of the sphere. The osmotic and the hydrostatic pressure gradients are determined by the external and internal pressures: $\Delta\Pi = \Pi_e - \Pi_i$, $\Delta p = p_e - p_i$. Considering only the turgor pressure Π_t, as acting hydrostatic pressure exerted by the cell wall on the cell membrane, simplifies Δp to $\Delta p = \Pi_t$. Additionally an ideal semi-permeable membrane is assumed resulting in $\sigma_r = 1$. Under this assumptions the ODE for the radius $r_{\mathrm{os}}(t)$ is given by

$$\dot{r}(t) = -L_p(\Pi_t + \Pi_e - \Pi_i). \tag{2.30}$$

The water flow was defined as influx, thus, the flow is identical with the change in volume of the cell.

Model Implementation and Parameter Estimation

SCGM and coupled-compartment growth model (cSCGM) were computationally implemented in the human readable and systems biology markup language (SBML) related, modeling language Antimony (L. P. Smith *et al.*, 2009) and are given in Sec. A.1.1 and in Sec. A.1.2. Utilizing the modular structure of the Antimony language, the cSCGM linked two instances of the SCGM. Both models were simulated and evaluated in Python using the tellurium package (Choi *et al.*, 2018). Model parameters were estimated by fitting the cSCGM simultaneously to temporal volume data for mother and bud, by minimizing the objective function(χ^2) using a Covariance Matrix Adaptation Evolution Strategy (CMA-ES)(Hansen & Ostermeier, 2001) implemented in Python. Profile-likelihoods were obtained by fitting the data for different fixed parameter values. For analysis further python packages, such as scipy and numpy (Eric *et al.*, 2001; Walt *et al.*, 2011), were used.

2.2 Experimental Methods

Experimental methods and materials used in this study will be described briefly in the following, comprising: yeast strains, culture conditions, microfluidics, light microscopy and scanning electron microscopy (SEM). Methods, which are essential for the study or uncommon, such as atomic force microscopy or nano-rheology, will be explained in more detail.

2.2.1 Yeast Strains Culture Conditions

S. cerevisiae strains, used in this study, are based on designer deletion strains introduced by Brachmann *et al.* (1998) and listed in Tab. 2.1. All cell cultures were grown at $30\,^{\circ}\mathrm{C}$ overnight under aerobic condition in yeast synthetic drop-out medium (SD medium) containing $0.17\,\%$ yeast nitrogen base without amino acids, $0.5\,\%$ ammonium sulfate, $2\,\%$ glucose, $55\,\mathrm{mg/l}$ adenine, $55\,\mathrm{mg/l}$ L-tyrosine, $55\,\mathrm{mg/l}$ uracil, $20\,\mathrm{mg/l}$ L-arginine, $10\,\mathrm{mg/l}$ L-histidine, $60\,\mathrm{mg/l}$ L-isoleucine, $60\,\mathrm{mg/l}$ L-leucine, $40\,\mathrm{mg/l}$ L-lysine, $10\,\mathrm{mg/l}$ L-methionine, $60\,\mathrm{mg/l}$ phenylalanine, $50\,\mathrm{mg/l}$ L-threonine and $40\,\mathrm{mg/l}$ L-tryptophan. Yeast cultures reached late exponential or

Tab. 2.1.: Yeast strains used in this study descend from designer deletion strain collection (Brachmann *et al.*, 1998)

Name	Genotype	experiment
BY4741	MATa his3Δ1 leu2Δ0 met15Δ0 ura3Δ0	AFM (Sec. 3.3, Sec. 4.1)
MATa bar1Δ	MATa bar1Δ his3Δ1 leu2Δ0 met15Δ0 ura3Δ0	AFM/MFD (Sec. 3.3, Sec. 5.6)
BY4742	MATαhis3Δ1 leu2Δ0 lys2Δ0 ura3Δ0	MFD (Sec. 3.4.1)
	cdc10-mKate2::loxP-ura3-loxP	

early stationary phase overnight and were subsequently diluted in SD medium to early log phase cell densities and allowed to grown for at least $2\,\mathrm{h}$ at $30\,^{\circ}\mathrm{C}$ prior to the measurements, if not stated otherwise. Medium osmolarity was determined with an osmometer (gonotec, Berlin, Germany).

2.2.2 Microfluidic Experiments

Microfluidics utilizes miniaturized experimental setups, so called microfluidic devices (MFDs), to manipulate small fluid volumes with high precision (Mark *et al.*, 2010) in an automatized manner. There are many different applications for MFDs, especially in cell biology, where they are used for various reasons (Halldorsson *et al.*, 2015). Among others, MFDs reduce the required amount of substances, enable a rapid change of extracellular conditions and allow stable concentration gradients, by taking advantage of the laminar flow in micro-channels. MFDs were particularly used for yeast experiments, e.g. to sort yeast according to their size (Pamme, 2007), to establish continuous cultures in a micro chemostat (Groisman *et al.*, 2005) or to study their response to a stable pheromone gradient (Moore *et al.*, 2008; Jin *et al.*, 2011). In a previous *in vitro* study I used MFDs to analyze the rolling velocity of infected peripheral blood mononuclear cells on primary lung-epithelial of horses *in vitro* (Spiesschaert *et al.*, 2015). In this thesis MFDs were used to monitor the volume expansion of proliferating yeast cells (Sec. 3.4) and to estimate the cell wall strain of shmooing yeast cells (Sec. 5.6).

Microfluidic Growth Experiments

A CellASIC ONIX microfluidic platform (Merck Millipore, Darmstadt, Germany) with the haploid yeast plates (Y04C) was used for growth analysis. Prior to the loading of cells into the plates following the ONIX yeast protocol, these plates

were primed with SD medium. Measurements were performed under constant flow condition using a control pressure of $2\,\mathrm{psi}$ and at constant temperature of $30\,^{\circ}\mathrm{C}$ utilizing a temperature control chamber (OL IX73/83 cellVivo, PeCon GmbH, Erbach, Germany). Cells were observed using a Visitron Visiscope inverted spinning disc laser confocal microscope (Visitron, Puchheim, Germany) with a Photometrics Evolve 512 EMCCD camera (Photometrics, Tuscon, USA) and a $150\times$ oil immersion objective (Olympus UPlanSApo $150\times/1.47$, Oil, TIRM). Fluorescence setup comprised a $561\,\mathrm{nm}$ diode laser for excitation and a multi-band dichroic filter (405, 488, 559 and $635\,\mathrm{nm}$) together with a $600/50\,\mathrm{nm}$ emission filter for the emission. While every $3\,\mathrm{min}$ a bright-field image was taken, fluorescent images were acquired only every $12\,\mathrm{min}$ to minimize phototoxicity. Each image was acquired as a z-stack (6 z-positions, $0.5\,\mu\mathrm{m}$ distance).

For further analysis only the sharpest plane of each z-stack was used, which was identified with the ImageJ plug-in "Find focused slices" by Quingzong Tseng (Schneider *et al.*, 2012). Segmentation and cell tracking was done using CellProfiler (Carpenter *et al.*, 2006) and the plug-in Cellstar (Versari *et al.*, 2017). Subsequently, tracking was manually checked, and mis-tracked cells were removed from the analysis. Time of bud emergence was manually defined as the time when a bud appeared in the bright-field image for the first time. Cell lineage was manually determined using the fluorescent signal of the bud neck marker Cdc10-mKate2. Cell volumes were calculated from cross-sectional cell areas assuming a spherical geometry.

Osmotic Shock Experiments to Assess Cell Wall Strain

The cell wall strain was assessed, after procedures by Misra *et al.* (2013) and Bonazzi *et al.* (2014), by monitoring and evaluating the deformation state of shmooing MATa bar1Δ cells, before and after rapid osmotic shocks. Cells were inoculated in SD medium on the previous day and diluted to an OD below 0.1 at the day of the measurement. After cells had grown to an OD between 0.3 to 0.6, they were treated with $10\,\mu\mathrm{M}$ and left for $2\,\mathrm{h}$ in a shaker at $30\,^{\circ}\mathrm{C}$. Subsequently, shmooing cells were seeded in self-made, Y-shaped MFD. To prevent wash-out during flow measurements cells were covalently attached to the MFD glass surface by concanavalin A (Sigma Aldrich, Taufkirchen, Germany). To monitor the cell shape z-stacked image time series were acquired in bright-field with a IX83 microscope (Olympus Deutschland GmbH, Hamburg, Germany) using a 100x oil immersion objective (Plan S Apo 1.4 NA, Olympus) and a back-illuminated EM-CCD camera (iXON Ultra 888). Rapid exchange of extracellular medium from SD medium to SD medium containing $2\,\mathrm{M}$ sorbitol (Sigma Aldrich, Taufkirchen, Germany) was achieved by using a fluid

pressure controller (Fluigent GmbH, Jena, Germany). For continuous pheromone induction $10\,\mu$M α-factor was added to both media. Analysis was done on extended focal images of the obtained image z-stacks using the software Cell Sense Dimensions (Olympus Deutschland GmbH,Hamburg, Germany) and imageJ Schneider *et al.* (2012).

2.2.3 Atomic Force Microscopy

Investigations on spatial aspects of microorganisms, such as *S. cerevisiae*, are often limited by the resolution of light microscopy. The so called "diffraction limit of light microscopy" can be overcome by surface scanning techniques. In the early eighties of the last century Binning *et al.* (1982) introduced scanning tunnel microscopy (STM), a technique which exploits the tunnel effect to obtain surface topographies at subnanometer resolution. Thereby, the tunnel current flows between a conductive surface and a metal tip in close proximity. The surface was scanned at constant tunnel current by displacing the metal tip accordingly, using a piezoelectric actuator. The applied voltage for displacing of the tip during scanning was used to generate topographic images of the surface. Only few years later STM was already used to investigate cell membranes and cyto-skeletons from human medulloblustoma (Ruppersberg *et al.*, 1989). Based on the STM, (Binnig *et al.*, 1986) invented AFM (also referred to as scanning force microscopy), where the contact or the proximity between tip and surface is not anymore controlled by a tunnel current but by the deflection of a cantilever holding the tip, which render the requirement for conductive surface and tip unnecessary. A scheme of the concept is shown in Fig. 2.4. The deflection of the cantilever is monitored by a laser focused to the top region of the cantilever and reflected to a photo-diode. The voltage signal of the photo-diode therefore yields information on the z-position of cantilever tip with respect to the undeflected state. This setup allows for detection of tip height with subnanometer precision. Over the last decades several modes of operation have been developed utilizing AFM. On the one hand, several horizontal scanning methods have been introduced to control or reduce tip-surface interactions, by scanning at constant height, constant force or constant damping of an excited cantilever oscillation. On the other hand, methods utilizing vertical probing have been developed which can provide information on physical properties of the surface and its interactions with the cantilever tip. The latter methods are subsumed under the term force spectroscopy.

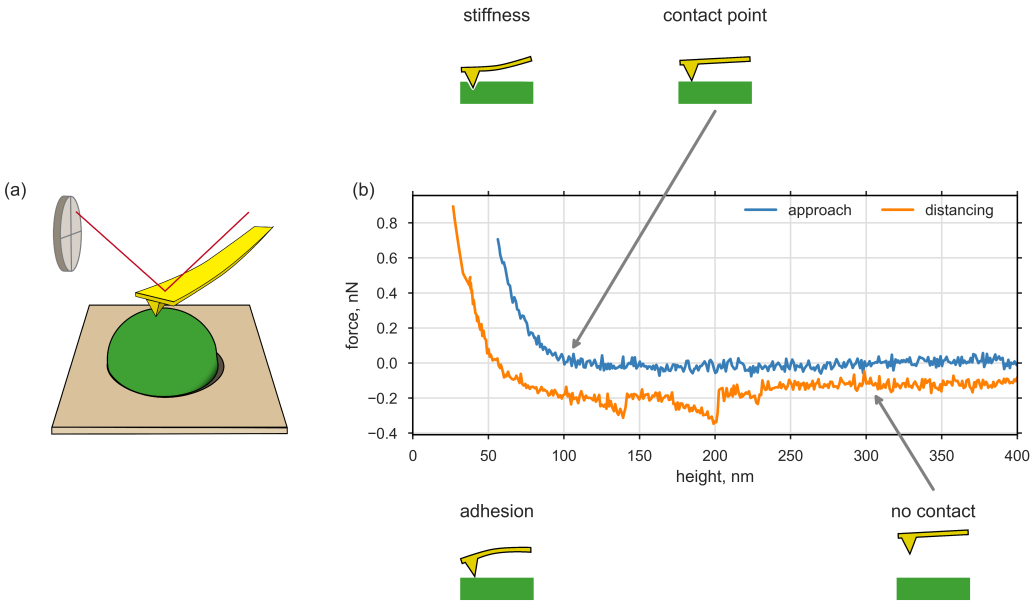

Fig. 2.4.: AFM-based force spectroscopy provides information on surface properties. (a) Work principle of the AFM. (b) Exemplary force distance cycle with approaching and distancing of the cantilever to the surface. Positions relevant for for multi-parametric imaging are marked: stiffness — slope of the approach curve after surface contact, contact point — height at which tip comes into surface contact, adhesion — either the area between distancing curve and baseline or maximal negative force of during retraction and no contact – i.e. baseline itself, when tip is not in contact to the surface and no acting force are measured.

Force Spectroscopy

In force spectroscopy the cantilever serves as force probe. Whereas the cantilever is approximated by a spring, for which the exerted force can be calculated by $F = kz_c$, given a known spring constant k and vertical deflection z_c of the cantilever. The assumption of the linear relationship between force and deflection is justified, since the deflection is very small ($z_c = 10\,\mathrm{nm}$ for $F = 1\,\mathrm{nN}$ and $k = 0.1\,\mathrm{N/m}$) compared to the length of the cantilever ($\approx 140\,\mu\mathrm{m}$ MLCT-E). Instead of horizontally, as for topography imaging, the scan is performed vertically, allowing to monitor forces between cantilever and tip for varying heights. To obtain the actual tip-sample distance z_{ts}, the displacement z of the cantilever by a piezo actuator has to be corrected for the cantilever deflection: $z_{ts} = z - z_c$. A typical force distance cycle, as shown in Fig. 2.4 contains at least two distinct phases: approach phase and distancing phase, although various other phases can be assigned as shown below in Sec. 2.2.4. Several repulsive and attractive tip surface interactions can be distinguished, depending on the tip-sample distance and the phase, including: Van der Waals interactions, which cause the tip to snap into contact when the tip approaches the surface; electro-static interactions, which can be detected for even longer tip-sample distances or various adhesion interactions (Fig. 2.4(b)), keeping the tip in surface contact when retracted above the initial contact point.

In this thesis I focus mainly on the repulsive forces during the approach after surface contact which can provide information on the material properties of the probed surface. In particular, when the cantilever tip penetrates the surface of soft elastic material, the measured repulsive force depends only on the indentation depth δ, the geometry of penetrating tip and the elasticity, i.e. the Young's modulus (YM) E. Note that the indentation depth δ equals the negative tip-sample distance after surface contact, i.e.

$$\delta = \begin{cases} -z_t s, & \text{if} \quad z_t s < 0 \\ 0, & \text{else.} \end{cases} \tag{2.31}$$

According to Sneddon (1965) the required vertical loading force to penetrate an extended elastic material with a conical indenter with half-angle θ to a depth of δ is given by:

$$F = \frac{E}{1-\nu} \frac{2\,\tan\theta}{\pi} \delta^2. \tag{2.32}$$

Where ν is the Poisson's ratio, which reflects the tendency of the material to extend in the direction perpendicular to the direction of compression and is commonly set to $\nu = 0.5$. Hence, fitting Sneddon's model to force distance curves obtained from indentation experiments, provide information on the YM as shown in Fig. 2.5. Besides Sneddon's model there are other models to describe the force distance relation for indentation experiments, such as the Hertzian model which assumes a spherical geometry of the indenter (Hertz, 1881). The Hertzian model is commonly used, also for deviating indenter geometries if the indentation is very shallow. Dimitriadis *et al.* (2002) reported that the YM could be overestimated for thin layers, particularly when the tip radius is in the range of the layer thickness. The tip radius of the cantilever used in the study is $\approx 20\,\mathrm{nm}$ according to the manufacturer and therefore significantly lower than the cell wall thickness ($115\,\mathrm{nm}$), though a small bias could not be ruled out. Note that the estimated YM can be biased by angle between surface and indentation direction. On tilted surfaces the cantilever slides over the surface rather than indenting it, which results in artificially low E-values Routier-Kierzkowska & R. S. Smith (2013). Furthermore, this analysis based on the assumption of an isotropic material. Although this assumption is not satisfied in direction perpendicular to the surface, since electron micrographs show a doubled layer structure of the cell wall (Sec. 1.3), it is good approximation. Alternatively, the double layer model by Mercadé-Prieto *et al.* (2013) could be used to analyze the force spectroscopy data, which accounts for the vertical anisotropy. However, the model requires additional information on the layer thickness, which might vary from cell to cell or from one surface region to another and thereby add an additional source of errors.

Multi-Parametric Imaging

In the beginning force spectroscopy was performed on one particular sample position or on a small array of positions (16×16). Recent technical advances allow for bigger arrays of subsequent force distance cycles due to faster acquisition and increased data storage capacity, which gave rise to force spectroscopy based imaging, or multi-parametric imaging Y. F. Dufrêne *et al.* (2013) and Alsteens, Trabelsi, *et al.* (2013). Arrays of 512×512 can provide detailed material information on complex surfaces, such as on living cells. Thereby, at each position a force distance cycle is measured and analyzed. As can be seen in concept Fig. 2.4 each force distance curve can provide different information on the surface, such as height, stiffness or adhesion. Fig. 2.6 shows the utilization of multi-parametric imaging to characterize nano-tubules and sheets build from cholesterol analogues and phospholipids.

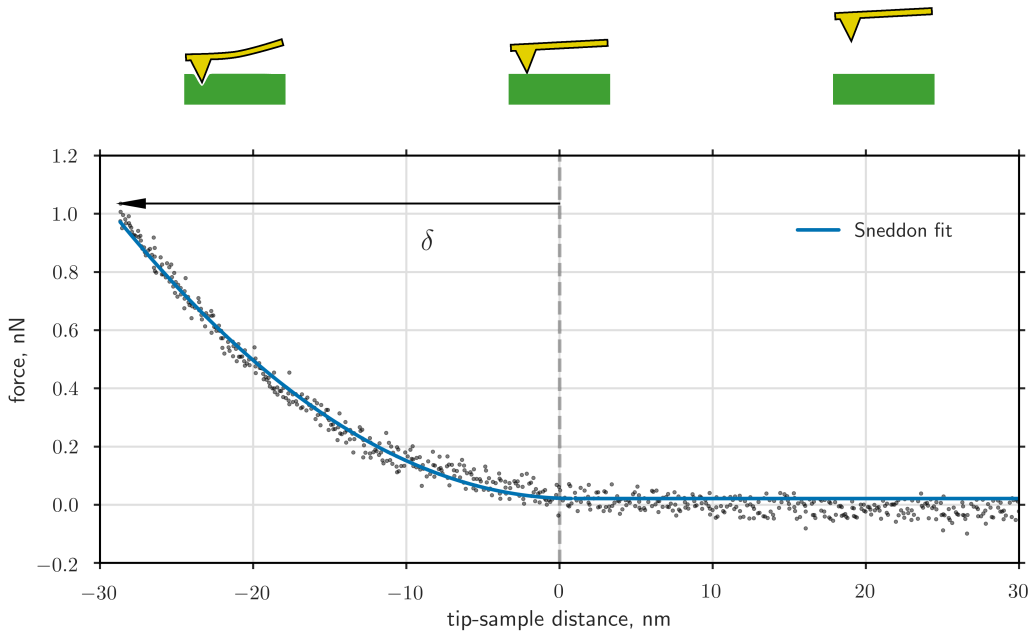

Fig. 2.5.: Nano-indentation measurement Force vs tip-sample distance during approach are shown as gray dots. Blue line represents fitted Hertz-Sneddon model for a conical intender with cone angle of $18°$ and δ is the indentation depth of the tip.

In the present study, I employed multi-parametric imaging to gain information on the local cell wall elasticity of living yeasts cells during morphogenesis. To this end, instead of relying on the apparent stiffness I used the YM, as explained in Sec. 2.2.3, to describe the elasticity parameter. The apparent stiffness is the linearized slope of the force after surface contact. Although the stiffness parameter can be used to resolve local inhomogeneity of the surface material its quantitative values are not comparable in between different measurements, since they depend on indentation depth and cantilever tip geometry.

Multi-parametric imaging of yeast cell walls was done in QI^{TM}-mode, provided by the manufacturer. The maximal applied force was set to $1.5\,\mathrm{nN}$, to limit the indentation depth (Fig. 5.5). A crucial factor when imaging the morphogenesis of living yeast cells was the acquisition time. To minimize acquisition time several adjustments had to be made. Distancing was performed at higher speeds compared to the approach to increase overall scanning speed. Further the approach speed was set to $v = 67\,\mu\mathrm{m/s}$, to optimize the scanning speed in such a way that deviations of the YM-values were still negligible, within the scope of this study (Fig. A.15).

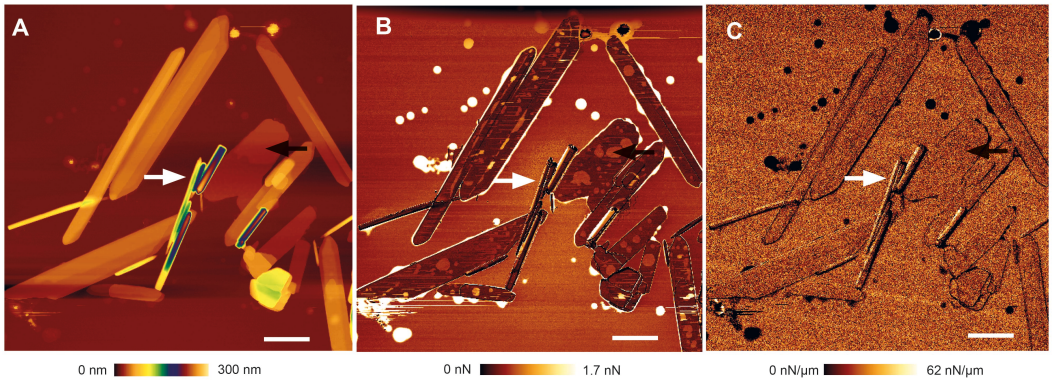

Fig. 2.6.: Multi-parametric images of nano-tubules and -sheets composed of cholesteryl nucleoside conjugate, cholesterylaminouridine and phosphatidylcholines on mica. Figure, taken from (Losensky *et al.*, 2016), shows (A) height, (B) adhesion, and (C) stiffness map ($512\,\mathrm{px} \times 512\,\mathrm{px}$) simultaneously acquired with AFM based multi-parametric imaging. Height maps provided information on geometry and structure of the nano-tubules and -sheets heights, while adhesion maps revealed soft lipid remnants on top of this nano-structures and stiffness maps confirmed the rigidity of those structures. White and black arrows point to nano-tubules and a nano-sheet with remnants of the lipid envelope, respectively. Scale bars is $2\,\mu\mathrm{m}$ and scales are represented by color codes.

AFM-Setup

All measurements described and analyzed in this thesis were performed on a Nanowizard III AFM (JPK Instruments AG, Berlin, Germany) mounted on an inverted optical microscope (Axio Observer.Z1 Carl Zeiss AG, Oberkochen, Germany) in a temperature controlled room set to $22\,^{\circ}\mathrm{C}$. The Microscope was placed on a noise canceling table in a noise reducing hood. As cantilever triangular-shaped MLCT-E/F (Bruker Corporation, Camarillo, CA) with a nominal spring constant of $0.1\,\mathrm{N/m}$ and $0.5\,\mathrm{N/m}$ were used. The spring constant of each cantilever was reevaluated by applying the thermal noise calibration method developed by Hutter & Bechhoefer (1993). AFM images and force–distance curves were analyzed with the JPK data processing software (JPK Instruments AG, Berlin, Germany) and in Python, using packages such as pandas, numpy, scipy (Mckinney, 2010; Walt *et al.*, 2011; Eric *et al.*, 2001).

Preliminary measurements were performed on an Nanowizard II AFM (JPK Instruments AG, Berlin, Germany) of the group of Prof. Jürgen P. Rabe (Physics of Macromolecules, physics department, Humboldt-Universität zu Berlin).

Cell Trapping for Live Cell Wall Nano-Indentation Experiments

To ensure stable and continuous measurements yeast cells were immobilized in porous membranes, after a procedure by Kasas & Ikai (1995). Prior to actual trapping log phase cells were strongly shaken to separate cells and reduce cell aggregates. About $10\,\mathrm{ml}$ of the cell suspension was subsequently pumped through a polycarbonate filter (Whatmann, GE Healthcare Europe GmbH, Freiburg, Germany) with a nominal pore diameter of $3\,\mathrm{nm}$ or $5\,\mathrm{nm}$. Hereby cells with a diameter in range of the pore diameter were likely to get trapped in the pores while other cells either passed through the filter or accumulated on top of it. To remove attached non-trapped cells together with sedimented cell debris from the filter surface, it was gently rinsed with sterile-filtrated, yeast synthetic drop-out medium (SFSD medium). Subsequently, the rinsed filter membrane was rapidly attached to the cleaned glass surface of a self-made fluid chamber, using addition vulcanizing silicone Alpa-Sil V 66 (Alpina-Technische Produkte GmbH, Geretsried, Germany). The cell containing filter membrane rested for a $5\,\mathrm{min}$ attachment period before it was again extensively rinsed with SFSD medium. After filter attachment the fluid chamber was filled with $1\,\mathrm{ml}$ SFSD medium, and mounted on an AFM sample holder. Cell trapping, filter hole occupancy and remaining free cells were assessed with bright-field microscopy and SEM. For investigations on the mating morphogenesis $10\,\mu\mathrm{M}$ α-factor (Sigma Aldrich, St Louis, MO) was added to the solution to induce shmoo formation.

2.2.4 Nano-Rheology

The yeast cell wall is thought to be mainly elastic. However, in order to grow, the cell wall has to expand also irreversible, i.e. plastically. A common approach to describe plastic cell wall expansion, is to assume viscous response to high stresses. To unravel the viscous and elastic properties of the cell wall, I applied a method, introduced by Alcaraz, Buscemi, Grabulosa, *et al.* (2003), which was used to investigate the viscoelastic response of lung epithelial cells. This method has been repeatedly applied to mammalian cells, e.g. by Rother *et al.* (2014), when they studied differences between malign and benign cells. This approach, however, has not yet been applied to walled cells.

Based on the principles of rheology, the method utilizes AFM to measure the complex shear modulus G^*. One method to estimate the viscoelastic properties of a material is to insert a probe, e.g. a magnetic bead or the tip of a cantilever, into the material, oscillate it at a defined frequency and record the force response of the material to this oscillation. If the material is purely elastic, the measured force oscillates

in phase with the probe and at the same frequency. This is due to the fact that in such an experiment the force depends only on the displacement of the probe. In contrast, if the material is purely viscous, the phase is shifted by $90°$. This phase shift results from the different constitutive relationships between force and displacement for viscous or elastic material. The force to displace viscous material depends on the rate of the displacement instead of the displacement itself, which peaks at the inflection point of the oscillating displacement. Hence, the phase angle is a measure for the viscoelastic behavior of the material.

When using this rheology concept with AFM, the rheology probe, i.e. the cantilever tip, has to remain in the material during the entire measurement. Accordingly, a trade-off for the selection of the exciting amplitude arises: On the one hand, the amplitude of the oscillation has to be smaller than the vertical dimension of the material, i.e. the cell wall thickness. On the other hand, the amplitude of the oscillation needs to be significantly higher than the intrinsic noise of the measurement to facilitate further analysis.

To determine the viscoelasticity of cell wall the cantilever was lowered to the cell surface until the tip indented the surface and the restoring force reached $1\,\mathrm{nN}$, corresponding to an indentation depth of $\approx 30\,\mathrm{nm}$ (Fig. 5.5). Subsequently, the cantilever was caused to oscillate at $1\,\mathrm{Hz}$, $5\,\mathrm{Hz}$, $10\,\mathrm{Hz}$, $50\,\mathrm{Hz}$ and $100\,\mathrm{Hz}$ for 3 cycles at each frequency until it was finally retracted from the surface to the starting position at a height of $400\,\mathrm{nm}$. One complete cycle took $\sim 5\,\mathrm{s}$ to complete. With $\Delta\delta = 2\,\mathrm{nm}$, the amplitudes of the input signal were chosen such that they were strong enough to sufficiently increase the signal to noise ratio, and small enough to ensure linear elastic response. Furthermore, small indentation amplitudes guaranteed that only the cell wall was indented, but not the whole cell. Indentation depth and applied forces are listed in Tab. 4.1. To avoid interference of the initial indentation with the first oscillation phase, e.g. through creeping of the material, the cantilever was halted for $0.75\,\mathrm{s}$ between both phases.

This procedure was repeated for 100 different positions at the top of the trapped cell. Measurement parameters, listed in Tab. 2.2 according to the different phases, were chosen such that the required time was minimal and the number of sampling points were comparable between phases with different oscillation frequency. The sampling points are the number of measured F, δ-pairs of each measurement phase and sampling frequency represents the corresponding temporal resolution. In Fig. 2.7 (a) and (b) exemplarily force-time and force-distance curves are shown for one complete rheology measurement.

Tab. 2.2.: Parameters of the nano-rheology measurements

phase	frequency Hz	time s	sampling rate kHz	sample points	cycles	velocity μm/s
extend		0.20	20	4000	-	2
pause		0.75	1	750	-	-
modulation 1	1	3	1	3000	3	-
modulation 2	5	0.6	1.5	1500	3	-
modulation 3	10	0.3	5	1500	3	-
modulation 4	50	0.06	25	1500	3	-
modulation 5	100	0.03	50	1500	3	-
retract		0.08	5	400	-	−5

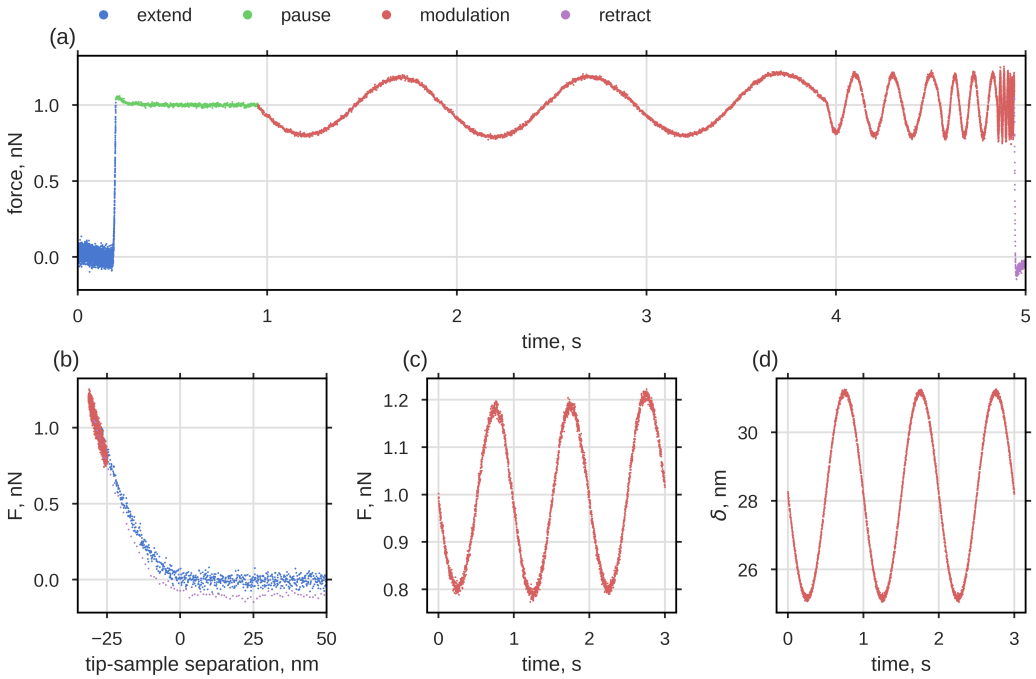

Fig. 2.7.: In AFM-based nano-rheology measurements the cantilever tip is excited to oscillate in the cell wall at low amplitudes. The tip approaches and indents the surface during the extend (blue), is halted for 0.75 s at 1 nN during the pause (green), is excited to oscillate for 3 cycles at 1 Hz to 100 Hz in the modulation phase (red) and is finally retracted (purple). For measurement parameters see Tab. 2.2. In (a) and (b) the force response over time and over tip-sample separation during an nano-rheology measurement is exemplarily shown. (c) and (d) show force F and indentation depth δ over time during oscillation at 1 Hz

As rheology probe, I used MLCT-E cantilever (Bruker, Camarillo, CA) with pyramidal tip geometry. As suggested by the manufacturer of the cantilever, the tip geometry was approximated by a cone with an angle of $\theta = 18°$. The repelling force F upon surface indentation δ (see Eq. 2.31) through a conical tip is given by the Herz-Sneddon formula (Sec. 2.2.3):

$$F(\delta) = \frac{E}{1-\nu}\frac{2\,\tan\theta}{\pi}\delta^2, \qquad \text{(2.32 revisited)}$$

where E is the YM of the material and ν the Poisson's ratio, which was assumed to be 0.5 throughout all calculations. Expanding $F(\delta)$ into a Taylor series around the mean indentation depth δ_0 yields:

$$F(\delta) = F(\delta_0) + \frac{\mathrm{d}F(\delta_0)}{\mathrm{d}\delta}(\delta-\delta_0) + \frac{\mathrm{d}^2F(\delta_0)}{\mathrm{d}\delta^2}\frac{(\delta-\delta_0)^2}{2} + \ldots. \qquad (2.33)$$

Since the displacement amplitude is very small, we can neglect higher orders of the Taylor series and use only the constant and the linear term. Hence, the ratio of the force and displacement amplitudes can be approximated by

$$\frac{F(\delta)-F(\delta_0)}{\delta-\delta_0} \approx \frac{E}{1-\nu^2}\frac{2\tan\theta}{\pi}\,2\,\delta_0. \qquad (2.34)$$

Given that the shear modulus G relates to the elastic modulus by

$$G = \frac{E}{2(1+\nu)}, \qquad (2.35)$$

(Landau *et al.*, 1960), Eq. 2.34 can be rearranged into

$$G(\delta) = \frac{1-\nu}{8}\frac{\pi}{\delta_0\,\tan\theta}\frac{F(\delta)-F(\delta_0)}{\delta-\delta_0}. \qquad (2.36)$$

Using the correspondence principle (Findley *et al.*, 1976) and considering that the indentation depth $\delta(t)$ is time dependent, Eq. 2.36 can be transformed from the time to the frequency domain

$$G^*(f) = \frac{1-\nu}{8}\frac{\pi}{\delta_0\,\tan\theta}\frac{F(f)}{\delta(f)}, \qquad (2.37)$$

where f is the frequency, and $F(f)$ and $\delta(f)$ are the Fourier transforms of the force and the indentation depth. To calculate the ratio $F(f)/\delta(f)$, I used the discrete

fourier transform of the modulation phase at each frequency. G^* is the complex shear modulus, which can be expressed as the sum of the storage modulus G' and the loss modulus G'' multiplied by the imaginary unit i,

$$G^* = G' + iG''. \tag{2.38}$$

G' represents the elastic or reversible part of the sinusoidal deformation, i.e. the energy which is stored and recovered during one oscillation cycle, while G'' represents the irreversible part and therefore is a measure for the dissipated energy.

Eq. 2.37 describes the material response on an inserted oscillating cantilever tip. However, not only the tip but the whole cantilever is excited to oscillate, and is subjected to hydrodynamic drag forces if the measurements are performed in liquid solution. To account for forces arising from hydrodynamic drag on the cantilever during oscillation the force displacement ratio needs to be corrected by the hydrodynamic drag transfer function at contact $H_d = 2\,\pi\,f\,b(0)$. The derivation of hydrodynamic drag transfer is explained later in this section. The corrected equation for the complex shear modulus now reads:

$$G^*(f) = \frac{1-\nu}{8}\frac{\pi}{\delta_0\,\tan\theta}\left(\frac{F(f)}{\delta(f)} - i2\,\pi\,f\,b(0)\right). \tag{2.39}$$

To compare the operating conditions for nano-indentation experiments (Tab. 4.1), in particular the applied pressure, with physiological conditions during yeast proliferation, the maximal applied pressure P_{max} had to be calculated, with $P_{\text{max}} = F_{\text{max}}/A$, where A is the cross-sectional area of the cone indenting the surface,

$$A = \pi\,\delta^2\,\tan^2\theta. \tag{2.40}$$

Complex Modulus of Basic Visco-Elastic Models: Maxwell Model

To challenge the mechanical description for the cell wall considered in the SCGM, I tested whether this model can explain the complex shear moduli obtained from nano-rheology measurements. In Sec. 2.1.2, I introduced the Bingham-Norten element to describe the viscoelastic-plastic properties of the cell wall in the SCGM. If the stress in this element is always above the yield criteria, the element can be reduced to a Maxwell body, which is one of the simplest viscoelastic models and connects a spring (s) and a dashpot (d) in series. If elements are connected in series,

each element is subjected to the same force ($\sigma = \sigma_d = \sigma_s$), while strain and strain rate are shared among the elements ($\varepsilon = \varepsilon_s + \varepsilon_d$, $\dot{\varepsilon} = \dot{\varepsilon}_s + \dot{\varepsilon}_d$). For the spring and the dashpot the constitutive relationships reads as

$$\sigma = E_0\,\varepsilon, \qquad \text{(revisited Eq. 2.18)}$$

and

$$\sigma = \dot{\varepsilon}\mu. \tag{2.41}$$

For simplification, I used $E_0 = \frac{E}{(1-\nu^2)}$. If both elements are combined in series the equation for the strain rate becomes,

$$\dot{\varepsilon} = \frac{\dot{\sigma}}{E_0} + \frac{\sigma}{\mu}. \tag{2.42}$$

When considering oscillating forces, stress and strain can be expressed more conveniently by two complex functions:

$$\sigma^*(t) = \sigma_0^* \mathrm{e}^{(i\omega t + phi)}, \tag{2.43}$$

$$\varepsilon^*(t) = \varepsilon_0^* \mathrm{e}^{i\omega t}. \tag{2.44}$$

Where ω is the angular frequency and ϕ is the phase shift between stress and strain. The phase angle ϕ should not be confused with the extensibility ϕ used in Sec. 3.1. Replacing the function for stress and strain in Eq. 2.42 with their complex functions yields

$$i\omega\varepsilon_0^* \mathrm{e}^{(i\omega t)} = \left(\frac{i\omega}{E_0} + \frac{1}{\mu}\right) \sigma_0^* \mathrm{e}^{(i\omega t + \phi)}. \tag{2.45}$$

This equation can be rearranged to calculate the complex tensile modulus as follows:

$$E^* = \frac{\sigma^*}{\varepsilon^*} = \frac{\omega^2\mu^2 E_0}{\omega^2\mu^2 + E_0^2} + i\frac{\omega\mu E_0^2}{\omega^2\mu^2 + E_0^2}. \tag{2.46}$$

Using Eq. 2.35 and the relation $G^* = G' + iG''$ we can obtain descriptions for storage and loss modulus, G' and G'':

$$G' = \frac{1}{2(1+\nu)} \frac{\omega^2 \mu^2 E_0}{\omega^2 \mu^2 + E_0^2}, \quad G'' = \frac{1}{2(1+\nu)} \frac{\omega \mu E_0^2}{\omega^2 \mu^2 + E_0^2}. \tag{2.47}$$

Hence, the storage modulus scales quadratically and the loss modulus linearly with ω, if ω is small. For $\omega \to \infty$, however, the storage modulus approaches a constant value, while the loss modulus decays with ω^{-1}.

Complex Modulus of Basic Viscoelastic Models: Kelvin-Voigt Model

Another basic viscoelastic model is the Kelvin-Voigt model, in which dashpot and spring element are arranged in parallel, in contrast to the serial arrangement in the Maxwell model. Using the same approach as for the Maxwell model, the complex modulus of the Kelvin-Voigt model can be determined by,

$$E^* = E + i\mu\omega. \tag{2.48}$$

In this model, the storage modulus is independent of the frequency, while the storage modulus scales linearly with it:

$$G' = \frac{1}{2(1+\nu)} E, \quad G'' = \mu\omega. \tag{2.49}$$

Therefore, when an oscillatory strain is imposed, the Kelvin-Voigt model show two distinct behaviors. At low frequencies the complex modulus is dominated by the storage modulus, since it is independent of the frequency and, thus, is constant, while the loss modulus approaches zero. In contrast, with increasing frequency the loss modulus, which exclusively depends on the viscosity, becomes the dominating part of G^*, as it scales linearly with ω and overtakes G' when $\omega > G'/\mu$ at some point.

Structural Damping

The empirical observed coupling of G' and G'' is called structural damping behavior and cannot be explained by the simple viscoelasticty models, explained above. To describe the structural damping various empirical laws have been formulated. An

extended empirical law, containing an additional Newtonian viscous term, to reflect the increase of the G'' at high frequencies, has been introduced by J. Fredberg & Fabry (2006), which reads

$$G^*(f) = G_0(1 + i\tan((x-1)\,\pi/2))\left(\frac{f}{f_0}\right)^{x-1}\Gamma(2-x)\cos((x-1)\pi/2) + i\,2\,\pi f\mu. \tag{2.50}$$

For $x \approx 1$ the equation can be simplified to

$$G^*(f) \approx G_0(1 + i\tan((x-1)\,\pi/2))\left(\frac{f}{f_0}\right)^{x-1} + i\,2\,\pi f\mu. \tag{2.51}$$

Eq. 2.51 was used in Sec. 4.3 to determine the viscoelastic properties of the yeast cell wall. To this end, Eq. 2.51 was fitted to $G^*(f)$ values obtained from nano-rheology measurements of single cells.

G_0 is the scaling factor for storage and loss moduli, $\alpha = x - 1$ is a power-law exponent and μ is the viscosity. Here, x defines the structural damping coefficient of the model, i.e. the hysteresivity $\eta = \tan((x-1)\,\pi/2)$. Additionally, x can be interpreted as an effective noise temperature of a soft glassy material, as discussed below and in Sec. 4.4. The scaling factor of the frequency f_0 was generally set to $1\,\mathrm{Hz}$, for simplicity. The structural-damping model assumes that the storage modulus increases with frequency following a power law with exponent α, while the loss modulus is the sum of two terms. One term is linked to the storage modulus through the structural-damping coefficient η and the other term represents the contribution of the Newtonian viscosity. Coupling both moduli, storage and loss, by $\tan(\alpha\,\pi/2)$ is a feature of the structural-damping behavior. By fitting Eq. 2.51 to mean $G^*(f)$ values from single-cell data, I could estimate three independent parameters: G_0, α and μ. Data analysis and fitting was done in Python using the scipy package (Eric *et al.*, 2001).

Soft Glassy Rheology

In the following, I will outline the concept of soft glassy rheology, as it was proposed by Sollich *et al.* (1997) to explain and characterize structural damping. Sec. 4.4 explores the relevance of the model to the mechanical analysis of the cell wall. Soft materials such as foams, emulsions, gels and cells differ in their rheological properties from established viscoelastic models. In particular, these materials show

structural damping (see Sec. 2.2.4), i.e. ratios of measured loss and storage moduli G''/G' of these materials are often nearly constant over a wide range of frequencies and additionally both moduli show either weak power-law or negligible dependence on the frequency (Ketz *et al.*, 1988; Mason *et al.*, 1995). This contrasts linear response theory where G'' is an odd function of ω while G' is an even function, as derived for the Maxwell model. The soft glassy rheology model formulated by Sollich *et al.* (1997) is a mesoscopic model of elastic elements with varying expansion states l and yield energies E_y. Here l is the expansion of each element with respect to its dimension, resulting in an elastic energy per element of $E = \frac{1}{2}kl^2$, with a spring constant k. The other varying property of each element is the yield energy E_y, which is the maximal elastic energy each element can posses before it yields and returns to the relaxed state ($l = 0$). If the ensemble is deformed at a strain rate $\dot{\gamma}$ each element is deformed with the same rate ($\dot{l} = \dot{\gamma}$). The time evolution of the probability distribution $P(E_y, l, t)$ can be then written as :

$$\frac{\partial P(E_y, l, t)}{\partial t} = -\dot{\gamma}\frac{\partial}{\partial l}P - \Gamma_0\, P\, e^{-(E_y - \frac{kl^2}{2})/x} + \Gamma(t)\rho(E_y)\delta(l). \tag{2.52}$$

The first term, is a drift, which shifts the probability distribution to larger deformation states when a strain rate $\dot{\gamma}$ is imposed onto the system. The second and third term cover the yielding and can be seen as , not necessarily synchronous, birth death processes. The death process is the second term and describes the reduction in probability density for larger l, since each element will yield with a transition probability depending on the activation energy $E_a = E_y - \frac{1}{2}kl^2$ and the effective temperature x, whereby Γ_0 is attempt frequency of the transition. The last term can be referred to as birth process, as it describes the emerging of new relaxed ($l = 0$) elements with yield energies randomly chosen from $\rho(E)$. Here $\Gamma(t)$ is the mean yielding rate,

$$\Gamma(t) = \Gamma_0 \left\langle e^{-(E_y - \frac{1}{2}kl^2)/x} \right\rangle_P, \tag{2.53}$$

which leads to potential asynchronous yield processes. Since only elastic contributions of the elements are considered, the macroscopic stress can be calculated by

$$\sigma(t) = k \left\langle l \right\rangle_p = k \int dE_y\, dl\, P(E_y, l, t)\, l. \tag{2.54}$$

x has a key role in the dimensionless model and represents the effective temperature and the thermal energy. It is an effective temperature since the glass transition temperature is supposed to be far from ambient temperature, which therefore could not carry enough energy for such a transition.

Combined Eq. 2.52 and Eq. 2.54 represent the soft glassy rheology model (SGR), reflecting the "glassy" features through the disordered states of E_y and l and the softness at large macroscopic strains through the material yielding.

Hydrodynamic Drag

AFM based nano-rheology in liquid, explained in above, is a powerful tool to disentangle elastic or viscous behavior of biological materials. From the phase shift of the force response on an oscillating cantilever tip inserted into the material of interest, the elastic and viscous contributions can be determined. However, concomitantly with the tip, the whole cantilever is excited to oscillate. This oscillating cantilever is exposed to hydrodynamic drag forces from the surrounding liquid. Alcaraz, Buscemi, Puig-De-Morales, *et al.* (2002) developed a method to correct the estimated complex shear modulus for the hydrodynamic drag onto the cantilever. The hydrodynamic drag is hereby determined from measurements close to but not at the surface.

The cantilever is considered as spring with an effective mass m_{eff} and spring constant k (spring-mass model), which is subjected to forces from the indented sample F_s as well as to hydrodynamic drag forces F_d, whereby the vertical displacement of the piezo-element is shared between deflection of the cantilever and the indentation of the material $z = z_c + \delta$. The resulting equation of motion reads in the time domain as

$$m_{eff} \frac{\mathrm{d}^2 z_c(t)}{\mathrm{d}t^2} + k\, z_c(t) = F_s(t) + F_d(t). \tag{2.55}$$

When transformed into the frequency domain the equation becomes

$$-\omega^2\, m_{eff}\, z_c(\omega) + k\, z_c(\omega) = F_s(\omega) + F_d(\omega), \tag{2.56}$$

where ω is the angular frequency. Substituting m_{eff} using the relationship for the resonance frequency $\omega_0^2 = \frac{k}{m_{eff}}$ while exploiting $\frac{F(\omega)}{\delta(\omega)} = \frac{F(f)}{\delta(f)}$ we can simplify Eq. 2.56 as follows:

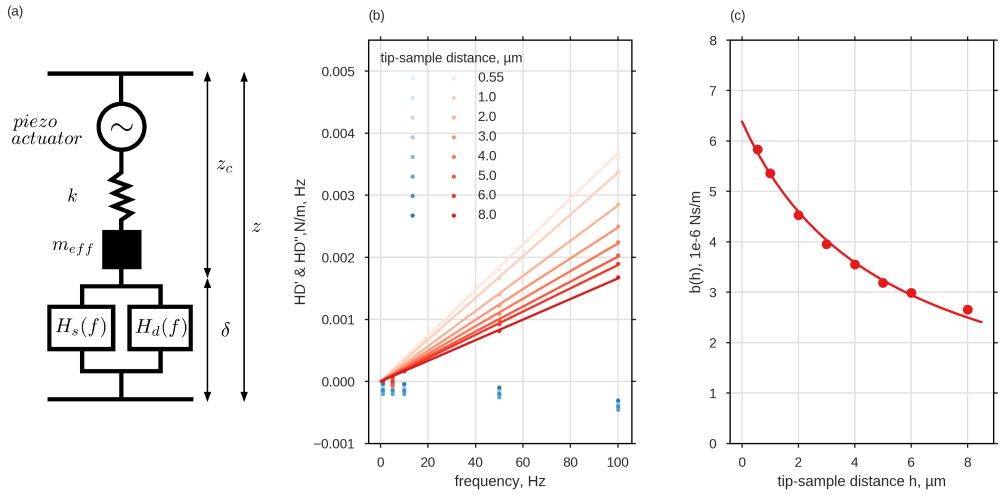

Fig. 2.8.: Determinig the hydrodynamic drag onto the cantilever (a) Mechanical model of the measurement. Piezo actuator oscillates the cantilever, represented as spring with constant k and effective mass m_eff. This cantilever is coupled to the sample and to the liquid via the frequency depending transfer functions $H_s(f)$ and $H_d(f)$, respectively. The scheme is adapted from (Alcaraz, Buscemi, Puig-De-Morales, *et al.*, 2002). (b) The mean real (blue) and imaginary (red) part of of the measured hydrodynamic drag transfer function H_d (N=100), for a non-surface contact measurement. Red lines show linear fits of $Hd'' = i\,2\,\pi\,f\,b(h)$ for different tip-sample distances h. (c) Fit of the hydrodynamic drag coefficient $b(h)$ for one measurement, assuming scaled spherical model of the cantilever, was used to calculate $b(0)$.

$$-k\,\frac{\omega^2}{\omega_0^2}\,z_c(\omega) + k\,z_c(\omega) = F_s(\omega) + F_d(\omega), \tag{2.57}$$

$$\left(1 - \frac{\omega^2}{\omega_0^2}\right) k\,z_c(\omega) = F_s(\omega) + F_d(\omega), \tag{2.58}$$

$$\left(1 - \left(\frac{f}{f_0}\right)^2\right) \frac{F(f)}{\delta(f)} = \frac{F_s(f)}{\delta(f)} + \frac{F_d(f)}{\delta(f)}. \tag{2.59}$$

$$\tag{2.60}$$

Rewriting this relation in terms of the transfer functions $H_d(f) = \frac{F_d(f)}{\delta(f)}$ and $H_s(f) = \frac{F_s(f)}{\delta(f)}$ gives us

$$\left(1 - \frac{f^2}{f_0^2}\right) H(f) = H_s(f) + H_d(f). \tag{2.61}$$

Since the resonance frequency of the cantilever f_0 ($\sim$300 kHz) is three orders of magnitude higher than the operating frequency ($f \ll f_0$), we can simplify this relation further to

$$H(f) = H_s(f) + H_d(f). \tag{2.62}$$

If the cantilever oscillates above the surface, $H(f)$ becomes $H(f) = H_d(f)$, since $H_s(f) = 0$. In addition, the hydrodynamic drag force at low Reynolds number can be written as

$$F_d = b(h)\,v, \tag{2.63}$$

where v is the velocity ($v = \mathrm{d}\delta/\,\mathrm{d}t$) and $b(h)$ is the height-dependent drag coefficient. Transforming Eq. 2.63 into the frequency domain and rearranging, provides the hydrodynamic transfer function:

$$H_d = \frac{F_d(f)}{\delta(f)} = i\,2\,\pi\,f\,b(h). \tag{2.64}$$

The transfer function $H_d(f)\Big|_{b(0)}$, evaluated at the surface, was used to correct the calculation of the complex shear modulus in Eq. 2.39. To estimate $b(0)$, first, the

transfer function $H_d(f)$ was measured at each required frequency f for different tip-surface distances h. Second, the drag coefficient $b(h)$ was determined from the slope of $H_d(f)$ for each measured tip-surface distances. Finally, $b(h)$ was extrapolated to $h = 0$ using the scaled spherical model of the cantilever,

$$b(h) = 6\,\pi\,\eta a^2/(h + h_{eff}). \tag{2.65}$$

The obtained hydrodynamic drag coefficient at $h = 0$ was used in Eq. 2.39 to correct the estimation on the complex modulus of the yeast cell wall.

Experimental Procedure

At the end of each measurement day, the hydrodynamic drag of the SD medium onto the cantilever was determined on a cell and pore free area of $\sim 3\,\mu\mathrm{m}^2$ of the surface. The experimental procedure was similar to the procedure explained in the beginning of this section, and if not otherwise stated, the same experimental settings were used. To obtain a reference position in z the cantilever was lowered to the surface until the force reached at set point of $1\,\mathrm{nN}$. Subsequently, the cantilever was retracted to a tip surface distance h of $0.55\,\mu\mathrm{m}$, $1\,\mu\mathrm{m}$, $2\,\mu\mathrm{m}$, $3\,\mu\mathrm{m}$, $4\,\mu\mathrm{m}$, $5\,\mu\mathrm{m}$, $6\,\mu\mathrm{m}$ and $8\,\mu\mathrm{m}$. At each distance the cantilever was caused to oscillate at frequencies f of $1\,\mathrm{Hz}$ to $100\,\mathrm{Hz}$. The procedure was repeated at each point of a 8×8 or 10×10 grid of the chosen area. Thereby recorded time series of force $F(t)$ and tip displacement $\delta(t)$ were transformed into the frequency domain using the fast Fourier transform (FFT) of the numpy package for Python (Walt *et al.*, 2011). From the obtained $F(f)$ and $\delta(f)$ the transfer function $H_d(f)$ was determined at each tip-sample distance. Eq. 2.64 was fitted to the mean of the imaginary part H_d'' to estimate the hydrodynamic drag coefficient $b(h)$, as shown inFig. 2.8(b). The estimated $b(h)$ was in turn used to fit the scaled spherical model of the cantilever (Eq. 2.65), from which the drag coefficient at the surface $b(0)$ was extrapolated. Fig. 2.8(c) shows the drag coefficient and the corresponding fit for one particular day. With the obtained $b(0)$ the measured complex shear modulus could now be corrected for the hydrodynamic drag onto the cantilever during the measurement, using Eq. 2.39. If the measurement was terminated to soon, due to loss of the cantilever or significant adhesion of cell debris the mean hydrodynamic drag coefficient of all measurements was used.

2.2.5 Scanning Electron Microscopy

SEM was employed as a complementary method to bright-field microscopy, since a sufficient assessment of the sample preparation was not possible with bright-field microscopy due to the relatively high opacity of the filter material (Fig. A.14). Assessing the trapping and shmooing efficiency were of particular interest because: First, the maximal scan region of the x,y-piezo-acutator was $100\,\mu\mathrm{m}\times100\,\mu\mathrm{m}$, which contained only ≈10 filter holes. Therefore a high filter hole occupancy drastically reduced the time needed to find a suitable cell to measure. Secondly, although bright-field images of non-trapped MATa bar1Δ cells on common glass sample holders showed that treatment with $10\,\mu\mathrm{M}$ α-factor is sufficient to induce shmoo formation in almost all cells, visible mating projection were rarely observed in AFM topography images for equally treated cells.

Electron micrographs (Fig. 2.9) confirmed, however, that the majority of the trapped cells underwent shmoo formation, when induced with $10\,\mu\mathrm{M}$ α-factor. Moreover, SEM revealed that the vertical arrangement of mother bud pairs in pores is responsible for the low number of observed mating projection in topography images. Without a spacial cue, i.e. α-factor gradient, shmoo formation is predominantly localized to sites of previous budding events. However, due to the vertical alignment of mother and bud in the pore, those sites were often embedded, causing cells near the surface, to direct their mating projection inwards, instead of outwards. Hence, from topography scans those cells could not be distinguished from non-induced cells.

SEM sample preparation and measurements were performed as follows: initially, cells were trapped in filter membranes as described in Sec. 2.2.3. Membrane samples of trapped cells were divided into two groups; one half was immersed in SD medium with $10\,\mu\mathrm{M}$ α-factor, while the other was immersed in pure SD medium. After $1\,\mathrm{h}$ incubation time all samples were treated with $2.5\,\%$ glutaraldehyd, $2.0\,\%$ paraformaldehyd and $0.1\,\mathrm{M}$ cacodylat-buffer, to fixate the cells. Subsequently, samples were washed with double-distilled water and dehydrated with $30\,\%$, $50\,\%$, $70\,\%$, $80\,\%$, $90\,\%$, $96\,\%$ and $100\,\%$ ethanol and hexamethyldisilazane. The dried samples were mounted on SEM-sample holder and gold coated with a sputter coater (SCD 040, Balzers Union, Liechtenstein). Micrographs were acquired with a LEO 1430 (Carl Zeiss Ltd - Meditec, Cambridge, UK). Preparation and measurement was repeated once.

(a)

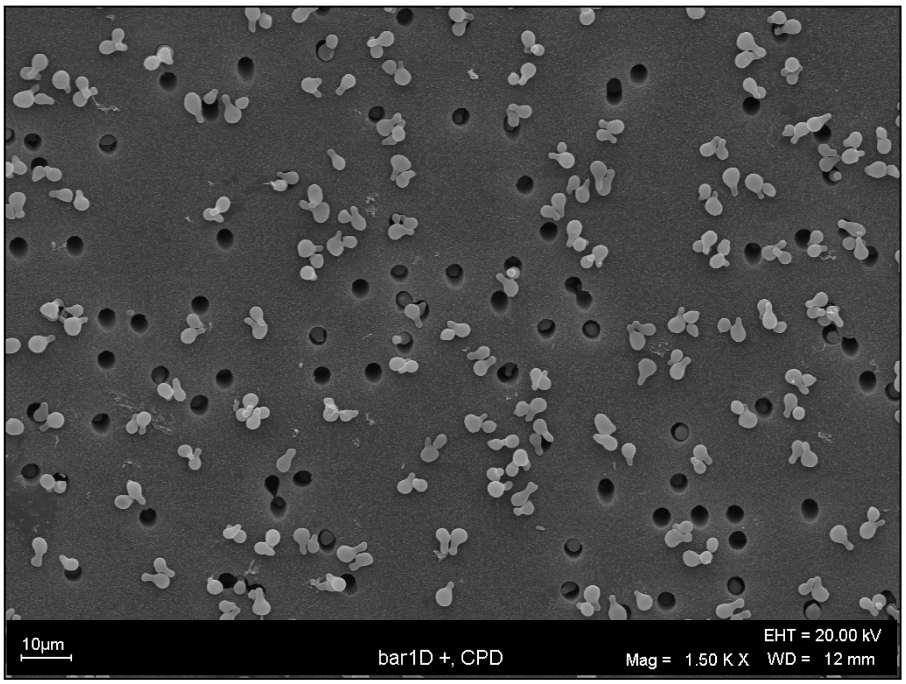

(b)

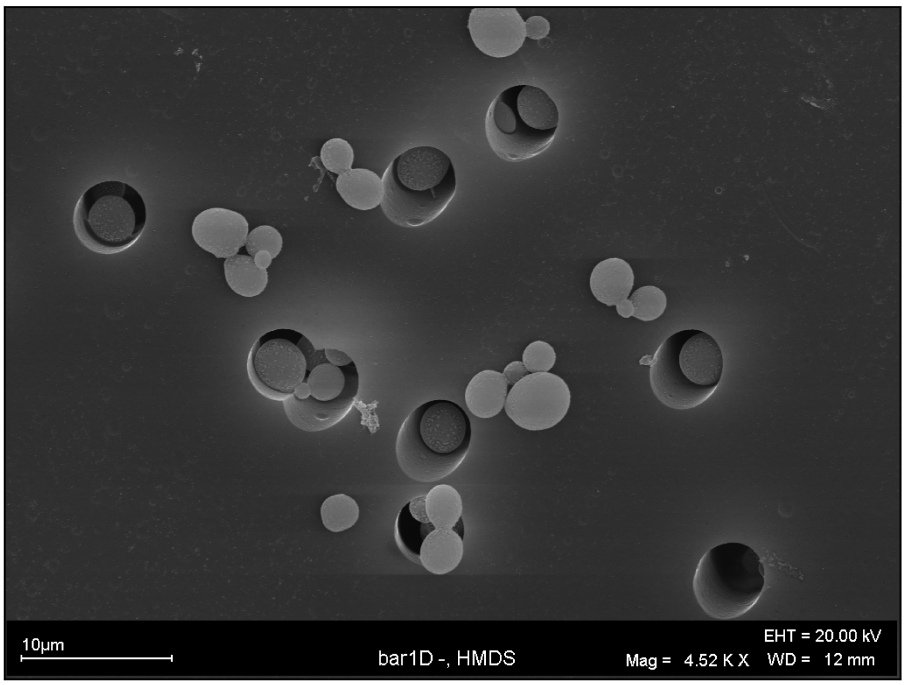

Fig. 2.9.: Assessment of filter hole occupancy and untrapped cells by SEM. Electron micrographs of polycarbonate filter with trapped and free bar1Δ, previously induced (a) and not induced (b) by $10\,\mu$M α-factor. Fixation led to cell shrinkage.

3 Cell Expansion during Vegetative Growth

The core of the mathematical model was designed by Tom Altenburg in his bachelor thesis and was further revised and refined by Jannis Uhlendorf and me. The study on the local cell wall elasticity was realized with the help of the student assistant Alice Wittig. Acquisition of microscopic images, cell tracking and volume calculation was done by Jannis Uhlendorf and will only be explained here briefly.

Altenburg, T., Goldenbogen, B., Uhlendorf, J. & Klipp, E. (2019). „Osmolyte homeostasis controls single-cell growth rate and maximum cell size of Saccharomyces cerevisiae.“ *(under review)*

In the following section I will explain the model for isotropic growth under the assumption of a spherical cell geometry and its extension to integrate the coupled growth of mother and bud. Subsequently, I will focus on the potential inhomogeneous cell wall elasticity of mother and bud and elaborate on the experimental approach, i.e. the nano-indentation measurements of the cell wall, as well as on the obtained results and its implications.

Growth dynamics of *S. cerevisiae* on the population level have been studied extensively in the past and became a part of the daily routine in microbiology laboratories, utilizing different growth measures. While for suspension cultures the optical density is used as proxy for the cell density, for cell cultures on agar plates the amount of colony serves as growth measure. In suspension the population density follows a sigmoid profile with three distinct phases: an initial lag-phase for low cell densities, a phase of logarithmic growth and a stationary phase at the maximum cell density.

In contrast, the growth dynamics of *S. cerevisiae* on the single-cell level is more controversial. While it appears evident, that the single-cell growth is exponential for several microorganisms, in particular for those that undergo symmetrical cell division, e.g. *Escherichia coli*, the growth behavior of *S. cerevisiae* is still subject to discussion (Amodeo & Skotheim, 2016). Both, exponential and linear behavior has been reported reported for the single-cell growth dynamics of *S. cerevisiae* (J. M. Mitchison, 2003; Turner *et al.*, 2012; Tyson & Hannsgen, 1985; Woldringh *et al.*,

1993). Furthermore, recent studies compared and correlated cellular volumes at characteristic events of the cell cycle, such as birth, cell division or bud emergence (Soifer *et al.*, 2016; Garmendia-Torres *et al.*, 2018) instead of whole volume trajectories to investigate the cell cycle dependent size control in yeast. Although they employed single-cell techniques, their analysis characterized rather the population than the single cell.

In the following section I will introduce, discuss and challenge an *a priori* model for the vegetative growth of *S. cerevisiae*, which is based on the interplay of four thermodynamic quantities: cell volume, osmolarity, turgor pressure and elastic energy. These thermodynamic quantities are highly linked via different concepts, comprising cell wall mechanics, osmo-homeostasis and water dynamics. As active driving force of cell expansion serves, in this model, the constant uptake of nutrients and osmolytes over the cell surface. Nutrient uptake not only provides building blocks and energy for the synthesis of new cell material, but also increases internal osmolarity. This generated osmotic pressure gradient drives water influx and thereby increases cell size, which, in turn, is counteracted by the elastic cell wall. The cell wall preserves not only the cellular integrity but also dampens the expansion rate. The model has been formulated, such that it covers, on the one hand, slow and steady expansion during cellular growth and, on the other hand, rapid and drastic volume variations caused by hyper- or hypoosmotic shocks.

The basic growth model, the SCGM, reflects the isotropic cell expansion of a spherical yeast cell during the G1 phase. To cover the whole cell cell cycle, the budding process had to be included, i.e. the expansion of two interlinked compartments (mother and bud). Therefore, two individual SCGM has been coupled, by allowing free transport of osmolytes and water between both compartments. Realistic coupled growth, i.e. the expansion of the smaller compartment, required distinctive mechanical properties of mother and bud cell wall. As potential distinguishing feature between mother and bud cell wall, the elasticity has been identified and tested. Therefore the cell wall of both compartments has been probed in nanometer-precision with AFM. The *a priori* cSCGM has been intensively tested against and constrained with single-cell volume data from independent data sets, acquired with bright-field microscopy.

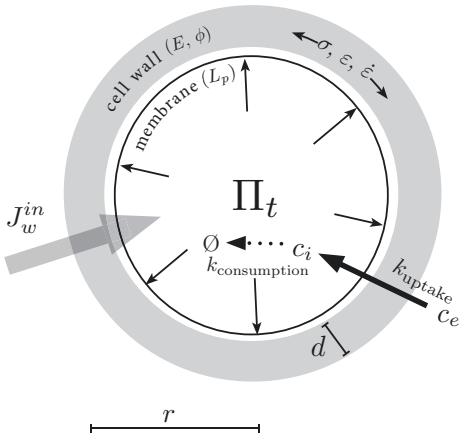

Fig. 3.1.: Scheme of the SCGM A detail description can be found in the text.

3.1 The Single-Compartment Growth Model

As described above in Sec. 1 *S. cerevisiae* is an unicellular fungus with spherical to ellipsoidal geometry and a strong cell wall that maintains the integrity against a high internal osmotic pressure. During non-stress conditions, single cell growth is characterized by isotropic expansion and formation of a single bud with again spherical to ellipsoidal geometry.

We formulated the SCGM for *S. cerevisiae* based on the four following assumptions: First, water influx follows the hydrostatic and osmotic pressure gradient and thereby drives the cell expansion. Second, the hydrostatic pressure arises from counter forces of the elastic cell wall expansion caused, in turn, by the water influx. Third, cell growth can be described as irreversible, i.e. plastic cell wall expansion. Fourth, continuous uptake of osmolytes, such as ions and nutrients, establishes and stabilizes the osmotic pressure gradient. From these assumptions we deduced three ODEs for the cellular volume, the internal osmolyte concentration and the turgor pressure. A scheme of the SCGM is depicted in Fig. 3.1.

Water Flux defines Volume Dynamics

To reduce complexity the cells were assumed to be perfect spheres, hence, their volume $V(r)$ depended solely on their cellular radius r. Further, we separated the volume ($V(r) = V_{\text{os}}(r) + V_{\text{b}}(r)$) into a volume $V_{\text{os}}(r)$, accessible for osmolytes and an inaccessible volume $V_{\text{b}}(r)$, e.g. consisting of bulky intracellular macromolecules

or compartments. It follows from the incompressibility of water that any change in $V_{\mathrm{os}}(r)$ must be equal to the water influx J_{w}^{in} over the enclosing membrane,

$$\dot{V}_{\mathrm{os}}(r) = J_{\mathrm{w}}^{in}. \tag{3.1}$$

According to Kedem & Katchalsky (1958), the water flux over a membrane follows the osmotic and hydrostatic pressure gradient ($\Delta\Pi = \Pi_{\mathrm{e}} - \Pi_{\mathrm{i}}$) and is limited by the hydraulic conductivity L_{p} and the permeability for solubles. As deduced in Sec. 2.1.2, the expansion rate of the osmotic radius $\dot{r}_{\mathrm{os}}(t)$ is given by

$$\dot{r}_{\mathrm{os}}(t) = -L_{\mathrm{p}}(\Pi_{\mathrm{t}} + \Pi_{\mathrm{e}} - \Pi_{\mathrm{i}}), \tag{3.2}$$

under the assumption of perfect semi-permeability and constant $V_{\mathrm{b}}(r)$. Where Π_{t} is the turgor pressure and Π_{e} and Π_{i} the external and internal pressures, which relate to the respective osmolyte concentration, c_i and c_e, via the van't Hoff equation:

$$\Pi = R\,T\,c, \tag{3.3}$$

with the temperature T and the ideal gas constant R. With Eq. 3.2 we now have a description for the volume development depending on the turgor pressure and the osmotic gradient. Note, that for negligible water fluxes ($J_{\mathrm{w}} = 0$) turgor pressure and osmotic pressure gradient cancel each other out.

Dynamics of Internal Osmolyte Concentration

The internal and external osmolyte concentrations, c_i and c_e, determine the osmotic pressure gradient. As an initial approximation c_e was chosen to be constant in order to focus on the contributions of the cell instead of the environment. Although the internal osmolyte concentration is the result of various complex processes, we considered only three mayor contributions: uptake, consumption and dilution. Since all new material has to cross the cytoplasmic membrane, we assumed the uptake rate to scale with the surface area A. In contrast, consumption and dilution scale with the cellular volume or the expansion rate of the volume, respectively. Here, consumption summarizes all processes in which the osmolyte concentration is actively reduced,

e.g. through respiration or synthesis of macromolecules from precursors. Combining these assumptions results in the implemented ODE for c_i, which reads:

$$\dot{c_i} = \frac{1}{V}(k_{\text{uptake}} A - k_{\text{consumption}} V - c_i \dot{V}). \tag{3.4}$$

Turgor Pressure and Cell Wall Mechanics

The turgor pressure is defined as the hydrostatic pressure exerted from the plasma membrane onto the cell wall. In the following, I will outline the concept behind the description of Π_t; for a more detailed derivation please see Sec. 2.1.2. At first, we need to consider the mechanical behavior of the cell wall under pressure. To this end, two principle assumptions have been made: First, the cell wall material is elasto-plastic, meaning that the cell wall will expand elastically until Π_t reaches a limit, the critical turgor pressure Π_c. Above this Π_c, the cell wall material will yield and additionally expand plastically, i.e. irreversibly. Second, the cells are perfect spherical thin shells $(d \ll r)$ with constant thickness d, which allows for convenient simplifications as described in Sec. 2.1.1. The strain ε and the strain rate $\dot{\varepsilon}$ of the cell wall arising from ideal elastic and ideal plastic expansion of such a shell are given by Eq. 2.20 and Eq. 2.21:

$$\varepsilon_{\text{elastic}} = \frac{1-\nu}{E} \frac{\Pi_t \, r}{2\,d}, \tag{2.20 revisited}$$

$$\dot{\varepsilon}_{\text{plastic}} = \frac{\phi \, r}{2\,d} \, f_m(\Pi_\text{t}, \Pi_\text{c}) \quad \text{where } f_m = \begin{cases} \Pi_\text{t} & \text{if} \quad \Pi_\text{t} > \Pi_\text{c} \\ 0, & \text{else} \end{cases}. \tag{2.21 revisited}$$

Where E, ϕ and ν being the Young's modulus YM, the extensibility and the Poisson's ratio. Together with Π_c, they represent the mechanical properties of the cell wall. To reflect the viscoelastic-plasticity of the cell wall we used a Bingham-Norton element (Fig. 2.3), in which the total strain is the sum of the elastic and plastic strains ($\varepsilon = \varepsilon_{\text{elastic}} + \varepsilon_{\text{plastic}}$), while the stress is equal for both deformations $\sigma = \sigma_{\text{elastic}} = \sigma_{\text{plastic}}$). Note, that cell wall extensibility has been used to describe different material responses in the past, such as viscoelasticity, plasticity an elasticity (Burgert & Fratzl, 2006). In this study the extensibility represents the viscous property of the cell during viscoelastic-plastic expansion. Integrating Eq. 2.20 and Eq. 2.21 into the time

derivative of the total strain and rearranging for $\dot{\Pi}_t$ provides the required ODE of the turgor pressure:

$$\dot{\Pi}_t = \frac{2Ed}{1-\nu}\frac{\dot{r}}{r^2} - \Pi_t\frac{\dot{r}}{r} - \frac{E\phi}{(1-\nu)}f_m(\Pi_t, \Pi_c). \qquad \text{(2.24 revisited)}$$

Similar equations, sharing two out of the three terms have already been formulated for other turgor related models (D. J. Cosgrove, 1981; J. K. Ortega, 1985; J. K. Ortega & Welch, 2013; Geitmann & J. K. Ortega, 2009). The additional term arises from the thin spherical shell approximation, in particular from the time derivative of the elastic element (Eq. 2.22). With Eq. 2.24, Eq. 2.30 and Eq. 3.4 we now have three coupled ODEs, describing the volume expansion of a single spherical cell. To follow the plastic expansion explicitly we defined the reference radius $R_{\text{ref}(t)}$ as the radius of the relaxed shell at any given time t and split Eq. 2.24 into two equations, Eq. 2.25 and Eq. 2.26, derived in Sec. 2.1.2.

3.1.1 Characteristics of the SCGM

As derived above, the core of the SCGM comprises four coupled ODEs for internal osmolyte concentration, turgor pressure, reference radius and cell radius. The ODEs where simulated numerically to characterize the volume evolution. Note that an analytical solution for the SCGM, under the assumption of constant external osmolyte concentration, has been found by Tom Altenburg and is described in Altenburg *et al.* (2019). For the numerical approach the model was implemented in the SBML based language Antimony (see and Sec. 2.1.2 and Sec. A.1.1) and simulated using the tellurium package in Python. Fig. 3.2 shows such a simulation for the key model parameters, using the initial values listed in Tab. 3.1. The simulation starts with a fairly small single volume, comparable with new formed buds and runs undisturbed for $300\,\text{min}$. After this time we allowed a rapid exchange of osmolytes between the intracellular and extracellular space according to the present osmotic gradient. With the resulting adaption of c_i and c_e the turgor pressure vanishes, leading to relaxation of the cell wall and subsequently to cell shrinkage. Additionally, the absence of Π_t prevents further plastic cell wall expansion, therefore allowing us to assess the relaxed volume. The reference volume V_{ref} represents the volume enclosed by the relaxed cell wall. Since it results solely from plastic but not from elastic cell wall expansion, its expansion reflects the actual material insertion in the cell wall. In the simulation, V_{ref} made up for $\sim 1/3$ of the maximum size, though its fraction is significantly higher for small cells. From simulated volume trajectories, excluding

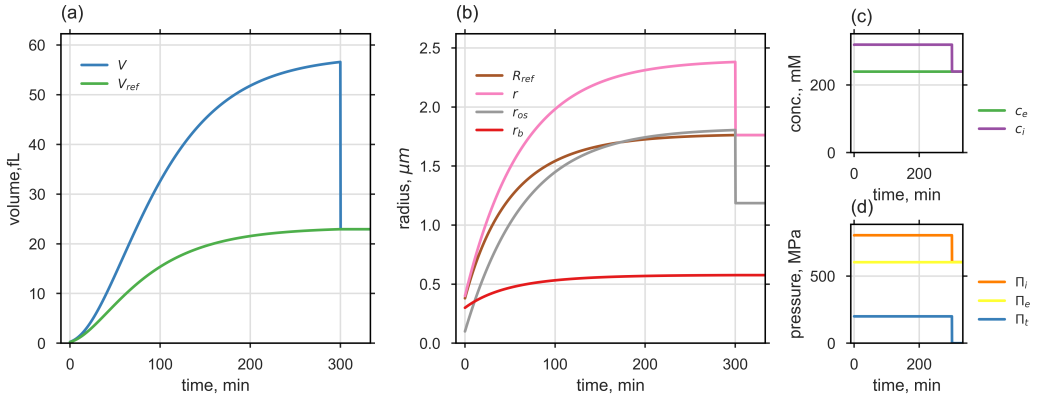

Fig. 3.2.: The SCGM shows initial exponential growth before asymptotically approaching a maximum volume.(a), (b), (c), (d) show the volume, radius, osmolyte concentration and pressure trajectories for the basic SCGM (parameter listed in Tab. 3.1). After 300 min the membrane was set to be ideally permeable for solubles, i.e. c_i adapt to c_e and therefore Π_t vanishes and the volume collapses to its relaxed state.

the equalization phase of c_i and c_e, general characteristics of SCGM with regard to volume expansion and internal osmolarity have been inferred and will be explained in the following.

Volume Expansion

In contrast to commonly assumed linear or exponential growth for single *S. cerevisiae* cells (J. M. Mitchison, 2003; Turner *et al.*, 2012; Tyson & Hannsgen, 1985; Woldringh *et al.*, 1993) the SCGM predicts a more complex growth behavior with a decreasing expansion rate. From an initial exponential increase in the volume for smalls cells, the expansion rate slows down with increasing cell size, is almost linear for intermediate sized cells and vanishes as the cell size approaches its maximum (Fig. 3.2(a)). Nevertheless, not all of the cellular volume is accessible for osmolytes. Bulky macromolecules reduce the intracellular space in which diffusion takes place. Therefore, we introduced the volume V_b and its radius r_b, and coupled its expansion rate to the expansion rate of R_{ref} assuming a constant ratio between both. $\dot{r}_{\text{b}}/\dot{R}_{\text{ref}} = 0.2$ was assumed *a priori*, since the dynamics of V_b has not yet been measured experimentally. Note that neither r_b nor R_{ref} decreases during the osmotic equalization.

Tab. 3.1.: Parameters and initial values of the SCGM.

parameter	value	unit	description	source
r_b^0	0.3	μm	initial radius (non-osmolytic volume)	assumption
r_{os}^0	0.1	μm	initial radius (osmolytic volume)	assumption
c_i^0	319.17	mM	osmolyte concentration (internal)	calculated from turgor pressure
c_e	240	mM	osmolyte concentration (external)	measured
Π_t^0	2×10^5	Pa	initial turgor pressure	Goldenbogen *et al.* (2016)
R	8.314	J/(mol K)	ideal gas constant	
T	303	K	temperature	optimal growth condition
Lp	1.19×10^{-6}	μm/(s Pa)	membrane water permeability	Klipp *et al.* (2005)
Π_{tc}	2×10^5	Pa	critical turgor pressure	Goldenbogen *et al.* (2016)
d	0.115	μm	cell wall thickness	Dupres, Y. Dufrêne, *et al.* (2010)
ϕ	1×10^{-4}	1/(s Pa)	extensibility	initial assumption
ν	0.5	–	Poisson's ratio	
E	2.58×10^6	Pa	Young's modulus (3D)	Goldenbogen *et al.* (2016)
k_{uptake}	2×10^{-16}	mmol/(μm^2 s)	osmolyte uptake rate constant	assumption
$k_{consumption}$	2.5e-16	mmol/(μm^3 s)	osmolyte consumption rate constant	assumption

Internal Osmolarity

As shown in Fig. 3.2(c,d) c_i as well as Π_t are in quasi steady state during the whole growth process. Uptake of osmolytes increases c_i and therefore Π_i, which steepens the pressure gradient that drives water over the membrane inside the cell. The resulting influx of water J_{w}^{in}, in turn, dilutes the intracellular osmolytes and expands the cell wall. The elastic expansion of the cell wall leads to an increase in Π_t, which reduces the apparent pressure gradient and therefore impedes further influx of water. Nevertheless, Π_t can not increase indefinitely since it is limited by Π_c. If Π_t raises above Π_c the cell wall will expand plastically, which reduces the stress in the wall and thus decreases Π_t. Therefore, Π_t is always close to Π_c under the constraint of constant osmolytes uptake.

The growth determining process is, apart from the mechanical response of the cell wall, the control of c_i, through uptake, consumption and dilution. Here, the uptake rate constant k_{uptake} dictates the expansion rate while the ratio between both rate constants $k_{\text{uptake}/k_{\text{consumption}}}$ defines the maximum cell size, as shown in Fig. 3.3. Note that the SCGM is very sensitive to alterations of those rate constants, as slight variations result in unreasonable volume trajectories.

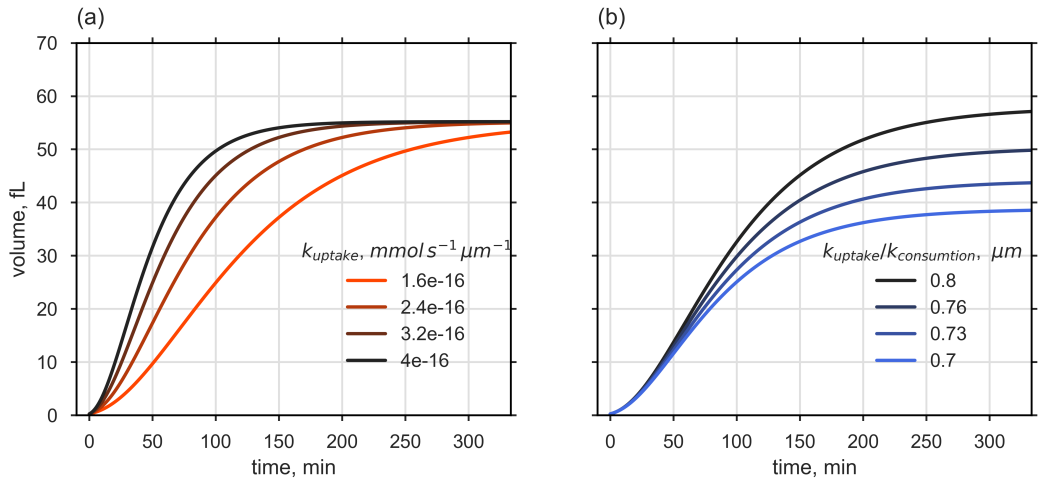

Fig. 3.3.: Uptake and consumption rate constant determine single cell growth rate and maximum volume. Volume trajectories under variation of either the uptake rate constant k_{uptake} or the ratio $k_{\text{uptake}}/k_{\text{consumption}}$ are shown in (a) and (b).

3.2 The Coupled SCGM - a Combined Model for Mother and Bud Expansion

The above described SCGM covers osmolyte, pressure and volume dynamics as well as cell wall mechanics and provides a consistent description of the expansion of a spherical walled cell. However, the assumption of a single spherical shell is only valid for yeast cells in G1 phase. During the other cell cycle phases a bud is connected to the mother cell, which forms and starts to grow in the S phase and separates from the mother cell in the M phase. Although mechanical unfavorable, the smaller bud expands at higher rates than the mother. Hence, a more general description of the yeast cell shape, during vegetative growth, comprises two connected spherical shells with different sizes and expansion rates (Ferrezuelo *et al.*, 2012). To reflect the distinct compartments, mother and bud, we introduced a cSCGM (see Sec. A.1.2) comprising of two SCGM instances with different initial radius r_0.

3.2.1 Coupling of the Compartments

The instances were linked by allowing water flow and free diffusion of osmolytes, according to the respective pressure gradients, between both compartments. For simplicity, we neglected any specificity of the bud localization at the mother and thereby the related decision-making process, including the polarization machinery (Giese *et al.*, 2015; Chiou *et al.*, 2017). The neck, the connection between mother

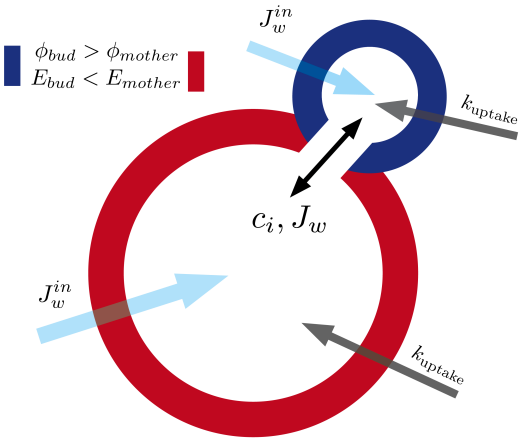

Fig. 3.4.: Scheme of the cSCGM. Mother and bud compartment are linked via a stable bud neck and share osmolyte uptake rates k_{uptake} and water influxes J_{w}^{in}, but differ in the mechanical property of their cell wall (E or ϕ).

and bud, was assumed to be stable (Cabib & Arroyo, 2013) and large enough for unrestricted water and osmolyte exchange, guaranteeing rapid balancing of eventual pressure differences between the compartments. Since this fluxes equalize the osmolyte concentration between the compartments, regardless the chosen rate constants for osmolyte uptake and consumption, they were assumed to be equal in the mother and in the bud. To follow initial growth of the new born daughter and subsequent bud expansion, a time delay t_{budstart} between the start of the expansion of both compartments have been introduced. When both compartments started with comparable sizes, t_{budstart} is an estimate of length of the first cell cycle, i.e. the time required for a daughter to grow and to initiate a new bud. Note that the model reflects the biophysical principles behind the growth process instead of the complex biochemical processes that govern cell division.

Although mechanical models of interconnected spherical compartments in conjunction with the final states have been reported (Merritt & Weinhaus, 1978; Weinhaus & Barker, 1978), those models lack the exchange of matter with their environment, a necessity for biological growth.

3.2.2 Distinguishing Property between Mother and Bud Cell Wall

Since both cell compartments expand in nature at different rates, they need to possess at least one distinguishing property. Reported differences in the cell wall

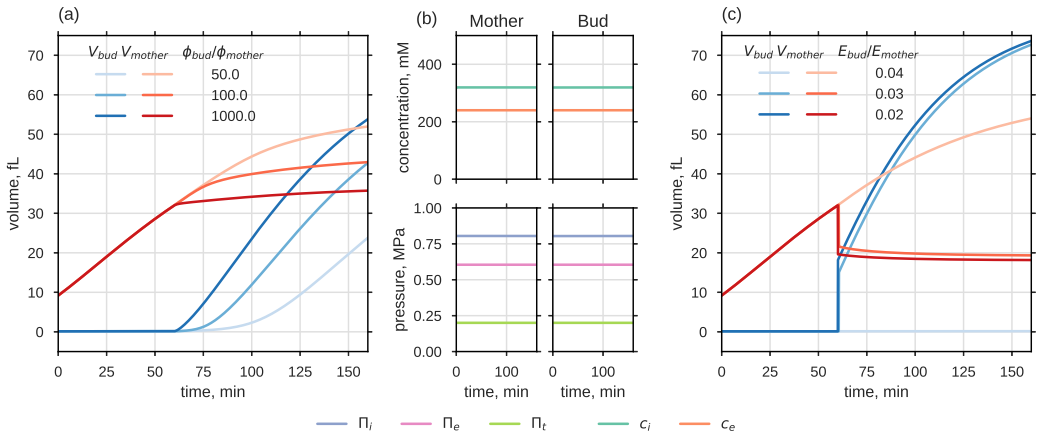

Fig. 3.5.: Coupled SCGM allows for different expansion rates of mother and bud. (a) and (c) Volume trajectories of mother (red) and bud (blue) for different extensibility ratios $\phi_{\text{bud}}/\phi_{\text{mother}}$ and elasticity ratios $E_{\text{bud}}/E_{\text{mother}}$, respectively. When changing extensibility ratio, the elasticity ratio was set to 1 and vise versa. (b) Quasi steady state of osmolyte concentration, osmotic pressure and turgor pressure during growth is conserved in mother and bud for simulations presented in (a) and (b). Non-stated simulation parameters are listed in Tab. 3.1.

composition of mother and bud suggests that the mechanical properties of the cell wall might vary locally. In particular, chitin incorporation in the lateral cell wall is delayed in the bud until after bud septation Cabib, Roh, *et al.* (2001). I considered the elasticity, i.e. Young's modulus E, and the extensibility ϕ of cell wall as potential distinguishing feature. For both mechanical properties ratios, $\phi_{\text{bud}}/\phi_{\text{mother}}$ or $E_{\text{bud}}/E_{\text{mother}}$, have been found, that facilitated bud expansion, as can be seen in Fig. 3.5(a,c). When $E_{\text{bud}}/E_{\text{mother}} < 0.04$ the bud expanded, though at the expense of the mother's volume (see Fig. 3.5(c)). In contrast, when ϕ was varied, both compartments continued to grow at different rates (Fig. 3.5(a)), as long as ϕ_{bud} was at least $1 \times 10^{1.5}$ times higher than ϕ_{mother}. Regardless of the specific growth scenario, whether it based on increased ϕ_{bud} or reduced E_{bud}, the quasi steady state of c_i was preserved in both compartments, due to the allowed water and osmolyte fluxes (Fig. 3.5(b)).

3.2.3 Cell Volume at Birth and at Cell Division

The dynamics of single cell growth is a current field of research. For example Soifer *et al.* (2016) measured and analyzed volumes of single yeast cells at birth vb, at division vd (vd comprises mother and bud) and the time between both events, the division time td. They reported that the asymmetry of division $a = v_{\text{bud}}/vs$, is independent of the initial bud size and averages around 0.6. Further they showed

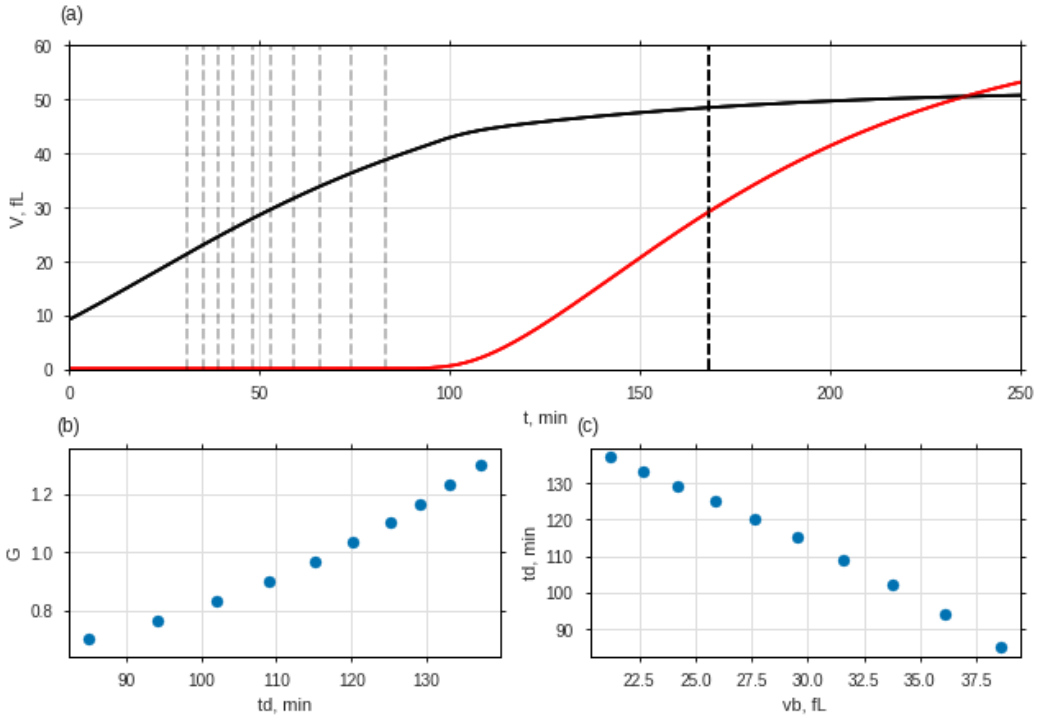

Fig. 3.6.: The cSCGM can recapitulate the observation on relations between division time td, the relative growth G and the initial bud volume vb, reported by Soifer *et al.* (2016). (a) shows volume trajectories of mother (black) and bud (bud) predicted by the cSCGM, parametrized as listed in Tab. 3.1. In (b) the relative growth $G = log(vd/vb)$ vs. the division time td is shown. Panel (c) shows the estimated division time td vs the initial bud size vb. To define time of birth (light dashed line) and division td (dark dashed line) as well as the corresponding volumes vb and vd, we used the reported division asymmetry of $a = 0.6$ between mother and sampled for different G-values between 0.7 and 1.3.

that the relative growth $G = \log(vd/vb)$ scaled linearly with the division time td and that the division time decreases with increasing vb. Combined these findings support the concept of a size-controlled budding process instead of a time-controlled process. The authors further inferred an exponential growth behavior for single cells.

To test whether the cSCGM is consistent with the reported data and the conclusion drawn, I analyzed simulations of the cSCGM with respect to the stated parameters, vb, G and td. Since, neither contained the SCGM a direct measure for td nor could the existing parameter t_{budstart} been directly translated into td, td had to be determined from the volume trajectories using additional assumptions (see Fig. 3.6(a)). The division time is defined as timespan, $td = t_2 - t_1$, between the time of cytokinesis $t2$ and the time $t2$ when the mother cell was separated from its mother cell as new born daughter cell, i.e. $V_{\text{mother}} = vb$. Using the reported constant asymmetry of division, $t2$ was determine as $t2 = t$ when $V(t)_{\text{bud}}/V(t)_{\text{mother}} = 0.6$.

Calculating td for different vb-values, which where consistent with the reported G-values, I could mimic the reported tendencies, of an increasing G for increasing td and a declining td for increasing vb (Fig. 3.6(b,c)). On the one hand, these results support the validity of the proposed model and, on the other hand, show that volume trajectories of single yeast cells do not necessarily follow an exponential dynamic, although population data might suggest it.

In summary, SCGM and cSCGM reflect very well the qualitative growth behavior of single yeast cells, nevertheless crucial parameters such as k_{uptake}, $k_{\text{consumption}}$, t_{budstart} and in particular those describing the mechanical cell wall properties, as E and ϕ, are yet to be determined. Moreover, the property, that distinguishes mother and bud cell wall, remains to be identified. All these open questions will be discussed in the following.

3.3 Local Cell Wall Elasticity of Mother and Bud

According to the in Sec. 3.2 derived cSCGM, mechanical properties must differ considerably between mother and bud cell wall for budding to occur. The model, however, cannot specify the exact property, which has to alter for budding to occur. Either an increase in the extensibility ϕ or a substantial reduction in the local YM of the cell wall region would be sufficient to facilitate bud expansion. To distinguish between both possibilities I focused first on the cell wall elasticity. Although the elasticity of the yeast cell wall has been repeatedly studied in the past (A. E. Smith, Zhang, Thomas, *et al.*, 2000; Touhami *et al.*, 2003; Alsteens, Dupres, *et al.*, 2008; Dague *et al.*, 2010), studies regarding its distribution in mother and bud compartment have not been reported.

To measure the elasticity of mother and bud cell wall, I applied multi-parametric-imaging on living single yeast cells from type BY-4741, as explained in Sec. 2.2.3. For this purpose, yeast cells were mechanically trapped in a porous polycarbonate membrane (see Sec. 2.2.3), leaving only the protruding part of the cell accessible for scanning. All measurements were performed in liquid, i.e. in SFSD medium containing all essential compounds for optimal growth, such as amino acids and glucose. Multi-parametric-imaging is an AFM based technique, which can provide height and elasticity maps in nanometer resolution as shown in Fig. 3.7(a, b). Its operating principle is explained in more detail in Sec. 2.2.3. Essentially, at each map position a force-spectroscopy measurement is performed and analyzed. To obtain information on the elasticity of the probed surface the material needs to be

indented during the force-distance cycle. The depth of such an indentation is of particular importance when measuring pressurized shells, such as the yeast cell. At large indentations, the whole shell deforms and the restoring force is mainly defined by the turgor pressure (Vella *et al.*, 2012), whereas at small indentations, only the shell material is deformed and force is governed by material properties of the shell (Digiuni *et al.*, 2015).

To compare the elasticity of mother [M] and bud [B], cell wall flat areas of equal size on top of each compartment have been chosen, while avoiding regions of former budding events, also known as bud scars. Including bud scars woulds systematically bias the YM of the mother cell wall, since they contain an increased amount of chitin, which stiffens the cell wall (Touhami *et al.*, 2003). Apart from the bud scars, the measured cell wall elasticity of vegetatively growing cells was homogeneously distributed in both the compartments, which is in agreement with earlier studies by Formosa *et al.* (2013) and Pillet *et al.* (2014).

Pairwise comparison of the measured mean YM for mother and bud as shown in Fig. 3.7(c) revealed that the bud cell wall is not, as initially assumed, softer but in fact slightly stiffer than that of the mother. From a linear fit, indicated in Fig. 3.7(c), I estimated an 1.30 ± 0.06 - fold increase in stiffness from mother to bud cell wall. This measured difference in elasticity is preserved during bud expansion, as time series of height and elasticity maps of single mother-bud pairs show (Fig. 3.7(d,e)). Even though the measured elasticity varied during bud growth, the mean YM of the bud cell wall was always higher than the mean YM of the mother cell wall. The only exception was observed after $200\,\mathrm{min}$ (cellID:3), a time when the budding process is typically finished and both compartments had already become separated single cells.

The apparent difference in elasticity between mother and bud cell wall, however, is only minor and might be due to the difference in local curvature between both surfaces. As described in Sec. 2.2.3, the cantilever can slip on tilted or curved surface instead of intending the material, leading to an apparent lower YM. Hence, the true YM of the cell wall might be even higher at the bud. Nevertheless, a substantial softening of the bud cell wall during bud expansion, as would be required by the cSCGM, can be rejected.

This reveals a considerable difference between two of the asymmetric growth processes in yeast, budding and shmooing, i.e. formation of a mating projection during sexual conjugation, as later discussed in Sec. 5. Since the elasticity could be ruled as distinguishing feature between mother and bud cell wall, I consequently focused in the following on its extensibility.

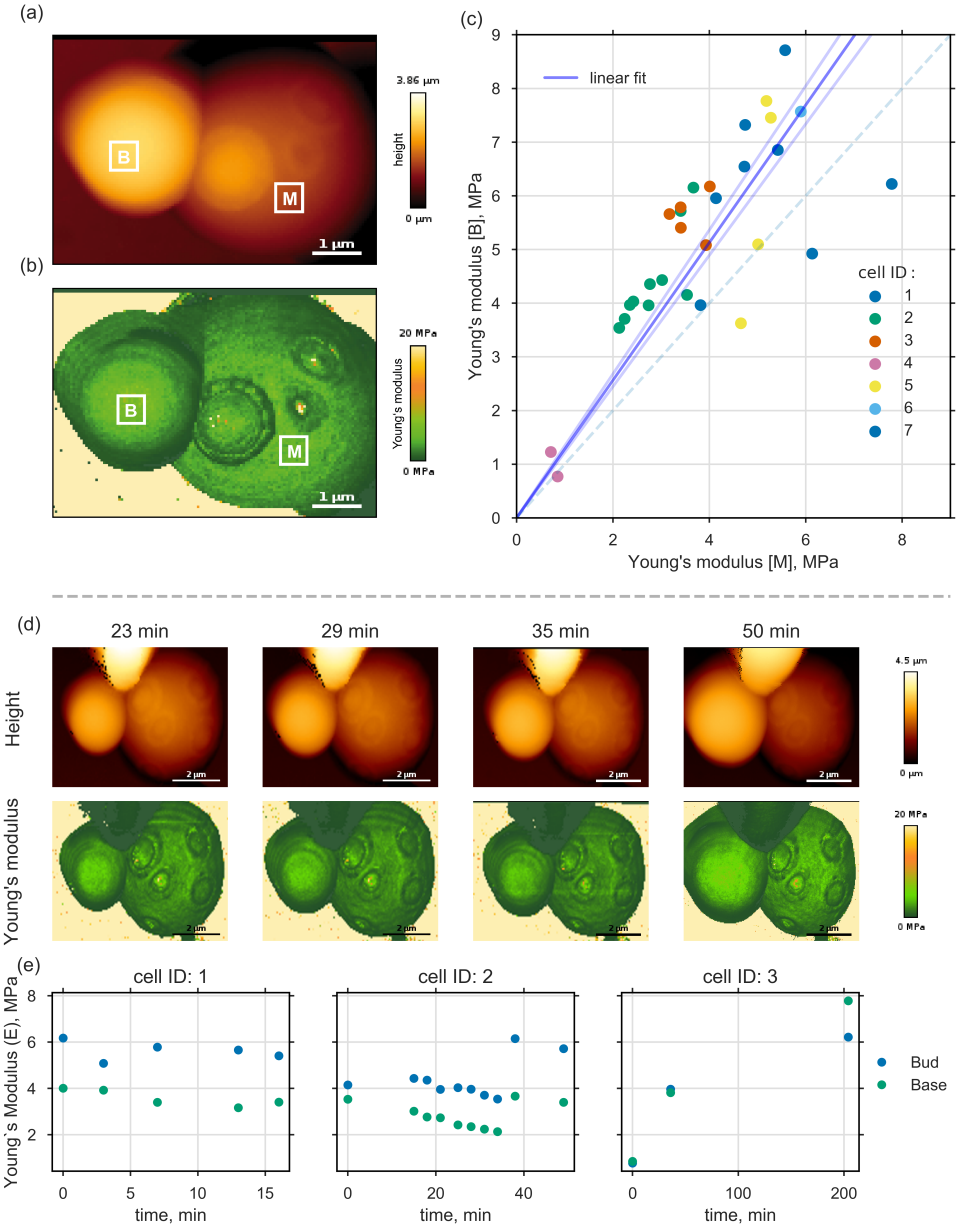

Fig. 3.7.: Bud cell wall is slightly stiffer than mother cell wall and this difference in YM is preserved during bud growth formation (a) and (b) show the height and elasticity map of one entrapped mother cell with adjacent bud. (c) shows the mean YM of comparable flat areas from mother and bud, marked areas as [M] and [B] in (a, b). The blue line represents a linear fit and the dashed line indicates equal E-values for mother and bud. Each measured cell is labeled with a different color. (d) Time series of height and YM maps during bud growth. The apparent high and soft object at the top of the maps is an measurement artifact arising from an adjacent nearby high object, e.g. a non-trapped cell. (e) Mean YM over time from comparable flat areas for mother and bud.

3.4 Estimation of Key Parameters of the cSCGM from Temporal Volume Data of Mother and Bud

The coupled-compartment growth model (cSCGM), introduced in Sec. 3.2, describes qualitatively the growth of a yeast cell from the expansion of a small singular compartment to the combined growth of two compartments, mother and bud. The cSCGM predicted that in order to facilitate coupled growth of two unequally sized compartments, both must vary in at least one mechanical property of their cell wall, either elasticity or extensibility (Sec. 3.2.2).

The bud cell wall, however, is not softer but stiffer than the mother cell wall, as I explained above in Sec. 3.3. Thus the elasticity can be rejected as a distinguishing property between mother and bud cell wall and only its elasticity remains as a possible property. To estimate the extensibility of the mother and bud cell wall, and to further constrain the cSCGM, it was fitted to measured volume trajectories of single yeast cells and their corresponding buds. Fitting of the experimentally gained volume trajectories allowed for a further assessment of the cSCGM, e.g. whether the model describes the real volume expansions qualitatively and quantitatively. Two completely independent data sets of volume trajectories (*data set 1* and *data set 2*) have used to constrain the cSCGM. While *data set 1* has been measured in our laboratory by Jannis Uhlendorf, *data set 2* has been measured in the laboratory of Gilles Charvin and was recently published by Garmendia-Torres *et al.* (2018).

3.4.1 Analysis of *data set 1* (Inhouse)

Acquisition of *data set 1* is described in more detail in Sec. 2.2.2 together with specifications of the subsequent image analysis. In brief, volume trajectories were obtained from time series of bright-field microscopy images of single haploid yeast cells grown as a monolayer in a microfluidic platform. While cells and their buds were tracked automatically in microscopic images using the software CellStar (Versari *et al.*, 2017) as shown in Fig. 3.8(a), time of bud emergence has been determined manually. For the identification of mother and bud pairs and for determination of the correct lineage, red fluorescence of a genomically introduced bud neck marker (Cdc10-mKate2) was utilized. Information on the lineage enabled us to follow 21 new born daughter cells over time, from the initial expansion phase to the subsequent coupled growth of mother and bud. The respective volume of the compartment was calculated from the obtained cross-sectional areas, assuming again a spherical geometry. Since the resulting volume trajectories varied significantly from cell to

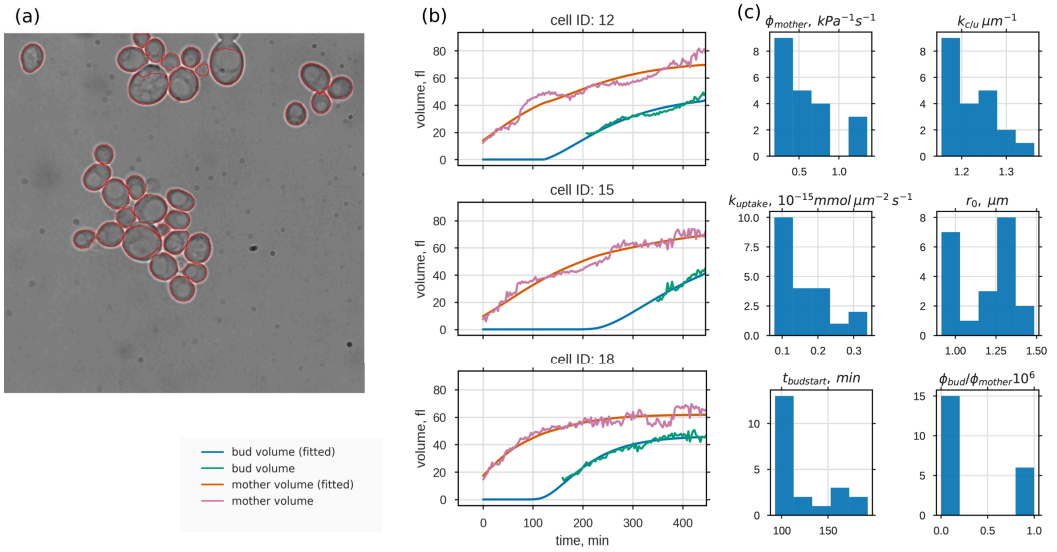

Fig. 3.8.: Growth parameter estimation of the cSCGM from volume trajectories obtained by bright-field microscopy. (a) 21 time series of automatically detected cross-sectional areas of single yeast cells and their buds were gathered from microscopic bright-field images. Obtained volume trajectories of mother and bud were used to fit the following model parameters: import rate of osmolytes k_{uptake}, ratio of import and degradation of osmolytes $k_{\text{u/c}}$, cell wall extensibility of the mother ϕ_{mother}, and ratio of cell wall extensibility of bud and mother $\phi_{\text{bud}}/\phi_{\text{mother}}$. As free initial conditions, time of bud start t_{budstart} and initial osmotic radius r_0 were estimated. Three exemplary data sets and their corresponding fits are shown in (b) (see Fig. A.1 for all data sets). Estimated parameters are presented as histograms in (c) and listed in Tab. 3.2. Despite the high variability in the data we could assign all but one ($\phi_{\text{bud}}/\phi_{\text{mother}}$) of the parameters with low variability.

cell, in particular the time of bud emergence, we used the single-cell data instead of population data to constrain the cSCGM (see Sec. 2.1.2).

The cSCGM was able to quantitatively describe the combined growth of mother and bud at different expansion rates (Fig. 3.8(b) and Fig. A.1). For the fitting, six independent parameters have been identified and estimated, from which four were considered cell-specific: the initial radius r_0, the time of bud emergence t_{budstart}, the osmolyte uptake rate constant k_{uptake} and the rate constant ratio between consumption and uptake $k_{\text{c/u}}$. Additionally, two parameters have been considered compartment-specific: the cell wall extensibility of the mother ϕ_{mother} and the extensibility ratio of bud and mother $\phi_{\text{bud}}/\phi_{\text{mother}}$. Median and interquartile range (IQR) of obtained parameter values are reported and listed in Tab. 3.2 as *data set 1*, while the parameter distribution is shown in Fig. 3.8(c). The radius of the initial osmotic volume of the later mother was estimated to be $r_0 = 1.2\ (1.0\text{–}1.3)\ \mu\text{m}$, corresponding to a volume of $V_0 = 7.2\ (4.2\text{–}9.2)\ \text{fL}$ of a small bud. The first value for the bud volume was in the same range, since this was the smallest volume,

which was automatically detectable. Hence, the determined time for the start of bud formation $t_{\text{budstart}} = 93\ (93\text{–}143)\ \text{min}$ differed decisively from the time when a bud was initially detected (first green data point in Fig. 3.8(b)). Note that some cells showed a significantly prolonged G1 phase.

The most sensitive parameters were those regarding the osmotic uptake and consumption. This is not surprising, since osmolyte uptake is the main driving force of growth in this model (see Sec. 3.1). The expansion rate determining parameter, the osmolyte uptake rate was estimated to be $k_{\text{uptake}} = 1.4\ (1.0\text{–}1.9) \times 10^{-16}\,\text{mmol}/(\mu\text{m}^2\,\text{s})$, while the estimated ratio of the consumption and uptake rate, determining the maximum volume, was $k_{\text{c/u}} = 1.21\ (1.18\text{–}1.27)\ 1/\mu\text{m}$. Both parameters showed little variation, though the maximum volume seems more conserved between cells than the expansion rate. Analysis of the mechanical cell wall properties provided direct estimates of the extensibility of the mother cell wall, $\phi_{\text{mother}} = 5.5\ (3.1\text{–}6.8) \times 10^{-4}/(\text{Pa}\,\text{s})$. Although a precise value of the extensibility ratio $\phi_{\text{bud}}/\phi_{\text{mother}}$ could not be determined for several cells, a lower limit could be identified from profile-likelihood analysis (Fig. A.2): ϕ_{bud} needs to be at least 100 times higher than ϕ_{mother}. Smaller ratios can be rejected. High extensibility ratios had no impact on the remaining parameters and are consistent with the cSCGM. Nevertheless, extensibilities above $1.3 \times 10^4/(\text{Pa}\,\text{s})$, corresponding to a viscosity below that of water ($\mu_{(T=30\,^\circ\text{C})} = 0.8\,\text{mPa}\,\text{s}$), are physically unreasonable and, thus, can be rejected, too.

3.4.2 Analysis of *data set 2* (provided by Gilles Charvin)

In the last section we analyzed the parameter landscape of the cSCGM based on a limited set of 21 volume-trajectory pairs of mothers and their corresponding buds. This analysis provided valuable, yet restricted, estimations for each parameter. For the extensibility ratio $\phi_{\text{bud}}/\phi_{\text{mother}}$, however, only a lower boundary could be determined and the relatively small sample size did not allow for a decisive characterization of the parameter distribution. To increase the sample size and challenge the cSCGM further I constrained the model with another single-cell data set of time resolved mother bud volumes, which was recently published by Garmendia-Torres *et al.* (2018).

In their study, they reported a new microscopy-based method to investigate cell-cycle and cell-size progression in parallel by monitoring both, volume and histone levels of individual cells. Using an automatized experimental setup they followed up to 15.000 cell cycles for each of the investigated 22 cell-cycle related mutants. This

innovative approach, tracking the fluorescence of fast maturating HTB2-sfGFP fusion proteins over time and assigning its intensity to distinct cell cycle phases, allowed them to relate mother and bud volume at certain cell cycle stages to the duration of each phase. For instance, they showed that the bud size at the end of the S phase negatively correlates to the timespan of the G2/M phase, supporting the theory from T. W. Spiesser *et al.* (2015), which predicts that the bud has to gain a certain size for cell cycle to proceed. Furthermore, they confirmed that yeast size control has not one but multiple size-dependent inputs. Although this analytic approach revealed intriguing relations between cell cycle and cell size, it partially neglects or simplifies the dynamics of the cell size progression in the data. In particular, they assumed different but linear growth during the budded and unbudded phase. To shed light on this cell-size dynamics and to improve the parameter estimation of the cSCGM, the model was fitted to the experimental data (*data set 2*) provided by Gilles Charvin. This allowed for comparison between completely independent data sets from different laboratories and analysis of data with drastically increased sample size.

Data and Data Selection

The advantage of *data set 2*, besides its large size, is the resemblance of the employed experimental and analytic approach to the approach we used. In particular, yeast strain background and culture medium, BY4741 and synthetic medium supplemented by amino acids and glucose, were similar. Furthermore, the proliferation of single cells, confined to a plane using a microfluidic device, was followed at the same sampling frequency (every $3\,\mathrm{min}$) using bright-field and fluorescence microscopy, while the volumes were calculated from cell contours, too, assuming ellipsoidal geometry.

In contrast to our approach Garmendia-Torres *et al.* (2018) used a super-folding GFP fused to one of the histone 2B loci (HTB2-sfGFP) instead of a bud-neck marker to monitor the cell cycle stage and to discriminate between buds and new born daughter cells. An additional distinction and strong advantage of their approach was to utilize the self-developed MATLAB software *Autotrack* for automatized cell segmentation and lineage tracking, enabling them to track and analyze thousands of cells.

The provided data set comprised temporal information on mother and bud volumes and histone levels over several cell cycles. For better comparison with *data set 1*

analyzed in Sec. 3.4.1, *data set 2* was limited to the first cell cycle of new born daughter cells (N= 6079), i.e. cells with a replicative age of 0. Cells already defined as outliers in the provided data were also neglected in the further analysis. The cSCGM was fitted to all of the remaining volume-trajectory pairs, using the same method as described in Sec. 3.4.1. In contrast to the previous approach, however, t_{budstart} was no fitting parameter but instead provided by the data set. Exemplary volume trajectories, representing data and model fits, are shown in Fig. 3.9(a) and Fig. A.3. Out of 6079 cells, 5880 yielded parameter sets that generated a sufficiently small distance between predicted and experimentally observed trajectories (Fig. A.4).

Data Restriction

The obtained free model parameters were either unimodal ($k_{\text{c/u}}$, $\phi_{\text{bud}}/\phi_{\text{mother}}$ and r_o) or bimodal (k_{uptake}, ϕ_{mother}) distributed (Fig. A.4). Some of the estimated values for ϕ_{mother} and $k_{\text{c/u}}$ did not follow the stated distribution but accumulated at the respective boundaries. These boundaries were necessary as they confined the parameter space to regions for which numerical simulations converge.

Not all obtained parameter sets, however, could be associated with acceptable model simulations. Two types of false optimization could be distinguished. The first type of false optimization concerns cases were the bud volume was not fitted at all. By principle there were fewer data points for the bud than for the mother volume and since both volume trajectories, those of the mother and those of the bud, were fitted simultaneously, the distance between fit and data could be inadequately optimized by neglecting the bud growth completely. Nevertheless, this was only the case when χ^2 was already significantly increased.

The second type of false optimization concerned again the underestimation of the measured bud volume. Pairwise scatter plots of the fitting parameters (Fig. A.10) revealed a correlation between fitted parameters only for low values of $k_{\text{c/u}}$ and k_{uptake}. Test samples of model fits (Fig. A.5) with such low $k_{\text{c/u}}$ values showed that, for those parameter sets, the predicted growth rate of the bud volume accelerates at the and of the cell cycle, instead of decelerating, as can been seen in the data and in model simulations with high $k_{\text{c/u}}$ values (Fig. A.6).

Considering the above described sources for deficient fitting, further analysis was restricted to a reduced data set (N=4680), discarding cells for which $k_{\text{c/u}} < 0.8/\mu\text{m}$ and $\chi^2 > 50$. The resulting distribution of the fitting parameters and χ^2 is shown in Fig. 3.9. Comparing histograms of the full and the reduced data set (Fig. A.4), revealed two effects of the restriction. First, the distribution of k_{uptake} changes from

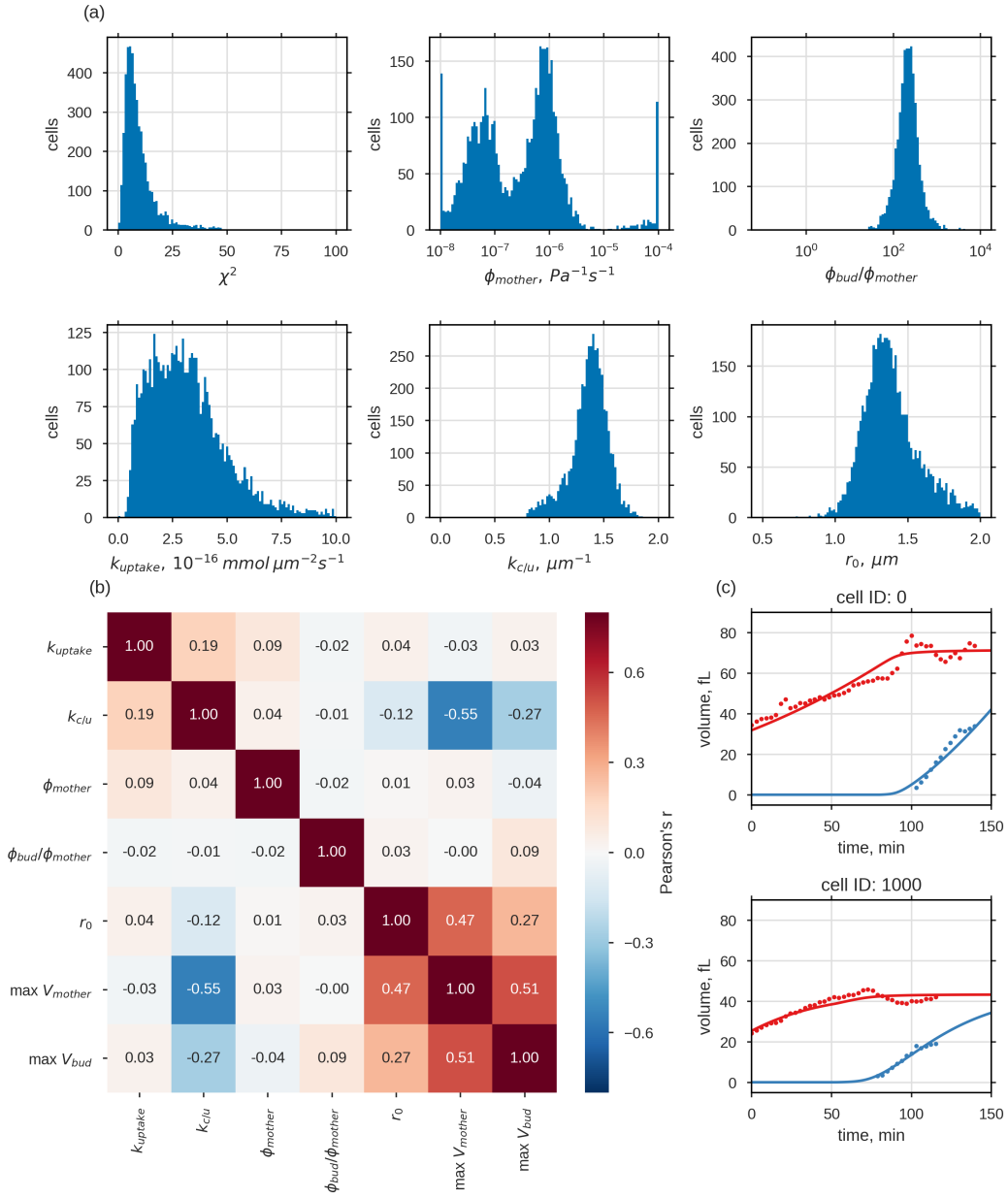

Fig. 3.9.: cSCGM fitted reported volume trajectories (Garmendia-Torres *et al.*, 2018) For 97% of the reported volume data for first-time mothers (N=6079) a parameter set for the cSCGM could be identified. a) Histograms of fitted parameter, excluding parameter sets where $k_{c/u} < 0.8/\mu m$ or $\chi^2 > 50$ (N=4680, histograms of complete and reduced parameter set shown in Fig. A.4). b) Pearson's correlation of best fitting parameters ($k_{c/u} > 0.8/\mu m$, $\chi^2 < 50$) and measured maximum volume of mother and bud, presented as correlogram. max V_{mother} and max V_{bud} where taken from the data. Values vary between -1 and 1, whereby a value of 0 represents no correlation, while positive or negative values represent a positive (red) or a negative correlation (blue). In c), two exemplary sets of measured and simulated volume trajectories are shown (additional 24 exemplary trajectories are shown in Fig. A.3).

bimodal to unimodal, whereby the first peak vanished while the second remained unaltered. This shows that the first peak resulted solely from incorrect fitting. Second, the two distinct peaks of the distribution of ϕ_{mother} separated even more, due to a shift of the first maximum towards lower values.

Fitted Model Parameters for *data set 1* and Comparison with *data set 2*

Except for ϕ_{mother} the free fit parameters showed a unimodal, though partially skewed, distribution and their medians as well as their interquartile range are listed in Tab. 3.2, together with parameter estimates from *data set 1*. Although t_{budstart} was not fitted for *data set 2*, because it was provided by the data, the parameter is listed in Tab. 3.2 for comparison. The extensibility ϕ, reflecting the capability of the cell for plastic cell wall expansion and readjustment of the turgor pressure in the cSCGM, varied drastically between *data set 1* and *data set 2*. While ϕ_{mother} values obtained from *data 2* followed a clear bimodal-distribution, values obtained from *data 1* showed no indication of a multimodal-distribution. Furthermore, both maxima, $max(\phi_{\text{mother}}|1) = 9.6 \times 10^{-8}/(\text{Pa}\,\text{s})$ and $max(\phi_{\text{mother}}|2) = 7.8 \times 10^{-7}/(\text{Pa}\,\text{s})$, were at least two magnitudes smaller compared to estimates from *data set 1* and thereby closer to reported extensibility values for plant cells ($\sim 1 \times 10^{-10}/(\text{Pa}\,\text{s})$)(J. K. Ortega, 1985; D. J. Cosgrove, 1985). For each maximum a group of parameter sets was selected, for which ϕ_{mother} was close to this maximum. Comparison of those parameter sets, however, revealed no differences (Fig. A.7). Analogous to analysis of k_{uptake}, test samples of simulated and experimentally observed volume trajectories were screened by eye, for which ϕ_{mother} was either close to $max(\phi_{\text{mother}}|1)$ or to $max(\phi_{\text{mother}}|2)$ (Fig. A.8, Fig. A.9). Again, no common pattern for those two groups could be identified. Whether this bimodal distribution of ϕ_{mother} results from numerical issues of the optimization algorithm or reflects two distinct populations remains to be clarified.

In contrast to the magnitude of ϕ, the ratio $\phi_{\text{bud}}/\phi_{\text{mother}}$ was comparable between *data set 2* and *data set 1*, with 220 $(150\text{–}300)$ and 230 $(130\text{–}8.1 \times 10^5)$, respectively, underscoring that ϕ_{bud} needs to be at least 100 times higher than ϕ_{mother}, regardless the magnitude of ϕ, to facilitate bud expansion. Osmolyte uptake rate k_{uptake} and ratio $k_{\text{c/u}}$ estimated from *data set 2* were slightly higher than estimates from *data set 1*, with $k_{\text{uptake}} = 3.0$ $(1.9\text{–}4.2)$ $\times 10^{-16}\,\text{mmol}/(\mu\text{m}\,\text{s})$ and $k_{\text{c/u}} = 1.4$ $(1.3\text{–}1.5)$ $1/\mu\text{m}$, indicating a higher single-cell growth rate and maximum volume for *data set 2*. Intriguingly, the estimated osmolyte uptake rates k_{uptake}, obtained from both data sets, were only two to five times higher than the average glucose uptake rate per surface area. According to Jouhten *et al.* (2008) the glucose uptake rate of *S. cerevisiae*

Tab. 3.2.: Estimated median (interquartile range) of fit parameters from both data sets. t_{budstart} of *data set 2* was provided by the data. ϕ_{mother} from *data set 2* showed bimodal distribution and was neglected in this table.

parameter	unit	factor	median (IQR)	
			***data set 1* (N=21)**	***data set 2* (N=4680)**
k_{uptake}	$\frac{\text{mmol}}{\mu\text{m}^2\,\text{s}}$	10^{-16}	1.4 (1.0–1.9)	3.0 (1.9–4.2)
$k_{\text{c/u}}$	$\frac{1}{\mu\text{m}}$		1.21 (1.18–1.27)	1.4 (1.3–1.5)
ϕ_{mother}	$\frac{1}{\text{Pa}\,\text{s}}$	10^{-4}	5.5 (3.1–6.8)	–
$\phi_{\text{bud}}/\phi_{\text{mother}}$		10^{2}	2.3 (1.3–8.1 $\times 10^3$)	2.2 (1.5–3.0)
r_0	μm		1.2 (1.0–1.3)	1.4 (1.3–1.5)
t_{budstart}	min	10^{1}	9.3 (9.3–14.3)	5.6 (4.1–7.4)

per gram dry weight and under aerobic conditions is $k_{glc} = 1.06\,\text{mmol}/(\text{g}\,\text{h})$ (mean of two replicates). When considering average cell surface area ($\overline{A}_{\text{cell}} = 60\,\mu\text{m}^2$) and cell dry weight ($\overline{m}_{cell} = 16.5\,\text{pg}$) (F. M. Klis, Koster, *et al.*, 2014), the average glucose uptake rate per surface area is given by,

$$k_{\text{glc,up}} = k_{glc}\frac{\overline{m}_{\text{cell}}}{\overline{A}_{\text{cell}}} \approx 0.8 \times 10^{-16}\,\frac{\text{mmol}}{\mu\text{m}^2\,\text{s}}.$$

Under this conditions, glucose would account for $30\,\%$ to $60\,\%$ of the osmolytes taken up by the cell, revealing a new aspect of the impact of glucose onto cellular growth: So far the impact of glucose onto cell growth based exclusively on the fact that glucose is a main nutrient source, providing chemical energy and building blocks for macromolecules, and thus can be regarded as fuel of the cell. Nevertheless, this study indicates, that additionally to those aspects, the massive glucose import could drive water influx and hence contribute significantly to cell expansion via its osmotic effect.

The initial volume of the new born daughter, i.e. a mother with replicative age 0, can be represented by its radius r_0. With $r_{0,1} = 1.2\ (1.0\text{–}1.3)\ \mu\text{m}$ this radius was slightly smaller for *data set 1* than for *data set 2*, where $r_{0,2} = 1.4\ (1.3\text{–}1.5)\ \mu\text{m}$. There are several, possible reasons for the discrepancy between $r_{0,1}$ and $r_{0,2}$. It might arise from differences in the experimental setup, in the preceding growth phase of the population or in the genome of the used yeast strains. In contrast to the initial volume, the time until the bud emergences t_{budstart} was increased for *data set 1* when compared with *data set 2*, with $t_{\text{budstart,1}} = 93\ (93\text{–}143)\ \text{min}$ and $t_{\text{budstart,2}} = 56\ (41\text{–}74)\ \text{min}$.

Parameter Correlations

Finally, for all fit parameters and the measured maximum volume of mother and bud, maxV_{mother} maxV_{bud}, the Pearson's correlation coefficient or Pearson's r was calculated, represented as correlogram in Fig. 3.9(b). Values of the correlation coefficient vary between -1 and 1, whereby a value of 0 represents no correlation, while positive or negative values represent a positive or a negative correlation. The upper left quadrant of the figure shows again that fit parameters were largely uncorrelated, except for a small correlation (0.19) between $k_{\text{c/u}}$ and k_{uptake}. The lower right quadrant displays the correlation between the volume measures, which in contrast were all positive correlated. Of particular interest is that maxV_{mother} and maxV_{bud} showed a strong correlation, since it confirms previous observations on the dependence of the daughter's size on the mother's size. The only correlation between volume measures and fitting parameters, was found for $k_{\text{c/u}}$. Thereby $k_{\text{c/u}}$ correlated negatively to all volume measures, though the correlation was much stronger for maxV_{mother} than for maxV_{bud} and even less for r_0 (see Fig. 3.9). This can be explained by the cSCGM, since $k_{\text{c/u}}$ determines the maximum volume of the cell compartment, which is reached for the bud not until after cell separation.

3.5 Discussion on Vegetative Single Cell Growth

Here, I introduced, justified and challenged a volume model for *S. cerevisiae*, combining concepts of water and osmolyte dynamics as well as cell wall mechanics while integrating experimental data on single cell growth and cell wall elasticity. The model applies to several scenarios, where cell volume is subjected to alterations: from the slow growth of an single spherical cell over the combined growth of a mother and a bud compartment to the fast adaptations to extracellular osmolyte variations.

The SCGM describes the expansion of a single compartment near the steady states for osmolytes and pressure. As discussed in the beginning of this section, two modes of single-cell growth have been considered for *S. cerevisiae* in the past, linear and exponential growth (J. Mitchison, 1958; Turner *et al.*, 2012; Tyson & Hannsgen, 1985; Soifer *et al.*, 2016). In contrast, the SCGM shows a different, more complex growth dynamic, following a sigmoidal curve: In the beginning, i.e. during the majority of the G1 phase, the cell size expands exponentially. The expansion rate subsequently decelerates while the size approaches its maximum. This growth dynamic could also be observed in the experimentally obtained volume trajectories of *data set 1*

and *data set 2*. The growth behavior of yeasts, thus, follows a sigmoidal trend at the single-cell level and at the population level. Although neglected in the past, a maximum cell size is necessary for asymmetrically dividing cells. Assuming that the cell size of most species is limited, indefinite exponential growth is only feasible if cell division is symmetric and happens at increased frequency. For asymmetrically dividing cells, such as *S. cerevisiae*, pure exponential growth would result in extreme cell size variations, even if the replication cycle of the mother cell is limited.

In the SCGM, this maximum cell volume is only determined by the ratio $k_{\mathrm{c/u}}$ of osmolyte (nutrient) consumption and uptake rate, but independent of the mechanical cell wall properties. Interestingly, osmo-homeostasis has been so far neglected as cell size determining factor for plants, mammalian and fungal cells (Marshall *et al.*, 2012). In contrast to the maximal cell volume, the growth rate is determined by the magnitude of the rates for osmolyte uptake and consumption.

To include further cell cycle phases into the volume model, the formation and expansion of the bud had to be considered. For this purpose, two separate instances of the SCGM have been permanently coupled by allowing for water and osmolyte exchange between the instances. Through the continuous influx of osmolytes and despite the fast equalizing inter-compartment fluxes, the cSCGM, as the SCGM, operates near to but not at equilibrium. The reported observation that mother and bud grow simultaneously, though at different rates (Woldringh *et al.*, 1993), could be simulated with the cSCGM.

As biophysical model, the cSCGM resembles, on the one hand , models for of inter-connected soap bubbles or balloons by Merritt & Weinhaus (1978) and Weinhaus & Barker (1978), on the other hand, it precedes them, as those models lack a crucial characteristic of cells: the controlled exchange of matter with the environment.

The current SCGM does not require any interaction with the cell cycle machinery, as it describes the continuous volume expansion during the G1 phase. In contrast, cSCGM covers the whole cell cycle duration, except for the separation of the bud and, hence, is not independent of the cell cycle. The cell cycle machinery, however, is a complex network of cyclins and cyclin dependent kinases and a complete implementation is beyond the scope of this study. The budding signal is therefore represented by the parameter t_{budstart} and was either estimated from or provided by experimental data. Nevertheless, coupling of two identical SCGMs, except for the initial size, is not sufficient to simulate bud expansion. The cSCGM showed that a simultaneous or even faster expansion of the bud compartment is only possible if mother and bud cell wall differ in their mechanical properties, either in their elasticity E or in their extensibility ϕ.

Time resolved height and elasticity maps of living and budding yeast cells acquired with AFM based multi-parametric imaging showed similar elasticity values for bud and mother cell wall. Therefore, the hypothesis that a strongly reduced YM facilitates bud expansion could be rejected. Leaving the extensibility as the remaining potentially distinguishing feature between the cell wall of both compartments.

From simulation of the cSCGM with varying ratio of $\phi_{\text{bud}}/\phi_{\text{mother}}$ I could infer that a significant higher extensibility of the bud cell wall compared to that of the mother is necessary and sufficient to facilitate bud expansion. In addition, the expansion rate of the mother compartment decreases with increasing expansion ratio $\phi_{\text{bud}}/\phi_{\text{mother}}$, while that of the bud compartment increases. Hence, an asymmetry in the cell wall extensibility between mother and bud can explain the observed higher growth rates of buds (Hartwell & Unger, 1977; Ferrezuelo *et al.*, 2012). New material is predominantly integrated at the bud cell wall, as autoradiographic analysis have shown (Johnson & Gibson, 1966). It remains unclear, however, at which point the alteration of the mechanical properties, particularly the extensibility, takes place. An increased extensibility of the bud cell wall can be caused by the integration of new, more expandable cell wall material that matures over the course of one cell cycle, or by subsequent loosening of already integrated cell wall material. Enzymes, modifying the cell wall extensibility and thereby influencing growth and cell shape, are already reported for plants (D. J. Cosgrove, 1999; D. Cosgrove, 2000; Okamoto-Nakazato *et al.*, 2001). Additional studies indicated that the cell wall plasticity in fungi is also controlled by hydrolytic enzymes, like chitinases or glucanases (F. Klis & Mol, 2002; Adams, 2004; Duo-Chuan, 2006; F. M. Klis, Boorsma, *et al.*, 2006). Synthesis and remodeling of the cell wall is highly regulated and under control of the CWI. The relation between the CWI and physical plastic expansion, however, remains to be discovered.

To estimate crucial growth parameters, as the extensibilities of mother and bud cell wall, ϕ_{mother} and ϕ_{bud}, as well as uptake and consumption rates for osmolytes, represented by k_{u} and the ratio $k_{\text{c/u}}$, the model was fitted to single-cell volume trajectories from two completely independent data sets, *data set 1* and *data set 2*. *data set 1* was measured in our laboratory while *data set 2* was recently published by Garmendia-Torres *et al.* (2018).

For both data sets, the cSCGM was capable to describe the volume development of new born daughter cells and the formation of their buds. Comparison of the data sets revealed two main observations: First, cell expansion of *S. cerevisae*, under non-limiting conditions, requires a total osmolyte uptake rate of 1.0 to $4.0\,\mathrm{mmol}/(\mu\mathrm{m}^2\,\mathrm{s})$ and a consumption rate which is 1.2 to $1.5\,\mu\mathrm{m}^{-1}$ times higher. Second, to facilitate

bud expansion, the extensibility of the bud cell wall has to be at least 100 times higher than the mother's. However both data sets differed with regard to single-cell growth rate and magnitude of the cell wall extensibility. Estimations of the latter were ~ 100 times higher for *data set 1* than for *data set 2*, which was still two magnitudes higher than reported extensibility values for plant cells (Taiz, 1984; J. K. Ortega, 1985; D. J. Cosgrove, 1985). Although the results are only an indication, one might speculate that the structural difference of the fungal cell allows for higher extensibilities compared to plant cell walls.

Fascinatingly, the estimated, average uptake rates for osmolytes were only two to five times higher than the average glucose uptake rate under aerobic conditions reported by Jouhten *et al.* (2008). Considering the range of uptake rates for both data sets, glucose would account for $30\,\%$ to $60\,\%$ of the osmolytes taken up by the cell, which reveals a new perspective on the role of glucose in cellular growth. So far, glucose was perceived almost exclusively as main nutrient source, providing chemical energy and building blocks for macromolecules and by that fueling the growth process. In addition to those aspects, I could show that glucose import can contribute significantly to cell expansion by forcing a concomitant water influx.

By following the volume of new born daughters and their buds over time, the data provided additional information on the length of the G1 phase of the first cell cycle. Defined as the time between the birth of a new daughter cell and the formation of its new bud, the parameter t_{budstart} corresponds exactly to this time-interval. Both, t_{budstart} and the initial radius of the new born daughter r_0, varied between both data sets. While r_0 was slightly increased, t_{budstart} was reduced in *data set 2* compared to *data set 1*. Hence, the finding that smaller daughter cells showed a prolonged G1 duration, is in agreement with earlier findings by Di Talia *et al.* (2007), who reported a strong size control on G1 duration for new born daughter cells. Although size control in yeast has been intensively studied in the past (Hartwell & Unger, 1977; Johnston, Ehrhardt, *et al.*, 1979; Turner *et al.*, 2012), it is still a subject to current research (Amir, 2014; T. Spiesser *et al.*, 2016; Soifer *et al.*, 2016; Garmendia-Torres *et al.*, 2018).

The SCGM integrates concepts, which have been used in similar fashion in growth models for other microorganisms or plants. In a growth model for rod-shaped bacteria, proposed and tested by Harris & Theriot (2016), the volume expansion rate was depending on the volume and not the surface, as we proposed in the SCGM, too. Assuming furthermore that the expansion rate of the surface depends on the volume resulted in a steady state for the surface to volume ratio. Such steady state, however, can be achieved as well if both rates depend on the surface instead of

the volume. Without any mechanism to slow down the expansion rate their model predicts exponential growth of single cells with frequent symmetric cell division. In asymmetric cell division, such as budding, however, an indefinite exponential growth of the bigger cell is unreasonable and a limited cell size more appropriate.

So far, the cSCGM only describes the volume development of the first cell cycle of a new born daughter with a single budding event. Extending the cSCGM, by allowing for several cell cycles, including several consecutive budding events, would substantially improve the model and its significance. Constraining such an extended volume model with single-cell volume data, spanning several cell cycles, e.g. the data set from Garmendia-Torres *et al.* (2018), might help to decipher the interplay of morphogenesis and aging in *S. cerevisiae*, especially with respect to osmolyte homeostasis and cell wall mechanics. Moreover, such an extended model would allow to relate the phenomenological "adder" model to the *a priori* approach used in the SCGM. The "adder" or "incremental" model is established for bacteria and states that a constant volume is added to the cellular volume during one cell cycle (Amir, 2014; Jun & Taheri-Araghi, 2015). Soifer *et al.* (2016) claimed that also in *S. cerevisiae* a volume increment is added, although not between birth and cell division but between two subsequent budding events, which excludes the first cell cycle. Following several budding events with the cSCGM would render a direct comparison to the "adder" model possible. The first cell cycle is excluded in the "adder" model because of its prolonged G1 phase, which is supposedly due to a size depended check point in this phase (Johnston, Pringle, *et al.*, 1977; Hartwell & Unger, 1977; T. W. Spiesser *et al.*, 2015), although recent research indicates additional inputs for size control (Garmendia-Torres *et al.*, 2018). Both size regulation models, the "sizer" and the "adder" model, are in part mutually exclusive and a unifying or improved theory is needed to reflect the growth process of *S. cerevisiae*. In this regard, a well parameterized extended cSCGM has the potential to contribute substantially to the understanding of size control mechanisms in yeast and help to establish a unified theory. This is supported particularly by the fact that, on the one hand, the cSCGM was consistent with experimental, single-cell data of mother and bud volumes at the beginning and the end of the cell cycle and the corresponding division times reported by Soifer *et al.* (2016) but, on the other hand, it varied from their interpretation of the growth dynamics of single cells. For a deeper understanding of the choreography of growth it will be helpful to integrate or merge models, describing the regulatory networks of the cell cycle with the cSCGM.

Knowledge on single-cell growth dynamics is crucial for the understanding of comprehensive biological systems, particularly for model systems such as *S. cerevisiae*. Volume fluctuations directly affect not only the concentration of all intracellular

species, but also the surface by which metabolites are exchanged with the surrounding environment. Hence, implications on the volume dynamics of single-cells will have a strong impact on mathematical whole-cell models.

The presented approach is not restricted to walled cells. Although almost all volume regulation models, formulated for animal cells base on the cytoskeleton as main shape-generating and integrity-maintaining structure (Jiang & Sun, 2013; Tao & Sun, 2015), there are growth conditions, also for animal cells, which resemble those of *S. cerevisiae*. For example, animals cells are often exposed to high osmotic pressure gradients, e.g. cells at the boundaries of tissues in higher eukaryotes often encounter a wide range of osmotic changes due to cytokines, hormones etc. Extracellular tissue structures, such as matrix, mucus or wax, might preserve cellular integrity against those pressure differences in the same way as the cell walls in fungi or plant cells. Hence, a model similar to the SCGM might also be appropriate to characterize growth of animal cells.

4 Visco-Elasticity of the Yeast Cell Wall

The mechanical properties of the cell wall determine kind and strength of the cell deformation upon an exerted force. Under optimal growth conditions the cell wall is under constant hydrostatic pressure due to the osmotic gradient between cellular interior and exterior. Depending on the height of the governing pressure difference the cell wall either expands or contracts elastically, which allows the cell to adapt its cell size to varying external conditions without deforming permanently. Nevertheless, for the cell to grow, its cell wall needs to expand irreversibly, e.g. in a viscous manner. Hence, the cell wall as a composite material needs to be elastic as well as viscous to meet both requirements. In Sec. 3.1, I addressed both mechanical properties separately. I measured the cell wall elasticity E of mother and and bud with AFM and estimated the extensibility, i.e. the inverse of the viscosity ($\phi = \mu^{-1}$), from fitting of the cSCGM to single-cell volume data. That the cell wall response mainly elastically to an applied force has been shown in the past (A. E. Smith, Zhang & Thomas, 2000; Touhami *et al.*, 2003; Dague *et al.*, 2010). Whether, and if so to what extent, the response of the cell wall to an applied can be characterized as viscoelastic, however, remains a open question. This question is crucial to relate the observed fast elastic response, e.g. during osmotic shocks, to the slow plastic expansion during cell growth. To shed light on viscoelasticity of the cell wall, the following chapter will focus on the combination of elasticity and viscosity, particularly on the ratio between them. Additionally, the chapter will include experimental estimations of the cell wall viscosity, from AFM based nano-rheology measurements. Finally, the results will be analyzed in the context of structural damping and soft-glassy rheology.

4.1 Nano Rheology of the Cell Wall

Rheology is the study of flow and deformation to estimate the viscosity or visco-elasticity of the material of interest and is usually measured at the macroscopic or microscopic level. To characterize the cell wall, I applied a rheological method at the nanoscale utilizing AFM. The method was developed and improved by Alcaraz

and colleagues (Alcaraz, Buscemi, Grabulosa, *et al.*, 2003; Alcaraz, Buscemi, Puig-De-Morales, *et al.*, 2002) to determine the viscoelasticity of mammalian cells, and further used by Rother *et al.* (2014) to distinguish between malign and benign cell lines. AFM and rheology has also been combined before to characterize material properties of cells or polymers (Mahaffy *et al.*, 2000; O'Shea & Welland, 1998). Furthermore, Brückner *et al.* (2017) analyzed the hysteresis between approach and retract during force cycle experiments to estimate the viscoelastic properties of MDCK II cells. To map the viscous properties of polyacrylamide gels and MEF cells, Hecht *et al.* (2015) performed force clamp measurements and analyzed the creep behavior of the materials that followed an initial force ramp.

Magnetic-bead twisting, optical tweezers, micro-pipette aspiration, particle tracking or micro-plates have been used in alternative rheology methods. Superior to those methods AFM based nano-rheology provides high spatial resolution, which is required for measurements on microorganisms, such as *S. cerevisiae*.

The applied rheology method based on the phase shift between the deformation and the force response of a material, when indented by an oscillating force probe. If the cantilever tip is inserted in an elastic material and its base is harmonically excited off-resonance, the detected deflection of the cantilever will be in phase with the excitation, since the force is proportional to the displacement, i.e. the amplitude of the oscillation. However, if the tip of the cantilever is immersed into a purely viscous material and excited similarly, the phase of the deflection signal will be shifted by $90°$, since, in contrast to the elastic material, the force is proportional to the displacement speed or rate, which is highest at the inflection point of the excited oscillation. Hence, based on the phase shift, the material can hence be characterized as solid and elastic or fluid-like and viscous.

In the following, I will describe the experimental method and state the required equations to understand the acquired data and its implications. For a more detailed description of the experimental method and a mathematical derivation of the used equations please see Sec. 2.2.4. To determine the viscoelastic properties of yeast cell walls, cells had to be first immobilized (Fig. 4.1(a)). This was done as described in Sec. 2.2.3 via cell-trapping in porous membranes with either $3\,\mu\mathrm{m}$ or $5\,\mu\mathrm{m}$ pore diameter. The different pore sizes were used to investigate whether viscoelastic properties differ between newborn cells ($3\,\mu\mathrm{m}$, $N = 14$) and maturated yeast cells ($5\,\mu\mathrm{m}$, $N = 17$). Coarse grained AFM scans of the membranes provided an overviews that helped to locate trapped cells and to identify regions on top of the cells for detailed measurements. In these regions, force-spectroscopy measurements were performed in 10×10 grids, spanning areas (mean$\pm$ standard deviation (SD)) of

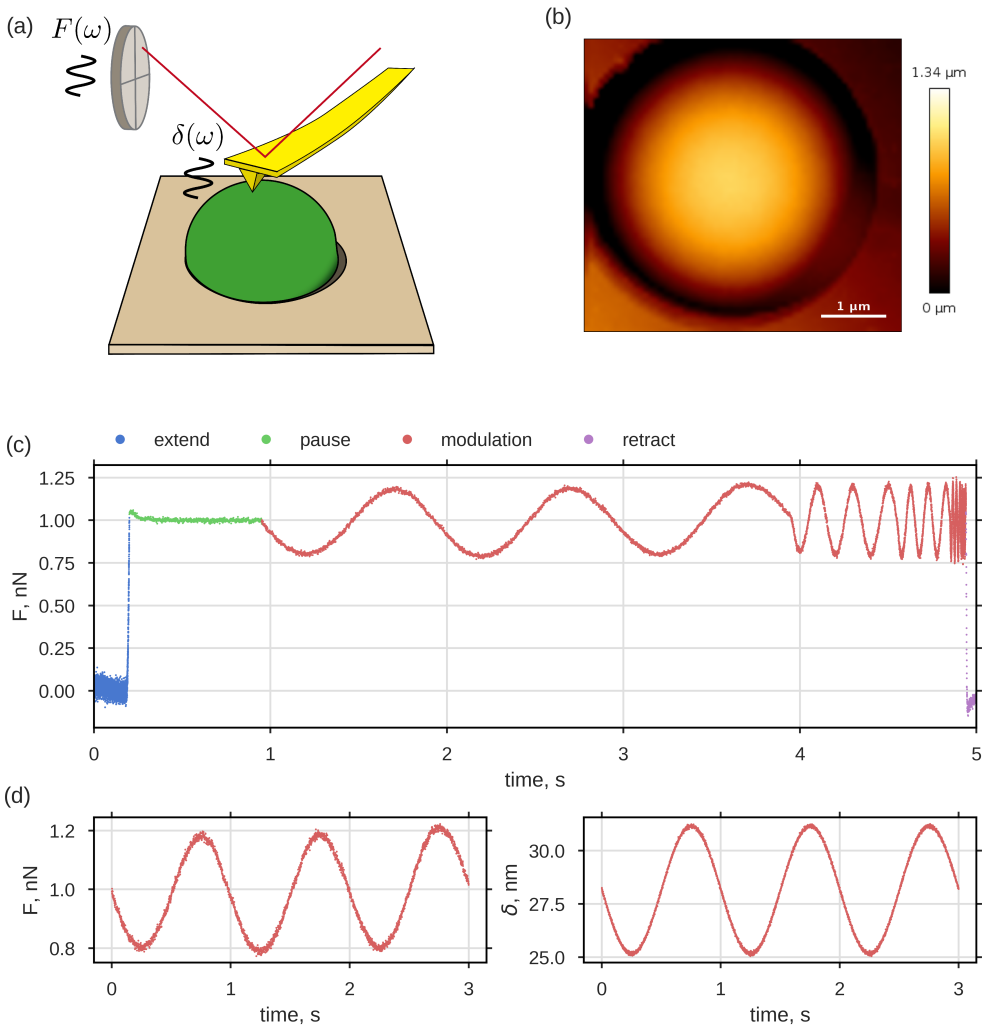

Fig. 4.1.: AFM based nano-rheology on the cell wall of living yeast cells. (a) Illustration of the experimental approach, in which the top of a trapped yeast cell is scanned with AFM. (b) Topographic AFM image of a trapped cell in a $5\mu m$ pore; color represents height. (c) Measured force $F(t)$ over time during approach, pause, modulation and retraction. (d) $F(t)$ and indentation depth $\delta(t)$ during modulation phase.

$(0.078 \pm 0.007)\,\mu\mathrm{m}^2$. At each position the cantilever was lowered until its tip indented the cell wall. To ensure that the tip only indents the cell wall, but not the whole cell, the applied force was so limited that the indentation depth δ was about a third of the cell wall thickness ($\sim 115\,\mathrm{nm}$). Subsequent to the initial approach phase, the cantilever was excited to oscillate in the modulation phase at frequencies ranging from $1\,\mathrm{Hz}$ to $100\,\mathrm{Hz}$, with an amplitude $\Delta\delta$ around a mean indentation depth δ_0, until it was finally retracted to the starting position. Small oscillation amplitudes $\Delta\delta \sim 2\,\mathrm{nm}$ were used, thus ensuring that the tip neither left the surface nor indented the cell wall beyond a third of its thickness (Tab. 4.1). Each complete measurement cycle for one position took $\sim 5\,\mathrm{s}$. In contrast to the successful mapping of the elasticity (see. Sec. 5), this rather long time made rheology mapping of the whole cell unfeasible. The acquisition of a high resolution (256×256) multi-parametric image with 65536 positions would take $91\,\mathrm{h}$, a multiple of the cell cycle time of a single yeast cell. Instead, the cyclic measurements were performed on small grids on top of the cells, as described above. An exemplary time trace of the detected force during one measurement is shown in Fig. 4.1(c). In addition, Fig. 4.1(d) compares the force F, calculated from the deflection of the cantilever, to the indentation depth δ at a frequency of 1Hz. The indentation depth δ is the negative tip-sample distance h, which can be obtained from the z-position of the cantilever base, corrected for the spring-like deflection of the cantilever due to acting forces, $z = F/k + h$. Whereby the z-position of the cantilever base directly relates to the extension of the piezo-element, and is set to zero when the tip touches the surfaces. Here, k is the spring constant of the used cantilever.

The mean indentation depth δ_0 was further used to approximate the impact area A of the cantilever tip, which together with the mean force F_0 provides an estimate of the applied pressure $P = F/A$ during modulation phase. When the geometry of the indenting part of the tip is approximated by a cone with height $h_c = \delta_0$ and angle $\theta = 18°$, its basal surface is given by $A = \pi\,\delta_0^2\,\tan^2\theta$. The resulting operating conditions for $3\,\mu\mathrm{m}$ and $5\,\mu\mathrm{m}$ cells are listed in Tab. 4.1. Please note that the applied pressure P, with $11.0\,\mathrm{MPa}$ and $4.4\,\mathrm{MPa}$, was above all reported values for the turgor pressure, ranging from $0.1\,\mathrm{MPa}$ to $1\,\mathrm{MPa}$ (F. Klis & Mol, 2002; Proctor *et al.*, 2012; Schaber *et al.*, 2010; Goldenbogen *et al.*, 2016). Hence, the applied stress in the cell wall should be above the yield limit of the cell wall (see Eq. 2.21). In this regard, comparisons of the obtained viscosities with the extensibilities estimated from the growth data (Sec. 3.4) and the SCGM are possible.

Tab. 4.1.: Operating conditions (mean ± standard error of the mean (SE)) of the oscillatory measurements explained in Sec. 2.2.4

d_{cell}, μm	A, nm^2	F_0, nN	ΔF, nN	P, MPa	δ_0, nm	$\Delta\delta$, nm	N
3	327 ± 73	0.98 ± 0.03	0.19 ± 0.01	11.0 ± 4.2	28.9 ± 0.3	2.09 ± 0.01	14
5	350 ± 93	0.55 ± 0.01	0.12 ± 0.00	4.4 ± 1.2	27.7 ± 0.3	1.95 ± 0.01	17

4.2 Complex Shear Modulus

For each modulation phase and each frequency the input and the output signal, $\delta(t)$ and $F(t)$, were transformed from the time to the frequency domain using FFT. The transfer function between input and output can now be defined as $H(f) = F(f)/\delta(f)$, including contributions from the sample as well as from the hydrodynamic drag of the liquid onto the cantilever. To consider only contributions from the sample, i.e. the cell wall, the function needs to be corrected for the hydrodynamic drag at the surface $H_d(f) = i2\pi f b(z = 0)$ (Alcaraz, Buscemi, Puig-De-Morales, *et al.*, 2002), as derived in Sec. 2.2.4. Assuming a Sneddon indentation model, the complex shear-modulus $G^*(f)$ is then given by:

$$G^*(f) = \frac{1-\nu}{8} \frac{\pi}{\delta_0 \tan\theta} \left(\frac{F(f)}{\delta(f)} - i2\pi f\, b(0) \right). \qquad \text{(2.39 revisited)}$$

This complex shear modulus can be separated into its real and imaginary part ($G^* = G' + iG''$). Whereby G' denotes the storage modulus and accounts for the elastic energy, which is restored after each cycle, and G'' is the loss modulus, representing the dissipated energy during each of these cycles. The ratio between loss and storage modulus is termed loss tangent ($\eta = G''/G'$) and describes the viscoelastic tendencies, whereby $\eta < 1$ describes solid-like and $\eta > 1$ fluid-like behavior. For a better comparison to reports on mammalian cells using the same approach (Alcaraz, Buscemi, Grabulosa, *et al.*, 2003; Rother *et al.*, 2014), I used the shear modulus instead of the Young's modulus E to describe the material properties. Nevertheless, both can easily be transformed using: $G = E/2(1+\nu)$ (Landau *et al.*, 1960).

At first glance, the measured complex shear modulus was comparable for all cells regardless their cell size. Fig. 4.2(a) shows two examples of the frequency depending on storage and loss modulus for cell diameter of $3\,\mu$m and $5\,\mu$m, and G' and G'' for all measured cells are shown in Fig. A.11 and Fig. A.12.

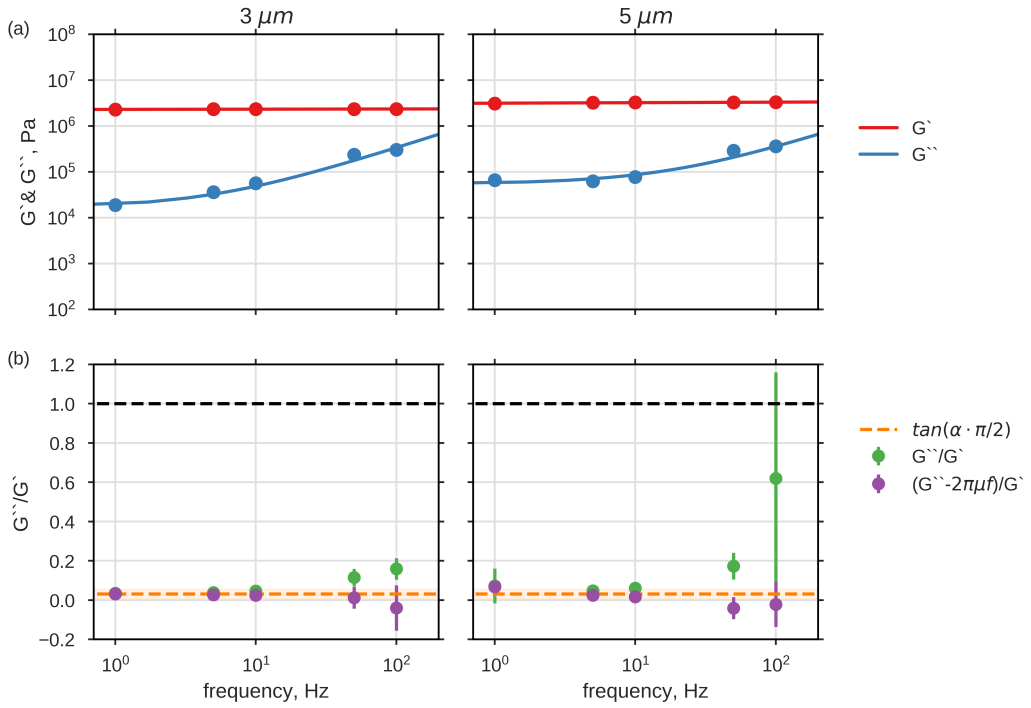

Fig. 4.2.: Visco-elastic cell wall response of yeast cells with cell diameter of $3\,\mu\mathrm{m}$ or $5\,\mu\mathrm{m}$. (a) Frequency depending mean of storage modulus $G‘$ (red dots) and loss modulus $G“$ (blue dots) and corresponding fit of the structural damping model (lines), for one cell of each diameter. (b) Mean $\pm$ SD of loss tangent $\eta = G“'/G‘'$ in green and the loss tangent $(G“ - 2\pi\mu f)/G‘$ with corrected loss modulus in purple, for all cells with given cell size. Black dashed line represents the transition to liquid like behavior.

The storage modulus G' showed almost no frequency dependence and stayed constant over the observed frequency range, as has been observed for other soft organic materials (Ross-Murphy & Shatwell (1993) and Ketz *et al.* (1988)). No significant difference of G' (mean$\pm$ SD) between $3\,\mu\mathrm{m}$ and $5\,\mu\mathrm{m}$ cells ($(2.64 \pm 1.50)\,\mathrm{MPa}$ and $(1.97 \pm 1.75)\,\mathrm{MPa}$) was observed (T-test, $p = 0.262$). This frequency independent G' is similar to the behavior of a linear elastic solid or a Kelvin-Voigt element but in contrast to the expected response of a Maxwell element. In such an element the storage modulus scales with $G' \sim \omega^2$ for small frequencies and saturates for large frequencies (Sec. 2.2.4). However, the assumption of a linear elastic solid or a Kelvin-Voigt element(Sec. 2.2.4) contradicts the frequency dependence of the loss modulus G'', since G'' stayed neither close to zero nor increased it linearly with the frequency. Further, a maxwell element is inadequate to describe the frequency dependence of G'', also, since G'' should scales with $G' \sim \omega$ for small frequencies and should approach zero for large frequencies (Sec. 2.2.4).

Instead, the ratio of both moduli stayed constant for low frequencies and G'' increased at higher frequencies. For $f < 100\,\mathrm{Hz}$ the loss modulus was smaller than the storage modulus ($G'' < G'$) for both cell sizes. At $f = 100\,\mathrm{Hz}$, G'' was still smaller than G' for $3\,\mu\mathrm{m}$ cells but not for all measured $5\,\mu\mathrm{m}$ cells (Fig. A.11 and Fig. A.12). However, no significant difference in mean G''-values between cells of both cell sizes have been found for any frequency (t-tests, p>0.05). The ratio $\eta = G‘'/G‘'$, also known as the loss tangent, describes the qualitative viscoelastic behavior, whereby $\eta < 1$ stands for a solid-like and $\eta > 1$ for a fluid-like material. For all measured cells the frequency depending mean loss tangent $\eta(f)$ is close to zero except for high frequencies ($\eta(f < 50\,\mathrm{Hz}) \sim 0$) (Fig. 4.2(b)), and even for high frequencies the loss tangent remains below 1 for most of the cells ($\eta(100\,\mathrm{Hz}) < 1$). Which implies that cell wall behaves solid-like in the range of the tested frequencies. Interestingly some larger cells ($d_{\mathrm{cell}} = 5\,\mu\mathrm{m}$) showed an $\eta(100\,\mathrm{Hz})$ close to or above 1 (9 out of 17 cells), while such values have not be found for smaller cells ($d_{\mathrm{cell}} = 3\,\mu\mathrm{m}$) (0 out of 14 cells). Tendencies of the G' and G'' suggest that for all cells a transition frequency f_t can be found for which $\eta(f_t) = 1$, though f_t might be higher for smaller cells. Why the transition to fluid-like behavior occurs at lower frequencies for larger cells remains unclear and should be addressed in future studies.

The here determined viscoelastic properties of the cell wall were acquired on living and proliferating yeast cells, with the advantage of an intact and complex cell structure. However, the cell wall is a composite material of glucans, mannan and chitin and conclusions on the properties of the individual polymers can not be drawn from this data alone. In addition, walled cells have several response mechanism to deal with mechanical stress, which may alter the mechanical properties of the cell

wall material, in case of yeast e.g. the CWI (Levin, 2005). It is therefore particularly interesting, that rheology on isolated cell wall particles of carrots and broccoli stems (Day *et al.*, 2010; Hemar *et al.*, 2011) as well as on barley β-glucan (Vaikousi & Biliaderis, 2005) show similar characteristics of the complex modulus with regard to frequency. In addition, Ross-Murphy & Shatwell (1993) reported that polysaccharide dispersions ($\sim$1%) behave as strong and weak gels, where $G'>G''$ and both are moduli ate independent of the frequency ω. This indicates that despite their dense packing, cell wall composing polysaccharides retain their mechanical properties.

Furthermore, micro- and macro-rheology by Luan *et al.* (2008) revealed similar frequency dependencies of both, shear and loss modulus, for highly cross-linked actin-networks. The storage modulus G' was almost independent and although the loss modulus G'' was always smaller than G' and increased slightly for higher f, it did not approach zero for low f. On the contrary, it even slightly increased again for the highest cross-linking ratio, similar to several measurements on the yeast cell wall. Although, with 1 out of 14 cells and 3 out of 17 cells for $3\mu\mathrm{m}$ an $5\mu\mathrm{m}$ sized cells, respectively, this effect was more prominent for larger cells, indicating a correlation to the maturation of the cell wall. The similarity between the reported complex modulus of the actin-network gradually vanishes with reduced cross-links between the actin fibers. G' more and more increases with f while G'' decrease more and more with reduced cross-links.

4.3 Structural Damping Model

From the analysis of the complex shear modulus we inferred that simple viscoelastic models, such as the Maxwell model, are not appropriate to describe the mechanical response of the cell wall. Instead of scaling differently with increasing frequency, both moduli showed a similar behavior, except for high frequencies. In fact, for low frequencies, the storage and the loss modulus were almost independent of f. Although they are unlikely, classical models cannot be ruled out completely because of limited experimental frequency range. The characteristic behavior might only manifest itself at other or extended frequency ranges.

Similar findings have been reported for gels and emulsions (Hoffmann & Rauscher, 1993; Mason *et al.*, 1995; Ketz *et al.*, 1988) as well as for different biological material (J. J. Fredberg & Stamenovic, 1989; Fabry *et al.*, 2001; Alcaraz, Buscemi, Grabulosa, *et al.*, 2003). In all these observations both moduli were coupled and showed a weak power-law dependence over a certain frequency range. This direct

Tab. 4.2.: Estimated fit parameters (mean ± SD) of the structural damping model (Eq. 2.51)

d_{cell}, μm	G_0, MPa	α	μ, kPa s	N
3	2.56 ± 1.49	0.020 ± 0.019	0.53 ± 0.27	14
5	1.90 ± 1.68	0.017 ± 0.010	0.64 ± 0.35	17

coupling of G' and G'' is known as structural damping behavior, which can not be explained by a Newtonian viscosity alone (Crandall, 1970). To reflect structural damping Fabry *et al.* (2001) formulated an empirical law (see Eq. 2.50), containing an additional Newtonian viscous term to reflect the increase of the loss modulus at high frequencies. For α-values close to zero this law can be written as

$$G^*(f) \approx \bar{G}_0(1 + i\tan(\alpha\,\pi/2))\left(\frac{f}{f_0}\right)^{\alpha} + i\,2\,\pi f\mu. \qquad \text{(2.51 revisited)}$$

G_0 and f_0 are scaling factors for storage and loss moduli and for the frequency, the latter was set to $1\,\text{Hz}$, for simplicity. Further, μ is the viscosity and $\alpha = x - 1$ is a power-law exponent. x can be interpreted as an effective temperature of a soft glassy material (see Sec. 4.4) and defines the structural damping coefficient of the model, i.e. the loss tangent or hysteresivity ($\eta = \tan((x-1)\,\pi/2)$). This frequency independent η couples the storage and loss moduli and therefore reflects the structural-damping behavior. This coupling, however, holds only for small frequencies, for higher frequencies the impact of the Newtonian term becomes dominant. In sum, this structural-damping model implies that, in the low frequency domain, both moduli are strongly coupled and increase with increasing frequency by following a power law with exponent α. In the high frequency domain, the coupling weakens. Although the storage modulus still increases according to the power law, the loss modulus becomes more and more dominated by the contribution of the Newtonian viscosity.

Constraining the Eq. 2.51 with mean $G^*(f)$ values from single-cell data allowed me to estimate the three independent parameters: G_0, α and μ. Here, Eq. 2.51 was used to estimate viscoelastic properties of the yeast cell wall, by fitting it to obtained $G^*(f)$ values from the nano-rheology measurements of single cells. Due to high cell-to-cell variations of obtained G^*s, each cell was considered individually (Fig. 4.2, Fig. A.11 and Fig. A.12).

Thereby estimated independent (mean±SD) parameters, G_0, α and μ, were grouped by cell size and listed in Tab. 4.2. Note, that the estimation of G_0 and μ can be biased by the tip cell geometry of the oscillating cantilever (see Eq. 2.39). Generally

no significant differences in either G_0, α or μ were found for differently sized cells. With $G_0 \sim 2\,\mathrm{MPa}$ compared to $G_0 = (0.3 \text{ to } 1.7)\,\mathrm{kPa}$ the obtained scaling factor for the moduli was three magnitudes higher than reported values for mammalian lung cell lines (Rother *et al.*, 2014), reflecting the stiffness differences between walled and non-walled cells. This aspect is also mirrored in the estimation of the power law exponent α, which was found to be 0.02 and thus, ten times lower then values reported for the lung cells. Estimated α values close to zero imply that the material is very close or at the glass transition, as discussed below. Furthermore, the apparent Newtonian viscosity μ was two magnitudes higher then reported values for non-walled cells (Rother *et al.*, 2014), reflecting again the higher rigidity of the cell wall. Values on μ are estimated at $\sim 0.5\,\mathrm{kPa\,s}$, which shifts the cell wall viscosity into the range of molten glass ($10\,\mathrm{kPa\,s}$ to $1000\,\mathrm{kPa\,s}$).

Most notably is that for both cell sizes, $3\,\mu\mathrm{m}$ and $5\,\mu\mathrm{m}$, the Newtonian viscosity μ, with $(0.53 \pm 0.27)\,\mathrm{kPa\,s}$ and $(0.64 \pm 0.35)\,\mathrm{kPa\,s}$, respectively, is close to the inverse of the estimated cell wall extensibility obtained by fitting cSCGM to *data set 1* but not to estimations from *data set 2* (see Sec. 3.4.2). For *data set 1* ϕ_{mother} was estimated to be $(0.57 \pm 0.34)/(\mathrm{kPa\,s})$, corresponding to a viscosity μ_{mother} from $1.1\,\mathrm{kPa\,s}$ to $4.3\,\mathrm{kPa\,s}$. In contrast, for *data set 2* the estimated ϕ_{mother} ranged from $1 \times 10^{-5}/(\mathrm{kPa\,s})$ to $1 \times 10^{-2}/(\mathrm{kPa\,s})$, thereby corresponding to viscosities of $1 \times 10^{5}\,\mathrm{kPa\,s}$ to $1 \times 10^{2}\,\mathrm{kPa\,s}$. Although the similarity between the experimental determined viscosity and the estimated viscosity resulting from the model fits for *data set 1* are striking, a comparison must be made with caution, since the assumed yielding process differs between cSCGM and SGR, as explained below. Apart from the transition frequency f_t no differences of viscoelastic properties between $3\,\mu\mathrm{m}$ and $5\,\mu\mathrm{m}$ sized cells have been found. A significant reduction in the apparent viscosity of the bud compartment, as predicted by the cSCGM, however, can not be rejected either.

To gather more informative data on the visco-elasticity of the bud cell wall an improvement of the experimental approach is required, since the budding process and the experimental measurement were in the same time range. Hence, a clear distinction between bud and new born cell was impossible by design.

4.4 Discussion and Remarks on Soft Glassy Rheology

The cell wall of yeast, like other material, such as foams and emulsions, shows structural damping behavior. The applied structural damping model is an empirical

law and thus cannot be completely decomposed in mechanical elements, like the Maxwell-model. With the soft glassy rheology model (SGR) Sollich *et al.* (1997) formulated an exciting generic model to explain structural damping. "Soft glassy" thereby refers to the characteristics of the model, which it shares with soft glassy material, such as *structural disorder* and *metastability*. In the model, glass transition temperature x_g , describes the temperature at which properties of a material changes abruptly, from hard, bristle and glassy (below x_g) to flexible and rubber like (above x_g).

The SGR is a mesoscopic model based on an ensemble of purely elastic entities, whose deformation states are distributed depending on the energy in the system. Additionally each entity possesses a yield capacity or energy E_y, which describes the maximal energy each entity can have before it yields. The transition probability per unit time for an element with deformation l to return to its undeformed state ($l = 0$) is given by:

$$\Gamma_0 \, e^{-(E_y - \frac{kl^2}{2})/x} \tag{4.1}$$

Where Γ_0 is the transition attempt frequency, k is the spring constant, P is the probability to be in the particular state and x refers to the effective temperature or noise level. Imposing a strain rate to the system adds energy to the system and has two opposing effects. On the one hand, it shifts the distribution towards higher deformation states of the entities and, on the other hand, it causes yielding and thereby reduces the probability for high deformation states while increasing the probability for the state with no deformation. Hence, the entities constantly "hoping" between certain states when the macroscopic system is exposed to constant strain rate. A more detailed description of the SGR can be found in Sec. 2.2.4

When analyzing the behavior of the SGR for relatively low frequencies Sollich *et al.* (1997) found that it diverges from that of linear viscoelastic models. Both contributions of the complex modulus G^*, the storage and loss modulus ,G' and G'' scale with a power-law of the angular frequency ω if the effective temperature x is close to the glass transition temperature $x_g = 1$ (using appropriate energy units).

$$G' \sim \begin{cases} \omega^2, & (3 < x) \\ \omega^{x-1}, & (1 < x < 3) \end{cases}, \quad G'' \sim \begin{cases} \omega, & (2 < x) \\ \omega^{x-1}, & (1 < x < 3) \end{cases} \tag{4.2}$$

For x above, yet close to one, the SGR shows, therefore, the typical structural damping behavior of a strong coupling between G' and G'' with respect to the angular frequency. Structural damping analysis of the yeast cell wall revealed in Sec. 4.3 an average power law coefficient for both cell sizes of $\alpha = 0.019 \pm 0.014$. Considering that $\alpha = x - 1$, the model predicts, therefore that the cell wall is in the rubber like state, but almost directly at the glass transition.

In summary the SGR represent an interesting model which can reflect the structural damping observed in various materials. As mentioned above Sollich *et al.* (1997) argue that glassy dynamics results from *structural disorder* and *metastability*. How this characteristics translate to structure of the cell wall remains to discovered.

Noteworthy, other cell integrity-maintaining structures, apart from the here studied yeast cell wall, have shown to behave as soft glassy materials. Fabry *et al.* (2001) studied the microrheology of human airway smooth muscle cells (HASM) with oscillating ferrimagnetic micro beads. Regarding the cytoskeleton he wrote: "data suggest that, rather than being thought of as a gel the cytoskeleton may be thought of more properly as a glassy material existing close to the glass transition, and that disorder and metastability may be essential features underlying its mechanical functions"

Both yield energy E_y and the attempt frequency Γ_0 are characteristic material properties according to the SGR and worth a closer look in future investigations. Estimations of both parameters from different structural elements of the cell might reveal common underlying principles of biological material, since they share common requirements: they have to be rigid enough to maintain the cellular structure and soft enough to allow for cellular deformations.

In summary, nano-rheology of the yeast cell wall revealed that for slow strain rates or small frequencies, the yeast cell wall can be interpreted as elastic solid or as soft glassy material very close to the glass transition temperature, e.g. during growth process and slow changes in the extracellular osmolyte concentration of the environment. The mechanical cell wall behavior, however, changes for fast strain rates, as it might occurs when the environmental osmolyte concentration changes rapidly. In this regime the impact of the Newtonian viscosity of the cell wall can become dominant.

The estimated viscosity was strikingly similar to the inverse of the average cell wall extensibility estimated from *data set 1*, but not for *data set 2*. Conclusions from this, however, should be drawn with caution. According to the theory of structural damping and soft glassy rheology, material yielding causes the coupling of storage

and loss modulus and is expressed in the effective temperature at low frequencies. The Newtonian viscous expansion however is independent of the yielding in this concept. In contrast to the SCGM, where the expansion above the yield condition ($\Pi = \Pi_c$) is modeled as a viscoelastic expansion, comprising a Newtonian viscous term. This issue is not limited to yeast cell walls. In experiments, plant cells showed a rather viscoelastic than plastic behavior, although this plastic behavior is essential for cell growth (Burgert & Fratzl, 2006). Hence, further research is needed to elucidate the mechanism of cell wall wall expansion.

5 Cell Wall Elasticity Pattern Shapes Yeast during Early Mating Morphogenesis

The mechanical models were build in cooperation with Wolfgang Giese, who also implemented the models. Multi-parametric images on cell wall deletion strains were done with the help of the student assistant Alice Wittig. Preparation of the SEM images was done in the group of molecular parasitology by Gabriele Drescher.

Goldenbogen, B., Giese, W., Hemmen, M., Uhlendorf, J., Herrmann, A. & Klipp, E. (2016). „Dynamics of cell wall elasticity pattern shapes the cell during yeast mating morphogenesis.“ *Open biology*, **6**(9): 160136

In Sec. 3.2 I addressed one polarized growth mode of *S. cerevisiae*: the budding. I showed, from a mechanical perspective, that cell wall properties, as the elasticity (Young's modulus) or the extensibility, need to differ significantly between mother and bud compartment to facilitate bud expansion. Applying AFM based nano-indentation measurements I was able to reject the elasticity as distinguishing feature between mother cell wall and bud cell wall and concluded that the cell wall extensibilities has to vary strongly instead. In the following, I focus on the directed growth during mating morphogenesis and work out similarities and differences between both modes of polarized-growth, budding and mating, from a mechanical point of view. In addition, this chapter contains a section on the estimation of the turgor pressure with AFM.

5.1 Yeast Mating Morphogenesis

Upon nutrient limitation, as already explained in Sec. 1.2, diploid yeast cells can exit the cell cycle in G1 phase and undergo sporulation (Neiman, 2005). By sporulation, cells enter a dormant and resistant state of stasis, enabling them to survive in harsh conditions or in uninhabitable environments such as soil (Knight & Goddard, 2015)

or the intestines of insects (Coluccio *et al.*, 2008; Stefanini *et al.*, 2016). Besides formation of stable spore capsule called ascus, cells undergo mitosis and meiosis, forming four individual haploid spores residing in each ascus. This four spores can be separated into two mating types, MATa and MATα. When environmental conditions improve, each spore either proliferates as haploid cell by going through the cell cycle or mates with a cell of opposing mating type to form a diploid cell again (Merlini *et al.*, 2013). Later stages of this mating process, such as cell fusion and karyogamy, require close cell-to-cell contact. Lagging mechanism for active movement, cells have to grow towards their mating partner in order to close a potential spatial gap. Hereby, cells form a mating protrusion and direct it towards the highest pheromone gradient, which eventually results in dumbbell-shaped zygotes (Tartakoff, 2015). Under the microscope, the combined shape of initially ellipsoidal cell and newly formed mating projection resembles a cartoon character from Al Capp (1948) named "shmoo", which became synonymous for this particular shape. The following chapter will focus on the formation of this shmoo shape, on its mechanical prerequisites and its dynamic.

Both mating types are exclusively sensitive to the complementary pheromone (Fig. 5.1), which is secreted or exported by the mating partner and sensed via the mating type specific G protein-coupled receptors (GPCRs), Ste2 and Ste3, i.e. MATa cells secrete a-factor and respond to α-factor and vica versa (Bardwell, 2005). Occupation of the receptor activates the Gα subunit of the heterotrimeric G-protein (G$\alpha\beta\gamma$) which results in the release of the heterodimeric G$\beta\gamma$. Among others, free G$\beta\gamma$ activates a mitogen activated protein kinase (MAPK) signaling cascade and interacts with the small GTPase of the Rho family Cdc42, which regulates cell polarization (Pruyne & Bretscher, 2000) and recruits members of the polarisome as the formin Bni1. The MAPK-signaling cascade amplifies the signal and ultimately activates Far1 and the transcription factor Ste12, leading to cell cycle arrest and the expression of mating specific genes.

The shmooing process is associated with drastic shape changes compared to the "normal" mode of growth. Single yeast cells are spherical or ellipsoidal in shape during G1 phase and even during budding both compartments, mother and bud, can be approximated by unevenly sized spheres as I discussed in Chapter 3.1. Growing a protrusion out of a spherical cell requires a break of the radial symmetry of the cell. This symmetry breaking or polarization in the context of mating morphogenesis is still a subject of current research (Giese *et al.*, 2015; Trogdon *et al.*, 2018) and concerns not only the geometry and mechanics of the cell wall but also the intracellular orientation and localization of certain proteins. For instance, Ste5, Ste7 and Fus3 as well as Rho1 and Pkc1, all key elements of the yeast pheromone

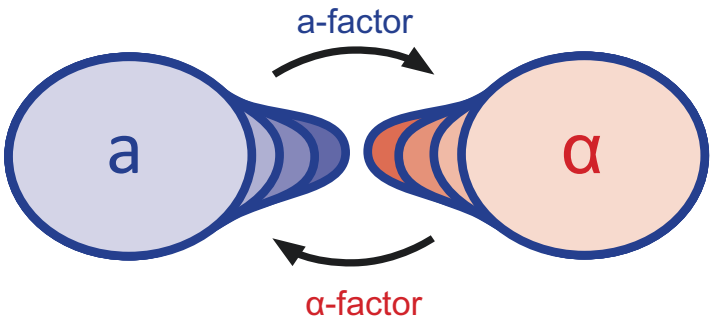

Fig. 5.1.: "Shmooing" - directed growth of a yeast mating projection towards the source of the corresponding pheromone. Both haploid cell types, MATa and MATα grow towards the highest gradient of α-factor and a-factor, respectively.

response pathway (PRP) (Bardwell, 2005) and CWI (Levin, 2011), localize to the tip of the protrusion, showing that this drastic morphogenic change is highly regulated by the two interlinked signaling pathways. The relevance of this regulation becomes evident when considering that cell death is increased after pheromone treatment and enhanced even further when PRP and CWI proteins such as Fus1, Fus2 or Mid2 are missing (Huberman & Murray, 2014; Banavar *et al.*, 2018).

In addition, proteins required for cell-cell adhesion, such as Aga1 and Fig2, as well as proteins required for intracellular transport, e.g. actin filaments or patches, are located at or are focused to the tip of the mating projection by the polarisome (Slaughter *et al.*, 2009). Baba *et al.* (1989) showed by transmission electron microscopy, that vesicles are enriched in the mating projection, too, in particular in proximity of the tip, which was later confirmed by Gammie *et al.* (1998). This vesicles carry cell wall precursors, cell wall modifying enzymes, such as glucanases or transglycosylases, and subunits of glucan synthases along actin fibers to the sites of active growth (Harold, 2002; Lesage & Bussey, 2006). Localization of these vesicles, therefore, directs cell wall synthesis to the tip and causes local modifications of the cell wall structure and presumably its mechanical properties.

The cell wall of *S. cerevisiae* is the main structure to preserve cellular integrity, as explained in Sec. 1.3. Thereby, composition and structure of the cell wall have to be adaptable to allow for morphological alterations and to cope with challenging environmental conditions (Orlean, 2012). For instance, Pillet *et al.* (2014) reported stiff circular structures of reinforced cell wall material appearing after severe heat shocks.

During mating morphogenesis and in particular during shmooing, the cell wall structure and composition (see Sec. 1.3.1) is subjected to alteration. In particular,

the ratio between mannan, i.e. mannoproteins, and glucan shifts in favor of glucan in shmooing cells and the mannan present is less branched and contains shorter side chains according to Lipke *et al.* (1976). Besides this increase in glucan, mainly due to an increase in 1,6-beta cross-links, chitin increases as well by tripling its content after pheromone treatment (Cid *et al.*, 1995). It can be assumed that structural changes of the cell wall are associated with changes in mechanical properties.

Alterations of the cell wall structure during shmooing were also indicated by transmission electron microscopy (Lipke *et al.*, 1976; Baba *et al.*, 1989; Gammie *et al.*, 1998). The cell wall at the protrusion exhibited a diffuse outer layer and showed increased susceptibility to lysis by glucanases (Lipke *et al.*, 1976). Interestingly, a deviating cell wall structure was visible already at very early stages of shmooing (Baba *et al.*, 1989). Nevertheless, the observed cell wall thickness showed no significant variations except for the tip of the mating projection (Lipke *et al.*, 1976; Baba *et al.*, 1989). Remodeling of the cell wall structure and composition is regulated by the CWI. The importance of this regulation is illustrated by the fact that $90\,\%$ of yeast lacking Mid2, a cell wall integrity sensor, die after pheromone treatment (Rajavel *et al.*, 1999). How this localized and controlled remodeling of the cell wall translates precisely into generation of the characteristic shmoo shape, so far, remained unclear. Most of theoretical studies on mating morphogenesis considered localized growth, yet neglected the cell wall structure and its possible spatial inhomogeneity (Slaughter *et al.*, 2009; Chou *et al.*, 2012; Angermann *et al.*, 2012). However, to understand the generation of the shmoo shape, it is necessary to account for both localized growth and variations of the cell wall structure, in particular its mechanical properties. Previous studies on tip growth of plants (Dumais *et al.*, 2006; Hamant *et al.*, 2008; Campàs & Mahadevan, 2009; Fayant *et al.*, 2010; Yanagisawa *et al.*, 2015) and fungi (Minc *et al.*, 2009; Drake & Vavylonis, 2013; Bonazzi *et al.*, 2014; Atilgan *et al.*, 2015) already addressed the issue of locally varying mechanical properties of the cell wall, but none was capable of describing the morphogenic switch from spherical to tip growth. In a recent study, Banavar *et al.* (2018) considered localized tip growth and inhomogeneous cell wall properties in the context of shmoo formation. Though they focused on the elongation of the mating projection and neglected the initial morphogenic switch.

Yeast mating has been studied intensively throughout the last decades, yet the mechanisms cells use to transform their shape and simultaneously preserve their integrity remained to be investigated. Of particular interest is whether the mechanical properties of the cell wall material are indeed altered during shmooing and which pattern this alteration follows.

To this end, we formulated the SM, describing the shmooing yeast cell as pressurized shell in mechanical equilibrium. From the model we inferred the plane stresses in the cell wall for a given shape. We obtained additional estimations on the strain and elasticity pattern of the cell wall from mechanistic descriptions of the underlying growth patterns. The relaxed shape was inferred from osmotic shock experiments. To validate the predicted elasticity pattern, I probed the cell wall of living shmooing yeast cells by applying AFM based multi-parametric imaging and thereby searched for local variations in mechanical properties of the cell wall over time, similar to the approach used for the examination of the mother and bud cell wall in Sec. 3.3. The obtained spatio-temporal information on the cell wall elasticity was subsequently used to build a dynamic cell wall model (DM). This model reflected not only a snapshot but the whole dynamic of the shmoo formation and thereby provided insights on the transition process. The DM enabled us further to asses different growth scenarios, i.e. different conditions upon which the cell wall yields and starts to expand irreversible.

In contrast to the SM, the DM does not require a presumption on the relaxed shape of the shmooing cell. Instead, simulations of the DM provided predictions on the temporal development of the relaxed shape and thus on the strain in the cell wall at any time. To assess the predicted cell wall strain, I compared the shape of cells under normal turgor pressure with the cell shape at zero turgor pressure, from microscopic images acquired during osmo-shock experiments.

5.2 The Shmoo as Mechanical Steady State Model

As initial step, I will characterize the mechanical state of the cell wall during shmooing using a SM for a given characteristic shape as depicted in Fig. 5.1 and Fig. 5.2. The model, though already described in (Goldenbogen *et al.*, 2016; Giese, 2016), will be explained in the following to highlight similarities and differences to the SCGM, described in Sec. 3.1.1, and to motivate subsequent elasticity analyses.

The SM describes a snapshot during the formation of the mating projection and therefore deliberately neglects growth dynamics. Cellular growth is slow compared to the mechanical relaxation time of the stressed cell wall, therefore, growth-related deviations from the mechanical equilibrium are assumed to be compensated in the time frame of the growth process. In the SM the hydrostatic pressure P, or turgor pressure, is the driving force for cell expansion. P acts constantly and homogeneously on the inner surface of the surrounding cell wall. The thickness d

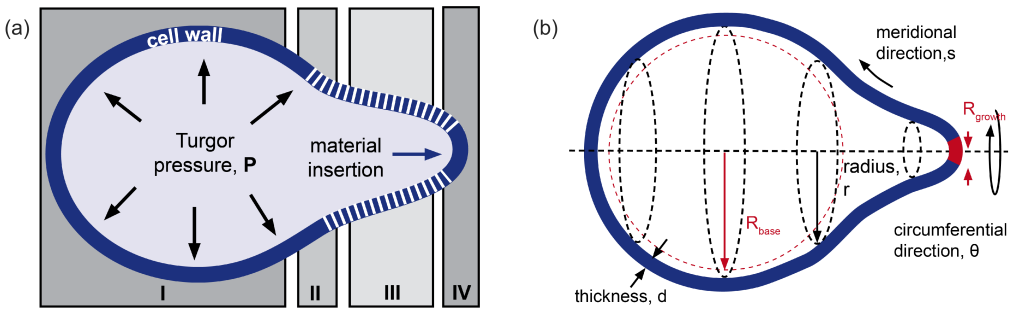

Fig. 5.2.: Preliminary considerations regarding geometry and cell wall mechanics. (a) Turgor pressure P elastically expands the whole cell wall (blue) according to the local YM while insertion of new cell wall material is limited to the tip. Shmoo shape segments were assigned to base [I], neck [II], shaft [III] and tip [IV] for improved comparability. (b) Illustration of the used coordinates: circumferential angle θ, meridional length s with respective distance r to the symmetry axis, relaxed radii for the mating projection R_{growth} and base R_{base} as well as cell wall thickness d.

of this wall is assumed to be constant, while the elasticity $E(s)$ is allowed to vary locally. Furthermore cell wall material can only be inserted at the tip of the mating projection. A scheme of the concept is depicted in Fig. 5.2(a). For comparison, we distinguish between four regions of similar shape: base [I], neck [II], shaft [III] and tip [IV]. The spherical part arising from vegetative growth is represented by the base while the protrusion is divided into the elongated cylindrical shaft and the tip. The neck was defined as the transition region between shaft and base.

Similar to the SCGM derived in Sec. 3.1, the SM considers the cell wall as thin shell, explained in more detail in Sec. 2.1.1. Although, in contrast to the SCGM the cellular shape can not be described as radial-symmetric but instead as axis-symmetric (Fig. 5.2(b)), implying that the relationships used for stress and strain in the SCGM are not valid for this geometry. The axis-symmetric shell geometry was described by two coordinates: the circumferential angle θ and the meridional distance from the tip s. Consequently, the distance from the symmetry axis $r(s)$ is given as function of s. The principle in-plane stresses σ_θ, σ_s for this geometry read as:

$$\sigma_\theta = \frac{P}{2d\kappa_\theta(s)}, \quad \sigma_s = \frac{P}{2d\kappa_\theta(s)}\left(2 - \frac{\kappa_s(s)}{\kappa_\theta(s)}\right). \qquad \text{(revisited 2.1)}$$

Where $\kappa_\theta(s)$ and $\kappa_s(s)$ are principle curvatures, parameterized for their meridional positions. From Eq.2.1 follows, that the stresses solely depend on the local curvature, i.e. the geometry of the cell, given that P acts uniformly on the inner shell surface

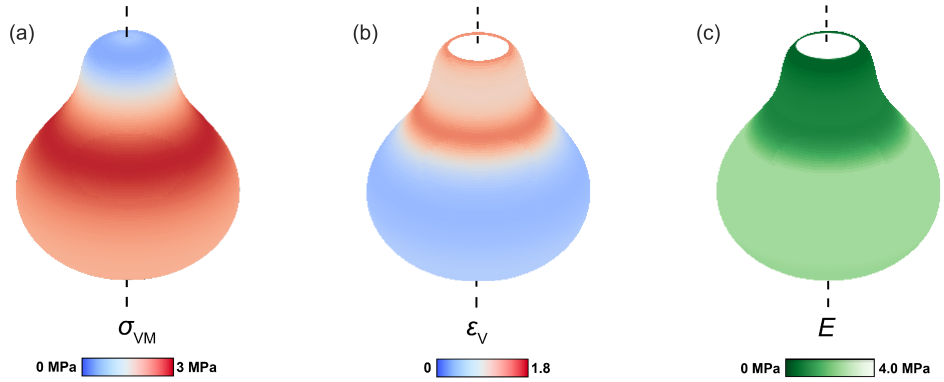

Fig. 5.3.: Low stress in the cell wall protrusion has to be compensated by reduction in YM to provide the given cell shape. Estimated profiles from the SM of von Mises stress, volumetric strain and YM are shown in (a)-(c). Used parameters specified in Tab. A.1.

and d is independent of θ or s. Using the von Mises stress σ_{VM} (Eq. 2.5), as measure for the magnitude of the in-plane stress at a given position, a geometry depending stress pattern (Fig. 5.3(a)) was obtained. While σ_{VM} at the base equals the stress of a similar sized spherical shell, it deviates near and at the protrusion. At the shaft and the tip σ_{VM} is strongly reduced, in contrast to the base, where at the neck σ_{VM} is slightly enhanced. This indicates that the force that expands cell wall material at the tip or in the shaft is reduced. To obtain stresses at the tip similar to the acting stresses in a vegetative growing cell, either P have to be increased or d have to be reduced.

Aiming at predicting the local elasticity of the cell wall, we need an estimation of the strain and an assumption of the nature of the elastic expansion, in addition to the stress pattern. For simplicity and without any further knowledge, the elasticity was assumed to be linear in the SM. The principle strains in the chosen coordinate system for the axis-symmetric geometry are given by:

$$\varepsilon_\theta(s) = \frac{r(s) - R_{\text{ref}}(s)}{R_{\text{ref}}(s)}, \quad \varepsilon_s(s) = \frac{ds - dS}{dS}. \qquad \text{(revisited 2.7)}$$

Since the strain is defined as the expansion of a body with respect to its unstressed, i.e. relaxed shape, (see Sec. 2.1.1) an assumptions on this relaxed shape is required in order to estimate strain distributions. Then used relaxed shape, described by R_{ref} and S, based on the observed growth pattern, which shifts from spherical to tip growth. Hence, the assumed relaxed shape combined a sphere with radius

R_{base} with a cylinder with radius R_{growth}, representing the base and the shaft (see Fig. 5.2(b)).

The magnitude of the local strains, ε_θ and ε_s, were estimated by the volumetric strain ε_{v} (Eq. 2.8) analogous to σ_{VM} and are shown in Fig. 5.3(b). Due to the small growth region at the tip represented by R_{Growth}, which defines the size of the cylindrical relaxed shape of the protrusion the strain raises rapidly at the neck and drops slightly with decreasing distance to the tip. The assumption that cell material at the shaft originates from growth at the tip implies that this growth region can not be entirely elastic. This region was, therefore, omitted in the calculation of the strain and the elasticity. Note that from limitation to axis-symmetry follows that neither the stresses, σ_θ and σ_s nor the strains, ε_θ and ε_s, depend explicitly on θ. It follows that the elasticity has to be independent of θ, i.e. $\partial E/\partial\theta = 0$, too.

The calculated local stresses and strains were used to predict the elasticity pattern of the cell wall shown in Fig. 5.3(c) by assuming linear elasticity (see Sec. 2.1.1). The figure elucidates that maintenance of this shape requires a drastic reduction of the Young's modulus E at this protrusion, to allow for increased strains at the protrusion despite reduced stresses at this very region. Intriguingly, both effects, reduction of the stress and increase of the strain in the protrusion region, have a similar impact on the elasticity pattern, e.g. even a homogeneous ε_{v} would lead to the same qualitative elasticity pattern.

In summary, the mechanical steady state model predicts a cell wall softening at the protrusion under the assumptions of an elastic and locally isotropic cell wall with constant wall thickness, a confined growth region at the tip, and constant turgor pressure.

5.3 Turgor Pressure Estimation

The turgor pressure is crucial for the yeast morphogenesis, as it is the mechanical force that drives cell wall expansion. Despite its significance, a direct measurement of the hydrostatic pressure inside the yeast cell has so far not been conducted, though several indirect approaches have been taken to determine the turgor pressure. These approaches either based on whole cell compression experiments or experiments varying the external osmolyte concentration and resulted in a wide range of turgor pressure estimations, from $0.05\,\text{MPa}$ to $0.8\,\text{MPa}$ (Meikle *et al.*, 1988; Martinez de Marañon *et al.*, 1996; A. E. Smith, Zhang & Thomas, 2000; Schaber *et al.*, 2010; Arfsten *et al.*, 2010). Considering such a wide range of turgor pressures in

mathematical models for morphogenesis consequently reduces prediction accuracy of those models. The turgor pressure, thus, had to be reassessed, optimally by simultaneously considering the used yeast strains and the accessible experimental methods. According to a recent study by Vella *et al.* (2012) the turgor pressure can be determined from force spectroscopy measurements for large indentation depth δ. In this study they examined indentation measurements of strongly pressurized, thin, spherical shells with radius r and shell thickness d and found relationships between inner pressure P and apparent stiffness k, depending on the indentation depth δ. Of particular interest is the case for $\delta \gg d$ where the apparent stiffness k is only governed by the pressure and the shell radius and can be approximated by $k \approx \pi P r$. Rearrangement of this equation provides a formula to estimate the turgor pressure:

$$\Pi_\mathrm{t} \approx k/(\pi r). \tag{5.1}$$

Utilizing this relation, the turgor pressure of three trapped yeast cells was estimated from nano-indentation experiments on yeast cell surfaces using AFM, as explained in Sec. 2.2.3. The apparent stiffness k was determined by linearizing the obtained force F with respect to the tip-sample distance, where $\delta - 10\,\mathrm{nm} < \delta < \delta_\mathrm{max}$ and plotted against the corresponding indentation depth δ (Fig. 5.4). Obtained k-values followed a sigmoidal trend, therefore supporting the model of Vella *et al.* (2012) with two distinctive regimes for k, one at low and one at high δ-values. Since Eq. 5.1 holds only for $\delta \gg d$, the limit to which k converges for high δ-values was approximated by fitting a sigmoidal function to the obtained data. From the resulting k_max-values and estimations for r from AFM height maps of each cell, the turgor pressure (mean $\pm$ SEM) was estimated to be $(0.24 \pm 0.09)\,\mathrm{MPa}$. The value used for further analysis was rounded to $\Pi_\mathrm{t} \approx 0.2\,\mathrm{MPa}$, due to the high uncertainty and the small sample size. To conclude, using indentation experiments I found Π_t to be in the lower region of the reported range.

5.4 Cell Wall Elasticity Pattern Obtained with AFM

To verify the local cell wall softening at the shaft during shmoo formation, as prediction by the SM, I experimentally studied the spatial cell wall elasticity distribution of living *S. cerevisiae* by probing its surface with AFM. Thereby obtained elasticity and height maps in high resolution allowed for comparison of different cell wall regions during morphogenesis. The applied approach is comparable to the approach used

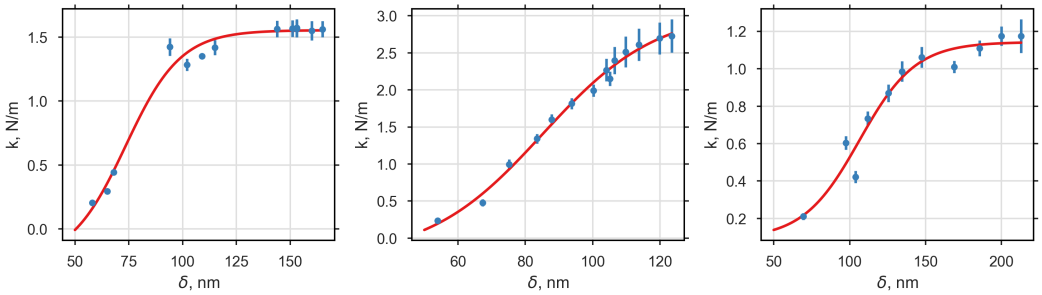

Fig. 5.4.: Stiffness saturates for deep indentation depth. Apparent stiffness k vs indentation depth δ of three MATa bar1Δ cells obtained with force-spectroscopy in blue, error bars show SD (N=1024). k is the slope of the force vs. tip-sample distance calculated for $\delta - 10\,\mathrm{nm} < \delta < \delta_{\mathrm{max}}$. Spring constant of the cantilever was $k_{\mathrm{cantilever}} = 0.64\,\mathrm{N/m}$. Red curve represents sigmoidal fit to estimate the maximal k.

for the determination of the cell wall elasticity of mother and bud in Sec. 3.3. The experimental setup and procedures are described in detail in Sec. 2.2.3 and will only be briefly explained in the following.

Living yeast cells were trapped in porous filter membranes as described in Sec. 2.2.3 and the occupied filter were kept in SFSD medium at $22\,^{\circ}\mathrm{C}$, thus guaranteeing almost optimal growth conditions to avoid apoptosis. The trapped cells were mapped in the multi-parametric imaging mode QI$^{\mathrm{TM}}$ first at low resolution ($64\,\mathrm{px}\times64\,\mathrm{px}$) to locate occupied filter holes and select suitable cells and then at high resolution ($256\,\mathrm{px}\times256\,\mathrm{px}$) to obtain elasticity and height maps at nanoscale resolution (Fig. 5.8). Here, "suitable" refers to the vertical position in the filter hole, i.e. the cell should be neither embedded to deep nor extended to far above the surrounding surface.

Multi-parametric imaging, explained in Sec. 2.2.3, based on force-distance cycles were performed at each image position. As discussed earlier in Sec. 2.1.1, from a mechanical point of view, yeast cells can be seen as pressurized thin shells. The apparent elasticity obtained from indentation experiments on such shells depends on the depth of the indentation. While deep indentation will provide information on the acting inner pressure, which was utilized for the estimation of the turgor pressure in Sec. 5.3, shallow indentation, i.e. smaller than the shell thickness, can provide information on the elasticity of the shell, in this case the cell wall. Therefore, the indentation depth was kept below the cell wall thickness ($115\,\mathrm{nm}$, Dupres, Y. Dufrêne, *et al.* (2010)) by limiting the maximum applied force to $1.5\,\mathrm{nN}$ (Fig. 5.5).

To combine information on geometry and elasticity, 3D-representations of the cell topography (Fig. 5.7(a,b)) were created based on the acquired height maps and

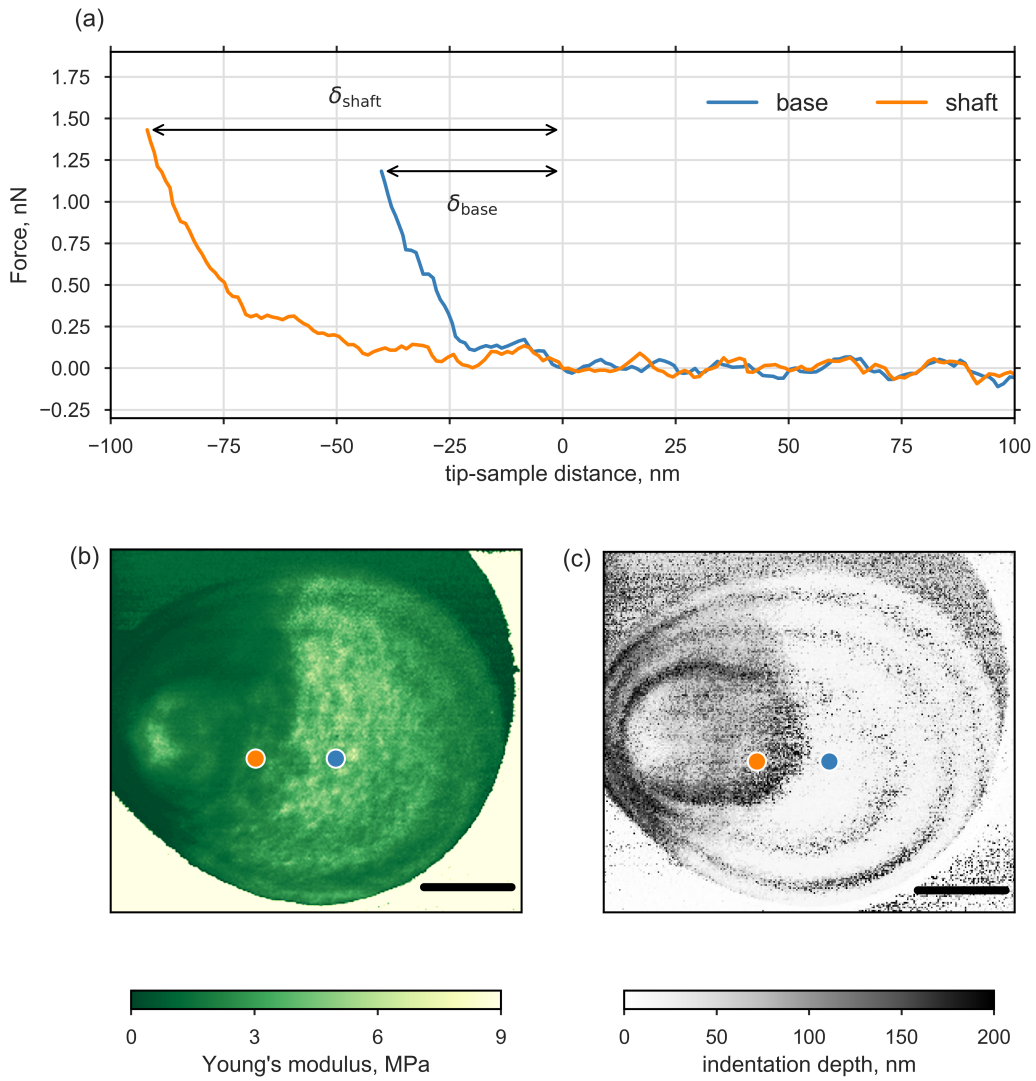

Fig. 5.5.: Indentation depth remains below cell wall thickness during nano-indentation measurements. (a) shows exemplarily singular force-distance curve with respective indentation depth δ obtained from base (red) and shaft (blue) at the marked positions in (b) and (c). (b) and (c) show the elasticity and the indentation map of a shmooing MATa bar1Δ cell, black bar represents $1\,\mu\text{m}$. For similar maximum forces, softer material led to higher δ-values at the shaft compared to the base. Nevertheless, the indentation depth (mean$\pm$SE, N=900) of quadratic regions at shaft and base, with $\delta_{\text{shaft}} = (97 \pm 26)\,\text{nm}$) and $\delta_{\text{base}} = (38 \pm 10)\,\text{nm}$, were less than or equal to the reported cell wall thickness of $d = 115\,\text{nm}$ (Dupres, Y. Dufrêne, *et al.*, 2010).

color-coded according to the measured YM. To study the cell wall elasticity during shmoo formation, measurements were conducted on MATa cells in the late exponential phase, constantly induced by $10\,\mu\mathrm{M}$ α-factor, and compared to measurements conducted with α-factor free media. A continuous induction by α-factor throughout the experiments was ensured by the choice of the used yeast strain, MATa bar1Δ, since it lacks the gene for the pheromone specific protease Bar1 (Chan & Otte, 1982). Assessment of the experimental setup by SEM (described in detail in Sec. 2.2.5) confirm that trapping does not prevent shmoo formation (Fig. 5.6).

Observations on untreated cells were similar to those made in the investigation on budding morphogenesis in Sec. 3.3. The cell geometry is spherical and the cell wall elasticity is almost homogeneously distributed, except for sites of previous budding events, so-called bud scars (Fig. 5.7(j) and Fig. 3.7). In addition, cross section analysis (Fig. 5.7(k,l)) showed clearly that the YM profile follows the height profile, i.e. the estimated YM decreases with increasing distance to the cell center, which can be explained by the apparent YM reduction at tilted surfaces (Routier-Kierzkowska & R. S. Smith, 2013).

When MATa bar1Δ cells were treated with α-factor typical morphogenic changes could be observed after $90\,\mathrm{min}$, both with SEM and AFM. Cells had protruded a mating projection and multi-parametric imaging revealed a concomitant reduced YM at these protrusions. Analysis of 3D-representations further showed that the observed soft material was confined to the protrusion, whereas the rest of the cell exhibited YM-values typical for untreated cells. Although the protrusion is a region of higher surface curvature, surface-tilting as reason for low YM can be rejected, since height and elasticity profiles from cross-sections (Fig. 5.7(m,n)) were not correlated at the protrusion, in contrast to those at the base region. Independent from the orientation of the mating projection, the YM dropped drastically and abruptly to about one-eighth of YM-values at the neck and remained low at the whole protrusion, except for the assumed tip, which shows a small region of higher YM-values. The location of the protrusion neck was defined as the position where the height profile deviates from the profile of a sphere. Note that the highest peak does not necessarily correspond to the tip of the mating projection, as it depends on the orientation of the protrusion with respect to the filter surface.

The elasticity pattern obtained form cross-sectional YM-profiles matched the pattern predicted by the SM. However, YM-profiles exhibited high point to point variations compared to height profiles. Therefore, I compared mean YM-values of the regions of interest, tip, shaft and base, as defined in Sec. 5.2, to quantitatively and systematically analyze the elasticity pattern of the cell wall. Further, to neglect the

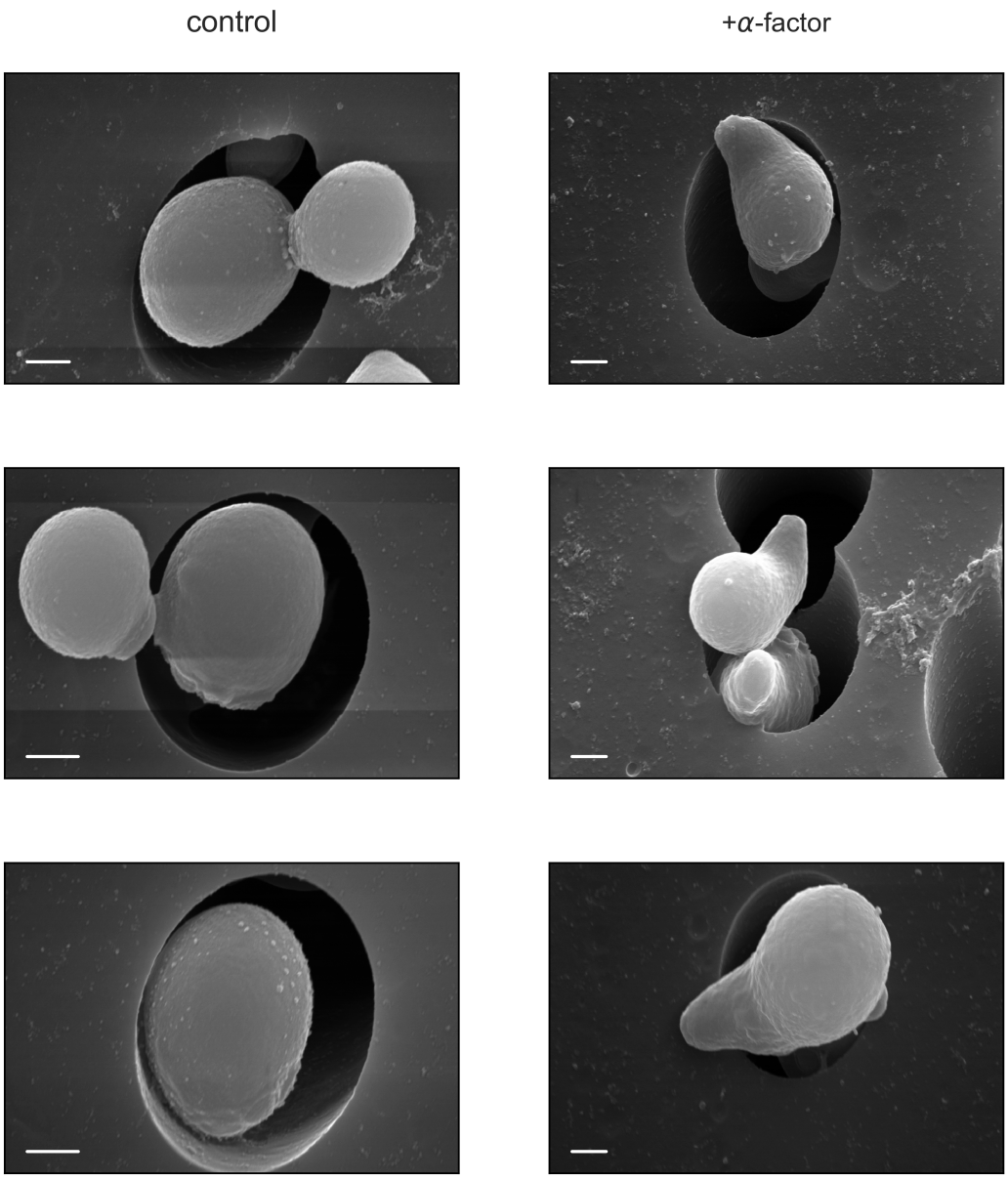

Fig. 5.6.: Assessment of trapping and α-factor treatment with SEM. AFM samples of trapped MATa bar1Δ cells investigated with SEM. Fixation led to cell shrinkage. Scale bar is $1\,\mu\mathrm{m}$.

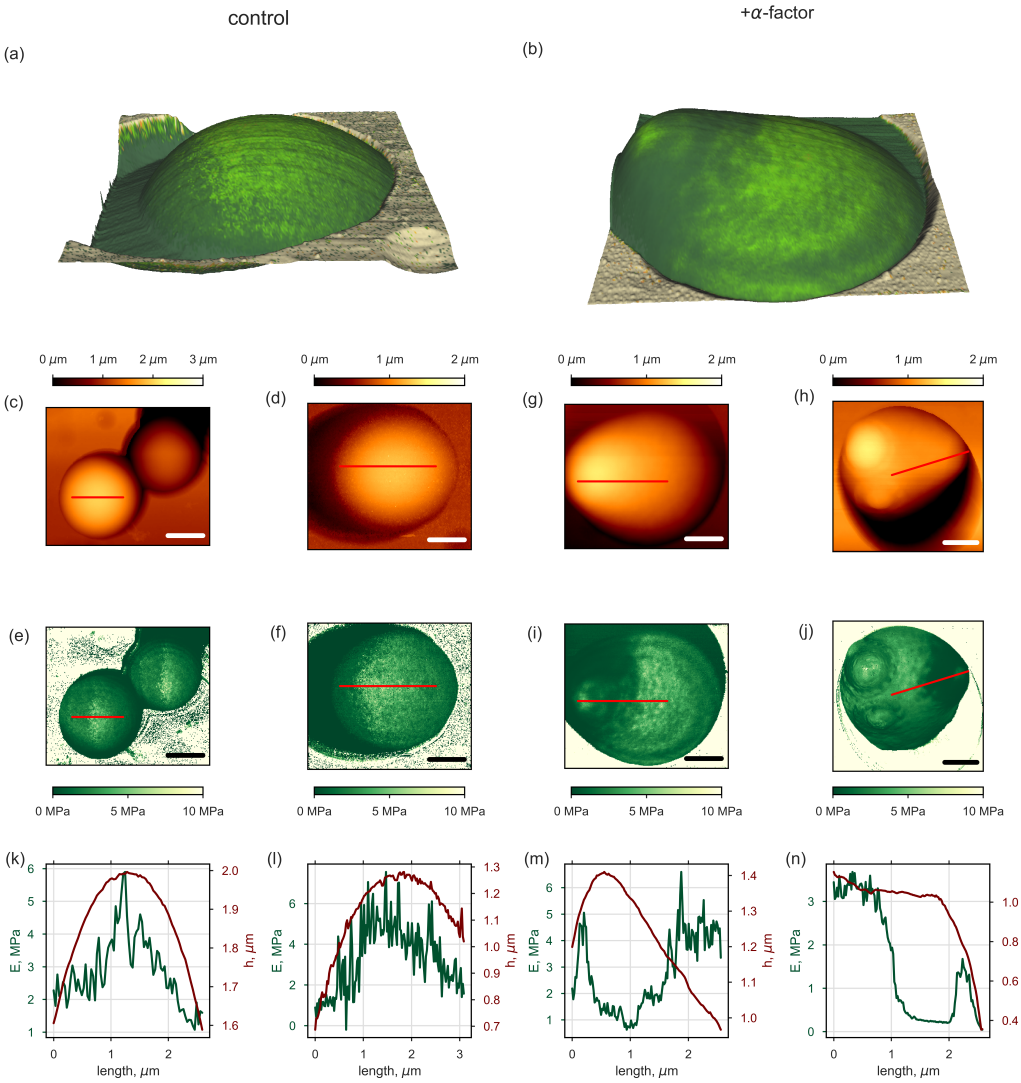

Fig. 5.7.: Cell wall elasticity is reduced in protrusion region, except for the very tip. Height and elasticity of MATa Δbar1 cells, not treated and treated with $1\,\mu\mathrm{m}$ α-factor (left panels and right panels), were provided by AFM-based nano-indentation measurements. (a),(b) 3D-representations of trapped cells shown in (d) and (h) with elasticity map overlay. Height and corresponding elasticity maps are shown in (c,d,g,h) and (e,f,i,j), white or black scale-bar represents $1\,\mu\mathrm{m}$. Profile comparison of cell wall elasticity and height of the indicated cross sections (red lines) are shown in (k,l,m,n).

aforementioned artificially low YM-values at the cell edges only values from flat areas ($2.5 \times 10^{-1}\,\mu\mathrm{m}^2$ to $4 \times 10^{-1}\,\mu\mathrm{m}^2$) at the top of the cells were considered for calculation of the mean YM-values. Due to the steep YM gradient at the neck, averaging over the corresponding YM-values would be meaningless. Thus, this regions were neglected in the analysis. Under the restriction of minimal height gradients, regions for tip, shaft and base shown in Fig. 5.8(a) were assigned by eye, based on the corresponding topographic images and general knowledge of the shmoo shape derived from microscopic images by.

Systematic analysis of the described regions from seven MATa bar1Δ cells with recognizable mating projection revealed that, despite strong cell-to-cell variations of YM (Fig. 5.8(b)), the elasticity pattern, with stiff base, soft shaft and stiff tip, was common to all observed cells, as can be seen in Fig. 5.8(c). In detail, the YM (median(IQR)) at the base with $2.98\ (1.67\text{–}3.30)\ \mathrm{MPa}$ was comparable to the YM obtained from untreated cells with $2.77\ (2.33\text{–}3.30)\ \mathrm{MPa}$, indicating that cell wall rearrangement and synthesis are confined to the mating projection and do not affect the rest of the cell wall. YM-values of shaft and tip, with $0.38\ (0.27\text{–}1.12)\ \mathrm{MPa}$ and $0.90\ (0.68\text{–}2.30)\ \mathrm{MPa}$, were considerably lower compared to the base. Note that YM-values at the tip might be underestimated, since the extend to which the YM was increased at this region was limited. All YM-values are listed in Tab. 5.1. Due to the high cell-to-cell variation, the differences in YM between tip, shaft and base were not significant with respect to analysis of the variance. Nevertheless, when taking into account that the YM-values are paired, these differences between the regions became significant (Friedman test $p < 0.01$).

Tab. 5.1.: Cell wall elasticity pattern of a shmooing yeast cell.

position	**N**	**Young's modulus,** E **median(IQR)**
base	7	$2.98\ (1.67\text{–}3.30)\ \mathrm{MPa}$
shaft	7	$0.38\ (0.27\text{–}1.12)\ \mathrm{MPa}$
tip	7	$0.90\ (0.68\text{–}2.30)\ \mathrm{MPa}$
control	12	$2.77\ (2.33\text{–}3.30)\ \mathrm{MPa}$

5.4.1 Temporal Elasticity Pattern

Above, I described the elasticity pattern observed for shmooing *S. cerevisiae* cells that was so far neither reported for other parts of the yeast morphogenesis nor for other organisms. To further investigate the development of the mating projection, particularly the morphogenic switch between ellipsoidal and shmoo form, I tracked shape and elasticity of α-factor treated MATa bar1Δ cells (N=3, in form of height

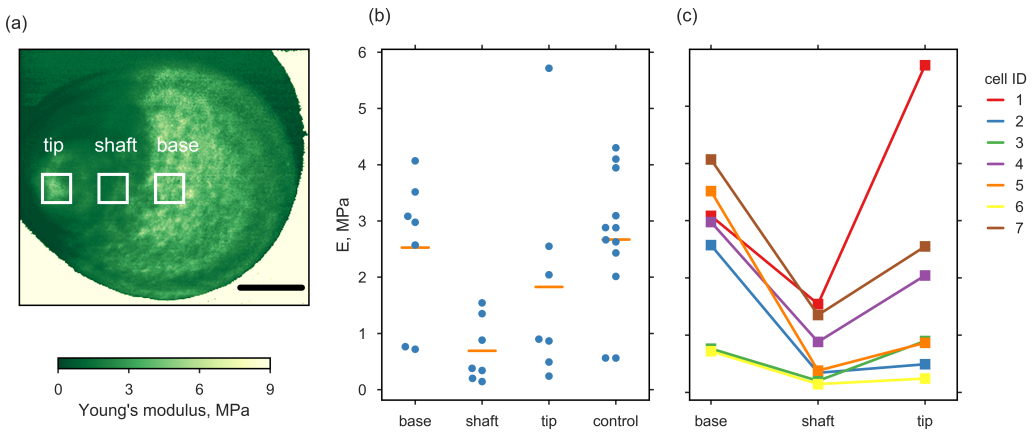

Fig. 5.8.: Cell wall elasticity pattern is conserved despite high cell to cell variations. (a) To compare individual elasticity patterns, three distinct regions were analyzed representing tip, shaft and base of the shmooing cell. (b) Mean E-values from the selected regions for tip, shaft and base of shmooing cells (N=7) and from comparable sized regions of non-treated cells (N=12), the line represents the overall mean of each region. ANOVA revealed no significant differences between populational mean YMs of the selected regions. (c) Elasticity profile is conserved for individual cells, despite strong variation of measured E-values (Friedmann test, $p < 0.01$).

and YM-maps, over time. The trapped cells were continuously scanned with AFM at optimized scan rate ($\approx 3.5\,\mathrm{s/line}$), providing complete height and YM maps every $12\,\mathrm{min}$ to $15\,\mathrm{min}$. The number of complete time series was limited mainly due to two reason: First, the identification of a suitable cell had to be completed before formation of the mating projection started. Here, "suitable" refers to the vertical position in the filter hole as defined in Sec. 2.2.3. Second, cells tended to escape from the filter holes during the measurement, which, on the one hand, underscored the gentleness of the trapping procedure but, on the other hand, complicated continuous scanning.

The expansion of the mating projection influenced the measurements. The projection was generally tilted with respect to the filter surface and its surface was more curved then the surface of the base. Hence, the accessible surface diverged increasingly from an optimal flat surface, which increased the uncertainty of the measured YM with elongation of the protrusion. The elongation of the protrusion was additionally linked to an increased occurrence of measurement artifacts, such as doubling of objects in the image or "shadows" in the proximity of high objects, indicated by white arrows in Fig. A.13. Hence, a quantitative analysis of YM over time was not performed. Nevertheless, qualitative analysis of the temporal resolved YM pattern provided remarkable insights on mating morphogenesis.

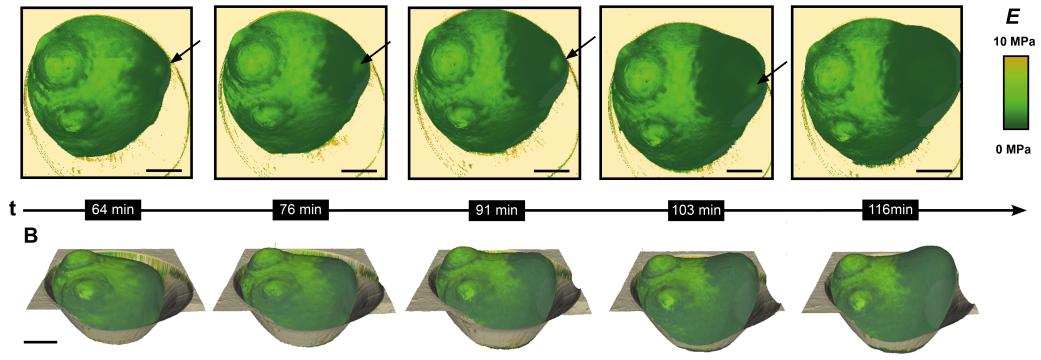

Fig. 5.9.: Temporal evolution of the cell wall elasticity profile during shmoo formation
Time series of YM-maps and 3D representations of a single trapped MATa bar1Δ cell, obtained from continuous scanning. First image was acquired $64\,\mathrm{min}$ after start with α-factor treatment. Regions of stiff material at the protrusion tip are indicated by black arrows. Scale bar is $1\,\mu\mathrm{m}$. Two additional time series are shown in Fig. A.13

Cell wall softening was the first indication of shmoo formation. Softer cell wall material, as described in Sec. 5.4, was also found for early stages of shmoo formation. Particularly, a circular region with reduced YM (Fig. A.13) was observed before a protrusion could be detected in the height maps. This circular region of softer cell wall material fascinatingly marked the origin of evolving mating projection and extended with increasing shmoo neck, while the rest of the cell wall remained unaltered. The boundaries between soft and stiff cell wall material appeared frayed at the beginning but became smooth over time, although the drop of YM from stiff to soft remained abruptly. During elongation of the mating projection no subsequent stiffening of the cell wall material could be observed. The region of low YM-values extended over the whole protrusion, except for the tip. Cell wall material at the tip was not reduced throughout the elongation process and even in the earliest stages of shmoo formation, a single spot of stiffer material has been observed (Fig. 5.9 and Fig. A.13). Since integration of new cell wall material is focused to the tip of the mating projection, as discussed in the beginning, the stiffer material at the tip is supposedly newly generated cell wall. Furthermore, the softer material at the shaft has, therefore, to result from subsequent modification of the cell wall most likely by one or more of the secreted putative-glucanases: Scw4, Scw10 and Scw11 (Cappellaro *et al.*, 1998; Huberman & Murray, 2014). Both Scw10 and Scw11 are regulated by Ste12, the transcription factor for the mating specific genes, and disruption of those genes reduces the mating deficiency significantly. Although Scw4, a paralog of Scw10 resulting from a whole genome duplication, seemed to be not regulated by Ste12, double disruption of Scw4Δ Scw10Δ shows increased mating deficiency compared to the single disruptions.

In summary, the observed elasticity pattern indicates that mechanical properties of the cell wall are not regulated during initial cell wall synthesis but rather through subsequent modifications. To resolve the initial dynamic of the cell wall elasticity in more detail, an improved temporal resolution of the multi-parametric imaging is required. Such an increased temporal resolution can, on the one hand, be achieved by increasing the scanning rate through utilization of soft, ultra high frequency cantilever such as the AC-10EGS from Olympus (Japan) or the USC-F1.2-k0.15 from Nano World AG (Switzerland). On the other hand, simultaneous scanning with different cantilevers, e.g. by taking advantage of multi cantilever arrays (Volden *et al.*, 2004), would also increase temporal resolution. Although this technique is not yet used, it is conceivable considering the technical advances in AFM during the last decades.

5.5 Dynamic cell wall model for shmoo formation

Time resolved multi-parametric imaging of shmooing cells provided qualitative insights on formation and dynamics of the cell wall elasticity pattern. Furthermore, it allowed to relate elasticity pattern and its dynamics with cell shape and formation of the mating projection. With protrusion begin, a small area of the cell wall is softened at the origin of this protrusion and extends with expansion of the mating projection until it covers the whole neck region. However, softening of this area was incomplete: in the center of that area remained a single spot of stiffer cell wall material, which marked the tip of the nascent mating projection at any time. In contrast, the cell wall at the projection shaft was softer everywhere and showed no additional domain of stiffer material.

Capturing these dynamics in local elasticity and shape as well as exploring potential implications was beyond the scope of the SM. We therefore formulated a DM able to describe the evolution of the cell shape during mating morphogenesis without previous knowledge on the development of deformation state. More precisely, only the initial deformation state of the sphere is required and the deformation evolution results from the model.

In the following, I will outline the derivation of the DM to the extend required for understanding of its key findings and implications. For a detailed derivation of the DM and its variations please see Giese (2016) or Goldenbogen *et al.* (2016). To follow mating morphogenesis from a sphere to the typical shmoo, the DM utilizes triangular surface meshes as representations for the cell wall, as depicted in Fig. 5.10.

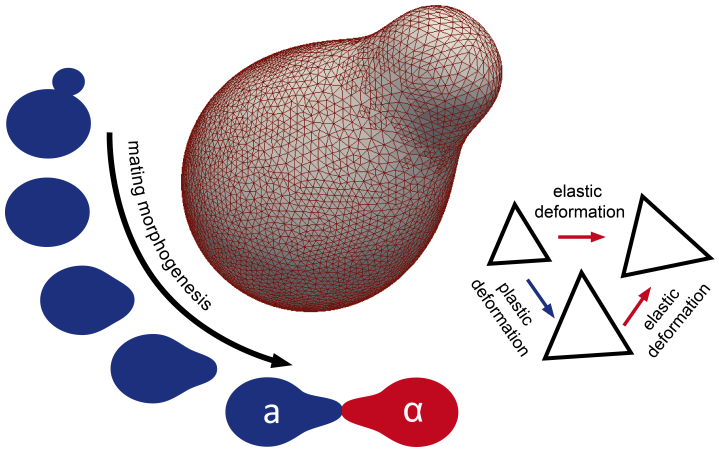

Fig. 5.10.: Simulating mating morphogenesis with mechanically-responsive triangular meshes.

Each of these triangles is allowed to deform plastically or elastically (Delingette, 2008), according to the plane strains and in-plane stresses exerted on it. These in-plane stresses caused by the turgor pressure that constantly acts on each surface element.

Utilizing sufficiently fine surface meshes bears two major advantages: on the one hand, it allowed to describe curved shapes without any restriction on symmetry and, on the other hand, it includes the possibility to subdivide the surface into domains with varying properties. The latter was of particular interest, as it allowed to apply the observed elasticity profile onto the modeled surface (Ω) by assigning particular YM-values to each mesh element. In this manner, spatial inhomogeneities were additionally considered for the cell wall plasticity $\phi(\boldsymbol{x})$ and can in principle be extended to other model parameters, such as the cell wall thickness.

The model started from a spherical shell with a homogeneously distributed YM with $E(\boldsymbol{x}) = 2.5\,\mathrm{MPa}, \forall \boldsymbol{x} \in \Omega$, as obtained for untreated cells. The observed reduction in YM at the origin of the emerging mating projection after α-factor induction was modeled by reducing the YM to $0.7\,\mathrm{MPa}$ in a circular area with radius r. To reflect the observed expansion of that area during elongation of the mating projection, r converged over time to the maximal neck radius r_n with $r = r_n(1 - \exp^{-t/\tau})$, where the time τ was arbitrarily set to $200\,\mathrm{s}$. Stiffer cell wall material at the tip was modeled by setting $E = 1.8\,\mathrm{MPa}$ for all mesh elements with a maximal distance of $0.4\,\mu\mathrm{m}$ to the center of that area of reduced YM. All model parameters are listed in Tab. 3.1. If no plasticity was considered, i.e. no growth, local reduction of YM led only to minor shape variations, where the shape resembled an egg as shown

in Fig 5.11(e). Elastic expansion is therefore not sufficient to generate the typical shmoo shape and cell growth has to be considered in addition.

The nascent fungal cell wall is supposed to expand plastically according to Ruiz-Herrera (2012). Hence, the cell expansion was modeled as irreversible, i.e. plastic, cell wall expansion upon a given yield criterium, caused by increased stresses σ in the cell wall, analogous to the concept used for the SCGM. Two yield criteria were considered: yield stress σ_{Y} (DM1) and yield strain ε_{Y} (DM2). Both conditions are synonymous under the restrain of homogeneous elasticity. Nevertheless, to allow for polarized growth of a mating projection this approach has to be adapted. The directed growth was reflected by restricting plastic expansion to the tip of the mating projection, which is in agreement with the current state of research that considers material insertion to be confined to the tip, as discussed above.

In the dynamic model 1 (DM1), we modelled cell growth as plastic cell wall expansion upon a yield limit following the concept of Lockhart (1965). In addition, the reported bell-shaped distribution of polarization markers around the tip (McClure *et al.*, 2015) motivated the used the distance relation of the extensibility, in which the extensibility ϕ of a given surface element at the position $\boldsymbol{x}$ scales with the distance to the center of the tip at $\boldsymbol{x}_{\mathrm{tip}}$ by

$$\phi(\boldsymbol{x}) = \lambda \cdot e^{\frac{-|(\boldsymbol{x}-\boldsymbol{x}_{\mathrm{tip}})|^2}{2\,R^2_{\mathrm{growth}}}}. \tag{5.2}$$

Here, λ is the positional independent extensibility coefficient and R_{growth} is a measure of the size of the growth zone. Although globally inhomogeneous the plasticity was assumed to be homogeneous and isometric for each triangular mesh element, where the expansion rate α or α^* scaled either with the von Mises stress σ_{VM} (DM1) or the volumetric strain ε_{V} (DM2) depending on the yield criterium,

$$\alpha(\boldsymbol{x}) = \phi(\boldsymbol{x}) \cdot \begin{cases} (\sigma_{\mathrm{VM}}(\boldsymbol{x}) - \sigma_{\mathrm{Y}}), & \text{if} \quad \sigma_{\mathrm{VM}}(\boldsymbol{x}) \gg \sigma_{\mathrm{Y}} \\ 0, & \text{otherwise} \end{cases} \tag{5.3}$$

$$\alpha^*(\boldsymbol{x}) = \phi^*(\boldsymbol{x}) \cdot \begin{cases} (\varepsilon_{\mathrm{V}}(\boldsymbol{x}) - \varepsilon_{\mathrm{Y}}), & \text{if} \quad \varepsilon_{\mathrm{V}}(\boldsymbol{x}) \gg \varepsilon_{\mathrm{Y}} \\ 0, & \text{otherwise}, \end{cases} \tag{5.4}$$

where α and α^* have the same units. ϕ^* represents the strain dependent expansibility which is given by $\phi^* = (\lambda^*/\lambda) \cdot \phi$ and, therefore, follows the same spatial pattern. To compare both model variations, the parameters σ_{Y}, ε_{Y}, λ and λ^* were chosen such

that the elongation velocities were similar. Though this does not infer a similarity between the expansion rates ($\alpha \neq \alpha^*$), generally. Both mechanical measures, σ_{VM} and ε_{V}, hereinafter referred to as stresses and strains, are explained in Sec. 2.1.1.

In Fig. 5.11 simulation snapshots of DM1 and DM2 after $1\,\mathrm{h}$ of simulated time are shown, considering both homogeneous and inhomogeneous cell wall elasticity. Additionally, Fig. A.16 displays stress, strain and elasticity profiles along the cell contour from these simulation snapshots of DM1 and DM2. Noticeable, the realistic elasticity pattern led to significantly longer and wider mating projections compared to growth assuming homogeneous elasticity (compare Fig. 5.11 (a) with (b) and (c) with (d)).

Both model variants, DM1 and DM2, can generate the characteristic shmoo shape, taking into account the observed elasticity profile. At mechanical equilibrium, i.e. slow growth rates, the stresses in the wall are solely defined by the shell geometry and, therefore, are comparable between DM1, DM2 and SM, given an identical cell shape. In all models, stresses at the protrusion were reduced compared to the base and enhanced in a belt around the neck. However, considering the observed elasticity profile alters the cell shape and hence the stress profile. For example, the increased stiffness at the tip reduces the local curvature and thus increases stresses at this tip. Further, softer wall material at the shaft led to expansion of the neck width and therefore to a smoother transition between base and shaft, which ultimately resulted in a more diffusive and less pronounced stress belt at the neck. This cellular response is most probably crucial for survival, since cell death is already increased during mating and tensile stress values might reach the critical failure stress of the cell wall (A. E. Smith, Zhang, Thomas, *et al.*, 2000). The challenge of pronounced stress belts is thereby not restricted to single walled cells, as Boudon *et al.* (2015) demonstrated in numerical simulations of the shoot apical meristem.

As long as homogeneous elasticity was assumed the volumetric strain profile followed the stress profile, but when inhomogeneous elasticity was considered both profiles became incongruous. Drastically reduced YM-values lead to massively increased strain values at the neck and at the shaft. In comparison to the stress belt, this belt of enhanced strains is slightly shifted towards the tip. Interestingly, the strain values at the tip remained low, since the increased stress was compensated by high YM-values.

The most striking differences between both yield scenarios, DM1 and DM2, arose from the different impact of the stiffer material at the protrusion tip in each model variant. While the enhanced stiffness and hence increased stresses led to a rather pointed tip geometry and narrow mating projection when yield stress (DM1) was

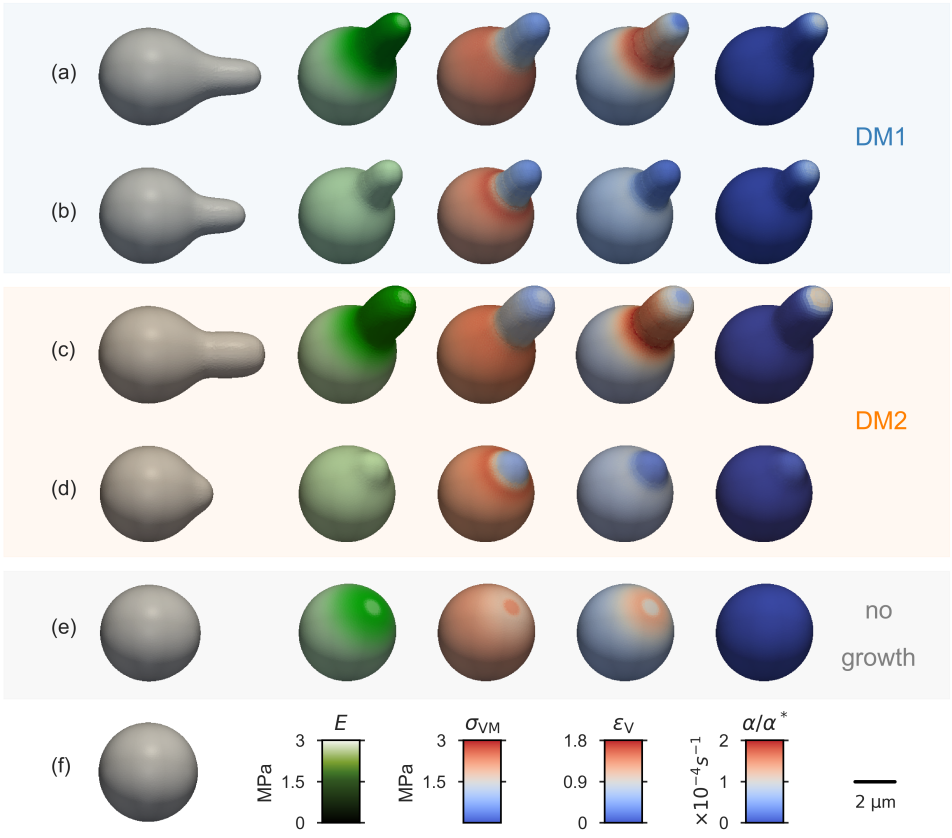

Fig. 5.11.: Impact of the elasticity pattern on growth dynamics. Comparison between simulation snapshots of the yield stress model DM1 (a-b), the yield strain model DM2 (c-d) and a control model (e) with no plastic expansion ($\alpha = 0$, everywhere). In (f) the spherical shape, from which all models started, is shown as reference. Corresponding model parameters are listed in Tab. 3.1. The columns show (from left to right) the observed shape, Young's modulus E, von Mises stress σ_{VM}, volumetric strain ε_{V} and the corresponding expansion rate, α or α^* for each snapshot, taken after $1\,\mathrm{h}$ simulation time. The first (a,c) and the second (b,d) rows of DM1 and DM2 display results of simulations with and without assumed elasticity pattern. Considering the elasticity pattern led to longer and wider mating projections for both models, although the effect was more pronounced for DM2. Stress, strain and elasticity profiles along the cell contour for both model variants are shown in Fig. A.16.

considered, the same elasticity pattern led to a broader tip geometry and consequently wider mating projection, instead, when yield strain (DM2) was considered. The chosen yield criterion, therefore, defined the geometry at the tip and the size of plastic region. Stresses were high at the tip center and decreased with distance to it while strains showed an inversed pattern with minimal values at the center. Further different tip geometries imply different elongation or expansion rates. Under the constrain of equally sized plastic regions, a broader tip requires higher expansion rates compared to a pointed tip in order to achieve comparable elongation rates: $\langle \alpha^* \rangle > \langle \alpha \rangle$, i.e. more cell wall material would be required.

Implication of the yield criteria on the mechanism of the mechanosensor in *S. cerevisiae*

The yield criterion can be perceived as intrinsic property of cell wall structure or as property of the link between the cell wall structure and the cell wall synthesis machinery. Following the second line of thought, plastic expansion, or rather yielding, represents the synthesis and insertion of new cell wall material according to the mechanical state of the cell wall and the characteristics of this link. In *S. cerevisiae* this link is supposed to be realized by two groups of mechanical cell wall sensors, which stimulate the cell wall integrity pathway via activation of the small G-protein Rho1 (Levin, 2005). The first group comprises Wsc1, Wsc2 an Wsc3 while the second group consists of Mid2 and Mtl1. Of particular interest is Mid2, whose primary function is to recognize and signal cell wall stress during mating morphogenesis (Rajavel *et al.*, 1999). Nevertheless, all of this cell wall sensors exhibit similar structures comprising a varying small C-terminal domain, responsible for the signal transmission, a single transmembrane domain for anchorage in the plasma membrane, and periplasmatic ectodomain. The ectodomain can be subdivided into a highly O-mannosylated serine/threonine-rich region (STR) (Philip & Levin, 2001), common to both sensor groups, and a group specific N-terminal head region, containing a serine-rich domain (CRD) in Wsc-type sensors and a conserved N-glycosylated asparagine residue in Mid-type sensors (Jendretzki *et al.*, 2011). The sensor group specific head group represents the second anchor, attached either to the glucan or to cell wall proteins, thereby establishing a connection between cell wall and plasma membrane.

Dupres, Alsteens, *et al.* (2009) reported that Wsc1 behaves as a nanospring and glycosylation is required for its spring properties. O-mannosylation of the STR does presumably result in elongation and stiffening of the polypeptide, which in turn led to the assumption by Rajavel *et al.* (1999) that the STRs act as a rigid probes of the

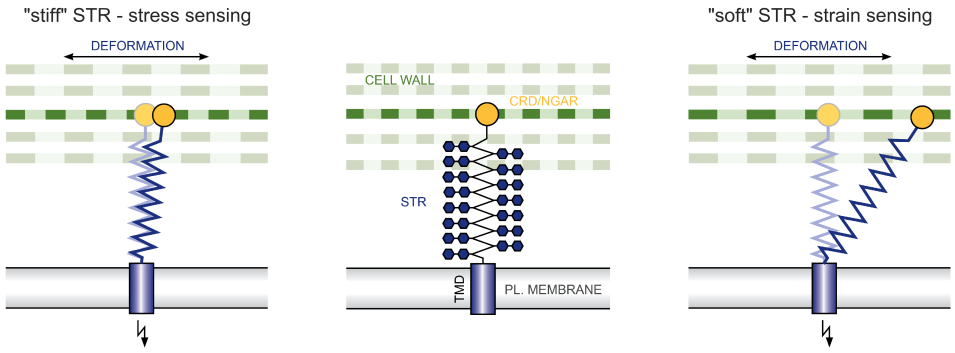

Fig. 5.12.: Proposed distinction between stress and strain sensing. The canonical structure of yeast's cell wall mechano-sensors is shown in the middle panel. A single transmembrane domain (TMD) anchors the sensor to the membrane and either a CRD or a N-glycosylated asparagine residue (NGAR) serves as anchor to the cell wall. A highly O-mannosylated rigid STR, loosely attached to the cell wall, connects both anchors. The hypothesis is that relative stiffness of STR compared to cell wall decides whether a sensor serves rather as strain than as stress sensor. The "soft" STR (right panel) will mirror the deformation of the cell wall and can serves as strain sensor, while a "stiff" STR (left panel) would hinder local cell wall deformation and, therefore, serve as stress sensor. Signal transmission after sensor activation is symbolized by a flash icon.

extracellular matrix. Stretching or compression of a glycosylated STR is supposed to induce conformational changes in the cytoplasmic tail and thereby stimulate signaling through the cell wall integrity pathway, although the direct mechanism is still a mystery (Levin, 2005; Straede & Heinisch, 2007).

Based on the aforementioned findings, I propose that the relative stiffness of the STR with respect to the stiffness of attached wall structure defines whether stresses or strains are sensed by the mechanosensors. An illustration of the concept is depicted in Fig. 5.12. If the STR is soft compared to the attached cell wall, the deflection of the sensor will mirror the displacement of the cell wall and the wall strain can be detected by the sensor. In contrast, if the STR is "stiff" the deformation of the attached cell wall is hindered and the deflection of the STR will reflect wall stress but not strain. The stiffness thereby depends on the dimension of the STR and could be adjusted by the cell via elongation or shortening of this region.

The intrinsic stiffness of the mechanosensor can be related to the two DM variants considering the elasticity profile. The DM1 based on the yield stress criterium, corresponding to a stiffer STR. As discussed above, the stresses were drastically reduced at the protrusion compared to the base, particularly at the tip, which could not been compensated by an increase in stress due to the higher YM-values at the tip. Elongation of the protrusion would, therefore, require lower σ_Y-values than

expansion of the spherical part, the base. Assuming that σ_{Y}-values are intrinsic properties of the mechanosensors, the varying wall stresses could explain the variety of different mechanosensors in *S. cerevisiae*, particularly the necessity of Mid2 during mating morphogenesis.

In contrast, if mechanosensors represent a yield strain criterium, as considered in DM2, the sensors could operate at a wider range of cell wall stresses. The strains differed not as drastically, compared to the stresses and, furthermore, modifications of the local cell wall elasticity had a stronger impact on the local cell wall strain. Hence, altering the local cell wall elasticity would provide a tool for the cell to equalize local strain, thus allowing the cell to reuse the same mechanosensor for different phases in morphogenesis. Further analysis of the mechanical properties of the STRs with respect to local stiffness of cell wall material the mechanosensor is attached to would help to determine the prevalent yield criterion. Moreover, such an analysis could provide a deeper understanding of the growth processes at the molecular level.

5.6 Assessment of Local Cell Wall Strain Profiles for Shmooing Cells

Estimations on the plane strains present in the cell walls of shmoo shaped cells were gained as results from simulation of the DM, although an estimate on the strain of the initial state was necessary, in addition.

To experimentally verify the cell wall strains predicted by the DMs, shmooing yeast cells were exposed to high external osmolyte concentration. The idea behind the experiments, illustrated in Fig. 5.13(d), is that a yeast cell falls back to its relaxed shape, when the osmotic pressure difference rapidly vanishes. The experiment allows for comparison of the expanded and relaxed shapes and hence provides estimates of the corresponding strains. The approach is supported by reports of Arnold & Lacy (1977) and Asami *et al.* (1977), that stated that plasmolysis, i.e. the detachment of the plasma membrane from the cell wall, occurs in yeast at external osmolarities of $1.15\,\mathrm{osmol/kg}$ or higher. Without forces exerted from the membrane onto the cell wall, the cell wall inevitably falls back to its relaxed state. The experimental procedure was adapted from reported protocols (Misra *et al.*, 2013; Bonazzi *et al.*, 2014; Atilgan *et al.*, 2015) and is described in detail in Sec. 2.2.2.

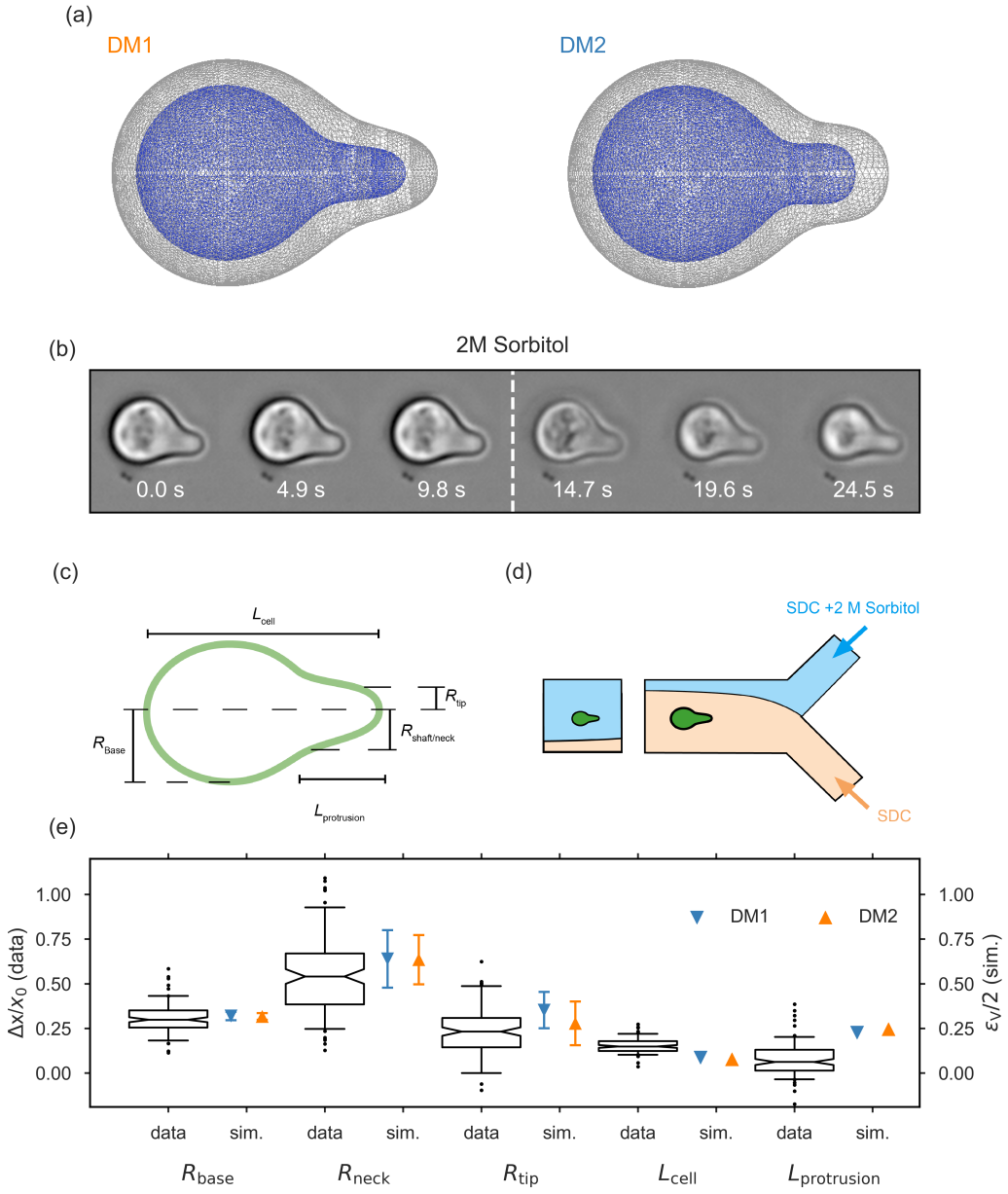

Fig. 5.13.: Osmotic experiments confirmed strain profiles predicted by the DMs. (a) Relaxed (blue) and expanded (gray) cell shape according to the yield condition: yield stress (DM1) and yield strain (DM2). (b) Exemplary bright-field time series of a shmooing MATa bar1Δ cell. Images were taken every $4.9\,\mathrm{s}$. After $10\,\mathrm{s}$ extracellular osmolyte concentration was increased by $2\,\mathrm{M}$ Sorbitol. (c) Dimensions considered for analysis: length of longest cell axis L_{cell}, protrusion length $L_{\mathrm{protrusion}}$ and radii of base, neck and tip (R_{base}, R_{neck}, R_{tip}). (d) Illustration of the MFD experiment: rapid switch from normal to high osmotic medium (SD medium to SD medium + $2\,\mathrm{M}$, from right to left) through adjustable pressure differences between the inlets. (e) Comparison of measured (data) and predicted (sim.) strain profiles (Fig A.16). Box-plots show relative deformation of each considered dimension ($(x - x_0)/x_0$) obtained from microscopic images (N=119) while color triangles represent the predicted half volumetric strain $\epsilon_v/2$ (mean ± SD) evaluated at corresponding regions by DM1 and DM2.

To this end, shmooing MATa bar1Δ cells were monitored with brightfield-microscopy, while rapidly exchanging the external medium from normal (SD medium) to high osmolarity (SD medium+$2\,\mathrm{M}$ sorbitol), utilizing a pressure controlled MFD. A rapid exchange was crucial to minimize the error arising from adaptation processes to the high external osmolyte concentration. Form time series during Sorbitol treatment, the expanded and relaxed shapes of 119 cells were obtained and manually analyzed with respect to the cell dimension of interest. Images taken $25\,\mathrm{s}$ to $35\,\mathrm{s}$ after Sorbitol treatment were used for analysis of the relaxed cell shape, as it was the time necessary for cells to reach minimum cell dimensions. As cell dimensions of interest I considered the radii of base, neck and tip (R_{base}, R_{neck}, R_{tip}), as well as cell and protrusion length (L_{cell}, $L_{\mathrm{protrusion}}$). For all dimensions of interest the relative expansion $\Delta x/x_0 = (x_1 - x_0)/x_0$ was determined and compared with the half volumetric strain $\varepsilon_{\mathrm{V}}/2$ predicted by the DMs. R_{base}, R_{neck}, R_{tip} were obtained from strain profiles along the cell contour shown in Fig. A.16, while L_{cell} was the maximal extension and $L_{\mathrm{protrusion}}$ was L_{cell} reduced by the base diameter, $L_{\mathrm{protrusion}} = L_{\mathrm{cell}} - 2R_{\mathrm{base}}$. Note that $\varepsilon_{\mathrm{V}}/2$ equals the principle strain $\varepsilon_\theta = \Delta r/r_0$ only if the shell geometry is spherical, e.g. at the base or tip. At the neck $\varepsilon_{\mathrm{V}}/2$ represents a lower estimate of ε_θ.

The resulting experimentally determined strain profiles and values were essentially consistent with the prediction of the DM as shown in Fig. 5.13(e). The measured strain profiles (low-high-low) mirrored the observed YM-profiles inversely from base to tip. The measured circumferential strains (mean $\pm$ SD, N=119) at base and tip were with 0.30 ± 0.08 and 0.23 ± 0.14 similar to each other and significantly lower than strain values at the neck 0.55 ± 0.21 (non-parametric Friedmann test, $p < 0.001$). The predicted half volumetric strains $\varepsilon_{\mathrm{V}}/2$ by both model variations (DM1, DM2) at base (0.32 ± 0.02, 0.32 ± 0.02), neck (0.64 ± 0.14, 0.64 ± 0.16) and tip (0.26 ± 0.12, 0.35 ± 0.10) were comparable to each another and slightly higher than the measured strains. Both experiment and model showed that the neck is most strained with over $50\,\%$ length gain during elastic expansion. To prevent material failure of the cell wall at the neck and consequent loss of cell integrity, cells might reinforce this region with localized chitin deposition as reported by Schekman & Brawley (1979). Interestingly, the longest axis and the protrusion length showed, in experiment and model, only a slight or no relative expansion with 0.15 ± 0.04 and 0.08 ± 0.09.

The experimentally determined strains furthermore allowed me to reassess the measured cell wall elasticity. Although estimations of the YM from the strain state for arbitrary geometries are difficult, the spherical base part provided the opportunity for a convenient simplification. Assuming a turgor pressure of $0.2\,\mathrm{MPa}$ and a cell

wall thickness of $115\,\mathrm{nm}$ the YM of the cell wall at the base was estimated to be $(2.58 \pm 0.80)\,\mathrm{MPa}$, which was strikingly similar to measured YM-values with $(2.67 \pm 1.20)\,\mathrm{MPa}$ from AFM-experiments.

5.7 Discussion on Mating Morphogenesis

In order, on the one hand, to investigate shmoo formation during mating morphogenesis in the context of cell wall mechanics, and on the other hand, to find similarities and differences between two polarized-growth modes of *S. cerevisiae*, a combined theoretical and experimental approach was taken. Particularly interesting is the switch from isotropic to directed growth during mating morphogenesis. The approach started with an assessment of the mechanical equilibrium between turgor pressure and elastic cell wall expansion using a mathematical model (SM). This SM predicted that a local softening of the cell wall material at the site of protrusion is required to generate the classical shmoo shape. The prediction could be confirmed by experimental information on the cell wall elasticity of single and living *S. cerevisiae* cells during the formation of the mating projection, reconstructed from time series of height and elasticity maps acquired by nano-indentation experiments of the accessible cell wall. The investigations revealed a characteristic cell wall elasticity pattern for a shmooing cell, comprising a softer or more elastic material at the protrusion and a spot of stiffer material at the tip of the mating projection. The elasticity pattern was observable already at early stages of the shmoo formation, indicating that cell wall modification might be a prerequisite for protrusion or elongation of the mating projection. To shed light on the dynamics of the formation process of the mating projection, computational cell wall models (DM1 and DM2) have been formulated and simulated. The models were further used to examine the influence of different yield conditions on the plastic cell wall expansion. In addition, the DMs provided estimations on the plane strain in the cell wall, i.e. of the deformation state, which were confirmed in osmo-shock experiments.

Elasticty Pattern

The described elasticity pattern of the cell wall based on three main observations from nano-indentation experiments on the cell walls of living, shmooing yeast cells:

1. The YM was locally and extensively reduced at the shaft of the emerging mating projection.
2. The cell wall material in a confined spot-like region at the presumed tip of the mating projection was stiffer then the surrounding material.
3. The cell wall elasticity of the non-protruding part of the shmoo remained constant and homogeneously distributed.

Soft Shaft

The most prominent effect was the reduced, local YM at the protrusion. Interestingly, the reduction of cell wall stiffness started at very early stages of the shmooing process. In fact, reduction of the local Young's modulus was the first indication of an emerging protrusion in AFM measurements. While areas with stiffer cell wall material have been reported in the past, for the first time I discovered a local softening of the yeast cell.

However, a reduction in cellular stiffness during directed growth has been reported for other walled cells, e.g. for plant pollen tubes (Fayant *et al.*, 2010; Zerzour *et al.*, 2009). Although the cellular stiffness not directly reflects the local YM, a similarity becomes apparent. In contrast to yeast mating projections, however, dropped the cellular elastic modulus here gradually from shaft to tip, instead of abruptly. Even simulation of multicellular plant tissues predicted material softening at the site of the emerging protrusion. Hence, a local reduction of the elastic surface modulus seems to be a common growth strategy of single walled cells and tissues when they morphogenetically switch from isotropic to directed growth.

Stiff Tip

The spot of stiffer cell material, at the position of the presumed tip of the mating projection, was particularly observable at early stages of the shmoo formation. Although theoretically discussed (Dumais *et al.*, 2006), a region of increased stiffness at the tip has been reported neither for fungi nor for plants, yet. Data on the elasticity in proximity of the tip, obtained from micro-indentation experiments, is ambiguous. Both increasing and decreasing stiffness has been reported for decreasing distance to the tip of the pollen tube (Zerzour *et al.*, 2009; Bolduc *et al.*, 2006; Parre & Geitmann, 2005). The uppermost tip, however, could not be accessed with the reported experimental set-ups.

An explanation for the mechanism behind the stiffer tip is provided by Green (1969), who hypothesized that vesicular transport defines stiffness of the cell wall. In particular, the time each vesicle spends to reach its destination is supposed to define the stiffness of that region. The rational behind this is that vesicles are supposed to transport cell wall material as well as lytic enzymes to the cell surface. The more time a vesicle needs to travel, the more time the lytic enzymes have to soften the carried cell wall material. Due to the transport along the focused actin fibres (Slaughter *et al.*, 2009), vesicles reach the polarization site faster. The transported cell wall material, when incorporated into the cell wall, therefore, is supposed to be stiffer at sites of polarizations, e.g. the tip of the mating projection, compared with more distant regions. Contradictory to this theory, however, a locally varying elasticity of the bud cell wall could not be observed (see Sec. 3.3) despite actin fibers focused to the bud (Slaughter *et al.*, 2009). Furthermore, according to the current state of research, main cell wall polysaccharides, such as β-1,3-glucan or chitin, are assembled directly at the cytoplasmic membrane from cytosolic UDP-Glc or UDP-GlcNac (Lesage & Bussey, 2006; Orlean, 2012) and modified in the periplasmic space or in the cell wall. Hence, the transport routes of cell wall building blocks and vesicular enzymes are presumably separated.

Unaltered Base

The base part of the shmoo remained unaltered throughout shmoo formation. Neither mean values nor distribution of the cell wall elasticity changed during shmoo formation. Measured YM-values (mean $\pm$ SD) of the cell wall from α-factor-induced and non-induced cells were with $(2.53 \pm 1.30)\,\mathrm{MPa}$ and $(2.67 \pm 1.20)\,\mathrm{MPa}$ similar to each other and comparable to reported values of $(1.62 \pm 0.22)\,\mathrm{MPa}$ (Dague *et al.*, 2010). These YM-values, however, differ significantly from YM-values estimated from whole cell compression experiments (A. E. Smith, Moxham, *et al.*, 1998). The YM was homogeneously distributed at the base, except for sites of previous budding events (Pillet *et al.*, 2014; Formosa *et al.*, 2013).

Resemblance to Spore Germination

The shmoo shape is reminiscent of early stages of spore germination of other ascomycetes, such as *Aspergillus niger* (Leeuwen *et al.*, 2013). This is not surprising, since shmooing is closely related to germination and shows characteristics of its process. Yeast mating requires a spore germination and can follow it very fast. Shmooing of the haploid spores can occur even before the first cell cycle is completed.

Furthermore, Joseph-Strauss *et al.* (2007) showed that mating genes are induced during spore germination. Of particular interest is Sph1, a protein expressed early in spore germination but also involved in shmoo formation as it localizes to the sites of polarized growth (Arkowitz & Lowe, 1997). The observed cell wall elasticity pattern of shmooing yeast cells adds another similarity between the two processes, since outgrow of the spores is associated with the localized digestion of the electron-dense outer spore wall (Kono *et al.*, 2005; Kreger-Van Rij, 1978). This outer spore wall layer consists of chitosan and dityrosine and is more robust and supposedly also stiffer than the inner spore wall layer, whose composition is similar to that of the vegetative cell wall (Lesage & Bussey, 2006). A localized digestion or breaking of the outer spore wall layer, thus, implies a localized softening of the surface material and, therefore, resembles aspects of the observed elasticity pattern during shmoo formation. This was reflected by Bonazzi *et al.* (2014) in their study on symmetry break in spore germination of *Schizosaccharomyces pombe*, when they considered a locally reduced elastic modulus at the site of outgrowth.

Notable differences between spore germination and shmooing lay, apart from the chemotropic character of shmooing, in the growth pattern. In *S. cerevisiae* germination instead of being focused, growth is evenly distributed over the whole protrusion surface. Moreover, the growth region exhibits no remnants of the outer spore wall layer, i.e. no regions of enhanced stiffness, as I've found at the tip of the mating projection.

Dynamic Cell Wall Models

Constructing the SM and the DMs enabled us to assess the role of mechanical properties in mating morphogenesis. The SM provided a prediction on the cell wall elasticity pattern for a given shmoo shape based on assumptions of the cell wall thickness, the turgor pressure and the growth pattern. In contrast, considering the same assumptions together with the experimentally-derived, time-resolved cell wall elasticity pattern, the DMs provided estimations on the expansion rate and the deformation state, i.e. the dynamics of the shmoo formation. The DMs showed that the observed elasticity pattern and a sufficiently confined growth region are enough to generate the characteristic shmoo shape. In addition, considering the characteristic elasticity pattern resulted in more elongated cells corresponding to a higher effective growth rate.

Two variants of the DM have been implemented, DM1 and DM2, distinguishable only in the yield condition upon which plastic expansion occurs. For homogeneous

elasticity distribution both yield conditions are synonymous, since strain and stress pattern are congruent in this case. However, if the elasticity is inhomogeneously distributed, both pattern diverge and a comparison of the yield condition became inevitable. Note, that it is sufficient to consider the tip of the mating projection since growth and, concomitantly, yielding is restricted to this area. Under yield strain conditions, the increased stiffness at the tip resulted in a broader and blunter tip with an extended ring-like growth region. This extended growth region eventually led to a wider mating projection, which in turn would require a higher surface expansion rate to provide a longitudinal expansion, equivalent to the longitudinal expansion under yield stress condition.

Further analysis of the DMs revealed possible implication of the yield criteria on structure and function of cell wall mechanosensors in *S. cerevisiae*. There are at least five known cell wall mechanosensors in *S. cerevisiae* which signal the mechanical state of the cell wall to the CWI. However, it is not yet known exactly how the signal is recognized by the sensor and transmitted in they molecule and, furthermore, whether the sensor detects strain or stress of the cell wall. Assuming that the yield criteria are properties of this mechanosensors, three statements can be made. First, the sensor respond in a switch-like manner to a mechanical cue. If the stress or the strain in the cell wall rises above a certain values characteristic for this sensor, this sensor will start to activate the downstream elements of the CWI. The next two statements depend on the sensing mechanism and are mutual exclusive. Second, the variety of existing mechanosensors can be explained if sensors detect the stress in the cell wall, instead of its strain. During morphogenesis the stress in the cell wall can change drastically, in particular if the cell forms a protrusion, as during budding or shmooing. Since the cell wall stress is significantly reduced in such protrusions, plastic expansion of the protrusion upon an yield criterion would require strongly reduced yield limits compared to the required limits for the plastic expansion of the spherical part, e.g. during growth of the mother. Third, if its working principle reflects a strain instead of a stress criterion, mechanosensors could work in a broader stress range, i.e. mechanosensors, active during bud or mother expansion, could successfully control wall synthesis during mating morphogenesis. Whether the mechanism of the sensors reflect a yield strain or a yield stress criterion, might depend on the stiffness of its extracellular STR relative to the stiffness of the cell wall it is anchored to. A soft STR would follow precisely the deformation of the cell wall and hence would serve as strain sensor, while a STR that is as stiff as the surrounding cell wall would serve as stress sensor. Nevertheless, it remains to be elucidated if and to which extent these statements are true. So far the DMs cover the first part of the mating morphogenesis: the formation and elongation of the

mating projection. Future models need to additionally address the mechanisms during cell-to-cell contact and zygote formation to gain a complete picture of the mating morphogenesis.

Turgor Pressure

As the main driving force of cell wall expansion, the turgor pressure is crucial in every mechanical growth model, regardless of the particular mode of morphogenesis the model represents. Although, so far a direct measurement of the turgor pressure is not possible in yeast, it has been estimated with a various indirect methods. The resulting estimations, however, stretched over a wide range of values, ranging from $0.05\,\mathrm{MPa}$ to $0.8\,\mathrm{MPa}$. To confine this range further and concomitantly obtain estimates of the turgor pressure for the same yeast strain, as I have used in the other experiments, I performed strong indentation experiment. Considering additionally the findings on indentation experiments on elastic pressurized shells by (Vella *et al.*, 2012), I estimated the turgor pressure to be $\Pi \sim 0.2$, which is at the lower end of the range of reported values. Interestingly the estimated value matches the reported mean turgor pressure of the pollen tubes of *Lilium longiflorum* obtained by direct measurements. More importantly, however, are calculations on the role of actin polymerization during clathrin-mediated endocytosis in yeast by Tweten *et al.* (2017). To overcome the turgor pressure the invagination of membrane is supported by the polymerization of actin. The calculations revealed that the force generated by actin is not high enough to overcome a turgor pressure of $\Pi = 0.5\,\mathrm{MPa}$ but is sufficient to facilitate endocytosis for $\Pi = 0.2\,\mathrm{MPa}$ (Tweten *et al.*, 2017). This indicates that here measured turgor pressure is more likely to be accurate.

Assessment of the Mechanical Cell Wall Strain

The DMs provided, among others, estimations on the development of volumetric strain, i.e. the time-resolved deformation states of the cell wall. To further challenge the models, their predictions on volumetric strain were tested against estimates from osmo-shock experiments. The experimentally observed and theoretically estimated profiles of the mechanical cell wall strain were in large parts congruent. Note, that the experimental estimates for the strain values were at the lower limit and could be twice as high.

Simulations of the DMs and osmo-shock experiments revealed a belt of maximal mechanical cell wall strain at the neck of mating projections. In this region, the

wall strain would reach critical values of material failure first, which would endanger cellular integrity. The reason for the reported chitin deposition at the neck (Schekman & Brawley, 1979) might be to counteract this threat of bursting by locally increasing cell wall stability and thus preventing cell lysis.

To assess the cell wall strain, the distance to the axis of symmetry was manually determined at three characteristic positions of the cellular contour, at the base, neck and tip. The volumetric strain was calculated from the determined radii and under assumption of a spherical expansion.

To improve estimation and resolution of the cell wall strain from microscopic bright-field images during osmo-shock, advanced algorithms for cell shape recognition, quantification and assignment are required. A first step in this direction is the identification and quantification of average shapes, as done by (Hemmen, 2017) in her master thesis. On the other hand embedding and tracking fluorescent agents (Helmke *et al.*, 2003; Jones *et al.*, 2015; Aydin *et al.*, 2016) or applying texture correlation (Gilchrist *et al.*, 2007) might also help to improve the experimental estimations on the mechanical cell wall strain.

Remarks on the Mechanical Feed Back Model

In a recent study, Banavar *et al.* (2018) investigated cell wall expansion and assembly in yeast mating morphogenesis using a comparable theoretical approach with common assumptions. The wall was considered as an axis-symmetrical, pressurized shell, whose expansion is driven by the turgor pressure and whose mechanical properties are inhomogeneously distributed. However, their approach deviates from our approach in a number of aspects.

First, they focused on the elongation of the mating tip and neglected the transition from spherical to tip growth as well as the geometry of the protrusion neck. Second, they considered only viscous contribution of the mechanical cell wall properties. In addition, they stated with respect to the observed elasticity pattern that: “the combination of the observed inhomogeneous stiffness of the cell wall during mating projection growth (Goldenbogen *et al.*, 2016) and cell wall remodeling can be theoretically described as an effective inhomogeneous viscosity at timescales longer than cell wall remodeling . . . ”. This approach is in several ways problematic. On the one hand, it is bound to long time scales and, therefore, cannot replicate changes in cell shape due to rapid changes in osmotic conditions. On the other hand, it neglects the influence of the elasticity on the cell shape and, concomitantly, on the growth zone, as can be seen in the comparison between DM1 and DM2. Hence,

the approach masks the underlying mechanistic principles, and thereby reduces the predictive power of the model. A third deviating aspect was that the cell wall thickness was not assumed to be constant but allowed to become thinner or thicker, according to the current material flow or the present rate of cell wall synthesis, which already touches on the fourth aspect. The fourth and most noticeable aspect, deviating from our approach, concerned the coupling of the cell wall synthesis to cell wall expansion via a mechanical feedback mechanism.

The feedback is supposed to be realized by the CWI, which signals, as described in Sec. 5.5, the mechanical state of the cell wall to the cell synthesis machinery. During mating the cell wall mechanosensors Wsc1 and Mid2 are supposed to increasingly activate membrane-localized cell wall synthases Fks1/2 upon faster cell wall expansion. Interestingly and conveniently, they considered the expansion or strain rate rather than the stress or the strain to be sensed by the mechanosensors of the CWI. Banavar *et al.* (2018) reported that this mechanical feedback counteracts thickening or thinning of the cell wall at the tip and thus ensures sustained growth. Remarkably, the growth of the mating projection is stabilized without affecting cell size or shape.

Nevertheless, despite the shortcomings discussed above, the study provides a remarkable approach to integrate the regulatory machinery of the CWI into a mechanical cell wall model. An integration of the CWI into a future version of the DM might, therefore, provide new insights into the regulation of growth zone and an explanation for the enhanced stiffness at the tip.

6 Conclusion & Outlook

In these thesis, I studied the morphogenesis of yeast and its interplay with and requirements of mechanical properties of the cell wall exemplified by the budding and the mating process. The two investigated polarized growth modes provided insights on the generation of the shape of walled cells, on the expansion process of the cell wall and on the growth dynamics.

Relevance, limitations and implications of the gained results are already discussed in the corresponding chapters. In the following, I will focus on aspects, concerning at least two chapters and put them in a larger context.

6.1 Cell Wall Elasticity & Cell Shape

Investigations on morphologies, occurring in budding and mating, revealed that the local cell wall elasticity governs the cell shape of *S. cerevisiae*. The homogeneously distributed elasticity of mother and bud cell wall, described in Sec. 3.3, reflects the spherical shape of both compartments. Nevertheless, the stable coupling of two spherical compartments requires a rigid link between both. Otherwise the increased stresses at this link region, i.e. the bud neck, would lead to an expansion of this region and concomitantly to an altered shape. Although the rigidity of the bud neck could not be measured directly during bud formation or expansion, it can be inferred from measurements on parts of this structure that remain on the surface of the mother cell after cell separation. In agreement with earlier reports by Touhami *et al.* (2003) these remnants or bud scars exhibited increased YM-values. Furthermore, the reported deposition of the rigid cell-wall component, chitin, supports this conclusion. That cell shape of yeast is governed by the elasticity of its cell wall became even more evident during the investigation of the shmoo formation described in Sec. 5. The prediction of the mechanical SM that yeast cells have to alter their cell wall elasticity locally to adopt the characteristic shmoo shape could be experimentally confirmed with time-resolved multi-parametric imaging. The YM of the cell wall at the shaft of the mating projection was drastically reduced compared to the base. Intriguingly, the measured elasticity pattern revealed that cell wall material directly

at the tip of the mating projection was not altered and showed values similar to those at the non-protruding part of the cell. On the one hand, this enhanced stiffness, compared to the surrounding material, defines the geometry of the tip (Sec. 5.5), on the other hand, this might imply common principles of the growth region. The similarity of the elastic properties between different growth regions, e.g. bud and tip, indicates that new cell material is integrated according to similar processes and any modification to the material is introduced afterwards.

While the mechanism of the bud neck formation and its regulation have been intensively studied in the past (Cabib & Arroyo, 2013), the processes which leading to the observed elasticity pattern during mating morphogenesis remain to a large extent unclear. Further work is required especially to assign the softening of the cell wall at the shaft of the mating projection to particular molecular processes and cell wall components. Nevertheless, recent progress has been made in this research area. For example, Banavar *et al.* (2018) showed that during elongation of the mating projection, a mechanical feedback mechanism can compensate thinning or thickening of the cell wall and, thus, maintain a constant cell wall thickness without interfering with cell size or shape.

Information regarding the cell wall thickness during shmooing is limited. Although electron micrographs revealed only weak variations in cell wall thickness, temporal information is still missing. In all models presented, the cell wall thickness was assumed to be constant, though its variation would have a strong impact on cell shape dynamics. Applying the sub-resolution microscopy approach, which Davì *et al.* (2018) used to monitor cell wall thickness of living *S. pombe*, could provide the necessary information to conclusively resolve this issue.

The gained insights on the relationship between cell wall elasticity and cell shape are most likely not restricted to the two analyzed modes of morphogenesis but applicable to other modes as well. For instance, Spitzenkörper-like structures, characteristic for hyphal growth, have been found at the tip of mating projections (Chapa-Y-Lazo *et al.*, 2011), suggesting common underlying growth principles. This is further supported by a study of Bartnicki-Garcia & Lippman (1972) in which they showed that hyphae predominately burst at the growing tip, indicating a softer cell wall structure in this region similar to my observations on the mating projections of yeast.

In addition, spore germination in *Shizosaccharomyces pombe* displays striking similarities with the formation of mating projection in *S. cerevisiae*. Bonazzi *et al.* (2014) showed that the primary cell wall dissolves locally at the site of outgrowth. The germinating spore resembles the shmoo shape and, moreover, exhibited the observed characteristics of the morphogenic switch from spherical to directed growth, in

particular reduced stiffness at the region of outgrowth. This morphogenic switch is characteristic for fungi, whether during germination, mating or filamentous growth and is particularly important in the case of the pathogenic organism *Candida albicans*, as its virulence has been linked to its ability to switch from budding to filamentous growth (Lo *et al.*, 1997). Insights on the morphogenic switch, therefore, might help to develop strategies against the virulent form of *C. albicans*.

6.2 Plastic Cell Wall Expansion & Cellular Growth

Growth of walled cells is inextricably linked to irreversible, i.e. plastic, expansion of their cell walls. According to Lockhart (1965), this irreversible cell wall expansion can be described as viscoelastic-plastic expansion upon an defined yield criterion, where the expansion depends linearly on the turgor pressure. Although a study on plants suggests that the dependence follows more likely a weak power law (D. J. Cosgrove, 1993), a linear relationship was assumed in all models, since estimations on the exponent were missing for yeast. The yield criteria and their implications will be discussed in the next subsection. Integrating Lockhart's description of plastic cell expansion into the model for the vegetative growth of *S. cerevisiae*, allowed me to investigate the plastic characteristics of mother and bud cell wall during the combined growth of both. Constraining the model with experimental data on the volume development of both compartments provided two main insights on the cell wall extensibility. First, in order to facilitate bud expansion the extensibility of the bud cell wall needs to be at least 100 times higher than that of the mother cell wall. Second, the extensibility of the yeast cell wall is at least two magnitudes higher than reported values for cell walls of plants (J. K. Ortega, 1985; D. J. Cosgrove, 1985), which can be explained by the high growth rates of yeast under optimal conditions. The extensibility is a mechanical property of the cell wall of a living cell and describes the response to high stresses. However, a precise assignment of this property to one or more components of the cell wall or to a process is not yet possible and is subject to current scientific debates (D. J. Cosgrove, 2016). Particularly interesting are observations on isolated cell walls, which show instead of a permanent deformation only a transient viscoelastic extension to an applied stress (Taiz, 1984). This might imply that the extensibility describes rather cell wall synthesis than intermolecular friction or that the yield criterion can not be met, as I will discuss below. Besides Lockhart's viscoelastic-plastic description, the irreversible cell wall expansion can also be described differently. Motivated by my observations on the response of the cell wall to an applied strong and oscillating force, I discussed in Sec. 4.4 the

possibility to describe this process analogous to the deformation of a soft glassy material. The considered mesoscopic model (SGR) by Sollich *et al.* (1997) is based on an ensemble of entities that, when exposed to an external strain rate, can either deform elastically or plastically. Plastic deformation or yielding in the SGR results in an instantaneous loss of the stored elastic energy, which could reflect the insertion of new cell wall components.

Whether the macroscopic, viscoelastic-plastic description by Lockhart and the mesoscopic elasto-plastic model by Sollich can be translated into each other, remains an open question. Although Sollich's SGR needs to be tested thoroughly in the context of cell wall expansion, this new perspective will certainly be helpful in understanding the growth processes of walled cells.

In contrast to yeast, the expansion of plant cell walls has been studied intensively. Many of the conclusions on the cell wall expansion of plant cells, however, are based on the orientation of the microfibrils (Burgert & Fratzl, 2006) and cannot be transferred to fungal cell walls easily, since no preferred horizontal alignment of the yeast glucan chains has been reported. The spherical geometry of the yeast cell is presumably achieved by isotropic growth, which is supported by the random orientation of the glucan chains. In contrast, a preferential orientation of linear cell wall components, such as the microfibrils of plant cells, leads to anisotropic growth (Burgert & Fratzl, 2006).

A crucial concept in models for cell wall expansion in plants is the "loosening" of material in the cell wall prior to the integration of new material. According to Burgert & Fratzl (2006), "loosening" can be regarded as "relaxation of wall stresses since it takes place in a high stress environment", which is accompanied by reduction of turgor pressure and water potential. This, however, depends on the perception of the term "loosening". If "loosening" refers to the plasticity of the cell wall according to Lockhart, as we have implemented it in the SCGM in Sec. 3.1, it has indeed the potential to reduce turgor pressure, though it depends on whether it relates to modifications of the yield criterion or the extensibility. Reducing the yield limit, i.e. the critical turgor pressure, will result in a new mechanical equilibrium, in which the turgor pressure approaches the critical turgor pressure. In contrast, increasing the cell wall extensibility will not lead to a reduced turgor pressure but to a faster equilibration. Furthermore, if "loosening" is perceived as reduction in the elastic modulus, the reduction in turgor is only transient. The stress will be immediately restored when the cell wall reaches its new equilibrium, as I have shown in Sec. 5.5 when simulating the shmoo formation with concomitant cell wall softening.

6.3 Yielding & Yield Criteria

That the cell wall of *S. cerevisiae* responses mainly elastically to an applied stress has been reported previously (A. E. Smith, Zhang, Thomas, *et al.*, 2000; Arfsten *et al.*, 2010; Schaber *et al.*, 2010) and could be verified by me in nano-rheology experiments (Sec. 4). According to all models considered in this thesis, the cell wall does not expand irreversibly, i.e. yields, until a certain yield criterion is reached. Although the yield criteria used in this thesis, Π_c, σ_y, ε_y and E_y appear to be different at first glance, they all refer to the maximum capacity of the cell wall for elastic energy. If the cell wall is stressed beyond this capacity it yields either viscoelastically or spontaneously, as discussed above. Of particular interest is the critical turgor pressure Π_c, used in the SCGM and the cSCGM in Sec. 3.1 as a representation of this capacity, since it implies a strong mutual dependence between osmo-homeostasis and plastic cell wall expansion. Furthermore it reflects a maximum for the tolerable variations of the osmotic pressure gradient from a mechanical point of view.

Regardless of the choice of the yield criterion, the question remains: What is the yield criterion and what are underlying molecular mechanisms? On the one hand, it can be interpreted as mechanical property of the glucan-chitin network, e.g. as the strength of the non-covalent bonds between the glucan and chitin fibrils. This is supported by the fact that in plants the yield threshold is supposed to be defined by the concentration of the individual cell wall components, cellulose and xyloglucan (Veytsman & D. J. Cosgrove, 1998). However, aforementioned experiments on isolated cell walls contradict this hypothesis as they show no permanent deformation when exposed to high stresses (Taiz, 1984). On the other hand, as I pointed out in Sec. 5.5, yield criteria might reflect the activation threshold of cell wall sensors that control cell wall synthesis, e.g. via the CWI (Levin, 2005).

Assuming that the criterion reflects the property of a mechanosensor, it matters how precisely the capacity of the elastic energy is measured by it. Is the strain of or the stress in the glucan-chitin network sensed? Under the assumption of a homogeneously distributed cell wall elasticity, both stress σ_y and strain ε_y yield criteria are interchangeable, i.e. the choice of the criterion has no impact on the growth behavior. If, however, the elasticity varies locally at the site of active growth, as observed in Sec. 5.4, the choice of the yield criterion influences cell shape and growth dynamics as I explained in Sec. 5.5.

The stress in the cell wall depends, apart from the applied pressure and the cell wall thickness on the local curvature of the cell surface. Since the stress scales inversely with the curvature, it is strongly reduced in the cell wall of smaller cells or regions

of protrusion, such as the bud oder the mating projection. One might speculate that the variety of reported mechanosensors indicates that each sensor covers only a range of possible cell wall stresses. With respect to the distinction between stress and strain yield criteria, I speculated in Sec. 5.5 on possible molecular mechanisms of the mechanosensors. In particular, I suggest that the ratio between stiffness of the STR and the surrounding cell wall determines whether the protein detects the strain or the stress.

The concept of the maximum stored energy provides also a possible explanation for the question how enzymes extend and cross-link the glucan-chitin network without having access to a constant biochemical energy pool, e.g. ATP. The stored elastic energy of the cell wall might provide enough energy for the extension and cross-linking of the olysaccharide chains.

Addressing the cell wall mechanics and its relevance for cell morphology and morphogenesis, I found principles that are not necessarily restricted to *S. cerevisiae* but might be common to all fungi or even all walled cells. In conclusion, the present study underlines that this small organism still provides answers and insights to open question in biology, with no end in sight.

Bibliography

Adams, D. J. (2004). „Fungal cell wall chitinases and glucanases.“ *Microbiology (Reading, England)*, **150**(Pt 7): 2029–35.

Aguilar-Uscanga, B. & J. M. François (2003). „A study of the yeast cell wall composition and structure in response to growth conditions and mode of cultivation.“ *Letters in applied microbiology*, **37**(3): 268–74.

Aimanianda, V., C. Clavaud, C. Simenel, T. Fontaine, M. Delepierre & J.-P. Latgé (2009). „Cell wall beta-(1,6)-glucan of Saccharomyces cerevisiae: structural characterization and in situ synthesis.“ *The Journal of biological chemistry*, **284**(20): 13401–12.

Alcaraz, J., L. Buscemi, M. Puig-De-Morales, J. Colchero, A. Baró & D. Navajas (2002). „Correction of Microrheological Measurements of Soft Samples with Atomic Force Microscopy for the Hydrodynamic Drag on the Cantilever“. *Langmuir*, **18**(3): 716–721.

Alcaraz, J., L. Buscemi, M. Grabulosa, X. Trepat, B. Fabry, R. Farré & D. Navajas (2003). „Microrheology of human lung epithelial cells measured by atomic force microscopy.“ *Biophysical journal*, **84**(3): 2071–9.

Alsteens, D., V. Dupres, K. Mc Evoy, L. Wildling, H. J. Gruber & Y. F. Dufrêne (2008). „Structure, cell wall elasticity and polysaccharide properties of living yeast cells, as probed by AFM.“ *Nanotechnology*, **19**(38): 384005.

Alsteens, D., H. Trabelsi, P. Soumillion & Y. F. Dufrêne (2013). „Multiparametric atomic force microscopy imaging of single bacteriophages extruding from living bacteria“. *Nature Communications*, **4**: 4–5.

Altenburg, T., B. Goldenbogen, J. Uhlendorf & E. Klipp (2019). „Osmolyte homeostasis controls single-cell growth rate and maximum cell size of Saccharomyces cerevisiae.“ *(under review)*.

Amir, A. (2014). „Cell size regulation in bacteria.“ *Physical review letters*, **112**(20): 208102. arXiv: 1312.6562.

Amodeo, A. A. & J. M. Skotheim (2016). „Cell-Size Control.“ *Cold Spring Harbor perspectives in biology*, **8**(4): a019083.

Angermann, B. R., F. Klauschen, A. D. Garcia, T. Prustel, F. Zhang, R. N. Germain & M. Meier-Schellersheim (2012). „Computational modeling of cellular signaling processes embedded into dynamic spatial contexts“. *Nature Methods*, **9**(3): 283–289. arXiv: NIHMS150003.

Arfsten, J., S. Leupold, C. Bradtmöller, I. Kampen & A. Kwade (2010). „Atomic force microscopy studies on the nanomechanical properties of Saccharomyces cerevisiae“. *Colloids and Surfaces B: Biointerfaces*, **79**(1): 284–290.

Arkowitz, R. A. & N. Lowe (1997). „A small conserved domain in the yeast Spa2p is necessary and sufficient for its polarized localization“. *Journal of Cell Biology*, **138**(1): 17–36.

Arnold, W. N. & J. S. Lacy (1977). „Permeability of the Cell Envelope and Osmotic Behavior in Saccharomyces cerevisiae Permeability of the Cell Envelope and Osmotic Behavior in Saccharomyces cerevisiae“. *Journal of Bacteriology*, **131**(2): 564–571.

Asami, K., T. Hanai & N. Koizumi (1977). „Dielectric properties of yeast cells: Effect of some ionic detergents on the plasma membranes“. *The Journal of membrane biology*, **34**(1): 145–156.

Atilgan, E., V. Magidson, A. Khodjakov & F. Chang (2015). „Morphogenesis of the Fission Yeast Cell through Cell Wall Expansion.“ *Current biology : CB*, **25**(16): 2150–7.

Aydin, O., B. Aksoy, O. B. Akalin, H. Bayraktar & B. E. Alaca (2016). „Time-resolved local strain tracking microscopy for cell mechanics.“ *The Review of scientific instruments*, **87**(2): 023905.

Baba, M., N. Baba, Y. Ohsumi, K. Kanaya & M. Osumi (1989). „Three-dimensional analysis of morphogenesis induced by mating pheromone alpha factor in Saccharomyces cerevisiae.“ *Journal of cell science*, **94 (Pt 2)**: 207–16.

Banavar, S. P., C. Gomez, M. Trogdon, L. R. Petzold, T.-M. Yi & O. Campàs (2018). „Mechanical feedback coordinates cell wall expansion and assembly in yeast mating morphogenesis.“ *PLoS computational biology*, **14**(1). Ed. by Umulis, D.: e1005940.

Bardwell, L. (2005). „A walk-through of the yeast mating pheromone response pathway.“ *Peptides*, **26**(2): 339–50.

Bartnicki-Garcia, S. & E. Lippman (1972). „The Bursting Tendency of Hyphal Tips of Fungi: Presumptive Evidence for a Delicate Balance between Wall Synthesis and Wall Lysis in Apical Growth“. *Journal of General Microbiology*, **73**(3): 487–500.

Bernal, R., E. Rojas & J. Dumais (2007). „The mechanics of tip growth morphogenesis: what we have learned from rubber balloons“. *Journal of Mechanics of Materials and Structures*, **2**(6): 1157–1168.

Binnig, G., C. F. Quate & C. Gerber (1986). „Atomic Force Microscope.“ *Physical review letters*, **56**(9): 930–933.

Binning, G., H. Rohrer, C. Gerber & E. Weibel (1982). „Surface studies by scanning tunneling microscopy“. *Physical review letters*, **49**(1): 57–61.

Bolduc, J.-E., L. J. Lewis, C.-E. Aubin & A. Geitmann (2006). „Finite-element analysis of geometrical factors in micro-indentation of pollen tubes.“ *Biomechanics and modeling in mechanobiology*, **5**(4): 227–36.

Bonazzi, D., J.-D. Julien, M. Romao, R. Seddiki, M. Piel, A. Boudaoud & N. Minc (2014). „Symmetry breaking in spore germination relies on an interplay between polar cap stability and spore wall mechanics.“ *Developmental cell*, **28**(5): 534–46.

Boudon, F., J. Chopard, O. Ali, B. Gilles, O. Hamant, A. Boudaoud, J. Traas & C. Godin (2015). „A Computational Framework for 3D Mechanical Modeling of Plant Morphogenesis with Cellular Resolution“. *PLoS Computational Biology*, **11**(1).

Brachmann, C. B., A. Davies, G. J. Cost, E. Caputo, J. Li, P. Hieter & J. D. Boeke (1998). „Designer deletion strains derived from Saccharomyces cerevisiae S288C: a useful set of strains and plasmids for PCR-mediated gene disruption and other applications.“ *Yeast (Chichester, England)*, **14**(2): 115–32.

Brückner, B. R., H. Nöding & A. Janshoff (2017). „Viscoelastic Properties of Confluent MDCK II Cells Obtained from Force Cycle Experiments.“ *Biophysical journal*, **112**(4): 724–735.

Burgert, I. & P. Fratzl (2006). „Mechanics of the Expanding Cell Wall“. In: The Expanding Cell. Plant Cell Monographs. Vol. 6. October. Springer, Berlin, Heidelberg: 191–215.

Cabib, E., D. H. Roh, M. Schmidt, L. B. Crotti & a. Varma (2001). „The yeast cell wall and septum as paradigms of cell growth and morphogenesis.“ *The Journal of biological chemistry*, **276**(23): 19679–82.

Cabib, E. & J. Arroyo (2013). „How carbohydrates sculpt cells: chemical control of morphogenesis in the yeast cell wall“. *Nature Reviews Microbiology*, **11**(9): 648.

Campàs, O. & L. Mahadevan (2009). „Shape and dynamics of tip-growing cells.“ *Current biology : CB*, **19**(24): 2102–7.

Cappellaro, C., V. Mrsa & W. Tanner (1998). „New potential cell wall glucanases of Saccharomycescerevisiae and their involvement in mating“. *J Bacteriol*, **180**(19): 5030–5037.

Carpenter, A. E., T. R. Jones, M. R. Lamprecht, C. Clarke, I. H. Kang, O. Friman, D. a. Guertin, J. H. Chang, R. a. Lindquist, J. Moffat, P. Golland & D. M. Sabatini (2006). „CellProfiler: image analysis software for identifying and quantifying cell phenotypes.“ *Genome biology*, **7**(10): R100. arXiv: 1201.3109v1.

Chan, R. K. & C. A. Otte (1982). „Isolation and genetic analysis of Saccharomyces cerevisiae mutants supersensitive to G1 arrest by a factor and alpha factor pheromones.“ *Molecular and cellular biology*, **2**(1): 11–20.

Chapa-Y-Lazo, B., S. Lee, H. Regan & P. Sudbery (2011). „The mating projections of Saccharomyces cerevisiae and Candida albicans show key characteristics of hyphal growth.“ *Fungal biology*, **115**(6): 547–56.

Chaudhari, R. D., J. D. Stenson, T. W. Overton & C. R. Thomas (2012). „Effect of bud scars on the mechanical properties of Saccharomyces cerevisiae cell walls“. *Chemical Engineering Science*, **84**: 188–196.

Chiou, J.-g., M. K. Balasubramanian & D. J. Lew (2017). „Cell Polarity in Yeast.“ *Annual review of cell and developmental biology*, **33**: 77–101.

Choi, K., J. K. Medley, M. König, K. Stocking, L. Smith, S. Gu & H. M. Sauro (2018). „Tellurium: An extensible python-based modeling environment for systems and synthetic biology.“ *Bio Systems*, **171**: 74–79.

Chou, C.-S., T. I. Moore, S. D. Chang, Q. Nie & T.-M. Yi (2012). „Signaling regulated endocytosis and exocytosis lead to mating pheromone concentration dependent morphologies in yeast.“ *FEBS letters*, **586**(23): 4208–4214. arXiv: NIHMS150003.

Cid, V. J., A. Durán, F. del Rey, M. P. Snyder, C. Nombela & M. Sánchez (1995). „Molecular basis of cell integrity and morphogenesis in Saccharomyces cerevisiae.“ *Microbiological reviews*, **59**(3): 345–86.

Coluccio, A. E., R. K. Rodriguez, M. J. Kernan & A. M. Neiman (2008). „The yeast spore wall enables spores to survive passage through the digestive tract of Drosophila.“ *PloS one*, **3**(8): e2873.

Cosgrove, D. J. (1981). „Analysis of the dynamic and steady-state responses of growth rate and turgor pressure to changes in cell parameters.“ *Plant physiology*, **68**(6): 1439–46.

Cosgrove, D. J. (1993). „Wall extensibility: its nature, measurement and relationship to plant cell growth.“ *The New phytologist*, **124**(1): 1–23.

Cosgrove, D. J. (1985). „Cell wall yield properties of growing tissue : evaluation by in vivo stress relaxation.“ *Plant physiology*, **78**(2): 347–56.

Cosgrove, D. J. (1999). „Enzymes and other agents that enhance cell wall extensibility.“ *Annual review of plant physiology and plant molecular biology*, **50**(1): 391–417.

Cosgrove, D. J. (2016). „Plant cell wall extensibility: connecting plant cell growth with cell wall structure, mechanics, and the action of wall-modifying enzymes“. *Journal of Experimental Botany*, **67**(2): 463–476.

Cosgrove, D. (2000). „Loosening of plant cell walls by expansins“. *Nature*, **407**(6802): 321–326.

Crandall, S. H. (1970). „The role of damping in vibration theory“. *Journal of Sound and Vibration*, **11**(1): 3–18.

Dague, E., R. Bitar, H. Ranchon, F. Durand, H. M. Yken & J. M. François (2010). „An atomic force microscopy analysis of yeast mutants defective in cell wall architecture.“ *Yeast (Chichester, England)*, **27**(8): 673–84.

Davì, V., H. Tanimoto, D. Ershov, A. Haupt, H. De Belly, R. Le Borgne, E. Couturier, A. Boudaoud & N. Minc (2018). „Mechanosensation Dynamically Coordinates Polar Growth and Cell Wall Assembly to Promote Cell Survival.“ *Developmental Cell*, **45**(2): 170–182.e7.

Day, L., M. Xu, S. K. Øiseth, L. Lundin & Y. Hemar (2010). „Dynamic rheological properties of plant cell-wall particle dispersions.“ *Colloids and surfaces. B, Biointerfaces*, **81**(2): 461–7.

Delingette, H. (2008). „Triangular springs for modeling nonlinear membranes“. *IEEE Transactions on Visualization and Computer Graphics*, **14**(2): 1–13.

Di Talia, S., J. M. Skotheim, J. M. Bean, E. D. Siggia & F. R. Cross (2007). „The effects of molecular noise and size control on variability in the budding yeast cell cycle.“ *Nature*, **448**(7156): 947–51.

Digiuni, S., A. Berne-Dedieu, C. Martinez-Torres, J. Szecsi, M. Bendahmane, A. Arneodo & F. Argoul (2015). „Single Cell Wall Nonlinear Mechanics Revealed by a Multiscale Analysis of AFM Force-Indentation Curves.“ *Biophysical journal*, **108**(9): 2235–48.

Dimitriadis, E. K., F. Horkay, J. Maresca, B. Kachar & R. S. Chadwick (2002). „Determination of elastic moduli of thin layers of soft material using the atomic force microscope." *Biophysical journal*, **82**(5): 2798–810.

Drake, T. & D. Vavylonis (2013). „Model of fission yeast cell shape driven by membrane-bound growth factors and the cytoskeleton." *PLoS computational biology*, **9**(10): e1003287.

Dufrêne, Y. F., D. Martínez-Martín, I. Medalsy, D. Alsteens & D. J. Müller (2013). „Multiparametric imaging of biological systems by force-distance curve-based AFM." *Nature methods*, **10**(9): 847–54.

Dumais, J., S. L. Shaw, C. R. Steele, S. R. Long & P. M. Ray (2006). „An anisotropic-viscoplastic model of plant cell morphogenesis by tip growth." *The International journal of developmental biology*, **50**(2-3): 209–22.

Duo-Chuan, L. (2006). „Review of fungal chitinases." *Mycopathologia*, **161**(6): 345–60.

Dupres, V., D. Alsteens, S. Wilk, B. Hansen, J. J. Heinisch & Y. F. Dufrêne (2009). „The yeast Wsc1 cell surface sensor behaves like a nanospring in vivo." *Nature chemical biology*, **5**(11): 857–62.

Dupres, V., Y. Dufrêne & J. Heinisch (2010). „Measuring cell wall thickness in living yeast cells using single molecular rulers". *ACS nano*, **4**(9): 5498–5504.

Erdman, S. & M. Snyder (2001). „A filamentous growth response mediated by the yeast mating pathway." *Genetics*, **159**(3): 919–28.

Eric, J., O. Travis & P. Pearu (2001). *SciPy: Open source scientific tools for Python*.

Fabry, B., G. N. Maksym, J. P. Butler, M. Glogauer, D. Navajas & J. J. Fredberg (2001). „Scaling the microrheology of living cells." *Physical review letters*, **87**(14): 148102.

Fayant, P., O. Girlanda, Y. Chebli, C.-E. Aubin, I. Villemure & A. Geitmann (2010). „Finite element model of polar growth in pollen tubes." *The Plant cell*, **22**(8): 2579–93.

Ferrezuelo, F., N. Colomina, A. Palmisano, E. Garí, C. Gallego, A. Csikász-Nagy & M. Aldea (2012). „The critical size is set at a single-cell level by growth rate to attain homeostasis and adaptation". *Nature Communications*, **3**: 1012.

Findley, W. N., J. S. Lai & K. Onaran (1976). *Creep and relaxation of nonlinear viscoelastic materials*. New York, New York, USA: dover puplications, inc.

Fleet, G. H. (1991). „The yeasts. 4, Yeast organells". In: ed. by Rose, A. H. & Harrison, J. S. 2nd ed. New York, New York, USA: Academic Press. Chap. Cell Walls: 199–277.

Flügge, W. (1973). *Stresses in Shells*. Vol. 0116598. Berlin, Heidelberg: Springer Berlin Heidelberg: 116598.

Formosa, C., M. Schiavone, H. Martin-Yken, J. M. François, R. E. Duval & E. Dague (2013). „Nanoscale effects of caspofungin against two yeast species, Saccharomyces cerevisiae and Candida albicans." *Antimicrobial agents and chemotherapy*, **57**(8): 3498–506.

Forsburg, S. L. & P. Nurse (1991). „Cell cycle regulation in the yeasts Saccharomyces cerevisiae and Schizosaccharomyces pombe." *Annual review of cell biology*, **7**(1): 227–56.

Fredberg, J. J. & D. Stamenovic (1989). „On the imperfect elasticity of lung tissue." *Journal of applied physiology (Bethesda, Md. : 1985)*, **67**(6): 2408–19.

Fredberg, J. & B. Fabry (2006). „The cytoskeleton as a soft glassy material". *Cytoskeletal Mechanics: Models and Measurements*, **9780521846**: 50–70.

Frýdlová, I., M. Basler, P. Vasicová, I. Malcová & J. Hasek (2007). „Special type of pheromone-induced invasive growth in Saccharomyces cerevisiae." *Current genetics*, **52**(2): 87–95.

Gammie, A. E., V. Brizzio & M. D. Rose (1998). „Distinct morphological phenotypes of cell fusion mutants." *Molecular biology of the cell*, **9**(6): 1395–410.

Garmendia-Torres, C., O. Tassy, A. Matifas, N. Molina & G. Charvin (2018). „Multiple inputs ensure yeast cell size homeostasis during cell cycle progression." *eLife*, **7**: e34025.

Geitmann, A. & J. K. Ortega (2009). „Mechanics and modeling of plant cell growth." *Trends in plant science*, **14**(9): 467–78.

Giese, W. (2016). „The choreography of yeast mating". PhD thesis. Humboldt-Universität zu Berlin, Lebenswissenschaftliche Fakultät.

Giese, W., M. Eigel, S. Westerheide, C. Engwer & E. Klipp (2015). „Influence of cell shape, inhomogeneities and diffusion barriers in cell polarization models." *Physical biology*, **12**(6): 066014.

Gilchrist, C. L., S. W. Witvoet-Braam, F. Guilak & L. A. Setton (2007). „Measurement of intracellular strain on deformable substrates with texture correlation". *Journal of Biomechanics*, **40**(4): 786–794.

Goddard, M. R. & D. Greig (2015). „Saccharomyces cerevisiae: a nomadic yeast with no niche?" *FEMS yeast research*, **15**(3): 1–6.

Goldenbogen, B., W. Giese, M. Hemmen, J. Uhlendorf, A. Herrmann & E. Klipp (2016). „Dynamics of cell wall elasticity pattern shapes the cell during yeast mating morphogenesis." *Open biology*, **6**(9): 160136.

Green, P. B. (1969). „Cell morphogenesis." *Annual review of plant physiology*, **20**(1): 365–394.

Groisman, A., C. Lobo, H. Cho, J. K. Campbell, Y. S. Dufour, A. M. Stevens & A. Levchenko (2005). „A microfluidic chemostat for experiments with bacterial and yeast cells." *Nature methods*, **2**(9): 685–689.

Groot, P. W. de, C. Ruiz, C. R. Vázquez de Aldana, E. Duenas, V. J. Cid, F. Del Rey, J. M. Rodríquez-Peña, P. Pérez, A. Andel, J. Caubín, J. Arroyo, J. C. García, C. Gil, M. Molina, L. J. García, C. Nombela & F. M. Klis (2001). „A genomic approach for the identification and classification of genes involved in cell wall formation and its regulation in Saccharomyces cerevisiae." *Comparative and functional genomics*, **2**(3): 124–42.

Halldorsson, S., E. Lucumi, R. Gómez-Sjöberg & R. M. T. Fleming (2015). „Advantages and challenges of microfluidic cell culture in polydimethylsiloxane devices." *Biosensors & bioelectronics*, **63**: 218–231.

Hamant, O., M. G. Heisler, H. Jönsson, P. Krupinski, M. Uyttewaal, P. Bokov, F. Corson, P. Sahlin, A. Boudaoud, E. M. Meyerowitz, Y. Couder & J. Traas (2008). „Developmental patterning by mechanical signals in Arabidopsis“. *Science*, **322**(5908): 1650–1655.

Hansen, N. & A. Ostermeier (2001). „Completely derandomized self-adaptation in evolution strategies.“ *Evolutionary computation*, **9**(2): 159–95.

Harold, F. M. (2002). „Force and compliance: rethinking morphogenesis in walled cells.“ *Fungal genetics and biology : FG & B*, **37**(3): 271–82.

Harris, L. K. & J. A. Theriot (2016). „Relative rates of surface and volume synthesis set bacterial cell size“. *Cell*, **165**(6): 1479–1492.

Hartwell, L. H. & M. W. Unger (1977). „Unequal division in Saccharomyces cerevisiae and its implications for the control of cell division.“ *The Journal of cell biology*, **75**(2 Pt 1): 422–35.

Hayles, J. & P. Nurse (1986). „Cell cycle regulation in yeast.“ *Journal of cell science. Supplement*, **4**(Supplement 4): 155–70.

Hecht, F. M., J. Rheinlaender, N. Schierbaum, W. H. Goldmann, B. Fabry & T. E. Schäffer (2015). „Imaging viscoelastic properties of live cells by AFM: power-law rheology on the nanoscale“. *Soft Matter*, **11**(23): 4584–4591.

Helmke, B. P., A. B. Rosen & P. F. Davies (2003). „Mapping mechanical strain of an endogenous cytoskeletal network in living endothelial cells.“ *Biophysical journal*, **84**(4): 2691–9.

Hemar, Y., S. Lebreton, M. Xu & L. Day (2011). „Small-deformation rheology investigation of rehydrated cell wall particles-xanthan mixtures“. *Food Hydrocolloids*, **25**(4): 668–676.

Hemmen, M. (2017). „A quantitative description of the mating morphology of Saccharomyces cerevisiae.“ PhD thesis. Humboldt-Universität zu Berlin.

Hertz, H. (1881). „H. Hertz, Über die Berührung fester elastischer Körper, Journal für die reine und angewandte Mathematik 92, 156-171 (1881)“. *Journal für die reine und angewandte Mathematik*, **171**(92): 156–171.

Hoffmann, H. & A. Rauscher (1993). „Aggregating systems with a yield stress value.“ *Colloid & Polymer Science*, **271**(4): 390–395.

Huberman, L. B. & A. W. Murray (2014). „A model for cell wall dissolution in mating yeast cells: polarized secretion and restricted diffusion of cell wall remodeling enzymes induces local dissolution.“ *PloS one*, **9**(10): e109780.

Hutter, J. L. & J. Bechhoefer (1993). „Calibration of atomic-force microscope tips“. *Review of Scientific Instruments*, **64**(7): 1868–1873.

Jendretzki, A., J. Wittland, S. Wilk, A. Straede & J. J. Heinisch (2011). „How do I begin? Sensing extracellular stress to maintain yeast cell wall integrity“. *European Journal of Cell Biology*, **90**(9): 740–744.

Jiang, H. & S. X. Sun (2013). „Cellular pressure and volume regulation and implications for cell mechanics.“ *Biophysical journal*, **105**(3): 609–19.

Jin, M., B. Errede, M. Behar, W. Mather, S. Nayak, J. Hasty, H. G. Dohlman & T. C. Elston (2011). „Yeast dynamically modify their environment to achieve better mating efficiency.“ *Science signaling*, **4**(186): ra54. arXiv: NIHMS150003.

Johnson, B. F. & E. J. Gibson (1966). „Autoradiographic analysis of regional cell wall growth of yeasts. III. Saccharomyces cerevisiae.“ *Experimental cell research*, **41**(3): 580–91.

Johnston, G. C., C. W. Ehrhardt, A. Lorincz & B. L. Carter (1979). „Regulation of cell size in the yeast Saccharomyces cerevisiae.“ *Journal of bacteriology*, **137**(1): 1–5.

Johnston, G. C., J. R. Pringle & L. H. Hartwell (1977). „Coordination of growth with cell division in the yeast Saccharomyces cerevisiae.“ *Experimental cell research*, **105**(1): 79–98.

Jones, C. A. R., M. Cibula, J. Feng, E. A. Krnacik, D. H. McIntyre, H. Levine & B. Sun (2015). „Micromechanics of cellularized biopolymer networks.“ *Proceedings of the National Academy of Sciences of the United States of America*, **112**(37): E5117–22. arXiv: 0504028 [q-bio].

Joseph-Strauss, D., D. Zenvirth, G. Simchen & N. Barkai (2007). „Spore germination in Saccharomyces cerevisiae: global gene expression patterns and cell cycle landmarks.“ *Genome biology*, **8**(11): R241.

Jouhten, P., E. Rintala, A. Huuskonen, A. Tamminen, M. Toivari, M. Wiebe, L. Ruohonen, M. Penttilä & H. Maaheimo (2008). „Oxygen dependence of metabolic fluxes and energy generation of Saccharomyces cerevisiae CEN.PK113-1A.“ *BMC systems biology*, **2**(1): 60.

Jun, S. & S. Taheri-Araghi (2015). „Cell-size maintenance: universal strategy revealed.“ *Trends in microbiology*, **23**(1): 4–6. arXiv: arXiv:1504.00043v1.

Kasas, S. & A. Ikai (1995). „A method for anchoring round shaped cells for atomic force microscope imaging.“ *Biophysical journal*, **68**(5): 1678–80.

Kedem, O. & A. Katchalsky (1958). „Thermodynamic analysis of the permeability of biological membranes to non-electrolytes.“ *Biochimica et biophysica acta*, **27**: 229–246.

Ketz, R. J., R. K. Prud'homme & W. W. Graessley (1988). „Rheology of concentrated microgel solutions“. *Rheologica Acta*, **27**(5): 531–539.

Klipp, E., B. Nordlander, R. Krüger, P. Gennemark & S. Hohmann (2005). „Integrative model of the response of yeast to osmotic shock.“ *Nature biotechnology*, **23**(8): 975–982.

Klis, F. & P. Mol (2002). „Dynamics of cell wall structure in Saccharomyces cerevisiae.“ *FEMS microbiology Revies*, **26**(3): 239–256.

Klis, F. M., A. Boorsma & P. W. J. De Groot (2006). „Cell wall construction in Saccharomyces cerevisiae.“ *Yeast (Chichester, England)*, **23**(3): 185–202.

Klis, F. M., C. G. de Koster & S. Brul (2014). „Cell wall-related bionumbers and bioestimates of Saccharomyces cerevisiae and Candida albicans.“ *Eukaryotic cell*, **13**(1): 2–9.

Knight, S. J. & M. R. Goddard (2015). „Sporulation in soil as an overwinter survival strategy in Saccharomyces cerevisiae“. *FEMS Yeast Research*, **16**(1): 1–8.

Kono, K., R. Matsunaga, A. Hirata, G. Suzuki, M. Abe & Y. Ohya (2005). „Involvement of actin and polarisome in morphological change during spore germination of Saccharomyces cerevisiae.“ *Yeast (Chichester, England)*, **22**(2): 129–39.

Kreger-Van Rij, N. J. (1978). „Electron microscopy of germinating ascospores of Saccharomyces cerevisiae.“ *Archives of microbiology*, **117**(1): 73–7.

Kron, S. J. & N. A. Gow (1995). „Budding yeast morphogenesis: signalling, cytoskeleton and cell cycle.“ *Current opinion in cell biology*, **7**(6): 845–55.

Landau, L. D., E. M. Lifshitz, J. B. Sykes, W. H. Reid & E. H. Dill (1960). *Theory of Elasticity: Vol. 7 of Course of Theoretical Physics*.

Leeuwen, M. R. van, P. Krijgsheld, R. Bleichrodt, H. Menke, H. Stam, J. Stark, H. A. B. Wösten & J. Dijksterhuis (2013). „Germination of conidia of Aspergillus niger is accompanied by major changes in RNA profiles.“ *Studies in mycology*, **74**(1): 59–70.

Lesage, G. & H. Bussey (2006). „Cell wall assembly in Saccharomyces cerevisiae.“ *Microbiology and molecular biology reviews : MMBR*, **70**(2): 317–43.

Levin, D. E. (2005). „Cell Wall Integrity Signaling in Saccharomyces cerevisiae“. *Microbiology and Molecular Biology Reviews*, **69**(2): 262–291.

Levin, D. E. (2011). „Regulation of cell wall biogenesis in Saccharomyces cerevisiae: the cell wall integrity signaling pathway.“ *Genetics*, **189**(4): 1145–75.

Lipke, P. N., A. Taylor & C. E. Ballou (1976). „Morphogenic Effects of a-Factor on Saccharomyces cerevisiae a Cells“. *Microbiology*, **127**(1): 610–618.

Lo, H. J., J. R. Köhler, B. DiDomenico, D. Loebenberg, A. Cacciapuoti & G. R. Fink (1997). „Nonfilamentous C. albicans mutants are avirulent.“ *Cell*, **90**(5): 939–49.

Lockhart, J. a. (1965). „An analysis of irreversible plant cell elongation.“ *Journal of theoretical biology*, **8**(2): 264–275.

Losensky, L., B. Goldenbogen, G. Holland, M. Laue, A. Petran, J. Liebscher, H. A. Scheidt, A. Vogel, D. Huster, E. Klipp & A. Arbuzova (2016). „Micro- and nano-tubules built from loosely and tightly rolled up thin sheets.“ *Physical chemistry chemical physics : PCCP*, **18**(2): 1292–301.

Luan, Y., O. Lieleg, B. Wagner & A. R. Bausch (2008). „Micro- and macrorheological properties of isotropically cross-linked actin networks.“ *Biophysical journal*, **94**(2): 688–93. arXiv: 0706.0393.

Mahaffy, R. E., C. K. Shih, F. C. MacKintosh & J. Käs (2000). „Scanning probe-based frequency-dependent microrheology of polymer gels and biological cells.“ *Physical review letters*, **85**(4): 880–883.

Mark, D., S. Haeberle, G. Roth, F. von Stetten & R. Zengerle (2010). „Microfluidic lab-on-a-chip platforms: requirements, characteristics and applications.“ *Chemical Society reviews*, **39**(3): 1153–82.

Marshall, W. F., K. D. Young, M. Swaffer, E. Wood, P. Nurse, A. Kimura, J. Frankel, J. Wallingford, V. Walbot, X. Qu & A. H. K. Roeder (2012). „What determines cell size?“ *BMC biology*, **10**: 101.

Martinez de Marañon, I., P.-A. A. Marechal & P. Gervais (1996). „Passive response of Saccharomyces cerevisiae to osmotic shifts: cell volume variations depending on the physiological state.“ *Biochemical and biophysical research communications*, **227**(2): 519–23.

Mason, T. G., J. Bibette & D. A. Weitz (1995). „Elasticity of Compressed Emulsions.“ *Physical review letters*, **75**(10): 2051–2054.

McClure, A. W., M. Minakova, J. M. Dyer, T. R. Zyla, T. C. Elston & D. J. Lew (2015). „Role of Polarized G Protein Signaling in Tracking Pheromone Gradients“. *Developmental Cell*, **35**(4): 471–482.

Mckinney, W. (2010). „Data Structures for Statistical Computing in Python“. *PROC. OF THE 9th PYTHON IN SCIENCE CONF*.

Meikle, A. J., R. H. Reed & G. M. Gadd (1988). „Osmotic adjustment and the accumulation of organic solutes in whole cells and protoplasts of Saccharomyces cerevisiae.“ *Journal of general microbiology*, **134**(11): 3049–60.

Mercadé-Prieto, R., C. R. Thomas & Z. Zhang (2013). „Mechanical double layer model for Saccharomyces cerevisiae cell wall.“ *European biophysics journal : EBJ*, **42**(8): 613–20.

Merlini, L., O. Dudin & S. G. Martin (2013). „Mate and fuse: how yeast cells do it“. *Open biology*, **3**(3): 130008.

Merritt, D. R. & F. Weinhaus (1978). „The pressure curve for a rubber balloon.“ *American journal of physics*, **46**(10): 976–977.

Minc, N., A. Boudaoud & F. Chang (2009). „Mechanical forces of fission yeast growth.“ *Current biology : CB*, **19**(13): 1096–101. arXiv: NIHMS150003.

Misra, G., E. R. Rojas, A. Gopinathan & K. C. Huang (2013). „Mechanical consequences of cell-wall turnover in the elongation of a Gram-positive bacterium.“ *Biophysical journal*, **104**(11): 2342–52.

Mitchison, J. M. (2003). „Growth during the cell cycle.“ *International review of cytology*, **226**: 165–258.

Mitchison, J. (1958). „The growth of single cells: II. Saccharomyces cerevisiae.“ *Experimental cell research*, **15**(1): 214–221.

Moore, T. I., C.-S. Chou, Q. Nie, N. L. Jeon & T.-M. Yi (2008). „Robust spatial sensing of mating pheromone gradients by yeast cells.“ *PloS one*, **3**(12): e3865.

Mostowy, S. & P. Cossart (2012). „Septins: the fourth component of the cytoskeleton.“ *Nature reviews. Molecular cell biology*, **13**(3): 183–94.

Neiman, A. M. (2005). „Ascospore formation in the yeast Saccharomyces cerevisiae.“ *Microbiology and molecular biology reviews : MMBR*, **69**(4): 565–84.

Neiman, A. M. (2011). „Sporulation in the budding yeast Saccharomyces cerevisiae.“ *Genetics*, **189**(3): 737–65.

Okamoto-Nakazato, A., K. Takahashi, R. Katoh-Semba & K. Katou (2001). „Distribution of yieldin, a regulatory protein of the cell wall yield threshold, in etiolated cowpea seedlings.“ *Plant & cell physiology*, **42**(9): 952–8.

Orlean, P. (2012). „Architecture and biosynthesis of the Saccharomyces cerevisiae cell wall“. *Genetics*, **192**(3): 775–818.

Ortega, J. K. E. (2017). „Dimensionless number is central to stress relaxation and expansive growth of the cell wall.“ *Scientific reports*, **7**(1): 3016.

Ortega, J. K. (1985). „Augmented growth equation for cell wall expansion.“ *Plant physiology*, **79**(1): 318–20.

Ortega, J. K., R. I. Gamow & C. N. Ahlquist (1975). „Phycomyces: a change in mechanical properties after a light stimulus.“ *Plant physiology*, **55**(2): 333–7.

Ortega, J. K. & S. Welch (2013). „Mathematical Models for Expansive Growth of Cells with Walls“. *Mathematical Modelling of Natural Phenomena*, **8**(4). Ed. by Chavarria-Krauser, A., Dupuy, L. & Ptashnyk, M.: 35–61.

O'Shea, S. J. & M. E. Welland (1998). „Atomic Force Microscopy at Solid-Liquid Interfaces“. *Langmuir*, **14**(15): 4186–4197.

Osumi, M. (1998). „The ultrastructure of yeast: cell wall structure and formation.“ *Micron*, **29**(2-3): 207–233.

Pamme, N. (2007). „Continuous flow separations in microfluidic devices.“ *Lab on a chip*, **7**(12): 1644–59.

Parre, E. & A. Geitmann (2005). „More than a leak sealant. The mechanical properties of callose in pollen tubes.“ *Plant physiology*, **137**(1): 274–286.

Philip, B. & D. E. Levin (2001). „Wsc1 and Mid2 are cell surface sensors for cell wall integrity signaling that act through Rom2, a guanine nucleotide exchange factor for Rho1.“ *Molecular and cellular biology*, **21**(1): 271–80.

Piccirillo, S. & S. M. Honigberg (2010). „Sporulation patterning and invasive growth in wild and domesticated yeast colonies“. *Research in Microbiology*, **161**(5): 390–398.

Pillet, F., S. Lemonier, M. Schiavone, C. Formosa, H. Martin-Yken, J. M. Francois & E. Dague (2014). „Uncovering by atomic force microscopy of an original circular structure at the yeast cell surface in response to heat shock.“ *BMC biology*, **12**: 6.

Proctor, S. a., N. Minc, A. Boudaoud & F. Chang (2012). „Contributions of turgor pressure, the contractile ring, and septum assembly to forces in cytokinesis in fission yeast.“ *Current biology : CB*, **22**(17): 1601–1608.

Pruyne, D. & A. Bretscher (2000). „Polarization of cell growth in yeast. I. Establishment and maintenance of polarity states.“ *Journal of cell science*, **113 (Pt 3**: 365–75.

Ragni, E., H. Piberger, C. Neupert, J. García-Cantalejo, L. Popolo, J. Arroyo, M. Aebi & S. Strahl (2011). „The genetic interaction network of CCW12, a Saccharomyces cerevisiae gene required for cell wall integrity during budding and formation of mating projections." *BMC genomics*, **12**(1): 107.

Rajavel, M., B. Philip, B. M. Buehrer, B. Errede & D. E. Levin (1999). „Mid2 is a putative sensor for cell integrity signaling in Saccharomyces cerevisiae." *Molecular and cellular biology*, **19**(6): 3969–76.

Reynolds, T. B. & G. R. Fink (2001). „Bakers' yeast, a model for fungal biofilm formation." *Science (New York, N.Y.)* **291**(5505): 878–81.

Ross-Murphy, S. B. & K. P. Shatwell (1993). „Polysaccharide strong and weak gels." *Biorheology*, **30**(3-4): 217–27.

Rother, J., H. Nöding, I. Mey & A. Janshoff (2014). „Atomic force microscopy-based microrheology reveals significant differences in the viscoelastic response between malign and benign cell lines." *Open biology*, **4**(5): 140046.

Routier-Kierzkowska, A.-L. & R. S. Smith (2013). „Measuring the mechanics of morphogenesis." *Current opinion in plant biology*, **16**(1): 25–32.

Ruiz-Herrera, J. (2012). *Fungal cell wall : structure, synthesis, and assembly.* 2. ed. Boca Raton: CRC Press, Taylor & Francis Group.

Ruppersberg, J. P., J. K. Hörber, C. Gerber & G. Binnig (1989). „Imaging of cell membraneous and cytoskeletal structures with a scanning tunneling microscope." *FEBS letters*, **257**(2): 460–4.

Schaber, J., M. A. Adrover, E. Eriksson, S. Pelet, E. Petelenz-Kurdziel, D. Klein, F. Posas, M. Goksör, M. Peter, S. Hohmann & E. Klipp (2010). „Biophysical properties of Saccharomyces cerevisiae and their relationship with HOG pathway activation." *European biophysics journal : EBJ*, **39**(11): 1547–56.

Schekman, R. & V. Brawley (1979). „Localized deposition of chitin on the yeast cell surface in response to mating pheromone." *Proceedings of the National Academy of Sciences of the United States of America*, **76**(2): 645–9.

Schneider, C. A., W. S. Rasband & K. W. Eliceiri (2012). „NIH Image to ImageJ: 25 years of image analysis." *Nature methods*, **9**(7): 671–5.

Shaw, J. A., P. C. Mol, B. Bowers, S. J. Silverman, M. H. Valdivieso, A. Durán & E. Cabib (1991). „The function of chitin synthases 2 and 3 in the Saccharomyces cerevisiae cell cycle." *The Journal of cell biology*, **114**(1): 111–23.

Shehata, A. M. E. T., E. M. Mrak & H. J. Phaff (1955). „Yeasts Isolated from Drosophila and from Their Suspected Feeding Places in Southern and Central California". *Mycologia*, **47**(6): 799.

Slaughter, B. D., S. E. Smith & R. Li (2009). „Symmetry breaking in the life cycle of the budding yeast." *Cold Spring Harbor perspectives in biology*, **1**(3): a003384.

Smith, A. E., K. E. Moxham & A. P. J. Middelberg (1998). „On uniquely determining cell–wall material properties with the compression experiment.“ *Chemical engineering science*, **53**(23): 3913–3922.

Smith, A. E., K. E. Moxham & A. P. J. Middelberg (2000). „Wall material properties of yeast cells. Part II. Analysis.“ *Chemical engineering science*, **55**(11): 2043–2053.

Smith, A. E., Z. Zhang & C. R. Thomas (2000). „Wall material properties of yeast cells: Part 1. Cell measurements and compression experiments.“ *Chemical engineering science*, **55**(11): 2031–2041.

Smith, A. E., Z. Zhang, C. R. Thomas, K. E. Moxham & A. P. Middelberg (2000). „The mechanical properties of Saccharomyces cerevisiae.“ *Proceedings of the National Academy of Sciences of the United States of America*, **97**(18): 9871–4.

Smith, L. P., F. T. Bergmann, D. Chandran & H. M. Sauro (2009). „Antimony: a modular model definition language.“ *Bioinformatics (Oxford, England)*, **25**(18): 2452–4.

Sneddon, I. N. (1965). „The relation between load and penetration in the axisymmetric boussinesq problem for a punch of arbitrary profile“. *International Journal of Engineering Science*, **3**(1): 47–57. arXiv: `arXiv:1011.1669v3`.

Sniegowski, P. D., P. G. Dombrowski & E. Fingerman (2002). „Saccharomyces cerevisiae and Saccharomyces paradoxus coexist in a natural woodland site in North America and display different levels of reproductive isolation from European conspecifics.“ *FEMS yeast research*, **1**(4): 299–306.

Soifer, I., L. Robert & A. Amir (2016). „Single-Cell Analysis of Growth in Budding Yeast and Bacteria Reveals a Common Size Regulation Strategy.“ *Current biology : CB*, **26**(3): 356–61. arXiv: `arXiv:1410.4771v2`.

Sollich, P., F. Lequeux, P. Hébraud & M. E. Cates (1997). „Rheology of soft glassy materials.“ *Physical review letters*, **78**(10): 2020–2023. arXiv: `9611228 [cond-mat]`.

Spiesschaert, B., B. Goldenbogen, S. Taferner, M. Schade, M. Mahmoud, E. Klipp, N. Osterrieder & W. Azab (2015). „Role of gB and pUS3 in Equine Herpesvirus 1 Transfer between Peripheral Blood Mononuclear Cells and Endothelial Cells : a Dynamic“. *Journal of Virology*, **89**(23): 11899–11908.

Spiesser, T. W., C. Kühn, M. Krantz & E. Klipp (2015). „Bud-Localization of CLB2 mRNA Can Constitute a Growth Rate Dependent Daughter Sizer.“ *PLoS computational biology*, **11**(4): e1004223.

Spiesser, T., C. Kühn, M. Krantz & E. Klipp (2016). „The MYpop toolbox: Putting yeast stress responses in cellular context on single cell and population scales.“ *Biotechnology journal*, **11**(9): 1158–68.

Stefanini, I., L. Dapporto, L. Berná, M. Polsinelli, S. Turillazzi & D. Cavalieri (2016). „Social wasps are a Saccharomyces mating nest“. *Proceedings of the National Academy of Sciences*, **113**(8): 2247–2251.

Straede, A. & J. J. Heinisch (2007). „Functional analyses of the extra- and intracellular domains of the yeast cell wall integrity sensors Mid2 and Wsc1.“ *FEBS letters*, **581**(23): 4495–500.

Suchodolskis, A., V. Feiza, A. Stirke, A. Timonina, A. Ramanaviciene & A. Ramanavicius (2011). „Elastic properties of chemically modified baker's yeast cells studied by AFM". *Surface and Interface Analysis*, **43**(13): 1636–1640.

Svaldo Lanero, T., O. Cavalleri, S. Krol, R. Rolandi & A. Gliozzi (2006). „Mechanical properties of single living cells encapsulated in polyelectrolyte matrixes". *Journal of Biotechnology*, **124**(4): 723–731.

Taiz, L. (1984). „Plant Cell Expansion: Regulation of Cell Wall Mechanical Properties". *Annual Review of Plant Physiology*, **35**(1): 585–657.

Tao, J. & S. X. Sun (2015). „Active Biochemical Regulation of Cell Volume and a Simple Model of Cell Tension Response." *Biophysical journal*, **109**(8): 1541–50.

Tartakoff, A. M. (2015). „Cell biology of yeast zygotes, from genesis to budding." *Biochimica et biophysica acta*, **1853**(7): 1702–14.

Touhami, A., B. Nysten & Y. F. Dufrêne (2003). „Nanoscale mapping of the elasticity of microbial cells by atomic force microscopy." *Langmuir*, **19**(11): 4539–4543.

Trogdon, M., B. Drawert, C. Gomez, S. P. Banavar, T.-M. Yi, O. Campàs & L. R. Petzold (2018). „The effect of cell geometry on polarization in budding yeast." *PLoS computational biology*, **14**(6): e1006241.

Turner, J. J., J. C. Ewald & J. M. Skotheim (2012). „Cell size control in yeast." *Current biology : CB*, **22**(9): R350–9.

Tweten, D. J., P. V. Bayly & A. E. Carlsson (2017). „Actin growth profile in clathrin-mediated endocytosis." *Physical review. E*, **95**(5-1): 052414.

Tyson, J. J. & K. B. Hannsgen (1985). „Global asymptotic stability of the size distribution in probabilistic models of the cell cycle". *Journal of Mathematical Biology*, **22**(1): 61–68.

Vaikousi, H. & C. G. Biliaderis (2005). „Processing and formulation effects on rheological behavior of barley β-glucan aqueous dispersions". *Food Chemistry*, **91**(3): 505–516.

Valentín, E., E. Herrero, H. Rico, F. Miragall & R. Sentandreu (1987). „Cell wall manno-proteins during the population growth phases in Saccharomyces cerevisiae." *Archives of microbiology*, **148**(2): 88–94.

Vella, D., A. Ajdari, A. Vaziri & A. Boudaoud (2012). „The indentation of pressurized elastic shells: from polymeric capsules to yeast cells." *Journal of the Royal Society, Interface*, **9**(68): 448–55. arXiv: 84856879660.

Versari, C., S. Stoma, K. Batmanov, A. Llamosi, F. Mroz, A. Kaczmarek, M. Deyell, C. Lhoussaine, P. Hersen & G. Batt (2017). „Long-term tracking of budding yeast cells in brightfield microscopy: CellStar and the Evaluation Platform". *J R Soc Interface*, **14**(127).

Veytsman, B. A. & D. J. Cosgrove (1998). „A model of cell wall expansion based on thermodynamics of polymer networks." *Biophysical journal*, **75**(5): 2240–50.

Volden, T., D. Barrettino, S. Hafizovic, K.-U. Kirstein, a. Hierlemann & H. Baltes (2004). „Single-chip AFM array with integrated digital controllers". *Proceedings of IEEE Sensors, 2004.* 1228–1231.

Walt, S. van der, S. C. Colbert & G. Varoquaux (2011). „The NumPy array: a structure for efficient numerical computation." *Computing in science & engineering*, **13**(2): 22–30.

Wedlich-Soldner, R. & R. Li (2008). „Yeast and fungal morphogenesis from an evolutionary perspective." *Seminars in cell & developmental biology*, **19**(3): 224–33.

Weinhaus, F. & W. Barker (1978). „On the equilibrium states of interconnected bubbles or balloons." *American journal of physics*, **46**(10): 978–982.

Woldringh, C. L., P. G. Huls & N. O. Vischer (1993). „Volume growth of daughter and parent cells during the cell cycle of Saccharomyces cerevisiae a/alpha as determined by image cytometry." *Journal of bacteriology*, **175**(10): 3174–81.

Yamaguchi, M., Y. Namiki, H. Okada, Y. Mori, H. Furukawa, J. Wang, M. Ohkusu & S. Kawamoto (2011). „Structome of Saccharomyces cerevisiae determined by freeze-substitution and serial ultrathin-sectioning electron microscopy". *Journal of Electron Microscopy*, **60**(5): 321–335.

Yanagisawa, M., A. S. Desyatova, S. A. Belteton, E. L. Mallery, J. A. Turner & D. B. Szymanski (2015). „Patterning mechanisms of cytoskeletal and cell wall systems during leaf trichome morphogenesis". *Nature Plants*, **1**(3): 1–8.

Yin, Q. Y., P. W. J. de Groot, L. de Jong, F. M. Klis & C. G. De Koster (2007). „Mass spectrometric quantitation of covalently bound cell wall proteins in Saccharomyces cerevisiae." *FEMS yeast research*, **7**(6): 887–96.

Yu, M. H., G. W. Ma, H. F. Qiang & Y. Q. Zhang (2006). *Generalized plasticity*. Springer Science & Business Media, 2006.

Zerzour, R., J. Kroeger & A. Geitmann (2009). „Polar growth in pollen tubes is associated with spatially confined dynamic changes in cell mechanical properties". *Developmental Biology*, **334**(2): 437–446.

Appendix

A

A.1 Code

A.1.1 The SCGM in Antimony

```
function MAXIMUM(a, b)
  piecewise(a, a >= b, b);
end

function modulo(a, b)
  a - b*floor(a/b);
end

function init_a(a)
  floor(a);
end

model SCGM

  ////////////////////////// compartments //////////////////////////

  compartment V_tot_liter;
  compartment extra = 1;
  dr_b := dR_ref * 0.2;
  r_b_0 = 0.3
  r_os_0 = 0.1
  r_os = r_os_0
  r_b = r_b_0
  r := r_os + r_b
  dr := dr_os + dr_b
  r_os' = dr_os
  r_b' = dr_b
```

```
//////////////////////////// volumes ////////////////////////////

V_tot_fl := 4 / 3 * pi * r^3 // fl
V_ref := 4 /3 * pi * R_ref^3 // fl
V_tot_liter := V_tot_fl * 1e-15; // um^3


//////////////////////////// species ////////////////////////////

species c_e in extra = 240; // mM  measured (SD-medium)
species c_i in V_tot_liter = 319.17 ; // mM

c_i_0 = 319.17; // mM ATTENTION: must be equal to species c_i
// initial value, cause inheriting antimony models depend
// on this value!

///////////////// mother and bud connection ///////////////

bud_start = 1;


//////// internal and external osmotic pressure /////////

pi_i := c_i * R * T; // Pa
pi_e := c_e * R * T; // Pa


//////////////////////////// constants ///////////////////////

R = 8.314; // J/mol/K
T = 303; // K 30 deggree C

////////////////////////// Surface area ////////////////////

G := 4*pi*r^2; // surface of sphere in um^2

///////////////// water flow over membrane ///////////////
```

```
Lp = 1.19e-6; // um/s/Pa, Klipp 2005
dV_exchange = 0; // um^2
dr_exchange := ((V_tot_fl + dV_exchange)*3/4/pi)^(1/3) - r;
dr_os := (- Lp *(pi_t + pi_e - pi_i) + dr_exchange ) * bud_start;


////////////////// plastic expansion rate /////////////////

pi_t = 0.20e6; // Pa
pi_tc_0 = 0.2e6; // Pa
d = 0.115; // um
phi = 1.e-4; // 1/Pa/s
pi_tc := pi_tc_0;


////////////////// cell wall mechanics ////////////////////

nu = 0.5; // Poisson's ratio
R_ref =  r / exp(pi_t  * r * (1-nu) / (2 * d * E));
E_adjustment = (1-nu^2)^(-1); // transformation:
3D to 2D Youngs modulus,

E_3d =  2.58e6; // Pa
E = E_adjustment * E_3d; // Pa Goldenbogen, Giese 2016

pi_t'  = E * 2 * d / (1-nu) * (dr/r^2 - dR_ref/(R_ref*r))
 - dr / r * pi_t

dR_ref :=  phi * R_ref * r / (2 * d) * MAXIMUM(pi_t - pi_tc, 0)
* bud_start;

R_ref' = dR_ref;


////////////// osmolyte uptake and consumption ///////////////

withSF = 1; // simulating with scaling factor k_cu
k_uptake_0 = 2.e-16 //3.5e-15; // mmol/s/um^2
```

```
  k_uptake = k_nutrient_0;
  k_cu = 1.27; // 1/um
  k_consumption_0 = 2.5e-16; // mmol/s/um^3
  k_consumption := k_cu * k_uptake * (withSF)
  + k_consumption_0*(1-withSF);//  mM/s/um^3


  ////////////////////// reactions ////////////////////////

  => c_i; k_nutrient * G * bud_start;
  c_i =>; k_consumption * V_tot_fl * bud_start;
  c_i=> c_e ; k_transport * (c_i - c_e);


  ////////////////////// events ///////////////////////////////

  // equalization of ci and ce  at time 7200
  k_transport = 0;
  //at time > 7200: k_uptake = 0;
  //at time > 7200: k_transport = 2.5e-10;


end
```

A.1.2 The cSCGM in Antimony

```
import "scgm.txt"

model cSCGM

  ////////////////////// Instances ////////////////////////////
  mother: SCGM();
  bud: SCGM();

  t_budstart = 3600; // s
  mother.r_os_0 = 1.0;  // um
  bud.r_os_0 = 0.01; // um

  /////////// osmolyte uptake and consumption ///////////////

  withSF = 0;
  mother.withSF := withSF;
  bud.withSF := withSF;
  k_uptake = 2.e-16 // mmol/s/um^2
  k_consumption_0 = 2.5e-16 // mmol/s/um^3;
  k_cu = 1.27;

  bud.k_uptake := k_uptake;
  bud.k_consumption_0 := k_deg_0;
  bud.k_cu := k_cu;

  mother.k_uptake := k_uptake;
  mother.k_consumption_0 := k_consumption_0;
  mother.k_cu := k_cu;


  //////// cell wall elasticity of mother and bud ////////////

  nu = 0.5; // Poisson's ratio
  E_adjustment = (1-nu^2)^(-1); //
  // transformation: 3D to 2D Youngs modulus, Goldenbogen, Giese 2016
  mother.E := 2.58e6 * E_adjustment; // Pa
  budE = 3.3e6 * E_adjustment; // Mother E * 1.28 as calculated
```

```
  bud.E :=  budE; // Pa


  //////// cell wall extensibility of mother and bud ///////////

  extens_factor = 1.e+2; // phi_bud/phi_mother
  mother.phi = 1.e-4;  // 1/Pa/s
  bud.phi := mother.phi * extens_factor; // 1/Pa/s


  ////////////////// budding event ////////////////////////////

  bud_start_in_the_bud = 0;
  bud.bud_start := bud_start_in_the_bud;
  at time > t_budstart: bud_start_in_the_bud = 1;
  at time > t_budstart: bud.c_i = mother.c_i;


  //////// solute diffusion between mother and bud ////////////

  c_i_diffusion_coeff = 1.0; // idea: apparent diffusion coefficient
  // in addition it describes the permeability through the budneck

  mother.c_i -> bud.c_i; c_i_diffusion_coeff * (mother.c_i - bud.c_i)
  * bud_start_in_the_bud ;


  //////// water exchange between mother and bud //////////////

  mother_bud_water_perm = 1.0; //
  mother.dV_exchange := - mother_bud_water_perm * (mother.pi_t - bud.pi_t)
   * bud_start_in_the_bud;

  bud.dV_exchange := mother_bud_water_perm * (mother.pi_t - bud.pi_t)
   * bud_start_in_the_bud;

end
```

A.2 Tables

Tab. A.1.: Parameter used in the SM and DM.

property	abbr.	value
General		
measured turgor pressure	P	$0.2\,\mathrm{MPa}$
cell wall thickness	d	$115\,\mathrm{nm}$
Poisson's ratio	ν	0.5
Steady state model		
relaxed base radius	R_{base}	$1.9\,\mu\mathrm{m}$
relaxed shaft radius	R_{shaft}	$0.5\,\mu\mathrm{m}$
expanded base radius	r_{base}	$2.5\,\mu\mathrm{m}$
turgor pressure	Π_{t}	$0.2\,\mathrm{MPa}$
Dynamic cell wall models		
mass density	ρ	0.5
yield stress	σ_{Y}	$0.4\,\mathrm{MPa}$
yield strain	ε_{Y}	$0.1\,\mathrm{MPa}$
Young's modulus at the base	E_{base}	$2.5\,\mathrm{MPa}$
Young's modulus at the shaft	E_{shaft}	$0.7\,\mathrm{MPa}$
Young's modulus at the tip	E_{tip}	$1.8\,\mathrm{MPa}$
characteristic elasticity time	τ	$200\,\mathrm{s}$
relaxed base radius	R_{base}	$1.9\,\mu\mathrm{m}$
initial expanded base radius	r_{base}	$2.5\,\mu\mathrm{m}$
radius of enhanced Young's modulus a the tip	R_{tip}	$0.4\,\mu\mathrm{m}$
radius of reduced Young's modulus at the shaft	R_{shaft}	$0.8\,\mu\mathrm{m}$
growth radius of the tip	R_{growth}	$0.45\,\mu\mathrm{m}$
extensibility (DM1)	λ	$0.004/(\mathrm{MPa\,s})$
extensibility (DM2)	λ^*	$0.004/\mathrm{s}$

A.3 Figures

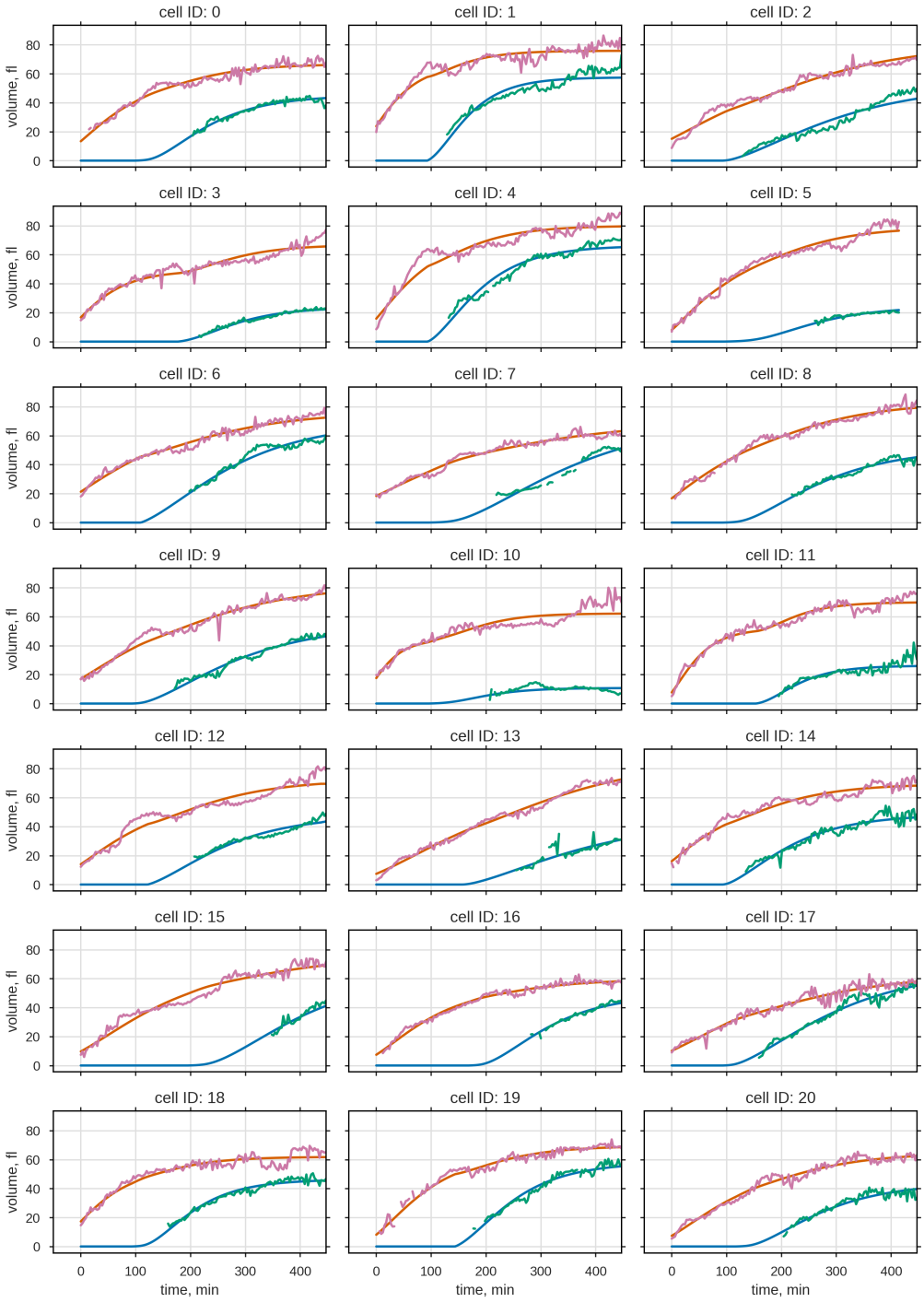

Fig. A.1.: Measured mother and bud volume trajectories for all analyzed cells of *data set 1* and corresponding model fits with estimated parameters in Fig. 3.8c.

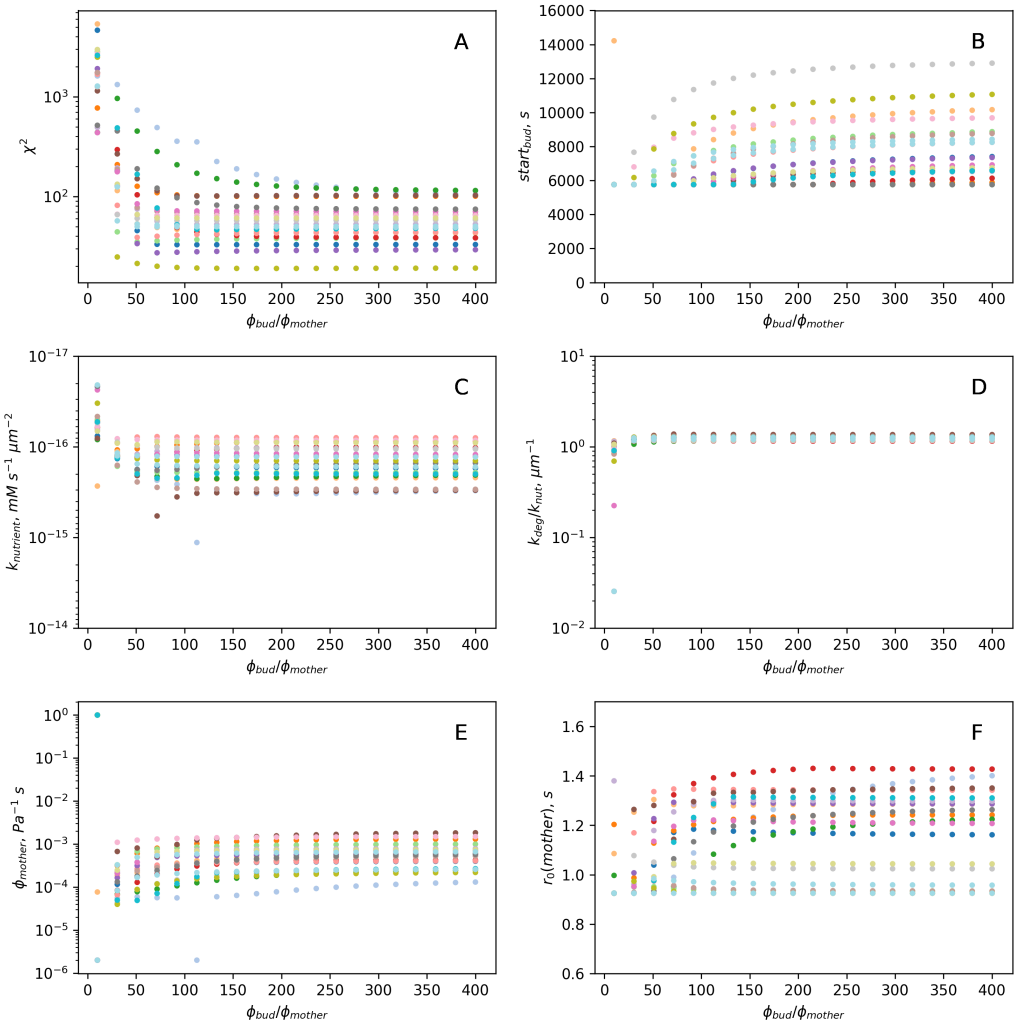

Fig. A.2.: Sensitivity analysis of the extensibility ratio $\phi_{\mathbf{bud}}/\phi_{\mathbf{mother}}$ for *data set 1*. A Profile likelihood analysis of the expansion rate ratio ϕ_{bud}/ϕ_{mother} revealed that ϕ_{bud} needs to be at least 100 times higher than ϕ_{mother}. The remaining free fitting parameters **B-F** to ϕ_{bud}/ϕ_{mother} were insensitive to variations of ϕ_{bud}/ϕ_{mother}.

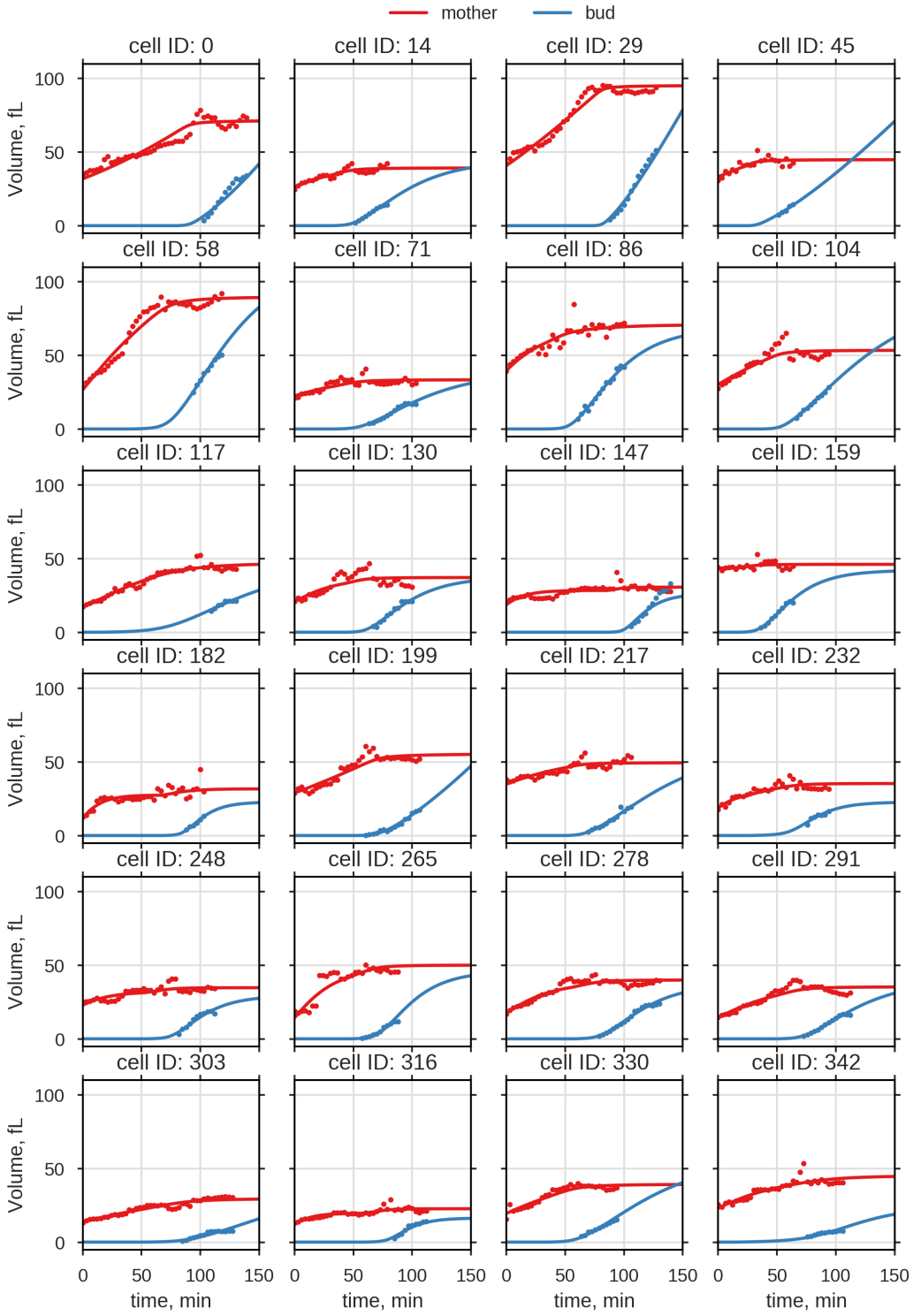

Fig. A.3.: 24/5880 analyzed volume trajectories from *data set 2* and corresponding fits of the cSCGM.

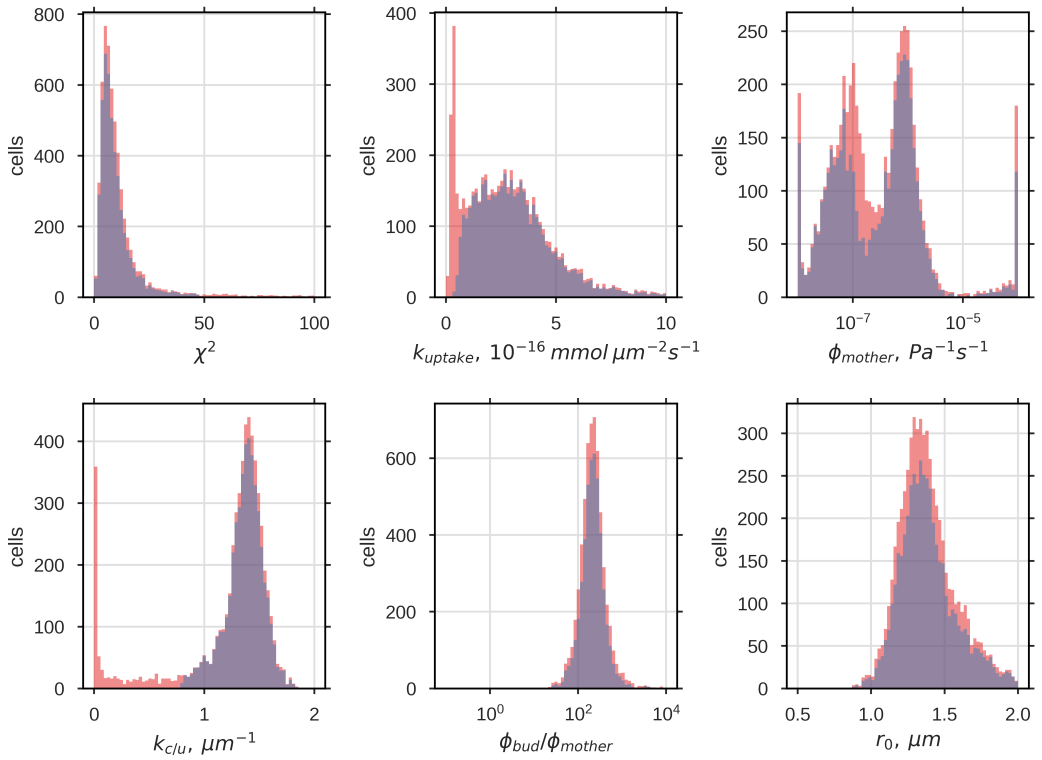

Fig. A.4.: Distributions of the estimated model parameters and χ^2 for *data set 2* In red distribution of all parameter set for all fitted cells (N=5880) and in blue the reduced parameter set for which $k_{\mathrm{u/c}} > 0.8\,\mu\mathrm{m}$ and $\chi^2 < 50$ (N=4680). First peak of k_{uptake} results solely from fits where $k_{\mathrm{u/c}}$ is below $0.8\,\mu\mathrm{m}$. Discarding sets with high χ^2 and low $k_{\mathrm{u/c}}$ shifts the first maxima of ϕ_{mother} to lower values while the second remains unaltered.

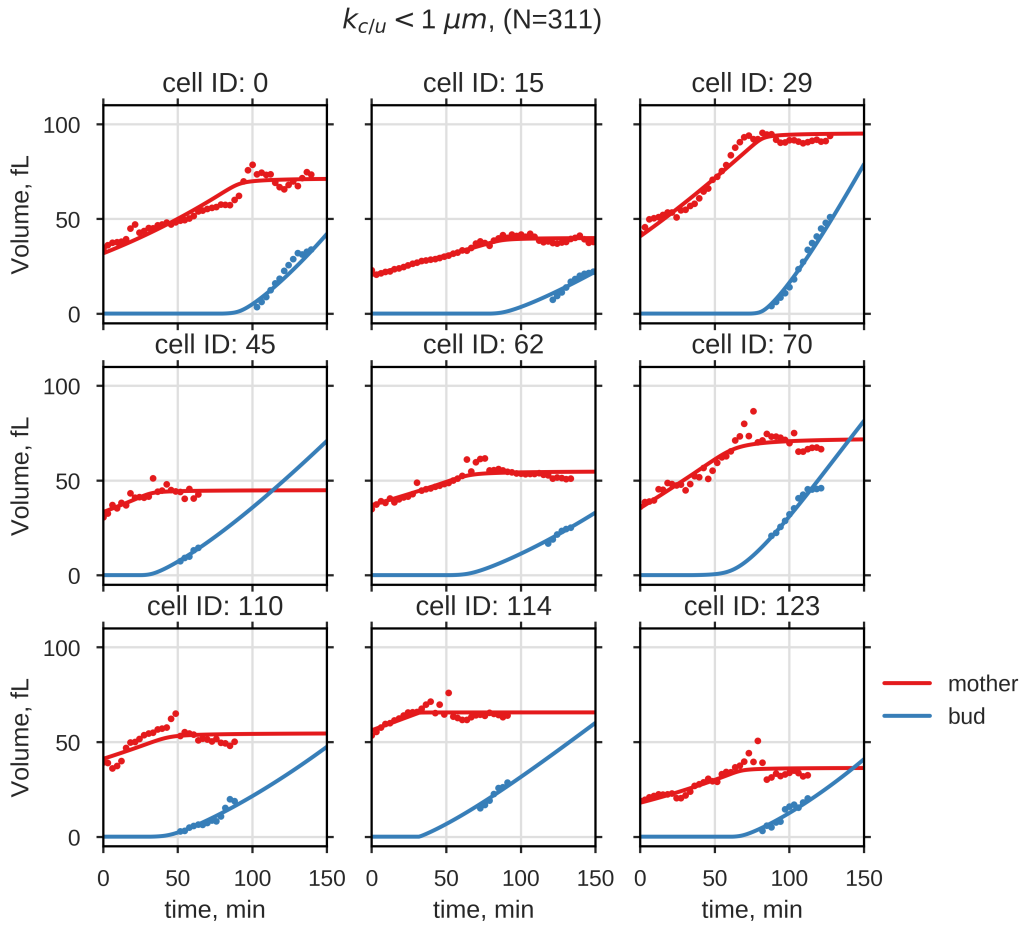

Fig. A.5.: Nine exemplary bud volume trajectories with corresponding fits from *data set 2*, where $k_{u/c} < 1\mu m$ Simulated bud volume shows no decreased growth rate at the end of the cell cycle.

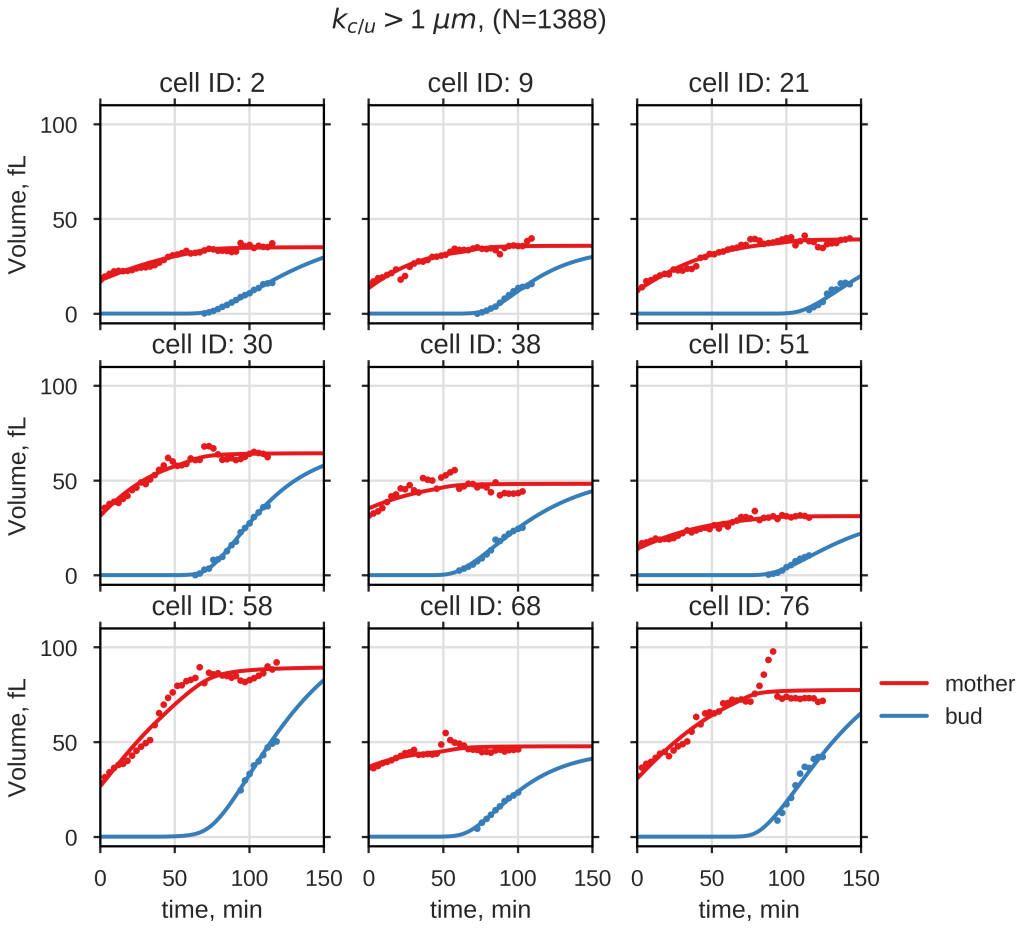

Fig. A.6.: Nine exemplary bud volume trajectories with corresponding fits from *data set 2*, where $k_{u/c} > 1\,\mu m$

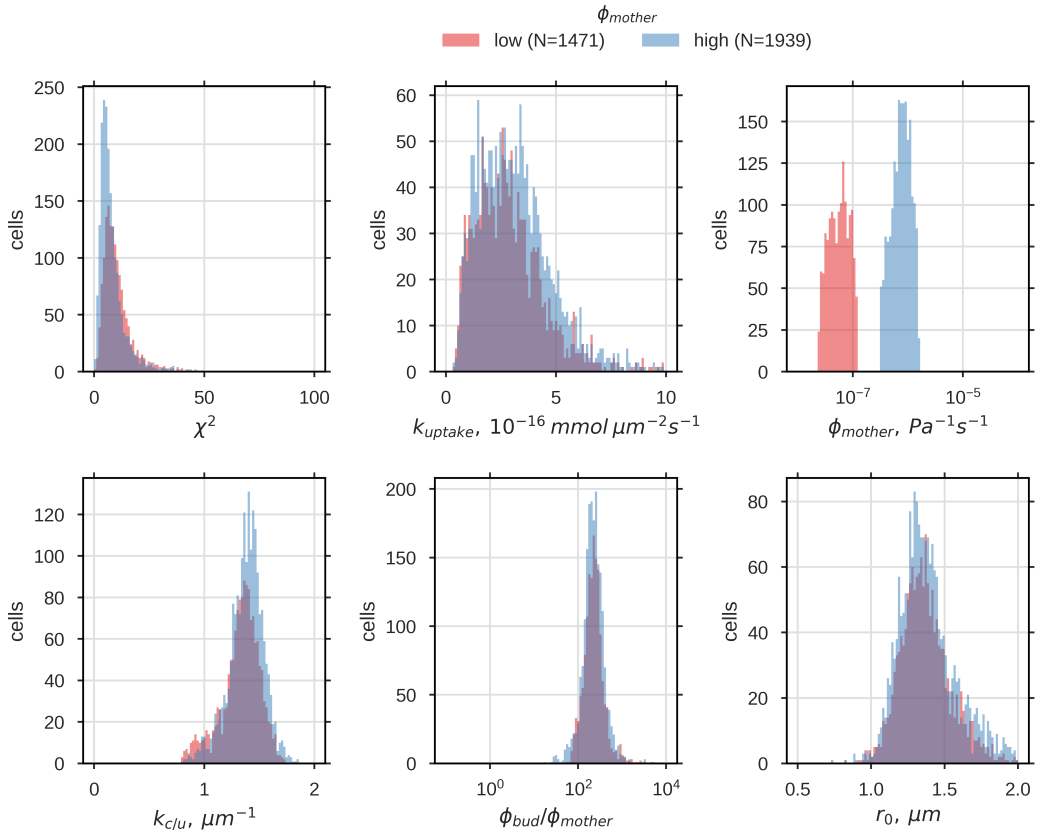

Fig. A.7.: Distributions of the estimated model parameters and χ^2 from *data set 2* for $\phi_{\mathbf{mother}} \approx \max(\phi_{\mathbf{mother}}|1)$ or $\phi_{\mathbf{mother}} \approx \max(\phi_{\mathbf{mother}}|2)$, red or blue.

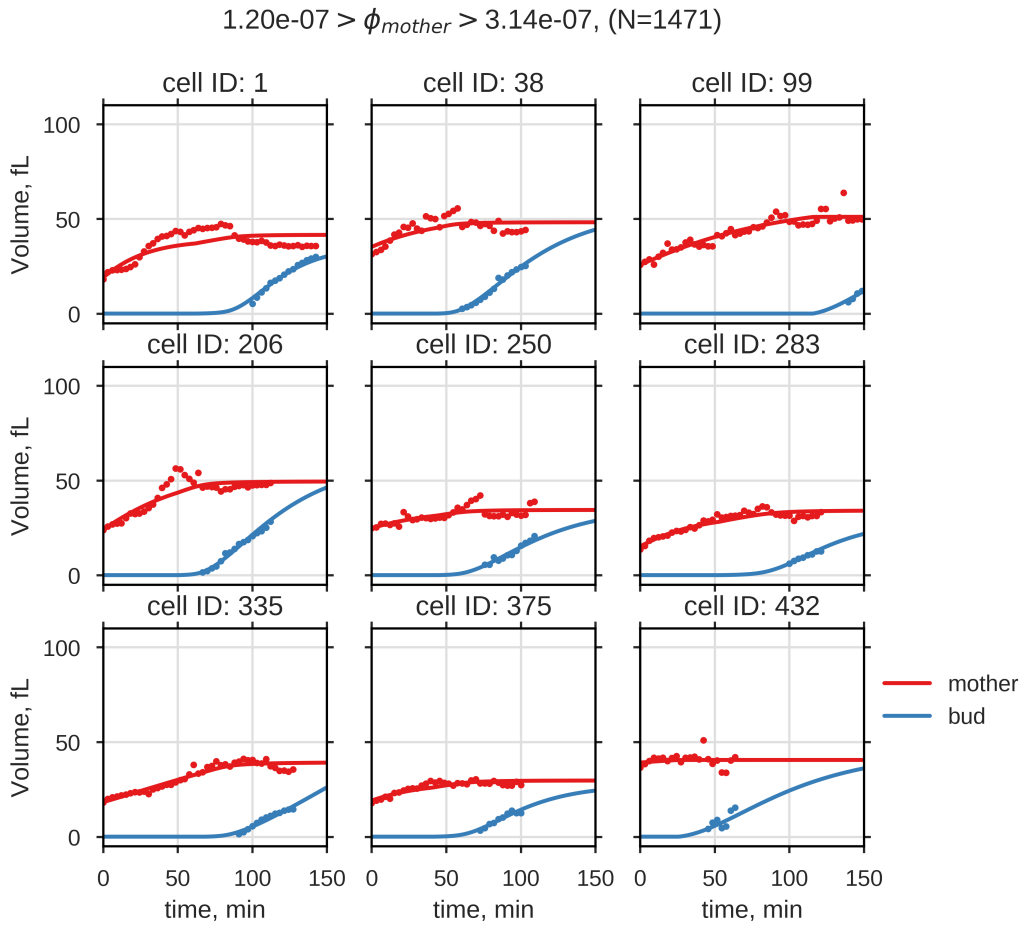

Fig. A.8.: Nine exemplary bud volume trajectories with corresponding fits from *data set 2*, where ϕ_{mother} is close to $\phi^{max}_{\text{mother}}(1)$

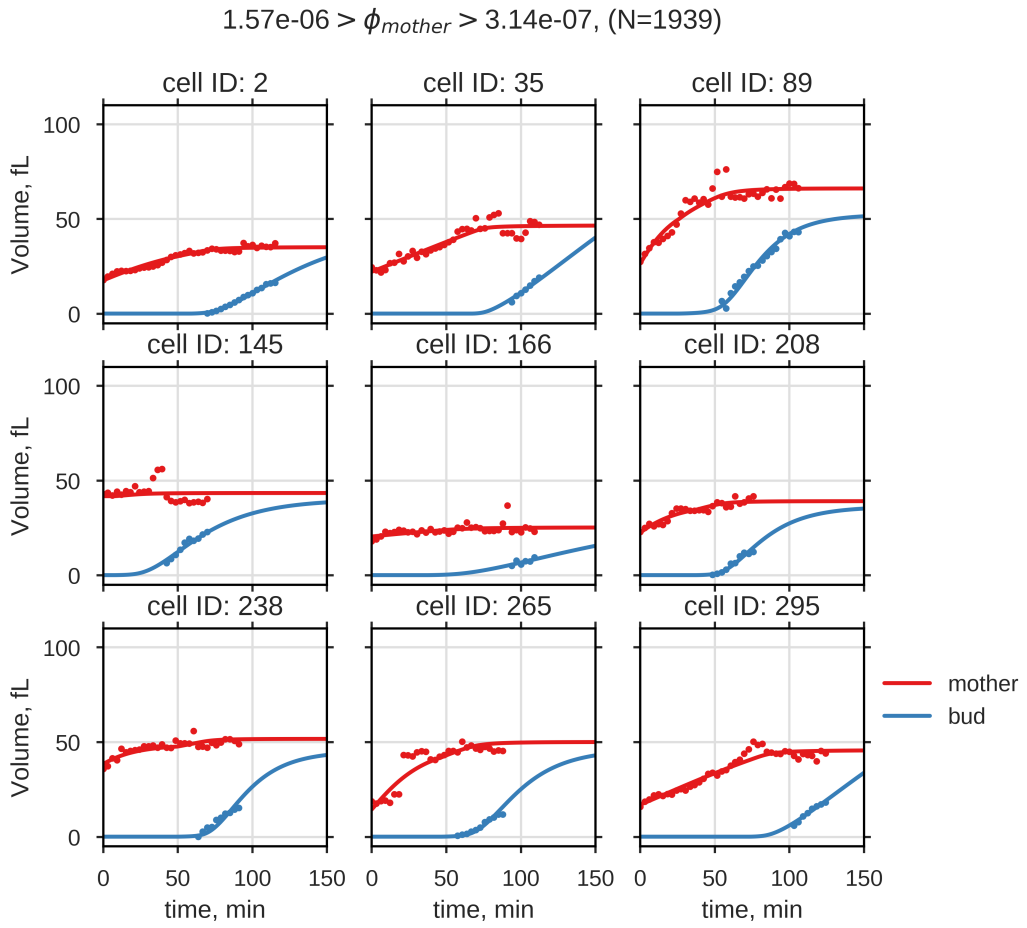

Fig. A.9.: Nine exemplary bud volume trajectories with corresponding fits from *data set 2*, where ϕ_{mother} is close to $\phi^{max}_{\text{mother}}(2)$

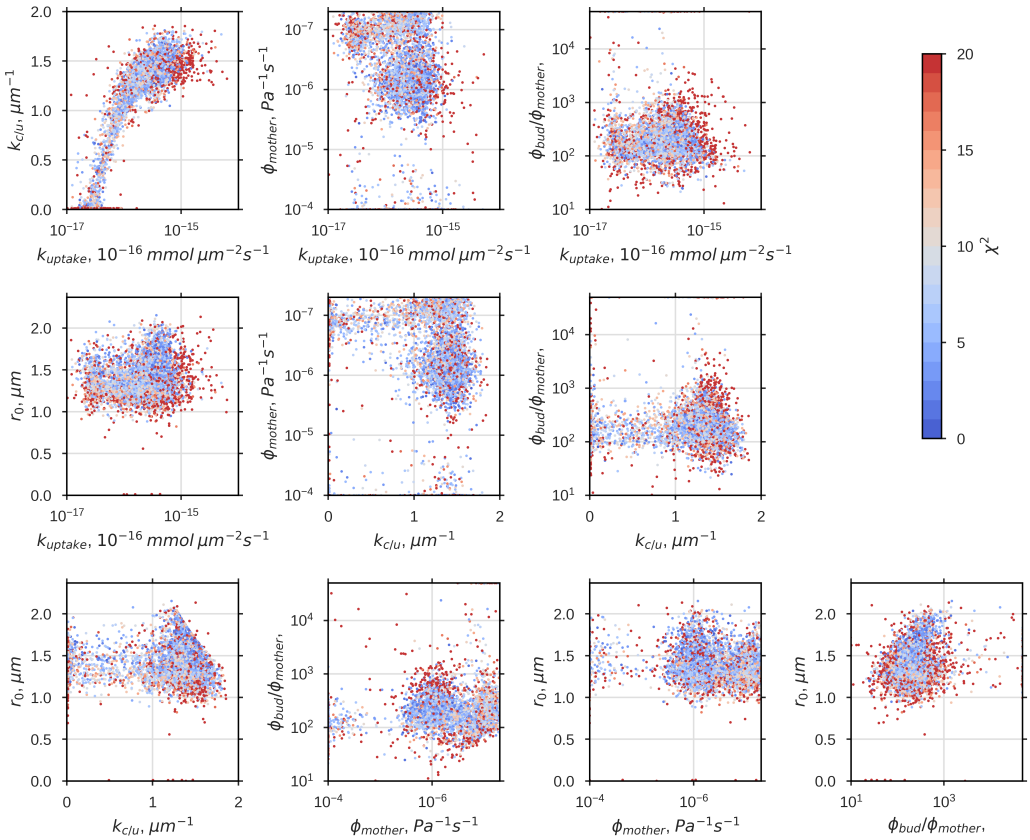

Fig. A.10.: Correlation between fitted parameters of *data set 2*. Color represents χ^2

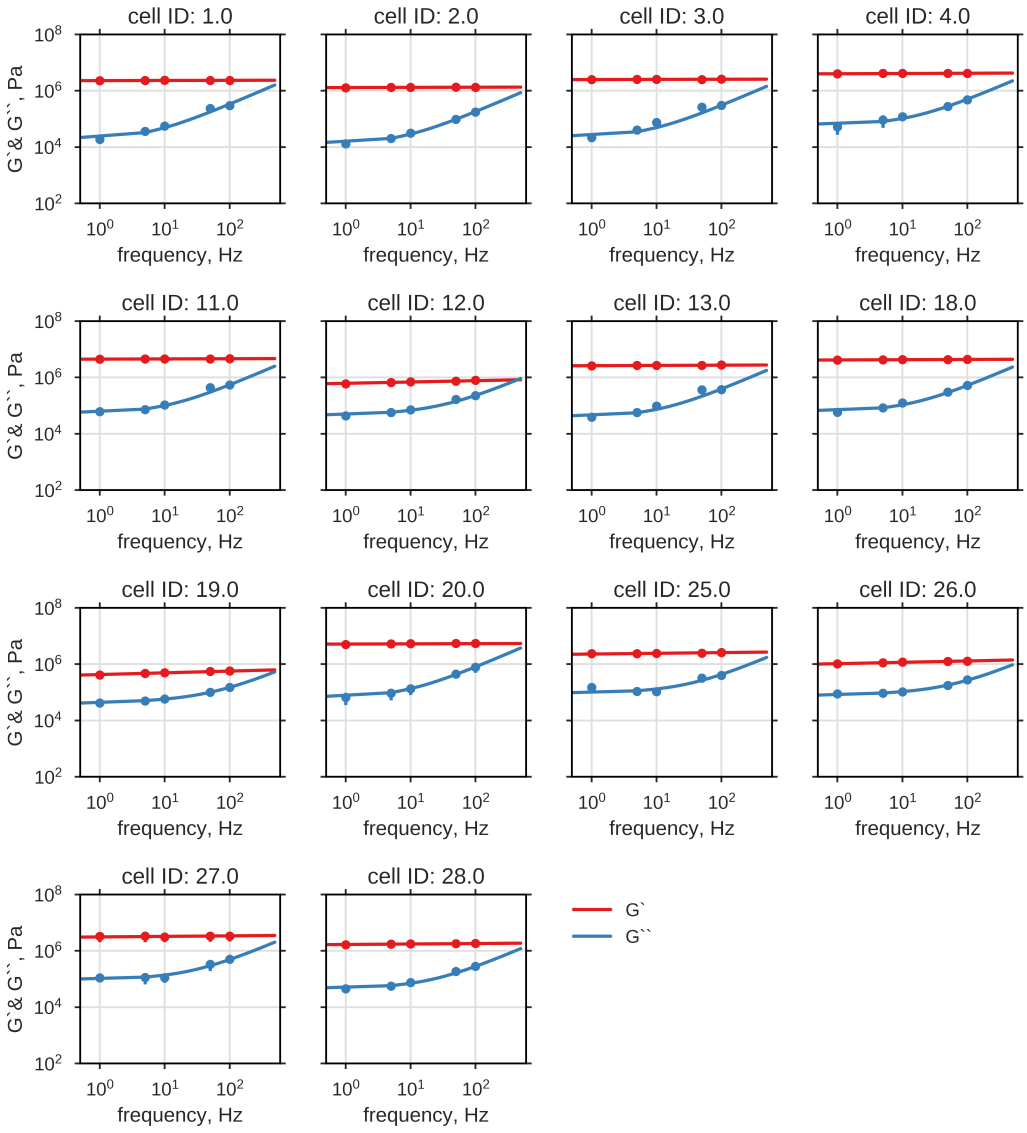

Fig. A.11.: Complex shear moduli of yeast cell walls from cells with $\approx 3\,\mu$m cell diameter. Frequency depending mean $\pm$ SEM of storage modulus G' (red dots) and loss modulus G'' (blue dots) with corresponding fit of the structural damping model (lines) is shown.

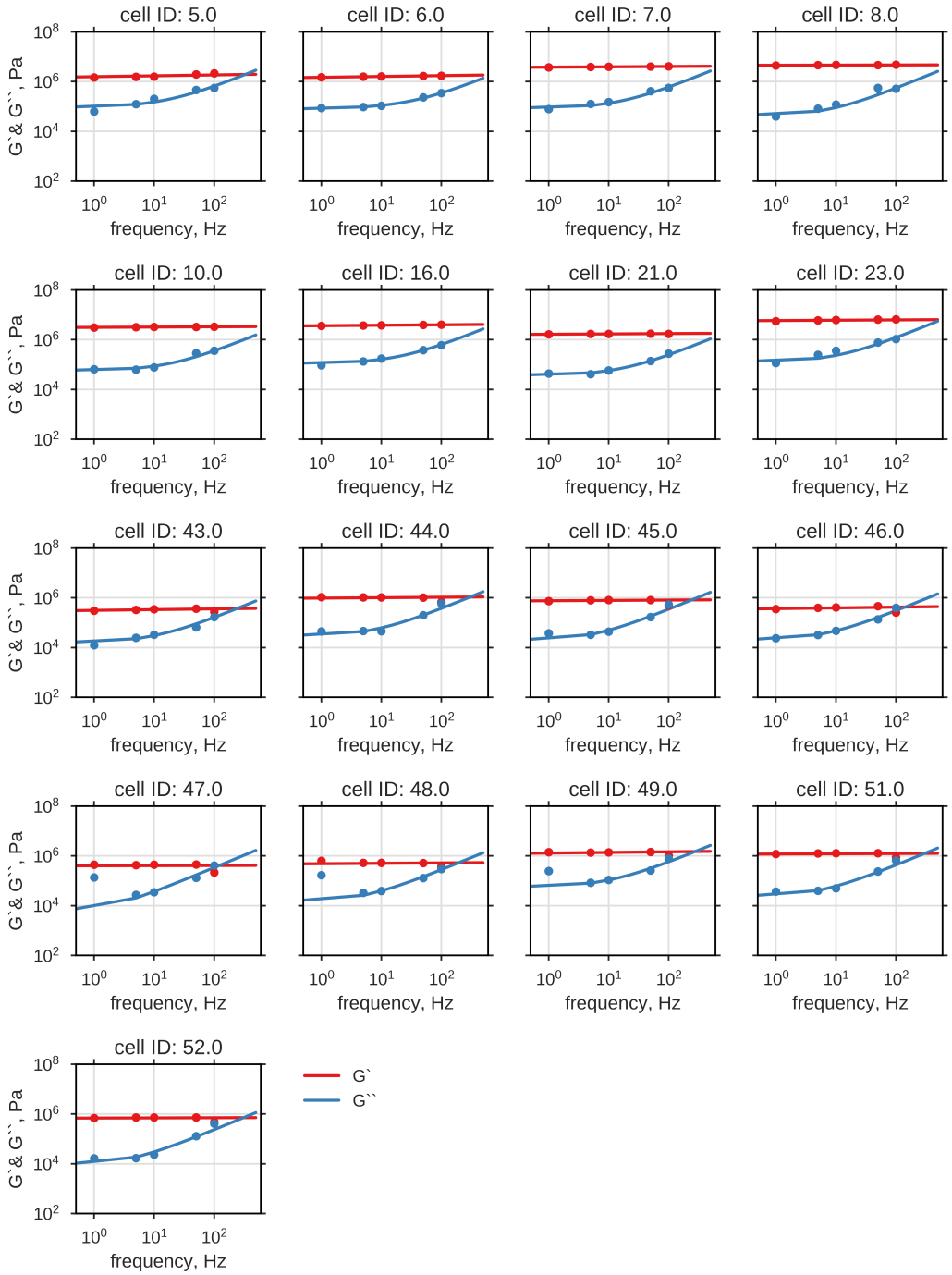

Fig. A.12.: Complex shear moduli of yeast cell walls from cells with $\approx 5\mu m$ cell diameter. Frequency depending mean $\pm$ SE of storage modulus G' (red dots) and loss modulus G'' (blue dots) with corresponding fit of the structural damping model (lines) is shown.

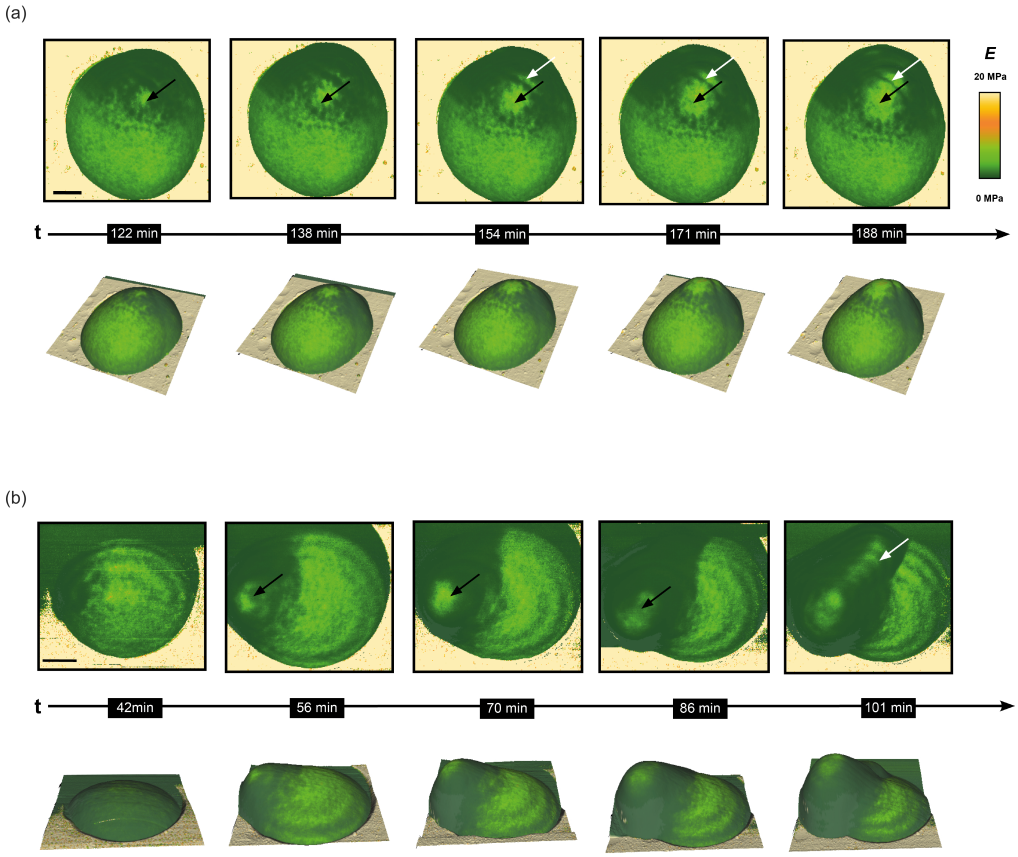

Fig. A.13.: Consecutive YM and height maps of shmooing MATa bar1Δ cells obtained with AFM. Acquisition of the time series was similar to the series shown in Fig. 5.9 and started $122\,\mathrm{min}$ and $42\,\mathrm{min}$ after α-factor treatment start. Cell in (a) and (b) were induced with $12\,\mu\mathrm{M}$ and $10\,\mu\mathrm{M}$ α-factor. Regions of stiff material at the protrusion tip are indicated by black arrows. Typical AFM-artifacts of tip-doubling (a) and "height shadow" (b) indicated by white arrows. Scale bar is $1\,\mu\mathrm{m}$.

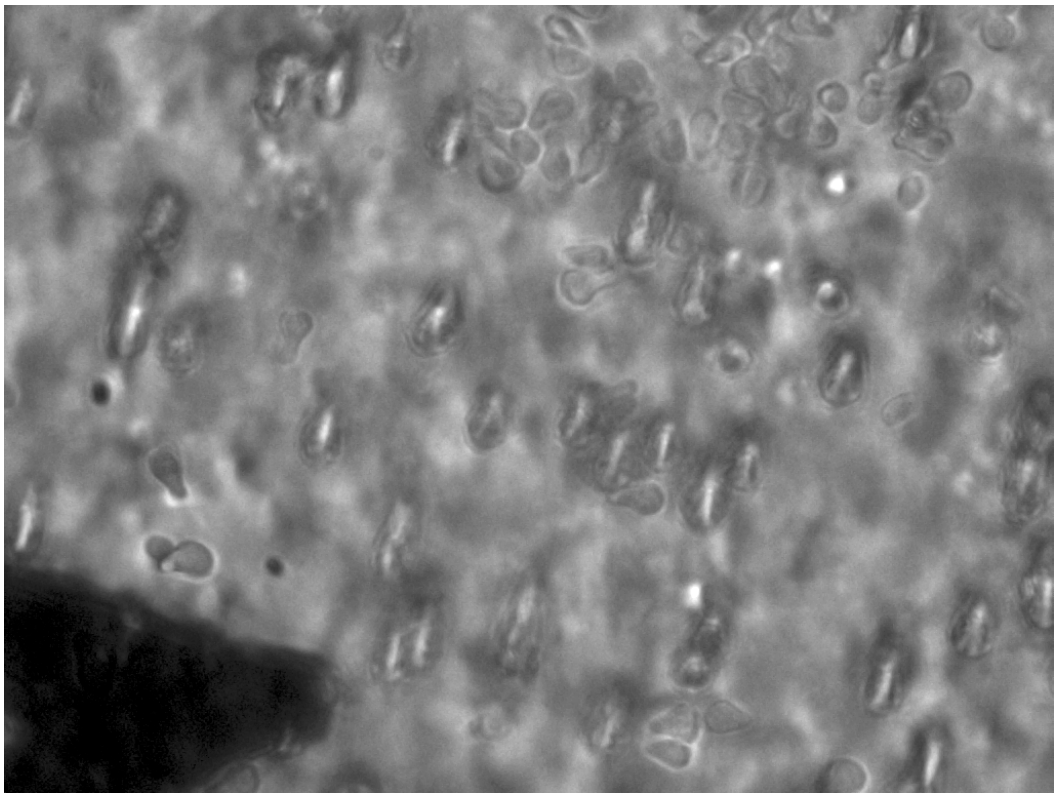

Fig. A.14.: AFM setup assessed with bright-field microscopy. Although non-trapped cells, i.e. only loosely attached to the filter surface, can be observed (top right), cells trapped in filter holes cannot be identified. Dark triangular shape in the left bottom is cantilever.

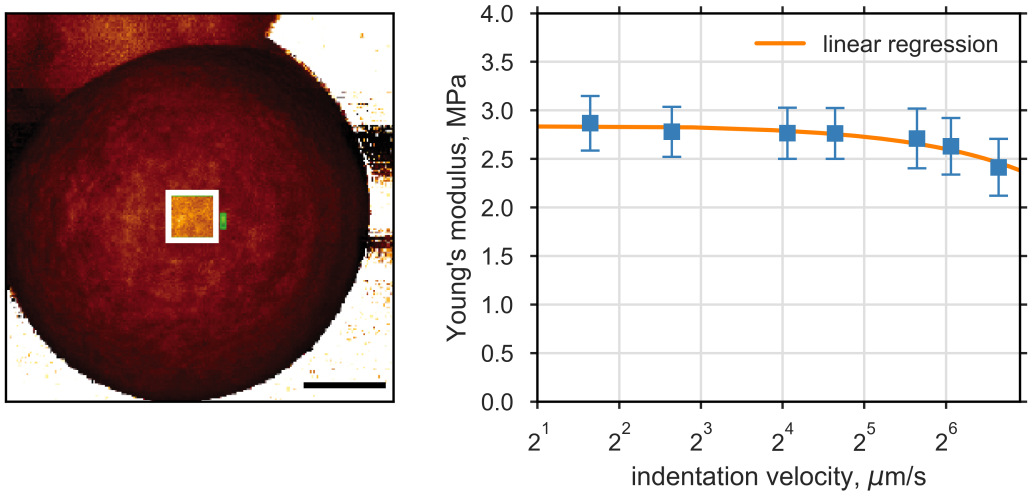

Fig. A.15.: Dependence of the measured Young's modulus E on the approach velocity. Measured cell wall YM (mean±SD, N=1024), obtained from a $400\,\mathrm{nm}\times400\,\mathrm{nm}$ region at the top of a non-induced MATa bar1Δ cell, plotted against indentation velocity (blue). Linear regression (red) revealed a minor decrease in E with $(-4.6\pm0.8)\times10^{-3}\,\mathrm{MPa}/(\mu\mathrm{m\,s})$.

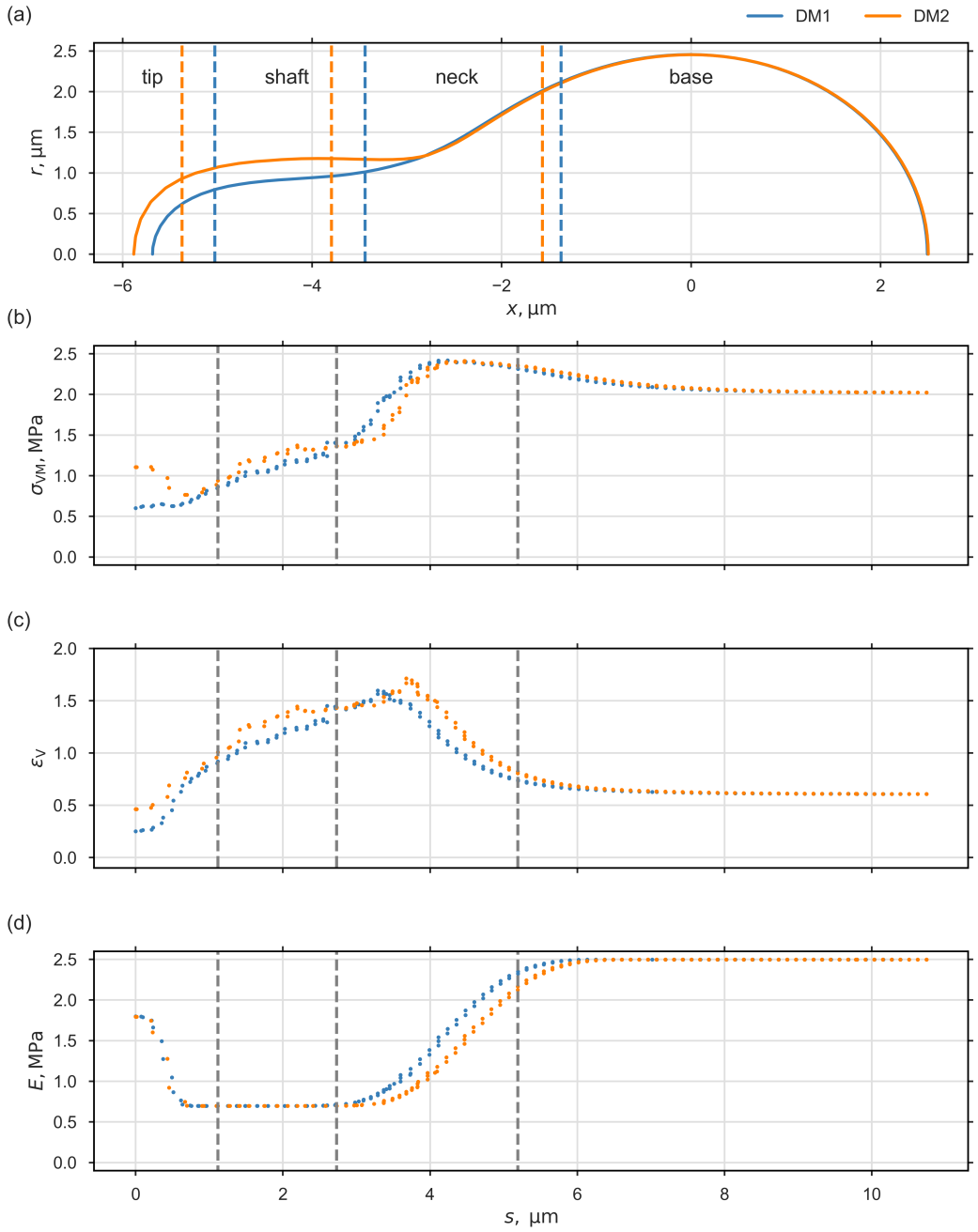

Fig. A.16.: Stress, strain and elasticity profiles from simulations of DM1 and DM2 (a) cell contours, after $54.2\,\mathrm{min}$ simulation time with, indicated regions tip, shaft, neck and base. Dashed lines correspond those position, with same arc length ($s = 0$ at the tip), which were compared to experimental data in Fig. 5.13. (b-d) von Mises stress σ_{VM}, volumetric strain ε_{V} and Young's modulus E with respect to the arc length s.

Nomenclature

α	power-law exponent
δ	indentation depth
η	loss tangent, hysteresivity
κ_θ	circumferential curvature
κ_s	meridional curvature
μ	viscosity
ν	Poisson's ratio
Ω	Surface
ω	angular frequency
ϕ	extensibility in the SCGM or angle in the SM
Π	osmotic pressure
Π_c	critical turgor pressure
Π_e	external osmotic pressure
Π_i	internal osmotic pressure
Π_t	turgor pressure
σ	stress, continuum mechanics
σ_r	reflection
σ_y	yield stress
σ_{VM}	von Mises stress

σ_θ principle circumferential stress circumferential

σ_s principle meridional stress

θ angle (angle of conical AFM tip, circumferential angle)

ε^e engineering strain

ε^t true strain

ε_y yield strain

$\varepsilon_{\text{Bingham}}$ strain of Bingham element

$\varepsilon_{\text{Hook}}$ elastic strain of Hookean element

ε_θ principle circumferential strain

ε_s principle meridional strain

ε_V volumetric strain

A surface area

b hydrodynamic drag coefficient

c concentration

c_e external concentration

c_i internal concentration

d cell wall thickness

E elastic modulus or Young's modulus (3D)

E^* elastic modulus or Young's modulus (2D), in-plane elasicity

E_y yield energie

F force

f frequency

f_m yield function

F_p force on the cross-section of a sphere caused by internal pressure

f_t transition frequency

F_w force on the cross-section of a the wall of a spherical shell caused by stress

G shear modulus

G' storage modulus

G'' loss modulus

G^* complex shear modulus

h tip-sample distance

H_d transfer function, hydrodynamic drag

H_s transfer function, sample

i imaginary unit

J_{w}^{in} water influx

k spring constant

$k_{\mathrm{consumption}}$ osmolyte consumption rate per unit volume

k_{uptake} osmolyte uptake rate per unit area

L_{p} hydraulic conductivity of the membrane per unit area

m_{eff} effective mass of the spring

P Pressure

R ideal gas constant

r radius

r_{os} radius of the osmotic volume

R_{ref}	reference radius
T	temperature
t	time
V	Volume
V_{b}	volume unaccessible for osmolytes
V_{os}	volume accessible for osmolytes

Abbreviations

AFM atomic force microscopy. 10, 11, 24, 25, 29–31, 43, 46, 57, 70, 75–77, 89, 93, 97, 100, 101, 104, 106, 116, 166, 167, 175

CMA-ES Covariance Matrix Adaptation Evolution Strategy. 21

CRD serine-rich domain. 111, 112

cSCGM coupled-compartment growth model. 21, 46, 53, 54, 56–58, 60–66, 68–70, 72, 75, 84, 129, 156

CWI yeast cell wall integrity signaling pathway. 8, 70, 82, 91, 92, 120, 123, 129

CWP cell wall protein. 8, 9

DM dynamic cell wall model. 93, 106, 108–116, 119–123, 153, 168

FFT fast Fourier transform. 42, 79

GPCR G protein-coupled receptor. 90

GPI glycosylphosphatidylinositol. 8

IQR interquartile range. 61, 103

MAPK mitogen activated protein kinase. 90

MATα mating type α. 4, 5, 22, 90, 91

MATa mating type a. 2, 4, 5, 22, 23, 43, 90, 91, 98–103, 105, 114, 115, 167

MFD microfluidic device. 22, 23, 114, 115

NGAR N-glycosylated asparagine residue. 112

ODE ordinary differential equation. 17, 19, 20, 47, 49, 50

PIR protein with internal repeats. 8

PRP yeast pheromone response pathway. 90, 91

SBML systems biology markup language. 21, 50

SCGM single-compartment growth model. 17, 19–21, 34, 46, 47, 50–53, 55–57, 68, 69, 71–73, 78, 87, 93, 94, 108, 128, 129, 169

SD standard deviation. 76, 80, 81, 83, 98, 114, 115, 118, 167

SD medium yeast synthetic drop-out medium. 21–23, 42, 43, 114, 115

SE standard error of the mean. 79, 99, 165

SEM scanning electron microscopy. 21, 30, 43, 44, 89, 97, 100, 101, 164

SFSD medium sterile-filtrated, yeast synthetic drop-out medium. 30, 57, 98

SGR soft glassy rheology model. 39, 84–86, 128

SM mechanical steady-state cell wall model. 16, 93–95, 97, 100, 106, 109, 116, 119, 125, 153, 169

STM scanning tunnel microscopy. 24

STR serine/threonine-rich region. 111–113, 120, 130

TMD transmembrane domain. 112

UDP-Glc uridine diphosphate glucose. 8, 118

UDP-GlcNac uridine diphosphate glucose N-acetylglucosamine. 8, 118

YM Young's modulus. 10, 16, 26–28, 33, 49, 57–59, 70, 94, 95, 100, 103–105, 107, 109, 112, 115–118, 125, 166, 167

Acknowledgement

First and foremost, I would like to express my sincere gratitude to my supervisor Edda Klipp for her unwavering support, for the challenges and the discussions and for the friendly environment she created, in which I could grow and develop as scientist. I would also like to thank Andreas Herrmann for his support and the opportunities he provided to explore the bandwidth of experimental methods. Furthermore, the assistance in the laboratories provided by Gabriele Schreiber, Lisa Mallis, Christiane Müller, Sabine Schiller and Alice Wittig was greatly appreciated and enabled some experiments in the first place.

At this point, I want to thank Anna Arbuzova deeply for her support and her advice during my first scientific steps and beyond. For introducing me into AFM and for all the coffee breaks and all the support I want to thank my dear colleague Manuel Gensler.

To all my former and present colleagues in the group for theoretical biophysics, I want to say: “Thank you, it was a great pleasure to work with you!” In particular I would like to thank Ivo Maintz, Wolfgang Giese, Jannis Uhlendorf, Friedemann Uschner and Max Schelker for their help with all the small and big difficulties I encountered and not least for their friendship. I would like to offer my special thanks to Katja Tummler and Judith Wolke for proofreading, extraordinary help on the last mile and the whip.

Furthermore, I would like to thank Andrea for placing the idea of a doctoral thesis in my head and for her unshakable faith in me and Thomas and Sandra for their friendship and the continuous moral support. In addition, I wish to thank my parents and my sister for their support and encouragement. Last but not least I would like to thank my love Maria and my sunshine Leonid for their patience and their smiles, which have picked me up again and again.

My work was supported by the Deutsche Forschungsgemeinschaft in the frame work of the Collaborative Research Center (SFB) 740 “From molecules to modules.”

Colophon

This thesis was typeset with LaTeX 2_ε. It uses the *Clean Thesis* style developed by Ricardo Langner. The design of the *Clean Thesis* style is inspired by user guide documents from Apple Inc.

Download the *Clean Thesis* style at `http://cleanthesis.der-ric.de/`.

Declaration

I hereby certify that this thesis has been composed by me and is based on my own work, unless stated otherwise. No other person's work has been used without due acknowledgment in this thesis. All references have been quoted and all sources of information, including graphs and data sets, have been specifically acknowledged.

Berlin, September 16, 2019

Björn Goldenbogen